Cost-Effective Energy Transfer for Offshore Wind

Victor Timmers

A thesis submitted for the degree of
Doctor of Philosophy

Department of Electronic and Electrical Engineering
University of Strathclyde

December 2024

Declaration

This thesis is the result of the author's original research. It has been composed by the author and has not been previously submitted for examination which has led to the award of a degree.

Victor Timmers

31 December 2024

Date

Acknowledgements

I would like to thank my academic supervisor Dr. Agustí Egea Àlvarez, for all his encouragement and support, which included everything from helping me with my control models and giving feedback on my papers, to assisting in my career development and providing behind-the-scenes administrative support. Most of all, I want to thank him for his never-ending enthusiasm for my work.

I also want to express my sincere gratitude to my industrial supervisor, Dr. Aris Gkountaras, and my colleagues at Siemens Gamesa, for their feedback and industrial insight, which were instrumental in raising the quality of my research and shaping its direction.

I am also grateful to Prof. Lie Xu for his help with my DC/DC converter modelling and to Prof. Khaled Ahmed for his advice and feedback on my chartership application.

I want to thank all my colleagues and friends at the university. Specifically, my thanks goes out to Sophie Coffey for the great time collaborating and attending conferences together. Thank you to Euan MacRae for the many technical and non-technical discussions. Thank you to Sam Harrison and Callum Henderson for their support with my grid forming models. Thank you to Mathieu Kervyn for his chartership advice, and thank you to Luke Benedetti, Irene Masenge, Rui Alves, Oyedotun Oyewole, Oswin Ashwood, and everyone else for making the office such an enjoyable place to work.

I would like to thank my parents, Paul and Kizito, for their unconditional love and support throughout my life, and my siblings, Nyanza, Justus, Paul, and Samuel, whose many successes inspire me to do my best.

I want to thank my wife, Jasmine, for supporting my decision to pursue a PhD, believing in me, and for having the patience to listen to me talk endlessly about my work. Thank you as well to my dog, Augie, for keeping me sane and active throughout these years.

Finally, I gratefully acknowledge the funding I received from Siemens Gamesa Renewable Energy and the UK Engineering and Physical Sciences Research Council, ICASE grant number EP/T517665/1.

Abstract

Offshore wind and green hydrogen have the potential to help address the energy trilemma of sustainability, security, and affordability. However, their high cost remains one of the main barriers to their rapid development. Using DC collection systems in offshore wind farms has the potential to make the transfer of electrical energy to shore more cost-effective by reducing the size of offshore platforms or by removing them entirely. Similarly, co-locating electrolysers and wind turbines without a grid connection can make the transfer of chemical energy more cost-effective by removing the need for the offshore platform, export cables, and collector cables.

The first part of this thesis identifies the most promising DC wind farm configurations and carries out a cost-benefit analysis. The results show that all-DC wind farms can lower the levelised cost of electricity, depending on factors such as the DC/DC converter costs, platform costs, and collector voltage. A multi-objective optimisation is then carried out for four promising DC/DC converter topologies, and their performance is compared in terms of reliability, volume, weight, and losses. The optimal operating frequency for each of the selected topologies is also determined. The results show that the single-phase single active bridge operating at 2.5 kHz or the three-phase dual active bridge operating at 1 kHz are optimal.

The second part of the thesis investigates the technical challenges associated with a standalone wind turbine and electrolyser system. A complete control system is developed to allow off-grid operation, and three strategies are proposed to balance the power between the wind turbine and electrolyser. The levelised cost of hydrogen is then investigated for each power balancing strategy, as well as for three alternative DC-based drivetrains to improve the system efficiency. The results show that using supercapacitor energy storage and the standard AC-based drivetrain is the most realistic and cost-effective option.

Contents

List of Figures

List of Tables

Nomenclature

Abbreviations

AC	Alternating current
BoL	Beginning of life
BPF	Band-pass filter
CAPEX	Capital expenditure
CCM	Continuous conduction mode
CSA	Cross-sectional area
DAB1	Single-phase, dual active bridge
DAB3	Three-phase, dual active bridge
DC	Direct current
DCM	Discontinuous conduction mode
DOHP	Decentralised Offshore Hydrogen Platform
EoL	End of life
ESCC	Electrolyser-side converter control
ESS	Energy storage system
ETYS	UK Electricity Ten Year Statement
FIT	Failure-in-time
GD	Gate drive
GDL	Gas diffusion layer
GIS	Gas-insulated switchgear
GR	González-Rodríguez cost data
HVAC	High voltage alternating current
HVDC	High voltage direct current
IGSE	Improved Generalised Steinmetz Equation
IPOP	Input-parallel, output-parallel
IPOS	Input-parallel, output-series

ISOP	Input-series, output-parallel
ISOS	Input-series, output-series
LB_{AC}	Lundberg cost data for AC cables
LB_{DC}	Lundberg cost data for DC cables
LCC	Line commutated converter
LCOE	Levelised cost of energy
LCOH	Levelised cost of hydrogen
LSCC	Line-side converter control
LUT	Look-up table
MEA	Membrane electrode assembly
MMC	Modular multilevel converter
MPPT	Maximum power point tracking
MPTA	Maximum torque per ampere
MSCC	Machine-side converter control
MVDC	Medium voltage direct current
NPV	Net present value
NSG	North Sea Grid
NZpitch1	Non-zero pitch with original rotor speed
NZpitch2	Non-zero pitch with increased rotor speed
OPEX	Operational expenditure
OVC	Overvoltage category used in IEC standard 61800-5-1
PD	Proportional-derivative
PEM	Proton-exchange membrane
PI	Proportional-integral
RMC	Reduced matrix converter
RMS	Root-mean-square
SAB1	Single-phase, single active bridge
SAB3	Three-phase, single active bridge
SEK	Swedish krona
VSC	Voltage source converter
WTG	Wind turbine generator
XLPE	Cross linked polyethylene
YSZ	Yttria-stabilized zirconia

Latin Symbols

A	Width of the transformer core limbs and yoke	m
A_c	Cross-sectional area of the cable conductor	m^2
A_c	Failure rate of the overall converter	yr^{-1}
A_{cell}	Electrolyser cell area	cm^2
A_{core}	Cross sectional area of the magnetic core	m^2
$A_{Cu1,2}$	Area of copper in the transformer primary or secondary winding	m^2
A_i	Wind speed van der Hoven amplitude terms	m s^{-1}
A_m	Base availability of one converter module	
A_r	Swept area by the wind turbine rotor	m^2
a	Transformer turns ratio	
$a_{1,2}$	Wind speed turbulence Kalman filter constants	
B	Thickness of the transformer core limbs	m
B_{max}	Maximum flux density	T
B_{sat}	Core magnetic saturation	T
$B(t)$	Instantaneous magnetic flux density	T
C	Capacitor capacitance	F
C_1	First voltage-dependent cable cost constant	M€ km^{-1}
C_2	Second voltage-dependent cable cost constant	M€ km^{-1}
C_3	Third voltage-dependent cable cost constant	MW^{-1}
C_{ACcab}	Cost of AC cables	M€ km^{-1}
$C_{AC/DCconv}$	Cost of the AC/DC converter	M€
C_{ACpl}	Cost of the AC platform	M€
C_{ACWT}	Cost of an AC wind turbine	M€
C_{cab}	Cable capacitance	µF km^{-1}
C_{DCplat}	Cost of the DC platform	M€
C_{DCWT}	Cost of a DC wind turbine	M€
$C_{dl,a,c}$	Electrolyser cell double layer capacitance of the anode or cathode	F
C_{el}	Electrolyser capital cost	M€
$C_{HVACcab}$	Cost of HVAC transmission cables	M€ km^{-1}
$C_{HVDCcab}$	Cost of the HVDC transmission cable	M€ km^{-1}
C_p	Wind turbine power coefficient	
C_{SG}	Cost of the switchgear	M€

C_{SR}	Cost of the shunt reactor	M€
C_t	Capital cost in year t	M€
C_{TR}	Cost of the transformer	M€
c	Wind turbine drive train damping coefficient	N s m^{-1}
$c_{1,\ldots,9}$	Wind turbine characteristic constants	
D	DC/DC converter duty cycle	
D_{max}	Maximum DC/DC converter duty cycle	
D_r	Discount rate	%
d_c	Insulation distance between transformer cores	m
d_i	Insulation distance between the transformer winding and core	m
d_{iso}	Isolation distance between the LV and HV transformer windings	m
d_{V_2}	Clearance distance between the converter and its enclosure	mm
d_{V_m}	Clearance distance between individual converter modules	mm
E_{ess}	Energy storage system energy capacity	MJ
E_{H_2}	Hydrogen production specific energy consumption	kWh kg^{-1}
E_{max}	Maximum insulation strength	kV mm^{-1}
E_{off}	Device turn-off losses	J
E_{on}	Device turn-on losses	J
E_{rr}	Device reverse recovery losses	J
F	Faraday constant	9.649×10^4 C mol^{-1}
f	DC/DC converter frequency	Hz
f_h	Harmonic frequency	Hz
f_i	Wind speed van der Hoven spectrum sampling frequencies	hr^{-1}
f_{obj}	Objective function minimised to select the optimal transformer design	
G_{ICC}	Inner current controller transfer function	
G_{M_f}	Marginal gravimetric power density gains at frequency f	
$G_{V_{AC}}$	AC voltage controller transfer function	
$G_{V_{DC}}$	Outer DC link voltage controller transfer function	
G_{V_f}	Marginal volumetric power density gains at frequency f	
G_β	Pitch controller transfer function	
$G_{\Delta\beta}$	Enhanced pitch controller transfer function	
$H_{2,t}$	Hydrogen production in year t hfill kg	
H_F	Wind speed turbulence Kalman filter transfer function	

HHV	Higher heating value of hydrogen	39.4 kWh kg^{-1}
h	Harmonic order	
$h_{1,2}$	Height of one turn in the transformer primary or secondary winding	m
$h_{1,2t}$	Transformer total height of the primary or secondary winding	m
h_w	Transformer winding window height	m
P_c	Current flowing through the cable	A
$I_{D,2}$	Output diode current rating	kA
I_h	Rms magnitude of the current at f_h	A
$I_{IGBT,1,2}$	IGBT current rating in the input or output bridge	kA
I_{max}	Maximum current rating of the semiconductor	A
I_{sw}	Current stress on the semiconductor	A
I_w	Root-mean square current in the transformer winding	A
i_{cell}	Electrolyser cell current	A
$i_{d,q}$	D-axis and q-axis stator currents	A
i_L	Instantaneous current through the transformer inductance	A
i_{on}	Instantaneous current through the semiconductor device	A
J_0	Electrolyser cell exchange current density	A cm^{-2}
J_{cell}	Electrolyser cell current density	A cm^{-2}
J_L	Electrolyser cell limiting current density	A cm^{-2}
J_m	Wind turbine machine inertia	kg m^2
J_r	Wind turbine rotor inertia	kg m^2
J_t	Wind turbine combined rotor and machine inertia	kg m^2
J_w	Transformer winding current density	A m^{-2}
K	Wind turbine drive train spring constant	N m^{-1}
K_{ac}	Ratio of AC to DC resistance of the transformer winding	
$K_{ac,h}$	Ratio of AC to DC resistance at harmonic frequency f_h	
K_{Cp}	Maximum power point tracking optimal gain	
$K_{d_{\Delta\beta}}$	Enhanced pitch controller derivative gain	
K_F	Wind speed turbulence Kalman filter magnitude	m s^{-1}
$K_{i_{ICC}}$	Current controller integral gain	
K_{i_V}	DC link voltage control integral gain	
$K_{i_{VAC}}$	AC voltage controller integral gain	
K_{i_β}	Pitch controller integral gain	

K_J	Wind turbine updated machine torque inertia factor	
$K_{p_{ICC}}$	Current controller proportional gain	
K_{p_V}	DC link voltage control proportional gain	
$K_{p_{VAC}}$	AC voltage controller proportional gain	
K_{p_β}	Pitch controller proportional gain	
$K_{p_{\Delta\beta}}$	Enhanced pitch controller proportional gain	
K_{WT}	Multiplication factor for DC wind turbines	
k	Minimum number of DC/DC converter modules	
k_c	Core fill factor	
k_{c0}	Capacitor constant volume factor	m^3
k_{c1}	Capacitor linear volume factor	$m^3\ F^{-1}$
k_f	Copper fill factor	
k_p	Number of parallel connected DC/DC converter modules	
k_S	First Steinmetz constant	$W\ m^{-3}$
k_s	Number of series connected DC/DC converter modules	
k_{saf}	Safety factor for transformer insulation distances	
$k_{\sigma,v}$	Wind speed turbulence regression curve slope	
L	DC/DC converter series inductance	H
L_{cab}	Cable length	km
$LCOH_{ideal}$	Ideal levelised cost of hydrogen for a 100% efficient system	$€\ kg^{-1}$
$L_{d,q}$	D-axis and q-axis stator inductances	H
L_F	Wind speed turbulence Kalman filter length scale	m
l_m	Magnetic mean path length of one transformer core	m
M_0	Mass of the converter at lowest frequency	kg
M_{cap}	Mass of the capacitor	kg
M_{core}	Mass of the transformer core	kg
M_f	Mass of the converter at frequency f	kg
$MLT_{1,2,iso}$	Mean length of a turn in the primary, secondary or insulation	m
M_{tot}	Total mass of the transformer	kg
m	DC/DC converter voltage conversion ratio	
$m_{1,2}$	Number of parallel windings in the transformer primary or secondary	
$\dot{m}_{H_2}$	Hydrogen mass flow rate	$kg\ s^{-1}$
$N_{1,2}$	Number of turns in the transformer primary or secondary winding	

N_c	Number of components with nominal failure rate λ_c	
N_{cab}	Number of cables	
$N_{d_{\Delta\beta}}$	Enhanced pitch controller filter coefficient	
$N_{O_2}^{evo}$	Electrolyser evolved oxygen flux	mmol m^{-2} s^{-1}
$N_{l1,2}$	Number of layers in the transformer primary or secondary winding	
$N_{H_2}^{perm}$	Electrolyser hydrogen permeation rate	mmol m^{-2} s^{-1}
N_{WT}	Number of wind turbines in a wind farm	
n	Total number of DC/DC converter modules	
n_c	Number of transformer core stacks	
OPEX_{NPV}	Net present value of the operational costs	M€
O_t	Fixed operating cost in year t	M€
O_x	Annual OPEX of component x	M€
P_0	Losses of the converter at lowest frequency	pu
$P_{1,2}$	DC/DC converter input or output power	MW
P_c	Power delivered through the cable	W
P_{cab}	Rated power of the cable	MW
P_{cond}	Semiconductor conduction losses	W
P_{conv}	Rated power of the converter	MW
P_{core}	Iron core losses per unit volume	W m^{-3}
P_{Cu}	Copper winding losses	W
P_{EL}	Electrolyser rated power	MW
P_{el}	Electrolyser ramp-limited power	MW
P_{ess}	Energy storage system balancing power	MW
P_f	Losses of the converter at frequency f	pu
$P_{gen,t}$	Wind turbine generator power output before losses	W
$P_{loss,cab}$	Power losses in the cable	W
$P_{loss,conv}$	Power losses in the converter	W
P_m^*	Maximum power point tracking set point	MW
P_{FLL}	Full-load losses	p.u.
P_{NLL}	No-load losses	p.u.
P_{sw}	Semiconductor switching losses	W
P_{TR}	Rated power of the transformer	MVA
P_{tr}	Nominal transformer losses	W

P_{WF}	Total active power of the wind farm	MW
P_{WT}	Rated power of an individual wind turbine	MW
P_{wt}	Aerodynamic power input of the wind turbine	MW
p	Wind turbine machine pole pairs	
p_{H_2}	Electrolyser hydrogen partial pressure	atm
p_{H_2O}	Electrolyser water partial pressure	atm
p_{O_2}	Electrolyser oxygen partial pressure	atm
Q_{comp}	Reactive compensation requirements	MVAr
Q_{off}	Proportion of reactive compensation located offshore	
R	Number of redundant converter modules	
$R_{dc,\#}$	Resistance of the cable at a given temperature	Ω
R_{dc}	DC resistance of the transformer winding	Ω
R_g	Ideal gas constant	8.314 J mol^{-1} K^{-1}
R_r	Wind turbine rotor radius	m
R_s	Wind turbine machine stator resistance	Ω
r	Electrolyser cell total resistance	Ω cm^2
r_{AB}	Ratio of the transformer core limb width to limb thickness	
$S(\omega_i)$	Wind speed van der Hoven spectrum power at frequency ω_i	m^2 s^{-2}
s	Laplace transform complex frequency variable	
T	Switching period	s
t	Year of operation	
T_{cell}	Electrolyser cell temperature	K
T_F	Wind speed turbulence Kalman filter time scale	s
T_K	Device temperature	K
T_M	Preventative maintenance interval	yr
T_{pos}	Positive half cycle time	s
T_s	Wind speed turbulence Kalman filter sampling period	s
T_t	Wind farm lifetime	yr
t_0	Time start of power mismatch event	s
t_1	Time end of power mismatch event	s
U_{cap}	Rated voltage of the capacitor	kV
V_0	Volume of the converter at lowest frequency	m^3
$V_{1,2}$	DC/DC converter input or output DC link voltage	kV

$V_{act,a,c}$	Electrolyser cell activation voltage in the anode or cathode	V
V_{app}	Applied voltage to a DC/DC converter component	V
V_{block}	Semiconductor blocking voltage	V
V_{cab}	Cable voltage	V
V_{cap}	Volume of the capacitor	m^3
V_{cell}	Electrolyser cell voltage	V
V_{con}	Electrolyser cell concentration overvoltage	V
V_{core}	Volume of the transformer core	m^3
$V_{D,2}$	Output diode voltage rating	kV
V_{DC}	DC link voltage	
V_{EL}	Electrolyser voltage	
V_f	Volume of the converter at frequency f	m^3
V_{HVAC}	Rated line-to-line voltage of the AC transmission system	kV
$V_{IGBT,1,2}$	IGBT voltage rating in the input or output bridge	kV
V_{max}	Maximum voltage rating of the semiconductor	V
V_{nom}	Nominal voltage rating of a DC/DC converter component	V
V_{oc}	Electrolyser open-circuit cell voltage	V
V_{SG}	Rated voltage of the switchgear	kV
V_{sw}	Voltage stress on the semiconductor	V
V_t	Variable operating cost in year t	M€
V_{tot}	Total volume of the transformer	m^3
$V_{w,max}$	Maximum voltage of the transformer winding	V
V_Ω	Electrolyser cell ohmic overvoltage	V
v	Wind speed	$m\ s^{-1}$
$v_{d,q}$	D-axis and q-axis stator voltages	V
v_{ml}	Wind speed medium- and long-term variation component	$m\ s^{-1}$
v_{on}	On-state forward voltage drop	V
v_p	Instantaneous voltage in the transformer primary winding	V
v_r	Wind speed turbulence component	$m\ s^{-1}$
$w_{1,2}$	Width of one turn in the transformer primary or secondary winding	m
$w_{1,2t}$	Transformer total width of the primary or secondary winding	m
w_c	Winding conductor width	m
w_w	Transformer winding window width	m

Greek symbols

α	Electrolyser cell charge transfer coefficient	
α_S	Second Steinmetz constant	
$B(x, y)$	Beta function or Euler integral of the first kind	
β	Wind turbine blade pitch angle	$^\circ$
β_{NZ}	Enhanced pitch controller non-zero pitch	$^\circ$
β_S	Third Steinmetz constant	
γ	Voltage derating factor	
δ	DC/DC converter phase shift angle	
ΔB	Peak-to-peak magnetic flux density excursion	T m^{-2}
ΔC_{ACplat}	Additional AC platform cost due to shunt reactor weight	M€
ΔE	Energy stored in the wind turbine rotor	MJ
ΔG	Change in Gibb's free energy	J mol^{-1}
δ_s	Conductor skin depth	m
ζ	Band-pass filter damping factor	
η	Voltage stress factor	
η_{cap}	Capacitor voltage stress factor	
η_D	Diode voltage stress factor	
η_{IGBT}	IGBT voltage stress factor	
θ_e	Wind turbine machine electrical angle	rad
θ_m	Wind turbine machine rotational angle	rad
θ_r	Wind turbine rotor rotational angle	rad
κ	Inner current control bandwidth tuning parameter	
λ	Wind turbine tip speed ratio	
λ_1	Maximum flux linkage	Wb
λ_a	Failure rate for the applied voltage V_{app}	yr^{-1}
λ_c	Component failure rate	yr^{-1}
λ_{cap}	Capacitor failure rate	yr^{-1}
λ_D	Diode failure rate	yr^{-1}
λ_{GD}	IGBT gate driver failure rate	yr^{-1}
λ_{IGBT}	IGBT failure rate	yr^{-1}
λ_m	Base failure rate of one module	yr^{-1}
λ_m	Wind turbine machine flux linkage	Wb

μ_0	Permeability of free space	$4\pi \times 10^{-7}$ H m^{-1}
μ_{Cu}	Permeability of copper	H m^{-1}
μ_r	Relative permeability of copper	
ρ	Air density	kg m^{-3}
ρ_c	Magnetic core density	kg m^{-3}
ρ_{cap}	Density of the capacitor	kg m^{-3}
ρ_{con}	Electrical resistivity of the conductor material	Ω m
ρ_{Cu}	Resistivity of copper	Ω m
σ_v	Wind speed turbulence intensity	
τ_m	Wind turbine machine torque	N m
$\tau^*_{m,J}$	Wind turbine updated machine torque reference	N m
τ_r	Wind turbine input rotor torque	N m
ϕ_i	Wind speed van der Hoven phase terms	rad
ϕ_{H_2}	Volume fraction of hydrogen in oxygen	
ω_{dt}	Wind turbine drivetrain natural frequency	rad s^{-1}
ω_e	Wind turbine machine electrical rotational speed	rad s^{-1}
ω_i	Wind speed van der Hoven frequency terms	rad s^{-1}
ω_m	Wind turbine machine rotational speed	rad s^{-1}
ω_{max}	Wind turbine maximum rotational speed for a given power	rad s^{-1}
ω_{min}	Wind turbine minimum rotational speed for a given power	rad s^{-1}
ω_{nom}	Wind turbine nominal rotor speed	rad s^{-1}
ω_r	Wind turbine rotor rotational speed	rad s^{-1}

Chapter 1

Introduction

1.1. Background

1.1.1 The energy trilemma

Offshore wind and hydrogen play an important role in addressing the energy trilemma of sustainability, security, and affordability [1]. Energy sustainability is essential as global energy demand continues to increase year-on-year, and global greenhouse gas emissions have still not yet reached their peak [1]. The latest global temperature assessments place the world at about 1.2°C above the pre-industrial average temperature [2], which is already leading to extreme weather in every region across the globe, negatively impacting food and water security, human health, economies, nature, and society [3].

At the same time, security of supply and energy affordability cannot be neglected, which was highlighted by recent events such as the Covid-19 pandemic and Russia's invasion of Ukraine. The rapid economic recovery following the Covid-19 pandemic resulted in energy price shocks from the release of pent-up energy demand. Russia's invasion of Ukraine in February 2022 subsequently escalated this into a full-blown global energy crisis [4], due the continued dependence of economies on foreign fossil fuels. During this time, wholesale gas prices reaches a peak of €339/MWh in Europe, compared to the historical average of €20/MWh [5,6]. Similarly, electricity prices peaked at €900/MWh, compared to the historical average of €30/MWh to €50/MWh, since gas-fired power stations are price-setting in most European power markets [6]. As a result, there is a need for cost-effective domestic energy production, diversification of energy sources, and decentralisation of supply chains [1].

1.1.2 Offshore wind development

Wind energy is an obvious candidate in addressing the energy trilemma due to its zero emission electricity production, widespread domestic resource, and cost-competitiveness with fossil fuel-based electricity production. Offshore wind has several advantages over onshore wind, such as high and consistent wind speeds, large available space, and lower visual and noise impacts. As a result, the offshore wind industry is expected to grow rapidly, with some estimates predicting 2000 GW of installed capacity by 2050, compared to just 35 GW in 2020 [1]. An overview of the historical and predicted offshore wind farm capacity is shown in Figure 1.1.

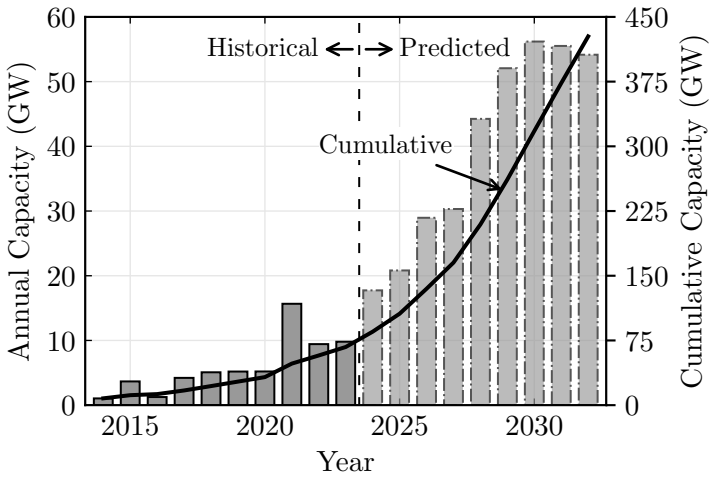

Figure 1.1: Historical and predicted growth in offshore wind annual and cumulative installed capacity, data from [7]

Offshore wind power plants and individual wind turbines have become increasingly large to benefit from economies of scale. For example, the largest offshore wind farms with capacities of more than 1 GW have all become operational in the last five years [8], and the latest generation of wind turbines have individual capacities of up to 15 MW [9]. At the same time, wind power plants are located increasingly far from shore as suitable near-shore locations are exhausted, and optimal wind resource is typically found in remote locations. Figure 1.2 shows the evolution in size and distance of wind farms against the year of commissioning.

At the moment, the vast majority of offshore wind farms use high voltage alternating current (HVAC) cables to connect to shore. However, as wind farms become larger and are located further from shore, high voltage direct current (HVDC) connections become more cost-effective, and are therefore expected to become more common. For exam-

ple, the UK and the Netherlands both recently announced their first HVDC-connected offshore wind farm projects, in Dogger Bank [10] and Ijmuiden Ver [11], respectively.

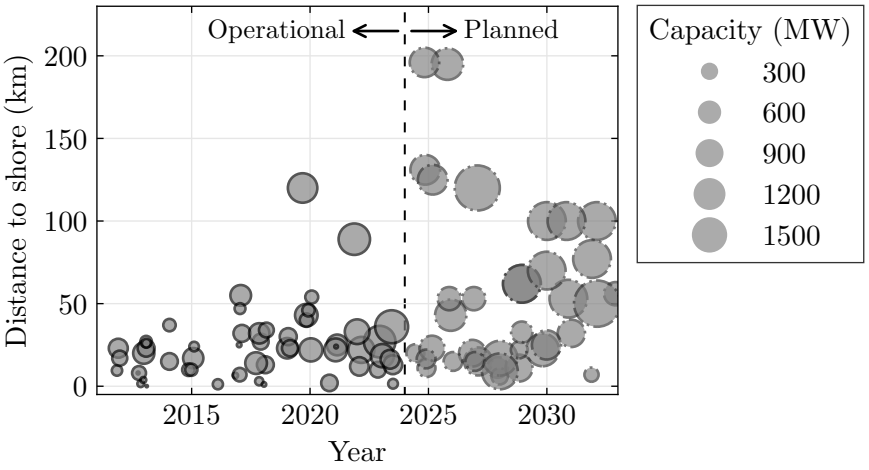

Figure 1.2: Wind farm capacity and distance to shore by year of (expected) commissioning, based on Western European wind farm data from [8]

Despite the compelling case for expanding wind energy, this does not mean that rapid growth is guaranteed. Significant issues have emerged for the wind power sector over the last year, including increases in the cost of capital due to high interest rates, challenges with turbine and rotor reliability, and increases in the cost of materials due to supply chain constraints [1]. These factors have disproportionately affected renewable projects, which typically have tighter margins than many oil and gas projects, and have lead to the postponement and cancellation of projects, as well as failed auctions [1].

1.1.3 Hydrogen development

Hydrogen is one of the most promising candidates to enable the wider Net Zero transition, beyond the decarbonisation of electricity generation [12]. It can be used in direct combustion, in fuel cells, or in synthetic fuel production, which allows it to reduce emissions in sectors which are otherwise difficult to decarbonise, such as heavy industry, shipping, and aviation [13]. It also has the potential to be an alternative to batteries for large scale, long-term energy storage [14], and can replace gas in gas-fired power plants to provide flexibility to the electricity grid [15]. Currently, most of the world's hydrogen comes from natural gas, emitting CO_2 in the process. To avoid these emissions, the hydrogen needs to be produced using water electrolysis powered by renewable energy, so called green hydrogen [13].

While green hydrogen electrolysis currently accounts for less than 1% of total hydrogen production, this is set to change rapidly [15]. The share of green hydrogen is estimated to increase to 50%–85% of total hydrogen production by 2050 [1,16,17] and the announced capacity for 2030 already represents a 200-fold increase over current levels of green hydrogen production, as shown in Figure 1.3.

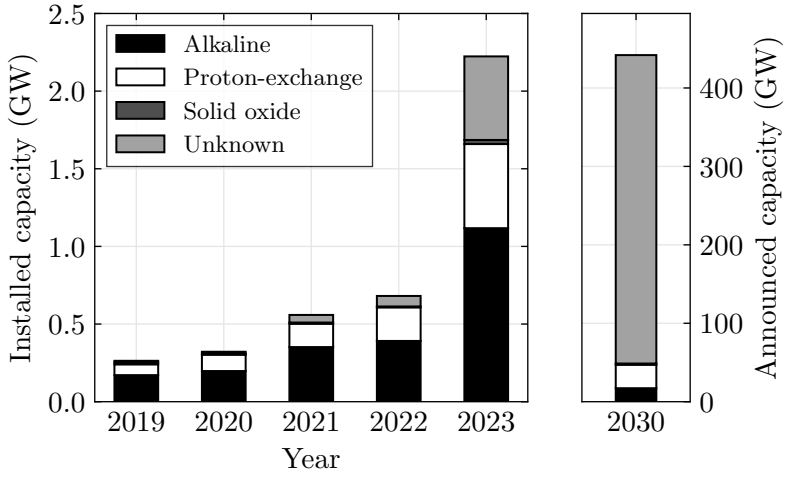

Figure 1.3: Cumulative installed and announced green hydrogen capacity by year for varying electrolyser technologies, based on [15]

As with offshore wind, the main barrier for adoption of green hydrogen is cost [18]. Before the global energy crisis, the levelised cost of hydrogen produced by water electrolysis was three or four times as expensive as fossil fuel based sources [15]. In addition, the cost pressures of labour and materials have significantly increased the installation cost of electrolysers over the past years. For green hydrogen to be cost competitive with fossil fuel-based hydrogen production, it would need access to abundant, low-cost renewable power, as well as large-scale investment in electrolyser manufacturing [16].

Green hydrogen has additional challenges, such as managing the intermittency of renewable energy sources, requirements for a steady water supply and limited conversion efficiency [19]. Electrolysers can have strict operating limits, such as minimum load requirements, maximum power ramp-up and ramp-down rates, and long start-up and restart times, which complicate their operation when connected to renewable energy [20].

Combining offshore wind energy and green hydrogen production mitigates some of these drawbacks. The relatively high and consistent wind speeds found offshore result in high capacity factors and less intermittency. The offshore location allows seawater to be used after desalination [21] and research into using seawater directly is ongoing [22].

1.1.4 Cost-effective energy transfer

The energy generated by offshore wind turbines needs to be transferred to shore before it can be used. This process includes several steps, including combining the energy in the wind farm collection system, transforming it to a higher voltage at the offshore substation, rectifying it to direct current at the converter platform, and transporting it to shore through subsea cables. Each of these stages raises the levelised cost of energy (LCOE) by adding additional capital costs and reducing the efficiency of the system.

A step change in the cost of energy is possible if the electrical infrastructure of offshore wind farms can be significantly reduced. Over the past three decades, the LCOE of offshore wind has been decreasing, primarily due to greater economies of scale and higher voltage levels. However, the required electrical infrastructure has remained relatively constant, or even increased in the case of HVDC wind farms. Continual developments in power electronics technology now offer the potential to drastically change the electrical infrastructure of offshore wind farms.

In conventional offshore wind farms, illustrated in Figure 1.4a, a large offshore substation is needed to house the transformers that step up the voltage to transmission levels [23]. The topside can be in excess of 10,000 tonnes and requires large installation vessels [24]. For offshore wind farms further from the shore, additional modular multilevel converters (MMCs) or reactive compensation equipment is needed, further adding to size and weight of the offshore substation.

High power DC/DC converters allow for a completely DC-based wind farm design, with a DC collection and export system. The voltage conversion is performed by DC/DC converters, which can be made much smaller than regular transformers [23], depending on their design, and can therefore significantly reduce the offshore platform space requirements. There have even been DC wind farm designs put forward that avoid using offshore platforms entirely [25–27].

The energy transferred by offshore wind turbines does not necessarily need to be electrical. The rapid development of power electronics and electrolysers has opened up the opportunity for wind turbines to transfer energy chemically as hydrogen. By connecting electrolysers with individual offshore wind turbines, the electrical infrastructure requirements can be significantly reduced, with no offshore substation, export cables, or even collector cables required [28]. The produced hydrogen can be transported using pipes, which are considerably cheaper and longer lasting compared to cables [13]. This layout is illustrated in Figure 1.4b.

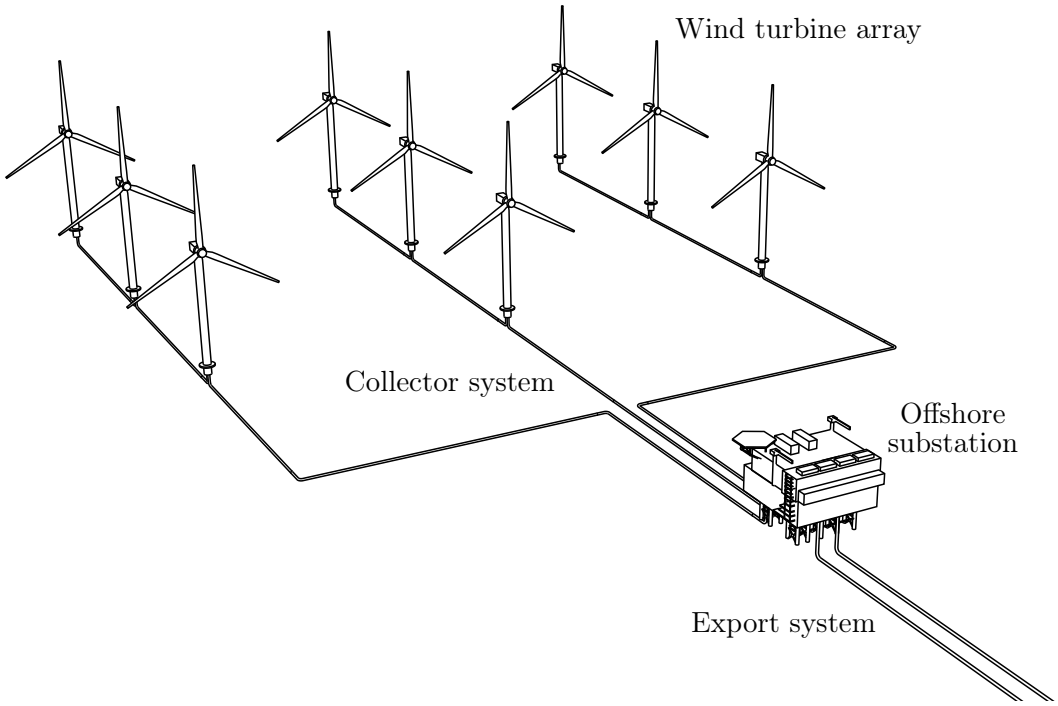

(a) Traditional wind farm with AC collection system

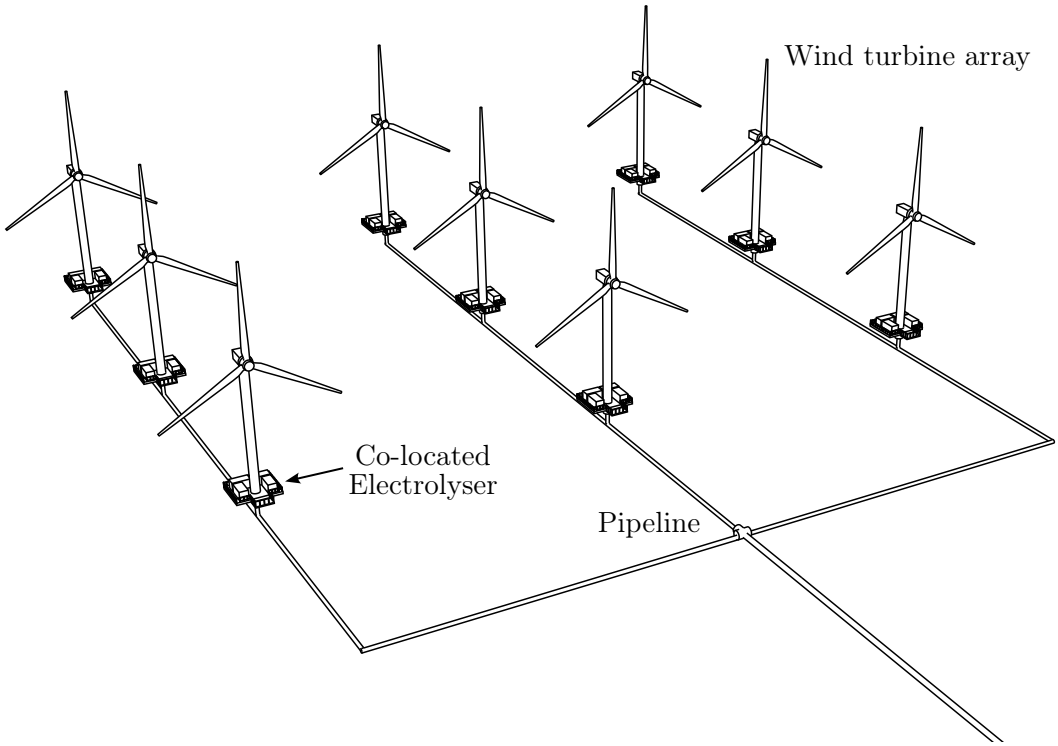

(b) Wind farm with decentralised hydrogen production

Figure 1.4: Offshore wind farm layout and main components

1.2. Thesis Overview

This thesis is divided into two parts, each consisting of three chapters. **Part I** focuses on cost-effective electrical energy transfer through the use of DC collection systems and optimised DC/DC converters. **Part II** focuses on cost-effective chemical energy transfer through the use of wind turbines with co-located electrolysers, and DC-based wind turbine drivetrains for electrolysis.

Part I – Electrical Energy

- **Chapter 2** provides a systematic literature review of proposed DC collection systems, including their design, relative costs, losses, and reliability. It also identifies the most promising all-DC wind farms for further study.
- **Chapter 3** carries out a cost-benefit comparison of two traditional AC wind farm topologies and two of the most promising all-DC wind farm topologies. It quantifies the conditions required for the all-DC wind farms to achieve a lower LCOE through a series of sensitivity studies.
- **Chapter 4** sets out a multi-objective design optimisation of four DC/DC converter candidates. This consists of a reliability assessment, a design optimisation of the medium frequency transformer, insulation coordination of the components, simulation of the losses, and an assessment of the optimal operating frequency.

Part II – Chemical Energy

- **Chapter 5** provides a review of commercial electrolysis technologies, including their operating principles, steady-state performance, and dynamic performance. It also discusses the options for integrating electrolysers with offshore wind and the current state of commercial development.
- **Chapter 6** investigates the technical challenges associated with a standalone wind turbine and electrolyser system. It sets out the design of an overall control system, proposes three power balancing strategies, and assesses their trade-offs in order to keep the system operational during wind speed changes.
- **Chapter 7** investigates the levelised cost of hydrogen for the proposed power balancing strategies, and assesses the potential for DC-based wind turbine drivetrains to reduce the cost of hydrogen production.

Chapter 8 summarises the key findings of the thesis and highlights areas of interest for future research.

1.3. Scientific Contributions

The contributions of the first part of this thesis include:

- The identification of the most promising DC wind farm configurations and the quantification of the conditions required for these topologies to lower the levelised cost of electricity compared to traditional AC designs.
- The identification of the most promising DC/DC converter topologies to enable DC collection systems, the optimal design of these topologies, and a comparison of their performance in terms of reliability, volume, weight, and losses.
- The quantification of the impact of operating frequency on DC/DC converter design and performance, and an evaluation of the optimal operating frequency for the selected topologies.

The contributions of the second part of this thesis include:

- The development of a complete control system for a standalone wind turbine and electrolyser system without grid connection.
- An evaluation of the impact of the dynamic electrolyser limitations, including a quantification of the expected power and energy mismatch between the wind turbine and electrolyser under typical wind speed conditions.
- The development of three power balancing strategies to manage the mismatch between wind turbine and electrolyser, and an assessment of the cost and efficiency trade-offs for each of these strategies.
- The quantification of the levelised cost of hydrogen for standalone offshore wind-electrolyser systems employing the proposed power balancing strategies.
- The evaluation of the impact of non-standard wind turbine electrical drivetrains on the levelised cost of hydrogen and an assessment of their technological and practical feasibility.

1.4. List of Publications

The following publications were produced over the course of this PhD project:

Journal publications

1. **V. Timmers**, A. Gkountaras, A. Egea-Àlvarez, and L. Xu, "Control and power balancing of an off-grid wind turbine with co-located electrolyser", *IEEE Transactions on Sustainable Energy*, 2024. DOI: 10.1109/tste.2024.3418043
2. **V. Timmers**, A. Egea-Àlvarez, A. Gkountaras, and L. Xu, "Multi-objective optimization and comparison of DC/DC converters for offshore wind turbines", *IEEE Access*, 2024. DOI: 10.1109/access.2024.3411152
3. **V. Timmers**, A. Egea-Àlvarez, A. Gkountaras, R. Li, and L. Xu, "All-DC offshore wind farms: When are they more cost-effective than AC designs?", *IET Renewable Power Generation*, pp. 1–13, 2022. DOI: 10.1049/rpg2.12550.
4. S. Coffey, **V. Timmers**, R. Li, G. Wu and A. Egea-Àlvarez, "Review of MVDC applications, technologies, and future prospects," *Energies*, Vol. 14, No. 24, 2021. DOI: 10.3390/en14248294.

Conference publications

1. **V. Timmers**, A. Egea-Àlvarez, and A. Gkountaras, "Frequency optimisation for DC/DC converters in DC-connected offshore wind turbines", *25th European Conference on Power Electronics and Applications*, Aalborg, Denmark, 2023. DOI: 10.23919/epe23ecceeurope58414.2023.10264511.
2. **V. Timmers**, A. Egea-Àlvarez, A. Gkountaras, and L. Xu, "Review and comparison of single and dual active bridge converters for MVDC-connected wind turbines", in *21st Wind and Solar Integration Workshop*, 2022. DOI: 10.1049/icp.2022.2819.
3. **V. Timmers**, A. Egea-Àlvarez, and A. Gkountaras, "A systematic review of DC wind farm collector cost-effectiveness," in *17th International Conference on AC and DC Power Transmission*, Glasgow, UK, 2021. DOI: 10.1049/icp.2021.2454.

Part I:

Electrical Energy

Chapter 2

Review of Wind Farm Electrical Design

2.1. Introduction

This chapter carries out an investigation of wind farm topologies proposed in the literature, following a formal systematic review procedure. The chapter first details conventional AC-based wind farm topologies, before presenting the various DC-based topologies set out in the literature.

In addition to describing the key features of each topology, the review includes a quantitative assessment of the reported cost, losses and reliability estimates in the literature to evaluate the cost-effectiveness of each topology. The calculation methodologies used in cost-effectiveness analyses have also been included to inform the cost-benefit analysis carried out in Chapter 3.

The review procedure is based on the guidelines set out in [29]. The systematic review was originally used in medicine and later in social science [30] and computer engineering [29] as a way to reduce the bias of individual studies and reach more robust conclusions compared to regular reviews [30]. This approach was selected for this research due to the diversity of methodologies, conclusions, and quality of the literature on this topic.

2.1.1 Research Questions

The systematic review aims to answer the following research questions:

1. Which DC wind farm configurations have been evaluated in the literature?
2. What methodologies are used to calculate the cost, losses and reliability of DC wind farms and their components?

3. What are the most cost-effective DC wind farm configurations and how do they compare to AC?

4. What are the technological readiness levels and barriers to commercialisation for DC wind farms?

2.1.2 Search Strategy

The search strategy consisted of an initial search on Google Scholar to identify a starting set of papers. Further relevant papers were then identified by searching three databases: IEEE Xplore, SCOPUS and Web of Science. The search terms included "wind farm", any of the following performance indicators: "cost", "losses", "efficiency", "reliability" or "feasibility", and any variation of "DC collector".

After the search, the starting set of papers was compared to the obtained records and the search string was amended iteratively to include all starting set papers. The results were limited to include peer reviewed journal articles and conference proceedings only. The systematic review procedure is shown in Figure 2.1.

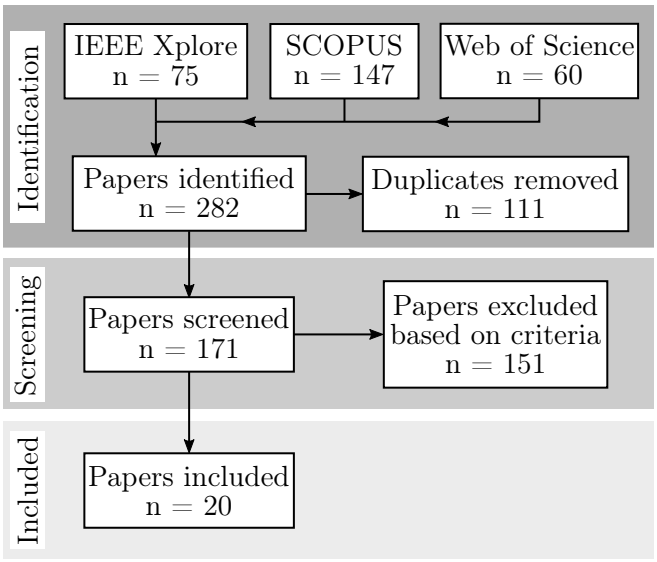

Figure 2.1: Systematic review flow diagram

2.1.3 Screening

The search strategy resulted in 282 records, with 171 records remaining after removal of duplicates. These records were screened for eligibility, with articles excluded based on the following criteria:

1. The evaluated design does not use a DC collection system.

2. The paper does not include any assessment of the wind farm collector topology, e.g. it only considers the DC/DC converter topology.

3. The paper only considers a single design without any comparison to other options.

4. The paper does not include any formal, quantitative analysis of costs, losses or reliability.

5. The full text of the paper is not available or not in English.

Following the screening, a total of 20 publications were included in the analysis. For each article, the metadata, evaluated design aspects, performance indicators, analysis methodology, and results were extracted. Any technological challenges of the proposed designs were recorded.

The quality of each of the selected studies was assessed on a scale of 0–6 by awarding up to two points for each of the following conditions:

1. Is the studied configuration well-defined? Does it state which components are included in the analysis? Are the power and voltage ratings of equipment specified?

2. Is the study reproducible? Does it include a detailed description of the methodology, sources of data, and assumptions used?

3. Is the study comprehensive? Does it take into account more than one aspect of cost-effectiveness? Does it perform any sensitivity analyses?

2.2. AC Topologies

All existing commercial wind farms use AC collection systems, which provide a baseline for the comparison with DC-based topologies. The AC collection system refers to the system of cables that connect wind turbines together in a string, gathering the power generated from all wind turbines [31]. These inter-array cables are also used to connect the wind turbines to a common medium voltage hub, which is typically an offshore substation [32], before the power is exported to shore.

2.2.1 all-AC

The all-AC topology employs both AC in the collection system as well as in the transmission system, as shown in Figure 2.2. In the traditional wind farm configuration, the wind turbines are connected in parallel in strings using 33 kV or 66 kV AC cables. The strings connect to an offshore substation with 50 Hz transformers to step up the voltage. The power is then exported using HVAC cables of voltages up to 230 kV. Reactive compensation in the form of shunt reactors are often connected to offset the cable capacitance. These can be located at the onshore substation, offshore substation, or on a separate platform, depending on the total cable length.

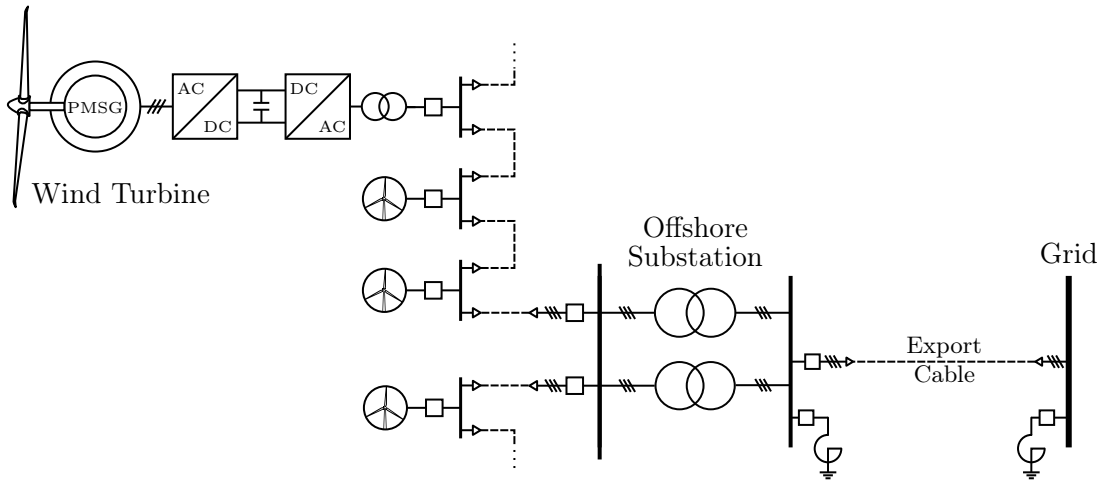

Figure 2.2: Wind farm with all-AC topology, using a radial AC collector and HVAC transmission system

The collector system can be designed using various layouts depending on the size of the wind farm and the level of redundancy required [33]. The most commonly employed topology is a radial layout. In this configuration, multiple wind turbines are connected

in strings where each wind turbine is connected to the next using shared cables, except for the first turbine on the string which is connected to the substation.

In AC designs, each cable connection consists of three separate conductors, *i.e.* one for each phase, typically situated together in a three-core cable. The cables connected close to the substation are shared by more wind turbines and therefore have higher current ratings compared to the cables connecting wind turbines towards the end of the string.

Large wind farms can consist of multiple strings which all connect to a common hub before the voltage is stepped up to be exported to the grid [34]. For all-AC wind farms, the voltage conversion is performed by one or more transformers at the offshore substation.

Note that it is not necessarily the case that all wind turbines have exactly two cable connections in the radial design, i.e. one downstream and one upstream. It is possible to have a more irregular 'tree' structure where cables branch out to connect multiple wind turbines downstream in order to reduce the total cable length. However, the number of cables that can be connected at a single turbine junction cabinet is limited due to space considerations [35].

The main advantages of using a radial collector system is that it is relatively inexpensive due to the low cable length required and the tapering of cable capacity away from the hub [33]. The control system for a radial design is also relatively simple. The major drawback of this design is its relatively poor reliability since any fault near the hub end of the string results in all downstream wind turbines being disconnected. Despite this, the AC radial topology is the most commonly used topology in commercially operating wind farms today [33, 34].

2.2.2 AC/HVDC

Wind farms that are located further from shore frequently use HVDC instead of the traditional HVAC in their export system. This is because at longer cable lengths, the cable capacitance results in significant reactive current, which lowers the available cable capacity for power transmission and increases losses. The classical way to reduce losses is to increase the voltage level, but because reactive power scales with the square of the voltage, any voltage increase reduces the available capacity for power transmission. HVDC cables produce no reactive power and can therefore be any length and operate at higher voltages, resulting in more efficient power transport [36].

To convert from the MVAC used in the collection to HVDC, one or more transformers

and a high power rectifier are required. In earlier offshore wind farm designs, two separate platforms were used to house the transformers and converters, such as at the Borwin [37] and Dolwin [38] platforms in Germany. Modern AC/HVDC wind farm topologies use a higher collection system voltage, which allows the use of a single platform for both the transformers and converters, such as at the Sofia [39] wind farms. The latter configuration is illustrated in Figure 2.3.

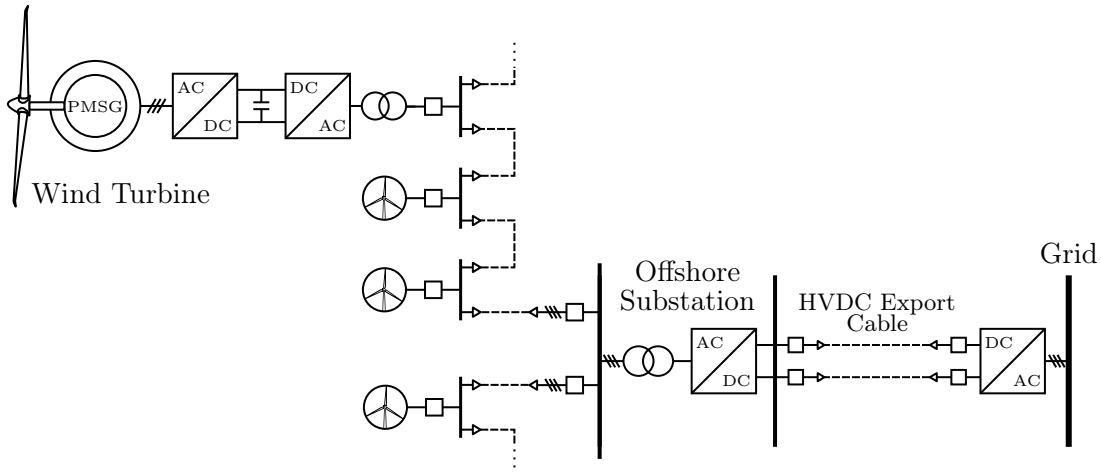

Figure 2.3: Wind farm with AC/HVDC topology using a radial AC collector system and a HVDC transmission system

In all cases, the high power converter used on the offshore and onshore substations is a voltage source converter (VSC). Despite their high technological maturity and power capacity, line commutated converters (LCC) are not used in offshore wind due to the large space requirements of their filters and their inability to operate without a strong grid connection [40].

2.3. DC Topologies

The proposed collector configurations considered in the literature can be categorised into parallel or series topologies. For each of these, several variants exist. The most commonly investigated parallel topology variants include the standard parallel [41–46], [47–50], the centralised parallel [26, 42–45, 51, 52], and the dispersed parallel [26, 41, 42, 50, 53]. The most commonly investigated series variants are the standard series [34, 52, 54–56] and the series-parallel designs [34, 41, 49, 50, 55, 57, 58]. The following subsections discuss these topologies in more detail.

2.3.1 Standard parallel

The standard DC parallel topology is the DC equivalent of the AC/HVDC topology. In the standard design, the wind turbine electrical drivetrain consists of a rectifier followed by a dedicated DC/DC converter with MFT to step up the voltage to MVDC levels of around ±20 kV to ±50 kV [45]. The power of each string is transported to the offshore substation where a DC/DC converter is used to step up the voltage to HVDC for transmission, typically at ±150 kV [44, 47] or ±300 kV [43]. This MVDC/HVDC standard parallel topology is illustrated in Figure 2.4.

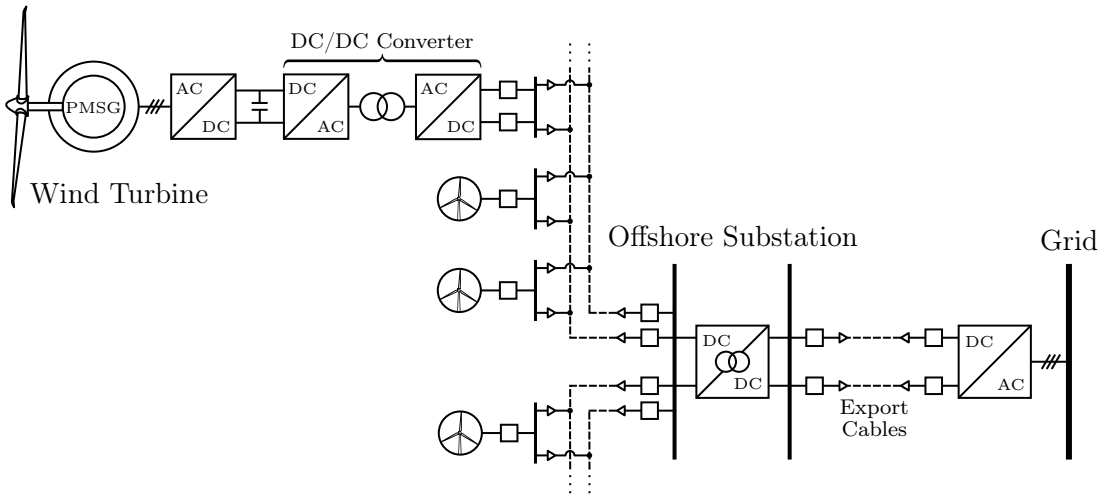

Figure 2.4: Wind farm with standard MVDC/HVDC topology using a parallel MVDC collector system and an HVDC transmission system

This design is most similar to commercial AC wind farm configurations as it connects the wind turbines in strings and uses two step-up stages, one in the turbines and one on an offshore platform [41]. This reduces the technological risk. However, it requires a large number of conversion stages [42], and is dependent on immature high power DC/DC converter technology [50].

2.3.2 Centralised parallel

The centralised parallel designs, shown in Figure 2.5, use a DC/DC converter to perform the control of multiple wind turbines. This allows the wind turbine drivetrain to be simplified. Designs have been proposed with a single-stage drivetrain to directly rectify the generator output [44], resulting in a LVDC collection system. Other designs use a 50 Hz transformer to raise the generator output voltage before converting this to DC

with an active or passive rectifier [43].

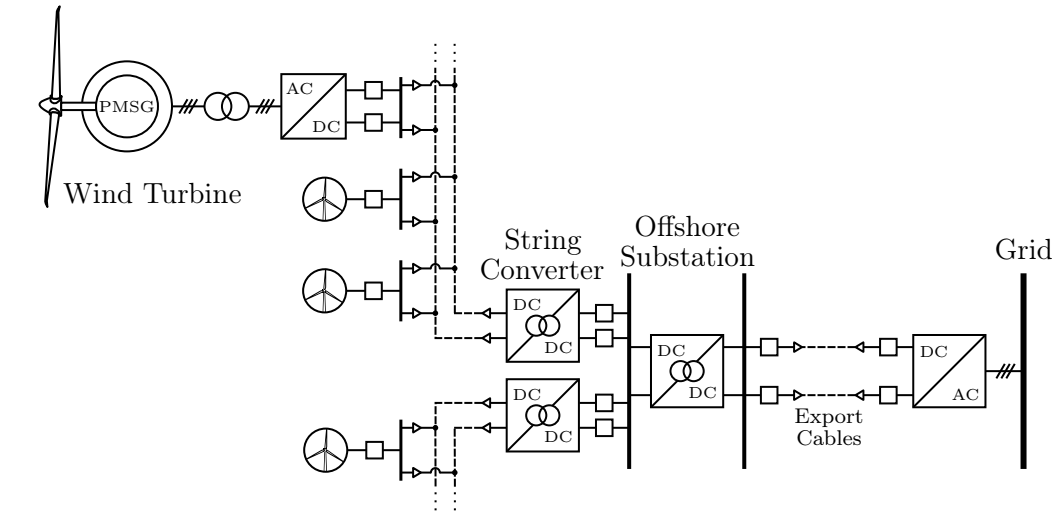

(a) Centralised string

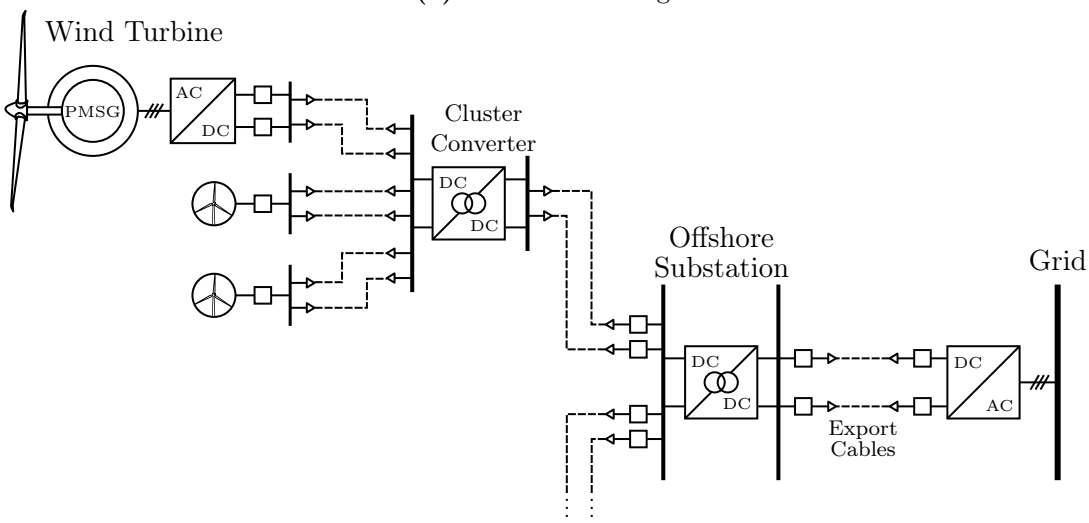

(b) Centralised cluster

Figure 2.5: Wind farm with centralised LVDC/MVDC/HVDC topology, using a parallel LVDC or MVDC collector system, and an HVDC transmission system

In the centralised string design, shown in Figure 2.5a, the turbines are connected in a string or daisy chain before a string-level converter steps up the voltage. In the centralised cluster design, shown in Figure 2.5b, each wind turbine is instead connected directly to the cluster converter. In both cases, a farm-level, high power DC/DC converter on a separate offshore platform is required to increase the voltage up to HVDC levels [43].

The centralised designs have the benefit of reducing the conversion stages in the wind

turbines [42], but require additional platforms for the string or cluster converters [45]. In addition, as the DC/DC converter controls multiple wind turbines, additional losses occur due to suboptimal wind energy extraction [43]. The non-standard drivetrain with a transformer before the converter is unproven and may have difficulties with control, increasing the technological risk of this configuration.

2.3.3 Dispersed parallel

The dispersed parallel configuration, illustrated in Figure 2.6, uses a high step-up ratio DC/DC transformer in each wind turbine to boost the voltage to MVDC-levels, such as ±50 kV [26], or even HVDC levels directly, such as ±150 kV [42, 53]. However, such a high voltage connection brings challenges with insulation and would require galvanic isolation in the wind turbines. If this can be achieved, it would allow this configuration to omit a central converter and large offshore platform [41]. Instead, there may be a small platform to house the protection equipment before connecting to shore. This configuration has the potential to reduce the capital costs associated with the offshore platform. However, the export voltage is limited by the step up ratio of the wind turbine converter, which may lead to higher transmission losses.

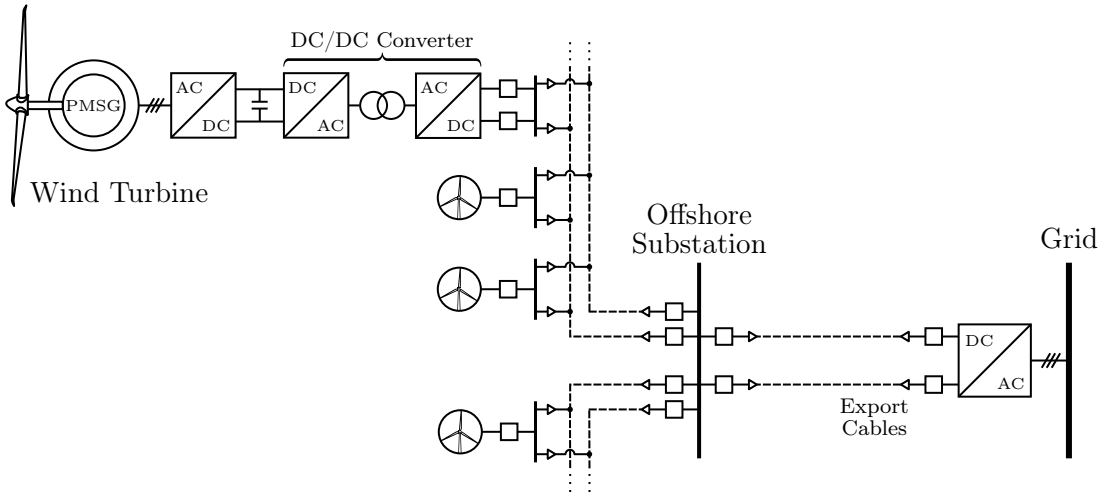

Figure 2.6: Wind farm with a dispersed all-MVDC topology, using an MVDC collector system and MVDC transmission system

2.3.4 Series

A frequently proposed alternative to the more conventional parallel DC topologies is a DC series-connected design. In this topology, all wind turbines in the wind farm are series-connected in a single string [54], as illustrated in Figure 2.7.

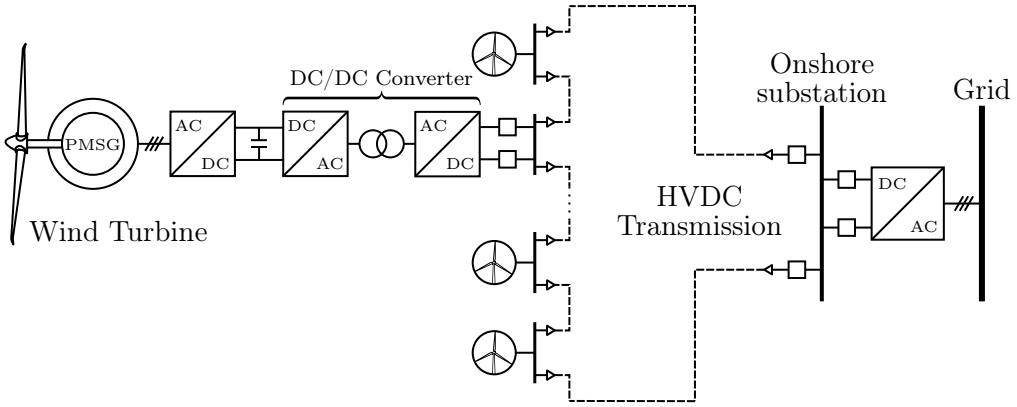

Figure 2.7: Wind farm with a series topology, using an HVDC collection and transmission system without additional conversion stages

For large wind farms, the individual wind turbine output voltage can be relatively low, in the order of a few kV, since many wind turbines can be used to build up the voltage [34]. The benefit of this configuration is that no offshore platform and converter are required [41]. In addition, a smaller number of cables can be used to connect the wind turbines compared to parallel configurations.

It is important to note that just like in the dispersed parallel configuration, the wind turbines must have galvanic isolation between the DC grid and the generator [41] in this configuration. Otherwise, the last turbine in the series connection will be subjected to the complete transmission voltage and the generator would need to be rated for this voltage, which is not technologically feasible [54].

The drawback of series topologies is that they pose significant challenges in operation and reliability. The current in the series connected wind array needs to be the same, which means that all wind turbines are required to produce identical output power [23]. In practice, wind turbines will produce different output powers due to non-uniform wind speeds and wake effects. Therefore, the wind turbine generators (WTGs) that are operating below the average wind speed must increase their terminal voltage and vice versa for WTGs that are operating above the average wind speed.

Due to all wind turbines being connected in a single string, any fault on the cable will

result in the entire wind farm disconnecting [54]. Even under unfaulted conditions, if the voltage at a WTG falls outside its limits of operation, the protection system will disconnect the wind turbine, which may also result in the shutdown of the entire string [23].

2.3.5 Series-parallel

The series-parallel configuration, shown in Figure 2.8, improves the wind farm reliability by dividing the series wind farm into multiple parallel-connected strings. This requires additional cables compared to the series wind farm, as well as more space on the wind turbines at either end of the string to accommodate the multiple cable connections.

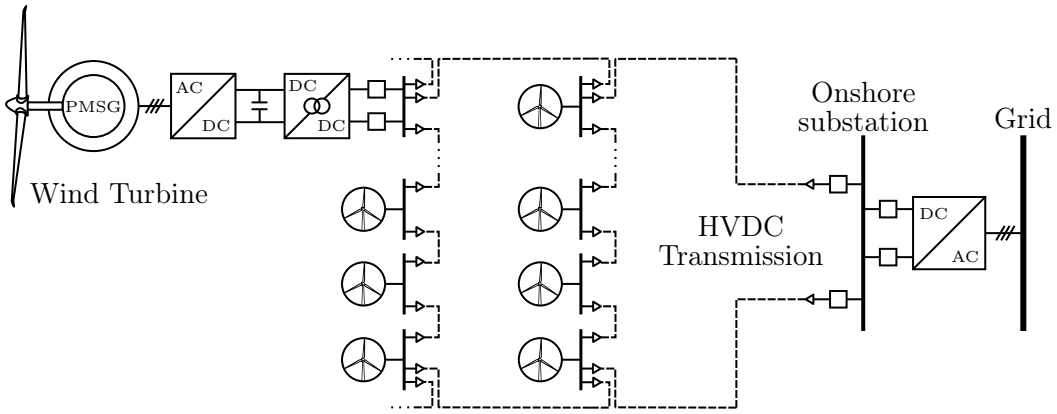

Figure 2.8: Wind farm with a series-parallel topology, using multiple HVDC strings in the collector and an HVDC transmission system

The strings in the series-parallel topology still suffer from the same issues as in the series configuration, including high insulation requirements [34], voltage balancing issues when wind turbines are subjected to unequal wind speeds [52], and challenges maintaining the transmission voltage when multiple wind turbines are out of service [50].

To address the voltage unbalance during wind turbine outages, a matrix collector topology has been proposed [58]. Here, additional normally-open switches are connected in between branches to allow the collector to be reconfigured when a wind turbine experiences a fault. However, this redundancy adds significant additional costs as branches may not be physically close to each other and a sophisticated control scheme is necessary to switch between adjacent branches in this topology [23].

2.4. Calculation Methods

2.4.1 Cost

Publications that investigate the cost of topologies typically estimate the capital cost investment required only [26, 49], rather than a full levelized cost analysis over the wind farm lifecycle [47]. Capital costs that are considered typically include the costs of the wind turbines, cables, transformers, converters and offshore platform. More rigorous publications also tend to include the costs of the losses over the wind farm lifetime [43, 45, 54].

Most publications use equations from the literature to determine costs of the various components. Since commercial data is often difficult to come by, these are often based on the same datasets. For example, a 2003 report by Lundberg [59] is used by various papers [43, 45, 54], to calculate the costs of MVDC cables. Other sources include publications by Dicorato et al. [60] and industry figures from the UK ETYS [61], NorthSeaGrid (NSG) project [62], ENTSO-E [63], OREC [64], among others. These provide cost estimates for cables, transformers, platforms and more. Cost figures from different sources can vary significantly.

The costs of DC components, such as the DC/DC converters and DC circuit breakers are generally not available. Therefore, papers instead use a bottom-up approach where they estimate the cost based on individual elements that make up larger components. For example, [43] use the costs of the semiconductors and transformers needed for the DC/DC converter to estimate its overall cost. Alternatively, papers can rely on assumptions to estimate the cost DC components as a proportion of AC component costs [45]. Due to the variability of estimation procedures it is important to detail the exact methodology and assumptions used. It is also recommended to perform sensitivity analyses for components with greater uncertainty in their cost, such as in [43, 45].

Despite the large influence of the offshore platform on overall cost, very few of the included publications quantitatively assessed the size and weight of the DC/DC converter, and the associated cost reduction of the offshore platform [44]. This is therefore investigated in greater detail in Chapter 3.

2.4.2 Losses

Publications that calculate the efficiency of the overall wind farm typically use datasheet information such as the resistance of cables, and transformer load and no load losses. The loss calculation can then be performed analytically [43] or through load flow simulation software [45]. Some papers only consider losses at rated power [34]. However, since wind farms do not produce rated power continuously, it is recommended to calculate the losses at varying operating conditions and wind speeds. The overall wind farm efficiency can then be calculated using a typical Weibull wind speed distribution curve [44, 45].

The efficiency of DC/DC converters will be dependent on the selected design. Some papers assume an efficiency as a proportion of existing AC/DC converters. Others perform more sophisticated calculations based on the power electronic components, either analytically [42] or by using simulation tools such as PLECS [44]. Research into DC/DC converters is ongoing, therefore, it may be an option to use efficiency measures of DC/DC converter lab prototypes [65].

2.4.3 Reliability

Very few publications assessed the reliability of configurations, despite the large impact this can have on cost-effectiveness. The approach used for the reliability assessments consists of using the failure rates per year for individual components and estimating the repair time and lost energy production in case of failure [49]. It is important to take into consideration how the protection will reconfigure the wind farm during equipment failure when calculating the energy lost [54, 55]. Similar to the cost estimates, the component failure rates and repair times can differ significantly depending on the sources used. Reliable failure rate data can typically be obtained from CIGRE brochures [66, 67].

2.5. Cost-Effectiveness Results

2.5.1 Cost results

Analysis of papers investigating the costs of DC wind farms shows a large range of cost estimates, from €0.3/W [26] to €3/W [47]. The disparity of estimates is mainly due to the difference in scope of the studies, and to a lesser extent because of varying wind farm characteristics, such as size, distance from shore, converter technology, etc. For example, some papers exclude the transmission system capital costs [43], others cover both the capital cost of the entire system and the cost associated with the losses [54]. Direct comparison is further complicated by heterogeneous reporting, with papers reporting costs using local currencies [46], in per unit values compared to AC [54], or in costs per energy produced [44].

In order to compare the costs of the various configurations, for each study the results were normalised by using the calculated AC configuration cost as a base. For studies that did not include an AC option for comparison [50], the mean cost of all tested configurations in that study was selected as the base for the per unit comparison. To increase the robustness of the comparison, only studies with a quality rating of 3 or more were included and studies that did not cover at least the costs of the wind turbines, collector system, converter and platform were excluded [34]. Furthermore, studies with unrealistic component costs that deviated by more than a factor 5 from the norm were excluded [49, 50]. The results of the analysis are shown in Figure 2.9.

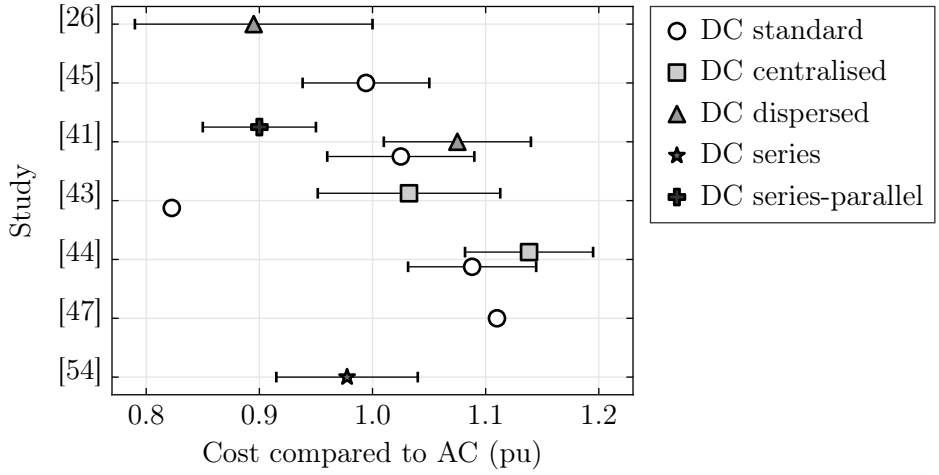

Figure 2.9: Normalised cost estimates for DC wind farm configurations, using AC radial cost of each study as base

It can be seen from Figure 2.9 that there is considerable disagreement on whether certain DC configurations provide cost savings. For example, [43] show potentially significant savings of up to 18% when using DC standard parallel collector systems compared to AC, whereas [44] find the same configuration to be 3% to 14% more expensive than AC, despite both studies following a similar calculation methodology. The main difference is the high DC circuit breaker costs included in the calculation by [44]. Other differences include the wind farm sizes (1000 MW vs 400 MW) and the wind turbine ratings (10 MW vs 5 MW).

Overall, the results show that the DC dispersed, series and series-parallel topologies have potential cost savings as they have mean costs of less than 1 pu. The centralised and cluster parallel designs, on the other hand, were found to be more expensive than AC in all included cases, making them unlikely candidates for commercialisation. The standard DC topology is most often investigated, however, its cost saving potential is uncertain as the mean cost reported in the literature is approximately 1 pu compared to AC.

2.5.2 Losses results

Similar to the cost results, analysis of the losses showed a large variation in loss estimates, from 2.1% [51] to 11.3% [57]. The variation of losses is due to the difference in scope of the studies: some studies only include the losses of the collector cables and converters, whereas others include losses in the wind turbines and the export system as well. In addition, the losses of DC/DC converters vary significantly between studies. In [57], the losses of the DC/DC converter are calculated to be 4%, compared to [51] who consider the losses to be 1.6%.

The losses of each of the configurations were normalised following the same procedure as for the costs. The results are shown in Figure 2.10. It can be seen that the DC standard parallel topology has the potential to reduce the losses in the system compared to the AC topology. The series and series-parallel topologies do not show the same advantage, with mean losses close to 1 pu. The centralised and cluster configuration loss performance is very dependent on the study assumptions. Studies that take into account clustering losses [43] and multiple step up stages show high losses, whereas those that neglect clustering losses and use a single conversion stage find losses to be lower than AC [51]. There is a lack of studies that investigate the losses of the DC dispersed topology.

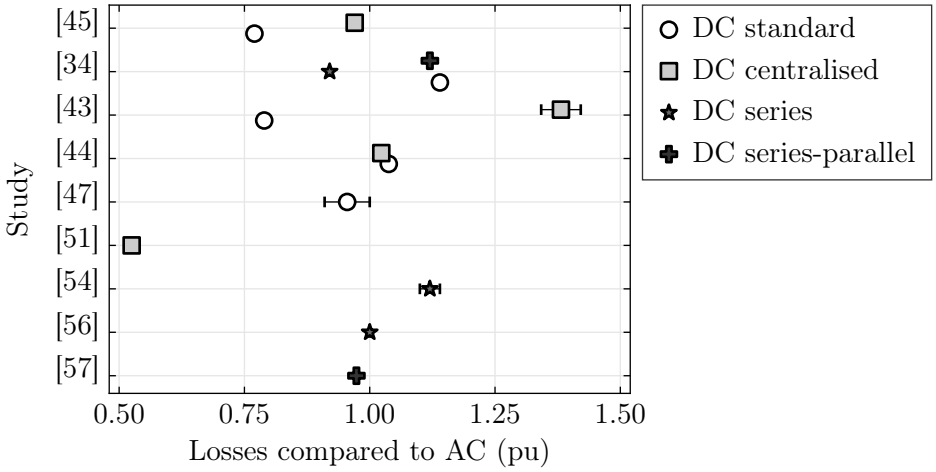

Figure 2.10: Normalised loss estimates for DC wind farm configurations, using AC radial losses of each study as base

2.5.3 Reliability results

The number of studies investigating the reliability of DC wind farm configurations is more limited compared to cost and efficiency. Reliability measures are typically given in terms of the average system availability index, which is the ratio of the number of hours the wind farm is operating compared to the total hours in a year. The results of the studies are shown in Figure 2.11.

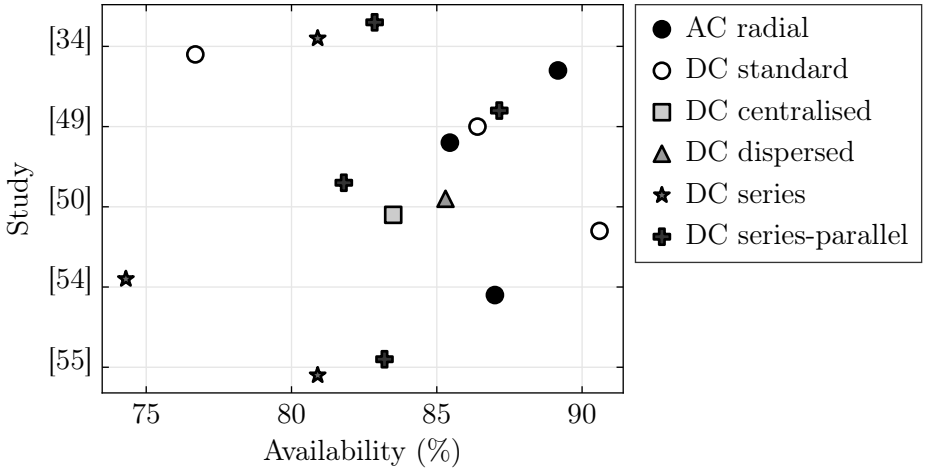

Figure 2.11: Average availability index for AC and DC configurations

The figure shows that the majority of studies agree that series and series-parallel config-

urations perform significantly worse than the AC radial topology. This is expected due to the large number of wind turbines being disconnected in the event of a failure. There is no consensus on the standard parallel DC configuration reliability. For example, [50] considers it to be the most reliable of the DC configurations, whereas [34] finds the opposite. There is a need for further reliability studies, especially as the DC/DC converter technology matures, to conclusively determine whether DC wind farm reliability will be significantly different than that of AC wind farms.

2.6. Conclusions

This chapter has provided a comprehensive investigation of the current research into DC-based wind farm cost-effectiveness. Using a systematic review methodology, data was extracted from 20 studies, including proposed topologies, calculation methodologies and results.

Existing commercial topologies use MVAC collection systems and either an HVAC or HVDC export system. The proposed DC-based wind farms in the literature use DC collection systems, and can be categorised based on their method of connection of the wind turbines. Proposed topologies include the standard parallel, centralised parallel, dispersed parallel, series, and series-parallel connection.

The results of the systematic review showed that the series and series-parallel DC designs performed well in terms of costs due to removing the need for an offshore platform. However, they were found to have challenges in operation and reliability that limit the short-term opportunity for commercialisation. The centralised DC parallel topology was found to have higher costs and losses than all other topologies, limiting its potential to make energy transfer more cost effective.

The most promising DC topologies were found to be the standard parallel topology using an MVDC collector and HVDC export system, as well as the dispersed parallel topology, which uses an MVDC collector and export system. The standard MVDC/HVDC topology has the lowest technological risk, but its cost savings are highly dependent on the study assumptions. The dispersed all-MVDC parallel topology has the potential to reduce costs, but little data is available on its losses and reliability. There is therefore a need to investigate these topologies using a comprehensive approach to obtain more generalisable results.

Chapter 3

DC Wind Farm Cost-Effectiveness

3.1. Introduction

Chapter 2 has highlighted the large range of designs for DC wind farms that are proposed in the literature and showed that the results of each study are highly dependent on the assumptions of factors such as wind farm size and distance to shore. This chapter undertakes a comprehensive evaluation of DC wind farm cost-effectiveness through a cost-benefit analysis of the most promising designs identified in the systematic literature review.

3.1.1 Contributions

The economic evaluations of all-DC wind farms in the literature vary significantly in their outcomes. Most studies only investigate a single wind farm size and distance from shore, which makes their conclusions difficult to generalise. Only a limited number of studies perform sensitivity analyses and none draw any quantitative conclusions about the requirements for component costs. The purpose of the cost-benefit analysis is to fill this gap and answer the question: what conditions are required for DC wind farms to be preferred over the traditional AC designs? As part of this work, the following contributions are made that have not yet been published in other literature:

This study is the first to quantitatively define the conditions that are required for DC wind farms to be cost-effective by performing sensitivity studies on wind farm size, distance from shore, DC/DC converter cost, platform cost, cable cost and collector voltage. The results of this can be used as design targets when developing novel components for DC wind farms, such as the DC/DC converter.

The analysis includes the assessment of an all-MVDC wind farm topology, as well as a comparison to two traditional designs (all-AC and AC/HVDC). There are currently

no cost estimates for this DC design and most studies only consider a comparison to a single AC wind farm topology.

The cost-benefit analysis of the AC and DC wind farms is the first which includes an assessment of multiple sources of data for wind farm cost components and their impact on the wind farm cost-effectiveness. Existing publications only consider a single source of data for their cost and rarely include any sensitivity analyses.

3.2. Selected Configurations

Four configurations were selected for investigation: two traditional designs with AC collectors and two novel designs using DC collectors. The systematic literature review in Section 2.1 showed that the standard parallel and dispersed parallel designs are the most promising in terms of economic performance. Series designs, despite having potential cost advantages, were found to have challenges with reliability [54], insulation [34], voltage balancing [68], and maintaining the transmission voltage [50]. This high technological risk means these series designs are unlikely candidates for commercialisation in the near future. These were therefore excluded from the analysis.

The first tested configuration is the traditional all-AC wind farm with radial collection system, illustrated in Figure 2.2. The collection voltage was set to be 66 kV AC, with an offshore substation using 50 Hz transformers stepping up the voltage to 230 kV for transmission. Reactive compensation in the form of shunt reactors were used to offset the export cable capacitance.

The AC/HVDC wind farm configuration is illustrated in Figure 2.3. This design has an identical collector system to that of the all-AC configuration. The voltage is stepped up using one or more 50 Hz transformers and is then converted to HVDC by an MMC. In the past, an offshore substation was typically used to house the step-up transformers before connecting to the HVDC platform, such as at the Dolwin cluster in Germany [69]. However, recent designs that use 66 kV cables remove the need for the offshore substation platform, instead housing all transformers on the HVDC platform [70]. This research considers this second design. The power is exported from the HVDC platform to shore using HVDC cables rated at ±320 kV. Finally, a second MMC is located at the onshore substation before connecting to the network.

The MVDC/HVDC configuration uses the standard parallel topology, shown in Figure 2.4. This configuration uses an MVDC collector system, typically rated at ±40 kV. The wind turbines use an isolated DC/DC converter with MFT after the rectification

stage to boost the voltage to this level. A large range of DC/DC converters have been proposed in the literature [71]. This study assumes the converter topology consists of a cascaded single-active bridge (SAB) with phase shift [65]. The offshore substation uses a high power version of this DC/DC converter. The DC/DC converter is smaller than the traditional MMC converter, resulting in a reduction in the HVDC platform footprint. An MMC converts the voltage back to AC at the onshore substation.

The final configuration is the all-MVDC wind farm, which uses the dispersed parallel topology, as shown in Figure 2.6. This design uses the same ±40 kV MVDC collector system as the previous design. This configuration however, does not have a central high power DC/DC converter on the offshore platform to step up the voltage. Instead, the offshore platform is much smaller and only consists of DC connection protection equipment. The export cables to shore have the same voltage as the collector system. Here too, an MMC is located at the onshore substation before connecting to the grid.

3.3. Wind Farm Design

The study considers wind farms ranging in size from 200 MW to 1500 MW, with a base case of 1000 MW. As a result, a generic design procedure was used to determine the wind farm parameters. The results for the base case design of each of the four configurations are shown in Table 3.1.

The collector system is considered to be a standard rectangular arrangement of the wind turbines, with an inter-turbine spacing of 7 rotor diameters [43] or 1.5 km. The number of wind turbines per string is limited by the maximum collector cable cross-sectional area (CSA), which is 800 mm^2 [64]. The wind turbines were distributed evenly to all strings. The CSA of all collector cables are then calculated based on the maximum current each is expected to conduct, resulting in smaller CSA for the first turbines in a string. The available AC and DC cable sizes and ratings were obtained from publicly available datasheets [72, 73].

For the AC designs, the number of MV busbars is calculated assuming a maximum continuous current rating of 2.5 kA per busbar [74, 75]. Each busbar has a step-up transformer connected with a rating taking into account a minimum power factor of 0.95, based on the grid code [76]. The MV busbars are connected together using normally open bus ties, which can reconfigure the power flow in case of transformer failure [75]. The maximum number of transformers per substation is assumed to be four due to the constructional constraints [74]. If more transformers are required, additional AC

substations will be needed to accommodate these.

The maximum HVAC and HVDC cable CSAs were set to be 2000 mm^2 and 3000 mm^2, respectively. Cable sizes, ratings, and AC capacitance were obtained or extrapolated from [72, 73]. For the all-AC configuration, the capacitance is considered to be fully compensated using reactive compensation equipment. The distribution of reactive compensation is based on [77, 78].

Parameter	all-AC	AC/HVDC	MVDC/HVDC	all-MVDC
Turbine rating (MW)	15	15	15	15
No. of strings	14	14	12	12
WTGs per string	5	5	6	6
String cable CSAs (mm^2)	95–630	95–630	95–800	95–800
No. of transformers	4	4	0	0
Transformer MVA	265	265	–	–
No. of export cables	3	1	1	6
Export cable CSA (mm^2)	1200	1400	1400	2400
Reactive comp. (MVAr)	950	0	0	0

Table 3.1: Wind farm design results for the base case

3.4. Cost Calculation

The aim of the cost calculation is to provide an estimate of the capital expenditure (CAPEX) for the investigated configurations. Offshore wind farms consist of a huge number of components. In the CAPEX estimation, only the most significant cost contributors are included. These consist of the wind turbines including drivetrain and foundation, the collector cables, the offshore substation including transformers and switchgear, the high power converters, the export cables and the onshore substation. For the all-AC wind farm, reactive compensation is required and the costs associated with shunt reactors and any additional platforms are also included.

Since cost information is provided in different currencies and available for various years, it is necessary to normalise all cost data. A base currency of M€$_{2021}$ was selected for this. The currency conversions are performed using the average exchange rate of the source year, obtained from [79]. Costs are then adjusted to the 2021 value of the euro based on the historical inflation rate, obtained from [80]. The equations for the median cost estimate of each of the components is provided in the following sections. For the equations of the non-median estimates, refer to Appendix A.

3.4.1 Wind turbines

AC wind turbines

The cost of AC wind turbines has been estimated by a number of sources [60,64,81] and is calculated based on the wind turbine rated power. The cost, including acquisition, foundation, transport and installation, is shown in Figure 3.1.

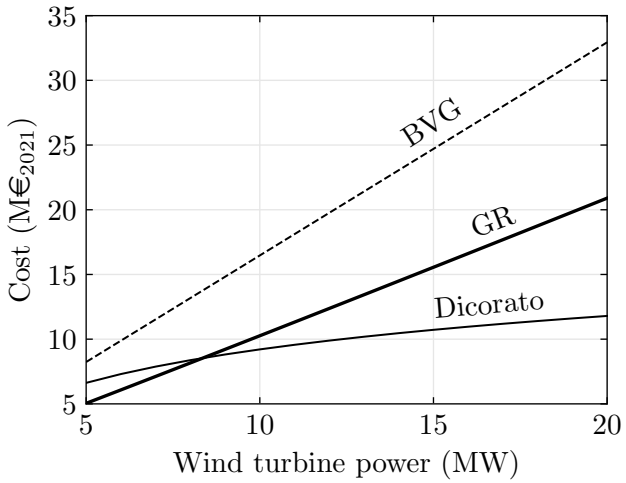

Figure 3.1: Wind turbine cost estimates based on Dicorato, González-Rodríguez (GR) and BVG Associates

The comparison shows that the three cost estimates differ significantly. The Dicorato method and González-Rodríguez (GR) method agree reasonably well for smaller wind turbine ratings of 10 MW and below, but diverge significantly for larger wind turbines. The BVG Associates estimate is consistently 60% higher than the GR estimate, and can reach differences of 180% with the Dicorato method for wind turbine ratings of 20 MW. For the base case calculations, the González-Rodríguez [81] method was used to obtain a median value, which can be described by the equation

$$C_{ACWT} = \underbrace{1.051}_{\text{inflation}} \cdot \Big(\underbrace{1.374 \cdot \frac{P_{WF}^{0.87}}{N_{WT}}}_{\text{wind turbine}} + \underbrace{0.363 \cdot P_{WT}^{1.06}}_{\text{foundation}} \Big) \tag{3.1}$$

where C_{ACWT} is the cost of the AC wind turbines in M€$_{2021}$, P_{WF} is the total active power of the wind farm, P_{WT} is the rated power of an individual wind turbine and N_{WT} is the number of wind turbines. All currencies were normalised using €$_{2021}$ as a common reference. The original equation is expressed in €$_{2016}$, hence an inflation factor

of 1.051 is used.

DC wind turbines

There is currently no cost data available for wind turbines that use DC electrical drivetrains as no commercial designs have been implemented. Most cost estimates in the literature therefore consider the cost of DC wind turbines to be a factor of the AC wind turbine cost [45]. This can be expressed as

$$C_{DCWT} = K_{WT} \cdot C_{ACWT} \tag{3.2}$$

where K_{WT} is the multiplication factor for DC wind turbines.

In [45], the factor ranges from 0.9 to 0.95 for the complete wind turbine, excluding foundation. The BVG Associates report considers the power take-off and control system to cost approximately 6.6% of the overall turbine cost, including the foundation and installation.

For this cost-benefit analysis, the four-stage DC/DC converter with MFT is assumed to have a cost that is 50% higher than the conventional back-to-back converter due to the additional conversion stage. This results in a DC wind turbine factor K_{WT} of 1.033.

3.4.2 Collector cables

Most current offshore wind farm projects use radial AC collection systems with voltages of 33 kV. More recent offshore wind farms are planned to have voltages of 66 kV. There is also ongoing research and industrial interest in increasing this voltage to 132 kV for future wind farms. Cost estimates for medium voltage cables are provided in [59, 60, 81] and are shown in Figure 3.2.

The median estimate for AC cables comes from a 2003 study by Lundberg (LB) [59], using a curve fit of manufacturer data. The equation used is

$$C_{ACcab} = \underbrace{0.144}_{\text{conversion}} \cdot \Bigg(\underbrace{C_1 + C_2 \cdot \exp\left(\frac{C_3 P_{cab}}{100}\right)}_{\text{cable}} + \underbrace{2.4}_{\text{inst.}} \Bigg) \tag{3.3}$$

where C_{ACcab} is the cable cost in M€$_{2021}$/km, C_1, C_2 and C_3 are constants dependent on the cable voltage, given in Table 3.2, and P_{cab} is the rated power of the cable. The original equation calculates the costs in SEK$_{2003}$, therefore a conversion factor of 0.1437

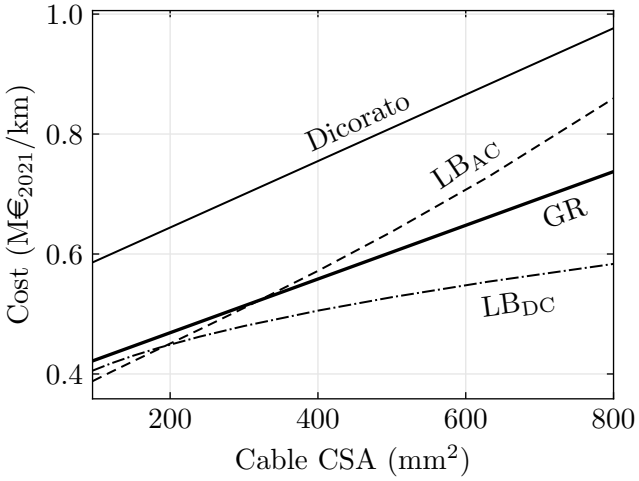

Figure 3.2: Collection system cable cost estimates, based on Dicorato, Lundberg AC cables (LB_{AC}) and DC cables (LB_{DC}), and González-Rodríguez (GR)

was used.

Voltage (kV)	C_1	C_2	C_3
33	0.411	0.596	4.1
66	0.688	0.625	2.05
132	1.971	0.209	1.66
220	3.181	0.11	1.16

Table 3.2: AC cable cost parameters used in Equation (3.3), taken from [59]

Cost estimates for DC collector cables are more difficult to obtain as medium voltage DC submarine cables are not yet widely used. The 2003 Lundberg study [59] provides a cost estimate specifically for DC cables, which has subsequently been used in many other publications [43, 45, 82]. The equation used is

$$C_{DCcab} = \underbrace{0.144}_{\text{conversion}} \left(\underbrace{C_1 + C_2 \cdot P_{cab}}_{\text{cable}} + \underbrace{2.4}_{\text{inst.}} \right) \tag{3.4}$$

where C_{DCcab} is the cost of the DC cables in M€$_{2021}$/km, P_{cab} is the rated power of the cable in MW, and C_1 and C_2 are parameters dependent on the voltage, given in Table 3.3. The installation cost of the DC cables is assumed by Lundberg to be the same as for AC cables.

Voltage (kV)	C_1	C_2
40	−0.314	0.0618
160	−0.100	0.0164
230	0.079	0.0120
300	0.286	0.0097

Table 3.3: DC cable cost parameters used in Equation (3.4), taken from [59]

3.4.3 AC transmission cables

Most of the equations for the collection system cables cannot be used for higher voltages seen in the export system, with the exception of Equation (3.3), which provides parameters for voltages up to 220 kV. Two other sources of data were found to estimate the cost of HVAC cables, including the UK's 2015 Electricity Ten Year Statement (ETYS) [61] and the 2014 NorthSeaGrid (NSG) project [62]. The cost estimates are shown in Figure 3.3.

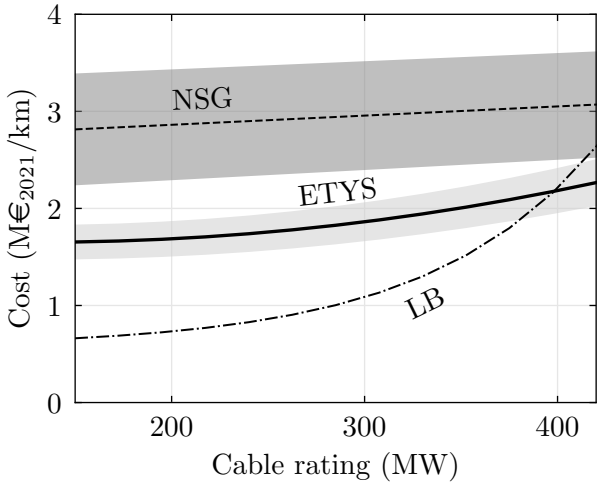

Figure 3.3: HVAC cable cost estimates, based on the NorthSeaGrid project (NSG), UK Electricity Ten Year Statement (ETYS), and Lundberg (LB)

The ETYS provides a median estimate between the extremes and was therefore selected to be used in the base case analysis. The HVAC cable cost can be approximated using the following second order equation

$$C_{HVACcab} = \underbrace{1.452}_{\text{conversion}} \cdot \Big(\underbrace{5.05 \cdot 10^{-6} \cdot P_{cab}^2 - 1.318 \cdot 10^{-3} \cdot P_{cab} + 0.4333}_{\text{cable}} + \underbrace{0.79}_{\text{inst.}} \Big) \quad (3.5)$$

where $C_{HVACcab}$ is the cost of the AC transmission cable in M€$_{2021}$/km and P_{cab} is the

rated power of the cable in MW.

3.4.4 DC transmission cables

The ETYS and NSG reports also provide cost estimates for HVDC cables of voltages in the range of 220 kV to 400 kV. These are shown in Figure 3.4. The ETYS [61] contains cost ranges for mass-impregnated and extruded cables with copper or aluminium conductors at two voltage levels and of power ratings from 600 MW to 1800 MW, whereas the NSG report provides cost ranges for single-core HVDC submarine cables with ratings of 700 MW, 1000 MW and 1400 MW. For this project, it was assumed the transmission cables would use copper conductors with cross linked polyethylene (XLPE) insulation at a voltage of 320 kV.

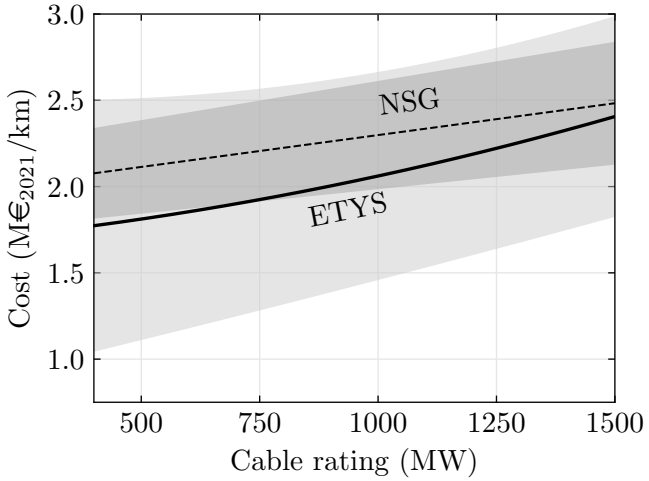

Figure 3.4: HVDC cable cost estimates, based on the NorthSeaGrid project (NSG) and UK Electricity Ten Year Statement (ETYS)

The mean of the two cost estimates was used in the base case calculations. The ETYS cost data can be approximated using a second order equation of the form

$$C_{HVDCcab} = \underbrace{1.452}_{\text{conversion}} \cdot \Big(\underbrace{1.31 \cdot 10^{-7} \cdot P_{cab}^2 + 1.473 \cdot 10^{-4} \cdot P_{cab} + 0.291}_{\text{cable}} + \underbrace{0.85}_{\text{inst.}} \Big) \quad (3.6)$$

where $C_{HVDCcab}$ is the cost of the DC transmission cable in M€$_{2021}$/km and P_{cab} is the rated power of the bipole in MW.

The NSG HVDC cable cost data can be approximated using the linear equation

$$C_{HVDCcab} = \underbrace{1.052}_{\text{inflation}} \cdot \Big(\underbrace{3.51 \cdot 10^{-4} \cdot P_{cab} + 0.079}_{\text{cable}} + \underbrace{1.755}_{\text{inst.}} \Big) \tag{3.7}$$

3.4.5 Offshore substation

The offshore substation of conventional AC wind farms contains the transformers and switchgear to step up the collector voltage to transmission voltage levels. The substation is located on an offshore platform. The costs for each of these three elements are estimated in this section.

The transformer costs can be approximated using the equation provided by Dicorato [60]

$$C_{TR} = \underbrace{1.15}_{\text{inflation}} \cdot \Big(0.0427 \cdot (P_{TR})^{0.7513} \Big) \tag{3.8}$$

where C_{TR} is the cost of the transformer in M€$_{2021}$ and P_{TR} is the rated power of the transformer in MVA. It was assumed that the offshore substation would contain two transformers capable of carrying the full power of the wind farm for redundancy.

The cost of the offshore gas-insulated switchgear (GIS) is provided in the 2015 ETYS [61] and can be approximated by the linear equation

$$C_{SG} = \underbrace{1.452}_{\text{conversion}} \cdot \big(0.0105 \cdot V_{SG} - 0.2007 \big) \tag{3.9}$$

where C_{SG} is the cost of the switchgear in M€$_{2021}$ and V_{SG} is the rated voltage of the switchgear in kV. The cost of DC switchgear used in the DC wind farm configurations was assumed to be twice the cost of AC switchgear, based on [82].

The offshore platform constitutes the largest costs of the offshore substation. Cost estimates are provided in Lundberg [59], the 2015 ETYS [61], and NorthSeaGrid report [62]. These are shown shown in Figure 3.5.

The median estimate is provided by [62] and is calculated using equation

$$C_{ACpl} = \underbrace{1.052}_{\text{inflation}} \cdot \big(0.0738 \cdot P_{WF} + 53.25 \big) \tag{3.10}$$

where C_{ACpl} is the cost of the AC platform in M€$_{2021}$ and P_{WF} is the rated power of the wind farm in MW.

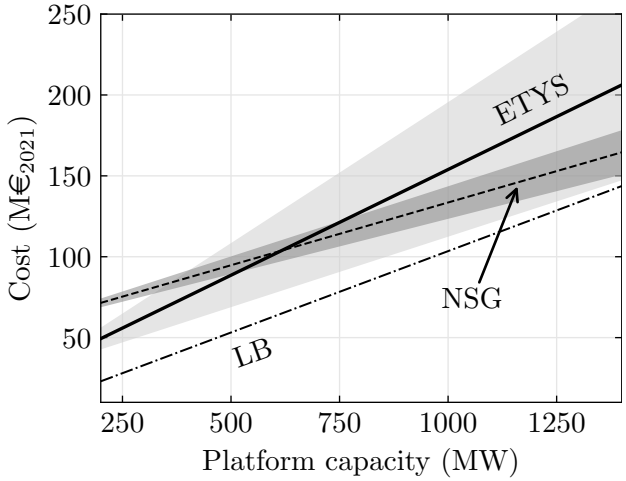

Figure 3.5: AC offshore platform cost estimates, based on the UK Electricity Ten Year Statement (ETYS), NorthSeaGrid project (NSG), and Lundberg (LB)

3.4.6 AC/DC converter

For the configurations that include HVDC transmission, costs need to be determined for the power electronic converters, both offshore and onshore. In the case of conventional wind farms, the AC/DC conversion is typically performed using MMCs. For the DC wind farm configurations, the offshore converter will be a DC/DC converter, whereas the onshore converter will be the same as in a conventional wind farm. In addition, the offshore converters are typically situated on a separate DC platform, whose cost also needs to be determined.

Three sources were consulted to obtain AC/DC converter cost data. These include Lundberg [59], the ETYS [61] and NSG report [62], shown in Figure 3.6.

The median cost estimate is provided by [59] and has been used as a basis for a number of other cost-benefit analyses [45, 82]. It makes the simple assumption that the cost of converters is 1 SEK/VA. This results in the equation

$$C_{AC/DCconv} = \underbrace{0.144}_{\text{conversion}} \cdot P_{conv} \tag{3.11}$$

where $C_{AC/DCconv}$ is the cost of the AC/DC converter in M€$_{2021}$ and P_{conv} is the rated power of the converter in MW.

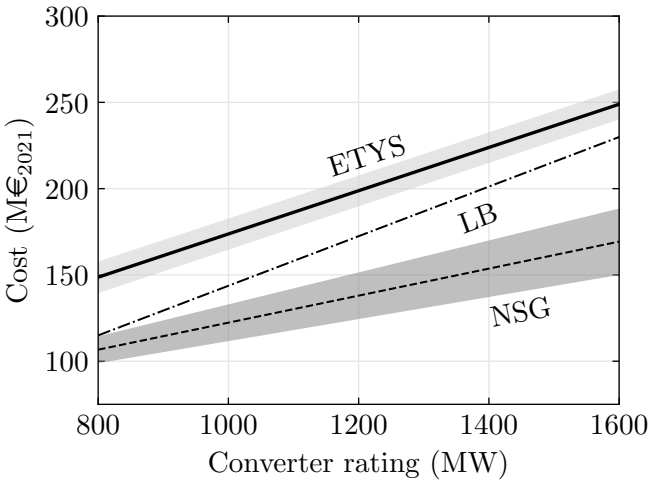

Figure 3.6: AC/DC converter cost estimates, based on the UK Electricity Ten Year Statement (ETYS), Lundberg (LB), and NorthSeaGrid project (NSG)

3.4.7 DC/DC converter

The cost of the DC/DC converter is difficult to quantify as there are currently no high power converters available on the market. Three sources have estimated their cost, including Lundberg [59], Stamatiou [82], and Parker and Anaya-Lara [43]. Their cost estimates are shown in Figure 3.7.

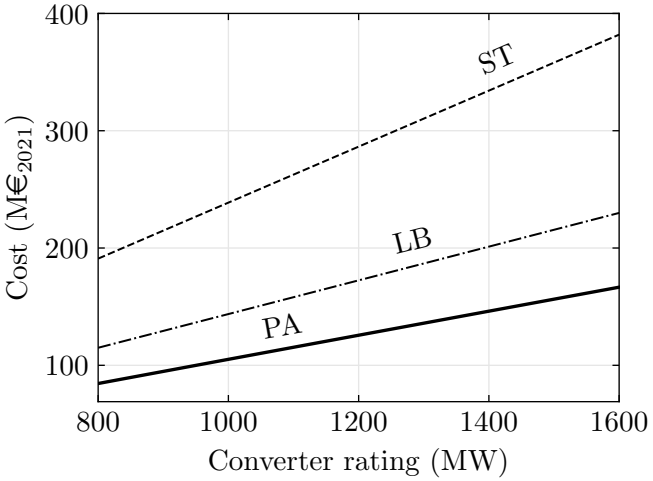

Figure 3.7: DC/DC converter cost estimates, based on Lundberg (LB), Stamatiou (ST), and Parker & Anaya-Lara (PA)

The Lundberg estimate for provides a middle ground and uses the same equation for AC/DC and DC/DC converters. This was therefore used in the base case analysis.

3.4.8 DC platform

Due to the large space requirements of the high voltage converter, this is typically located on a separate DC platform. Cost data for platforms supporting the HVDC conversion stage is provided in the ETYS [61] and NSG [62], as well as by a 2011 report by the European Network of Transmission System Operators for Electricity (ENTSO-E) [63]. These are shown in Figure 3.8.

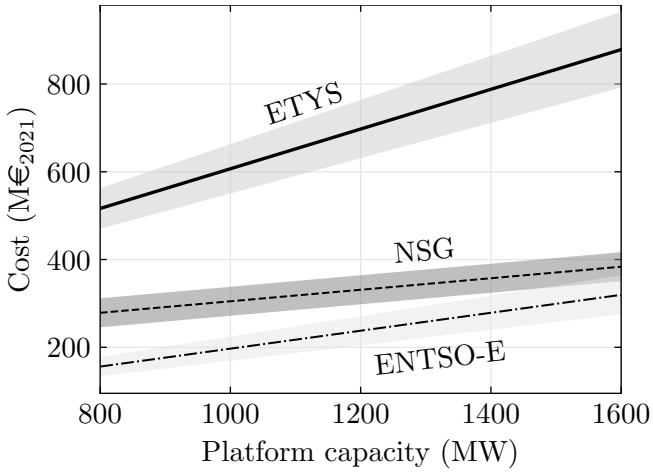

Figure 3.8: DC platform cost estimates, based on ETYS, NSG, and ENTSO-E

The median cost provided by [62] is calculated using equation

$$C_{DCplat} = \underbrace{1.051}_{\text{inflation}} \cdot \big(0.125 \cdot P_{WF} + 165\big) \tag{3.12}$$

where C_{DCplat} is the DC platform cost in M€$_{2021}$ and P_{WF} is the wind farm power in MW.

The all-MVDC configuration uses a small protection platform which is assumed to be half the cost of the AC platform. The MVDC/HVDC configuration uses a smaller and lighter DC/DC converter compared to the conventional HVDC converters used in the AC/HVDC design. The cost of this platform was assumed to be 75% of the DC platform cost in the base case.

3.4.9 Reactive compensation

For wind farms that use AC export cables, reactive compensation is required to offset the cable capacitance. This reactive compensation typically takes the form of a shunt

reactor, which can be installed at the onshore substation, offshore substation, on a separate platform at the export cable midpoint, or a combination of these locations [77, 78]. The optimal locations and distribution of the shunt reactors are dependent on the wind farm design. For this study, the results of [77, 78] are approximated based on export cable length alone, as shown in Figure 3.9.

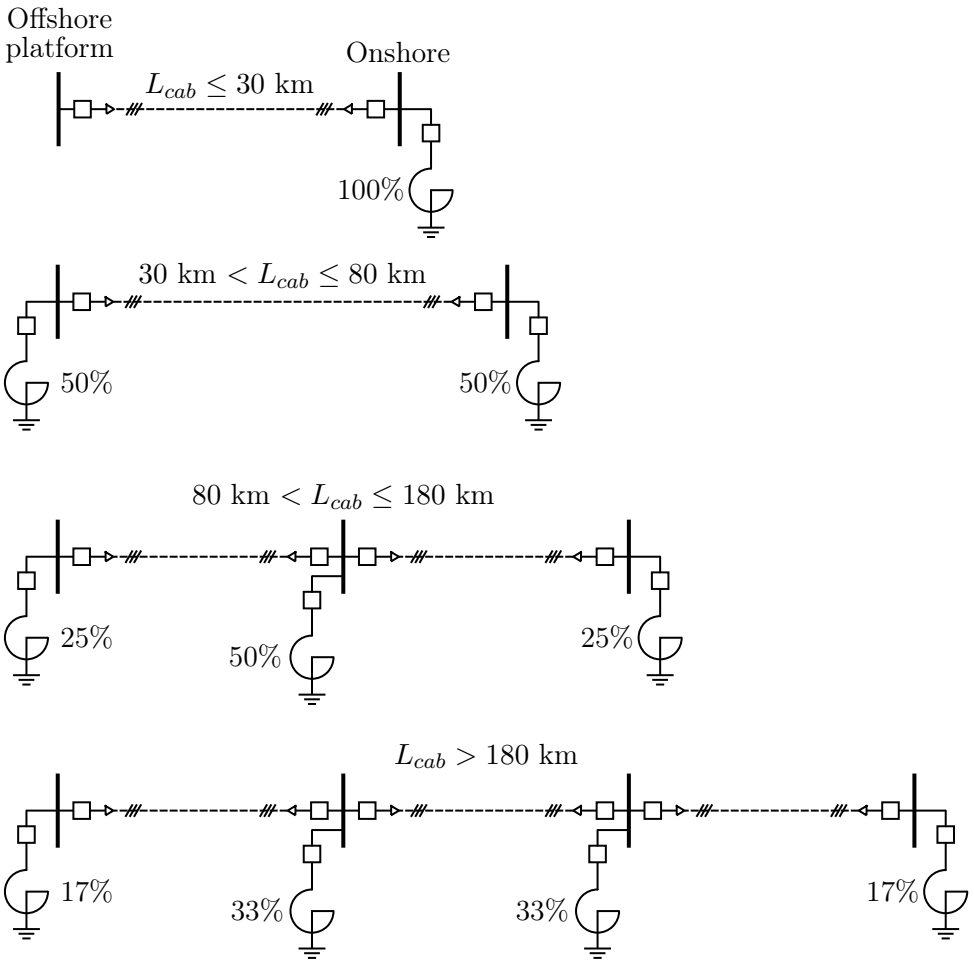

Figure 3.9: Reactive compensation locations and distribution, based on export cable length

The reactive compensation requirements were calculated using

$$Q_{comp} = \frac{V_{HVAC}^2}{2\pi f N_{cab} C_{cab} L_{cab}} \tag{3.13}$$

where V_{HVAC} is the AC transmission line-to-line voltage, f is the system frequency, assumed to be 50 Hz, N_{cab} is the number of export cables, L_{cab} is the export cable length,

and C_{cab} is the export cable capacitance per km, obtained from publicly available ABB datasheets [83].

The ETYS [61] provides costs estimates for shunt reactors. This can be approximated using the linear equation

$$C_{SR} = \underbrace{1.452}_{\text{conversion}} \cdot\big(0.0177 \cdot Q_{comp} + 0.9603\big) \tag{3.14}$$

where C_{SR} is the cost of the shunt reactor in M€$_{2021}$ and Q_{comp} is the reactor rating in MVAr.

If a shunt reactor is located on the existing offshore platform, the additional platform cost due to the shunt reactor weight is calculated using the approach from [84], with the equation

$$\Delta C_{ACplat} = \underbrace{1.084}_{\text{inflation}} \cdot\big(6.08 \cdot 10^{-4} \cdot Q_{off}^{0.765}\big) \tag{3.15}$$

where ΔC_{ACplat} is the additional AC platform cost in M€$_{2021}$ and Q_{off} is the proportion of compensation located offshore, based on Figure 3.9.

For wind farms that require additional platform(s) along the cable, the cost of the platforms is calculated using Equation (3.10), based on the reactive compensation rating from Figure 3.9.

3.4.10 Operational costs

The annual operational expenditure (OPEX) of each component was estimated as a proportion of the CAPEX, based on median values suggested in [62]. These are given in Table 3.4. The net present value (NPV) of the OPEX is calculated by discounting the annual OPEX over the lifetime of the wind farm, using the equation

$$\text{OPEX}_{\text{NPV}} = \frac{\sum_{x=1}^{X} O_x}{D_r} \cdot \big(1 - \frac{1}{(1+D_r)^{L_T}}\big) \tag{3.16}$$

where OPEX_{NPV} is the net present value of the operational costs in M€$_{2021}$, O_x is the annual OPEX of component x, D_r is the discount rate, and L_T is the lifetime in years. The base case considers a discount rate of 6% and a lifetime of 27 years [64].

Table 3.4: Component annual operational expenditures, with CAPEX as base [62]

Component	OPEX (pu)
Cables	0.025
Platform	0.02
Onshore converter	0.007
Offshore converter	0.02
Switchgear	0.007
Transformer	0.0015
Shunt reactor	0.0015

3.5. Losses, Reliability and LCOE Calculation

3.5.1 Losses

The energy losses of each component are dependent on the power output of the wind turbines. A Weibull probability distribution of the wind speed was assumed, resulting in the following expression

$$T(v) = 8760 \cdot \frac{k}{c}\Big(\frac{v}{c}\Big)^{k-1} \cdot \exp\Big[-\Big(\frac{v}{c}\Big)^{k}\Big] \tag{3.17}$$

where $T(v)$ is the annual hours with wind speed v, c is the scale parameter, and k is the shape parameter. A typical value of 2.3 for k and 11 for c was selected, resulting in the distribution illustrated in Figure 3.10a. The power output of the wind turbines at each wind speed is calculated using a generic power curve, scaled to the wind turbine rating. This is shown in Figure 3.10b. A typical reduction of 8.5% in the wind speed is included to take into account the effect of wakes in the wind farm.

The losses for each cable run were calculated using the equation

$$L_{cab} = \sum_{v=v_{min}}^{v_{max}} T(v) \cdot 3\big(I_{cab}(v)\big)^2 R_{cab} \tag{3.18}$$

where $T(v)$ is the annual hours with wind speed v, $I_{cab}(v)$ is the current passing through the cable at wind speed v, and R_{cab} is the cable resistance. For DC cables, the factor 3 is replaced by a factor 2 due to the reduction in conductors per cable.

The losses of the wind turbine converter, transformer, AC/DC converter and shunt

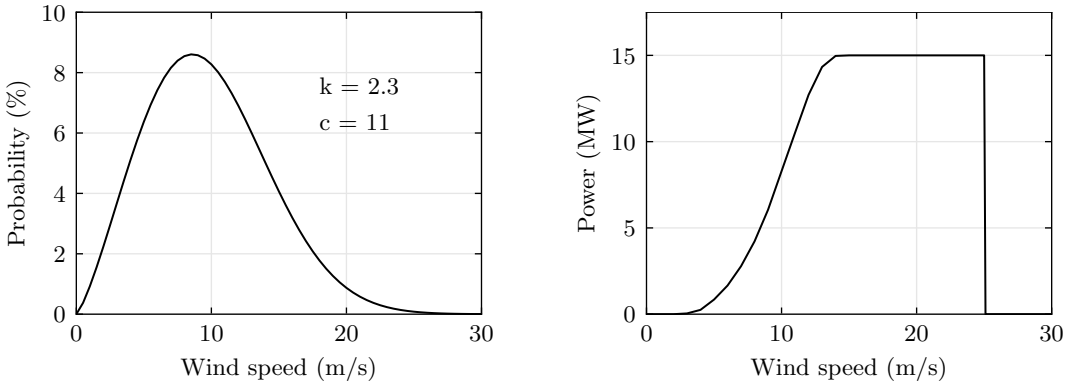

(a) Weibull probability distribution **(b)** Wind turbine power curve

Figure 3.10: Gross AEP calculation inputs

reactor were calculated using the equation

$$L_n = \sum_{v=v_{min}}^{v_{max}} T(v) \cdot \left(NLL + \left(\frac{P_n(v)}{P_{max}} \right)^2 \cdot FLL \right) \tag{3.19}$$

where L_n are the losses in per unit of component n, $P_n(v)$ is the power at wind speed v, P_{max} is the component rated power, NLL and FLL are the component no-load and full-load losses in per unit, respectively. These are provided in Table 3.5. The shunt reactors are assumed to have identical losses to the transformers.

The losses of DC/DC converters with various topologies were estimated in [65]. The base case assumes a single-active bridge topology with phase shift operation, which has losses ranging from 2.75% at low loading to 1.4% losses at full load [65].

Table 3.5: Component no-load and full-load losses

Component	Source	NLL (%)	FLL (%)
WT converter	[85]	0.2	2.0
MMC converter	[86]	0.1	0.8
Transformer	[87]	0.055	0.3

3.5.2 Reliability

The reliability of each configuration was taken into account by calculating the expected energy not supplied (EENS) due to repairs of each component, based on the approach

in [88]. The unavailability due to the failure of a component n is expressed using

$$U_n = \sum_{v=v_{min}}^{v_{max}} T(v) \cdot F_n(v) \cdot \lambda_n \cdot r_n \tag{3.20}$$

where $T(v)$ is the annual hours with wind speed v, λ_n is the failure rate of component n, r_n is the repair time, and $F_n(v)$ is the proportion of the wind farm out of service due to the failure of the component. The failure rates and repair times used in the calculation are set out in Table 3.6.

Table 3.6: Component failure rates and repair times

Component	Source	λ (yr^{-1})	r (hrs)
AC cable (per km)	[66]	0.0007	1440
DC cable (per km)	[66]	0.0004	2304
AC circuit breaker	[89]	0.024	720
Transformer	[90]	0.025	3000
WT converter	[91]	0.15	720
MMC converter	[67]	0.0153	1664

Failure rate and repair time data varies significantly between sources. In [90], the failure rate of offshore converters is found to be 1 failure per year with a repair time of up to 168 hours, whereas the failure rate and repair time used in [67] differ by an order of magnitude: 0.0153 failures/year and 1664 hours, respectively. This difference is due to the types of failures considered, as well as the consideration of travel time.

For offshore wind farms, the transportation of technicians and equipment has a major impact on overall repair time, especially since this is impacted by adverse weather conditions [92]. The downtime of the wind turbine converter and circuit breakers were therefore assumed to be 30 days, despite their much lower onshore repair times.

The reliability of the DC technology such as the DC/DC converter and DC circuit breakers is not known and will be dependent on the topology used. For this study, the unavailability of the DC/DC converter was assumed to be twice that of the AC/ DC converter plus the unavailability of the transformer. The failure rate of DC circuit breakers was assumed to be twice that of AC circuit breakers [82].

For the calculation of $F_n(v)$, it was assumed that any failure of the collector cables or string circuit breaker would result in the disconnection of the entire string. For transformer failures, the wind farm was assumed to be reconfigured to divert the energy to the remaining transformers, curtailing the wind turbine output to prevent exceeding

the transformer ratings if necessary. Similarly, if one of the export cables fails, the energy is assumed to be diverted to any remaining healthy cables up to their maximum rated capability.

3.5.3 Levelised cost of energy

The levelised cost of energy was used to compare the economic performance of the four configurations. This is calculated using the equation

$$LCOE = \frac{C_{total} + OPEX_{NPV}}{(1 - L_{total} - U_{total}) \cdot AEP_{NPV}} \tag{3.21}$$

where C_{total} is the total CAPEX, $OPEX_{NPV}$ is the net present value of the OPEX, L_{total} are the total losses in per unit, U_{total} is the total unavailability in per unit, and AEP_{NPV} is the discounted gross annual energy production.

3.6. Results

3.6.1 Base case

The base case considers a 1000 MW wind farm at a distance of 100 km from shore. The cost, losses, and reliability breakdown for each of the four configurations is shown in Figure 3.11. The cost results show that the MVDC/HVDC configuration has the lowest overall cost, mainly due to the lower DC platform and cable costs. The all-AC and AC/HVDC configurations have similar capital costs. The latter has a reduction in cable costs but these are largely offset by the converter and DC platform costs. The all-MVDC configuration does not provide significant cost savings in this case despite having the lowest platform cost of all configurations. This is because it requires a large number of export cable circuits due to the low export voltage. This significantly increases the cable costs.

In terms of efficiency, the AC/HVDC and MVDC/HVDC configurations provide improvements over the all-AC configuration due to the reduction in export cable losses. The MVDC/HVDC configuration, however, suffers from high converter losses in the base case, resulting in more limited efficiency improvements. The all-MVDC configuration has increased overall losses due to the lower export voltage, despite having no converter or transformer losses on its offshore substation.

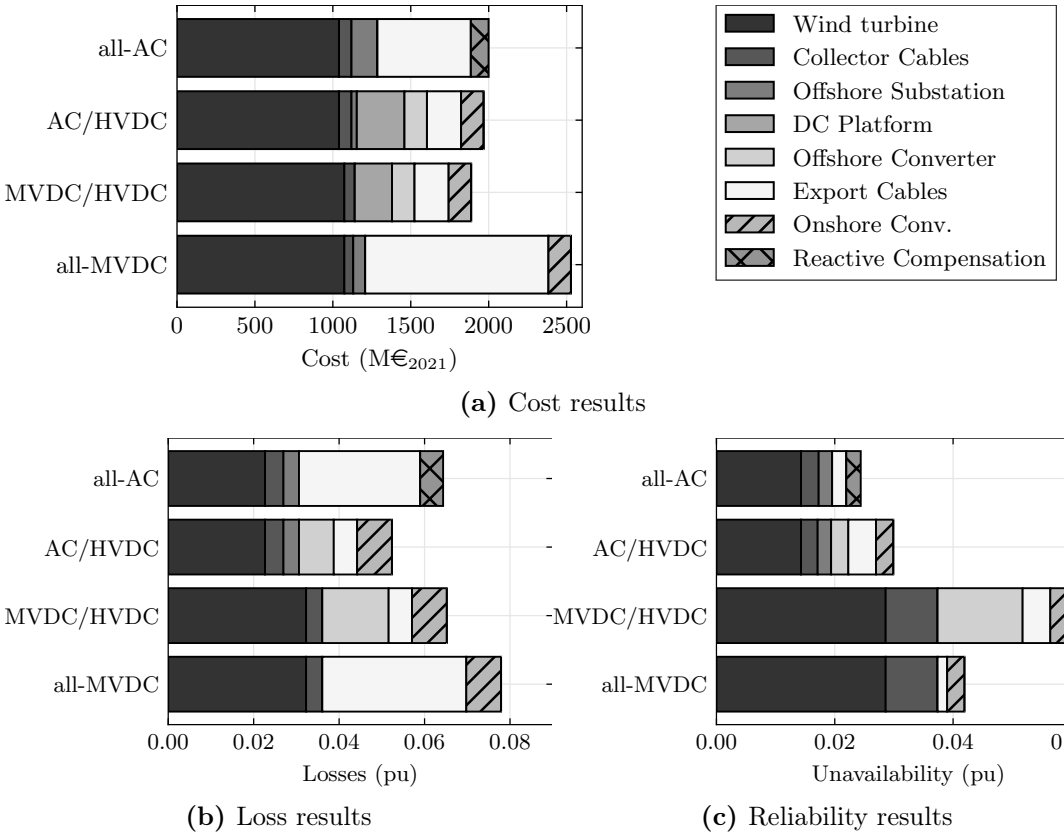

(a) Cost results

(b) Loss results

(c) Reliability results

Figure 3.11: Base case cost-benefit analysis results, showing the contribution of each component for the considered configurations

The unavailability figure shows that the all-AC configuration has the highest reliability due to the mature technology used and absence of converters. Conversely, the MVDC/HVDC and all-MVDC configurations have the lowest reliability due to the relatively high assumed failure rate of the DC/DC converter and DC switchgear.

3.6.2 Optimal configuration

The calculated LCOE for the base case shows that the MVDC/HVDC configuration is the preferred option with an LCOE of 47 €$_{2021}$/MWh. The calculated LCOE for other distances are shown in Figure 3.12. The figure shows that for a 1000 MW wind farm, the all-AC configuration has the lowest LCOE up to 80 km. The AC/HVDC and MVDC/HVDC configurations have near identical LCOEs and are most cost-effective beyond 80 km. The all-MVDC option is more expensive for all distances.

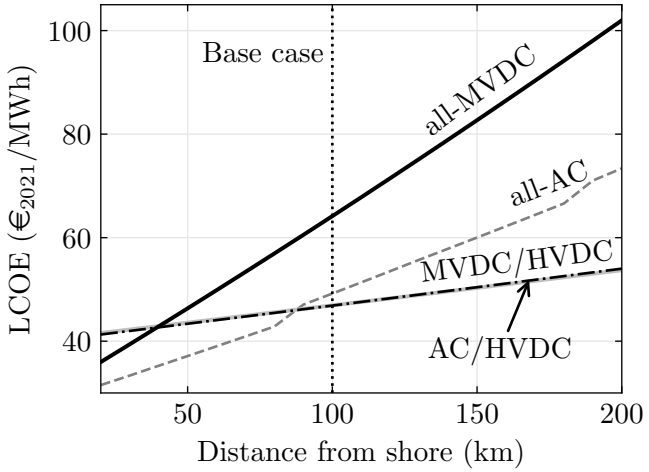

Figure 3.12: Levelised cost of energy by distance from shore for a 1000 MW wind farm using the considered configurations

It can be seen from the figure that as the distance to shore increases, the LCOE of the configurations increases linearly due to a rise in export cable costs and losses. The all-AC option has additional step increases at 90 km and 190 km because at these distances additional platforms are required to house the reactive compensation equipment along the cable circuit.

The optimal configuration was calculated for each combination of wind farm size ranging from 200 MW to 1500 MW and distance from shore between 20 km and 200 km. The base case considers a collector voltage of 66 kV AC or ±40 kV DC. The result of this calculation is shown in Figure 3.13. The results show that the traditional all-AC

configuration is the most cost-effective for wind farms of any size up to approximately 80 km from shore, or small wind farms of up to 500 MW at any distance from shore. The MVDC/HVDC option has the lowest LCOE in two regions: large wind farms of more than 800 MW at medium distances of 80 km to 140 km, and medium wind farm sizes of 400 MW to 600 MW at long distances of more than 120 km. For large wind farms at far distances, the AC/HVDC option becomes more cost-effective. The all-MVDC option does not have the lowest LCOE at any point in the base case.

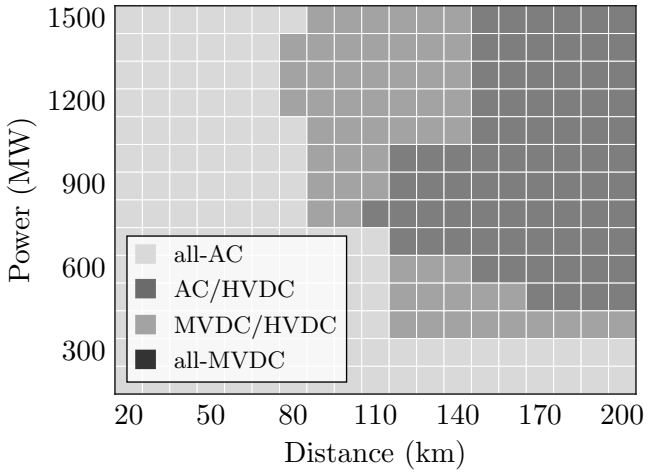

Figure 3.13: Optimal configuration in the base case for varying wind farm size and distance from shore

3.7. Sensitivity Studies

A series of sensitivity studies were performed to take into account the uncertainties of the most important elements for both all-DC configurations including the cost and performance of the DC/DC converter, the DC platform costs, the collector voltage and the export cable installation costs.

3.7.1 DC/DC converter

A sensitivity study was performed to take into account the uncertainty of the DC/DC converter technology. The cost, losses and failure rate of the DC/DC converter were varied as a proportion of the base case values. The results of this sensitivity analysis are shown in Figure 3.14.

The figure shows the DC/DC converter cost and performance have a large impact on the

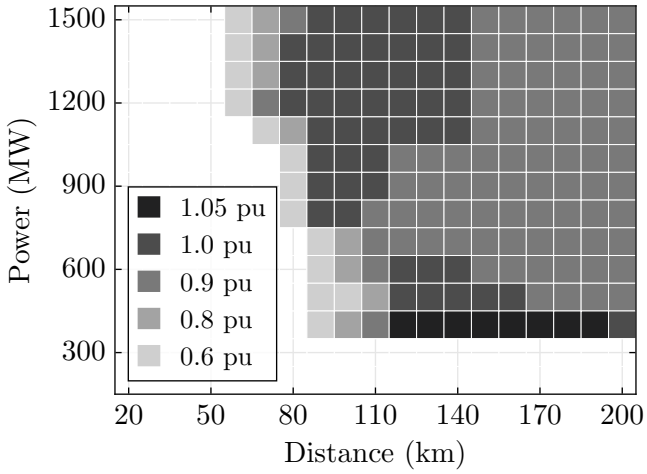

Figure 3.14: DC/DC converter sensitivity study results showing the power and distance at which the MVDC/HVDC configuration has the lowest LCOE. The per unit values represent the relative cost, losses, and reliability of the DC/DC converter compared to the base case

cost-effectiveness of the MVDC/HVDC configuration. The maximum DC/DC converter allowable cost, losses, and failure rate are 1.05 pu of the base case values. At this point, the MVDC/HVDC configuration has the lowest LCOE under very limited conditions: 400 MW wind farms located between 120 km and 190 km from shore.

As the cost and performance improve, the MVDC/HVDC option becomes the optimal configuration for more wind farms. The largest improvement can be seen at 0.9 pu, at which point the MVDC/HVDC configuration is preferred over the AC/HVDC option for all wind farm sizes and distances from shore. Further cost reductions and performance improvements have a smaller impact, marginally reducing the distance from shore at which the MVDC/HVDC configuration becomes the most cost-effective option.

3.7.2 DC platform cost

The main advantage of the MVDC/HVDC configuration over the AC/HVDC configuration is its DC platform cost reduction. The precise cost savings will be dependent on the weight and space requirements of the DC/DC converter and the DC platform design. A sensitivity study was performed to determine the cost reduction requirements. The results of this analysis are shown in Figure 3.15.

The figure shows that the MVDC platform must provide a minimum of 20% cost savings for the MVDC/HVDC option to be the optimal configuration under limited conditions.

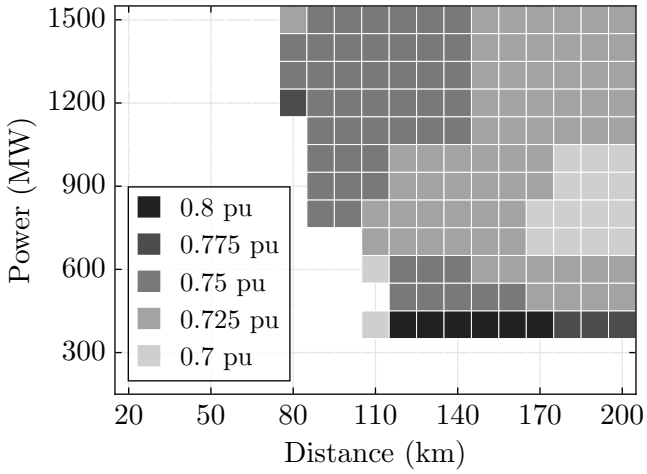

Figure 3.15: DC platform sensitivity study results showing the power and distance at which the MVDC/HVDC configuration has the lowest LCOE. The per unit values represent the relative cost of the MVDC platform compared to cost of the HVDC platform

A significant improvement can be seen when the MVDC platform is 27.5% cheaper than an equivalent HVDC platform. For the MVDC/HVDC configuration to be more cost-effective than the AC/HVDC configuration for all wind farm sizes and distances from shore, a cost reduction in the DC platform of 30% is required.

3.7.3 Collector voltage

The all-MVDC configuration is highly dependent on the selected collector voltage. Increasing the voltage will reduce the number of cable circuits required in the all-MVDC export system, which is the main source of capital costs for this configuration. A sensitivity study was performed varying the collector voltage up to ±140 kV DC. Note that higher collector voltages result in additional challenges in terms of insulation requirements and wind turbine converter capability, which have not been taken into account here. The results for this study are shown in Figure 3.16.

The figure shows that a minimum voltage of ±60 kV is required for the all-MVDC option to have the lowest LCOE for 200 MW wind farms at distances of more than 110 km from shore. Further increases in the voltage show the all-MVDC option becomes increasingly cost-effective for larger wind farms at medium distances. At a collector voltage of ±100 kV, the all-MVDC option is the most cost-effective for wind farms up to 900 MW at distances between 90 km and 120 km. If the collector voltage can be increased to ±140 kV, the all-MVDC option has the lowest LCOE for the majority of wind farm

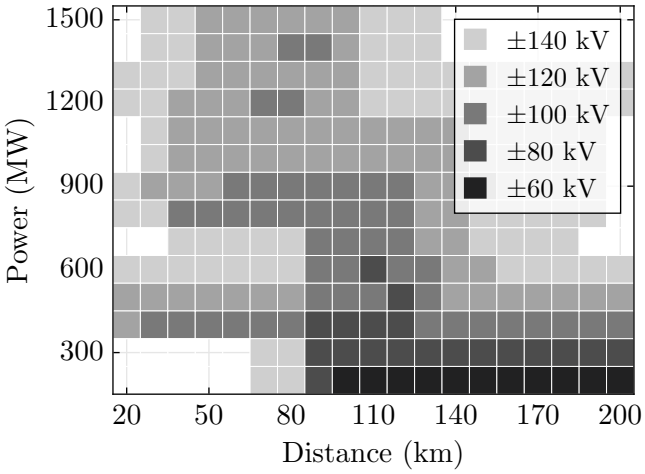

Figure 3.16: Collector voltage sensitivity study results showing the power and distance at which the all-MVDC configuration has the lowest LCOE

sizes and distances.

3.7.4 Cable installation cost

The all-MVDC configuration requires a large number of export cables, therefore any reduction in the cable installation cost will disproportionately benefit this configuration. A sensitivity study was performed on the cable installation cost, with the results shown in Figure 3.17.

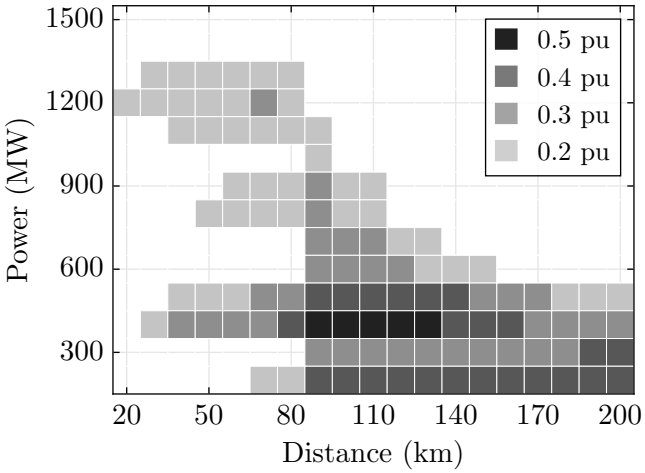

Figure 3.17: Cable installation cost sensitivity study results showing the power and distance at which the all-MVDC configuration has the lowest LCOE

The figure shows that if the cable installation cost can be reduced by 50% or more, the

all-MVDC option becomes cost-effective for small wind farms at large distances from shore, even when using ±40 kV cable circuits. Most of the installation cost is due to the hiring of vessels [64]. Therefore to achieve such a significant cost reduction, specialised equipment that can install several cables at once would likely be required.

3.8. Conclusion

This chapter investigated the conditions required for all-DC wind farms to be more cost-effective than existing AC configurations. A total of four wind farm configurations were assessed, including the all-AC, AC/HVDC, MVDC/HVDC, and all-MVDC designs. The analysis took into account the costs, losses, and reliability to calculate the wind farm LCOE. The optimal configuration with the lowest LCOE was calculated for wind farms ranging in size from 200 MW to 1500 MW at a distance from shore between 20 km and 200 km.

The results showed that for the base case, the all-AC option is preferred for wind farms of any size at distances up to 80 km from shore. The AC/HVDC option is optimal for large wind farms at very long distances of more than 150 km from shore. The MVDC/HVDC option has a very similar LCOE to the AC/HVDC option and is most cost-effective at the transition between all-AC and AC/HVDC. The all-MVDC option was found to always be more expensive than the other configurations in the base case.

The sensitivity studies showed that the main factors affecting the MVDC/HVDC cost-effectiveness were the costs of the DC/DC converter and DC platform. For the MVDC/HVDC to be more cost-effective than equivalent AC/HVDC wind farms at any size and distance, the DC/DC converter cost must be less than 90% of the cost of an equivalent MMC, with a cost reduction of 25% for the DC platform. Alternatively, if the DC platform of the MVDC/HVDC configuration costs 30% less than that of the AC/HVDC option, then the DC/DC converter can be the same cost as an equivalent MMC.

The main factors affecting the all-MVDC option are the collector voltage and cable installation costs. A collector voltage of ±100 kV or more results in the all-MVDC option being preferred for small and medium wind farms at distances above 80 km from shore. If collector voltages of ±140 kV can be achieved, the all-MVDC option becomes the optimal configuration for most wind farm sizes and distances from shore. Alternatively, a reduction in cable installation costs of 50% or more is required for the all-MVDC option to be the most cost-effective configuration for small wind farms at long distances from shore.

Chapter 4

DC/DC converters for Offshore Wind

4.1. Introduction

Chapter 3 has shown that the potential benefits of using DC collection systems are highly dependent on the design of the DC/DC converter. The selected converter topology and operating frequency will influence the cost, efficiency and reliability of the system and therefore play a large role in the overall cost-effectiveness. This chapter investigates the DC/DC converter used in the wind turbine in greater detail. A downselection of DC/DC converter topologies is performed, and the four selected converter topologies were subjected to a multi-objective design optimisation, taking into account reliability, volume, mass, efficiency, and operating frequency.

4.1.1 State of the art

A number of publications have attempted to compare DC/DC converter designs for wind turbine applications. In [71], the characteristics of six 6 MW, 2.8/100 kV converter topologies were compared, including non-resonant and resonant topologies. The assessment covered the component stresses, component count and losses. However, the study was limited since it assumed a single converter operating frequency and did not include any dimensional or reliability analysis of the converters.

A study by [93] investigated the power loss, volume and weight of six isolated 10 MW converter topologies, including three matrix-based converters and three back-to-back converters. They also investigated the impact of the MFT frequency and number of parallel connected modules. Their results show that the reduced matrix converter (RMC) had the highest efficiency over the whole frequency range, and low volume at frequencies

above 7 kHz. The 1-phase and 3-phase full bridge converters were the next most efficient with comparable volumes at frequencies up to 3 kHz. However, matrix converters are unlikely to be commercially available in the near future due to their relatively high control complexity and lack of practical applications. The study also does not include any assessment of the reliability or insulation requirements.

In [94], the 1-phase dual active bridge (DAB1) and 3-phase dual active bridge (DAB3) were compared in terms of losses, volume and weight for a 10 MW, 1/50 kV converter. The converter consisted of 50 modules, each with a 1:1 transformer ratio. They found that the DAB1 and DAB3 have similar losses of around 1.5%, with the DAB3 having approximately 20% lower volume and weight. However, the study considered only bidirectional converters operating with a single frequency and did not assess the converter reliability or insulation.

4.1.2 Contributions

This research provides a comprehensive DC/DC converter optimisation and comparison for DC-connected offshore wind turbines. The study is comprehensive as it covers multiple aspects of converter design, including the reliability, dielectric insulation, volume, weight, and losses for varying operating frequencies. The study includes a multi-objective optimisation of the MFT and a volume optimisation considering the insulation requirements. The DC/DC converter topologies included in the study include both 1-phase and 3-phase, unidirectional and bidirectional DC/DC converters.

Existing research only considers a limited number of these factors. For example, most studies consider a single DC/DC converter topology, which can be unidirectional or bidirectional. Proponents of the unidirectional converters argue that these provide the most cost-effective solution since wind turbines only need to deliver power. However, bidirectional power converters would allow for self-start capabilities in case of a black start, since power is required to energize the DC bus and to supply the auxiliary equipment [95]. The fault ride-through ability of unidirectional and bidirectional converters may also differ due to their differing degree of controllability. There is a lack of studies investigating how these two topology designs compare to each other.

This research is particularly relevant for offshore wind applications by being one of the first to include a dedicated reliability study. Reliability is a key factor due to the difficulty in accessing offshore equipment. In addition, the reliability calculations have knock-on effects for the rest of the converter design. For example, the desired reliability will influence the converter redundancy requirements, which in turn affects component

stresses, which influence transformer design, which impacts the size and efficiency of the converter. This interplay of factors is frequently overlooked in existing comparison studies, especially where reliability is concerned.

This chapter includes a frequency sensitivity study, which details how the selection of the operating frequency can influence the performance and size of the converters. Existing comparison studies typically assume a single converter operating frequency, which can range from as little as 500 Hz [71] up to 10 kHz [96]. This study aims to fill this research gap by providing a quantitative method to select the converter operating frequency.

This research is one of the first to include an insulation coordination study and to physically arrange the components as part of the volume calculations. This is important because at higher frequencies, the dielectric insulation requirements play an increasingly important role. This is a factor that is currently not addressed in any of existing literature.

Finally, this chapter examines DC/DC converters fit for modern wind turbines. The rapid development of wind turbines has resulted in assumptions from previous studies to already be outdated. The latest generation of offshore wind turbines are rated at 15 MW. Offshore wind farm array voltages of 66 kV are now standard, with plans for further increases to 132 kV [97]. Wind turbine generator voltages are typically below 1 kV [98], whereas the DC collection system is expected to operate at around ±40 kV (80 kV pole to pole), which is the DC equivalent of 66 kV AC [99]. The DC/DC converter must be designed to be able to handle these high power ratings and large step-up ratios.

The chapter is organized as follows: In Section 4.2, the DC/DC converter topologies are reviewed, and a downselection is performed to determined the most promising candidates. In Section 4.3, the four selected topologies and the methodology used in the comparison are set out. In Section 4.4, the reliability calculations are performed to determine the required converter redundancy. In Section 4.5, the size and weight of the converter components is calculated, including the transformer, semiconductors and cooling, capacitors, and required isolation clearance. Section 4.6 details the efficiency calculation for each of the converters and Section 4.7 sets out the results of the frequency sensitivity studies. Finally, Section 4.8 presents the conclusions of the research.

4.2. DC/DC Converter Review

A multitude of converter topologies has been put forward for high power DC/DC conversion, which can broadly be categorised into isolated [100–102] and non-isolated designs [103–105], resonant and non-resonant designs, modular and non-modular designs [106]. Refer to Figure 4.1 for a classification of the designs [106]. It is therefore necessary to perform a downselection of DC/DC converter topologies to determine topologies that are most suited for use in DC wind turbines.

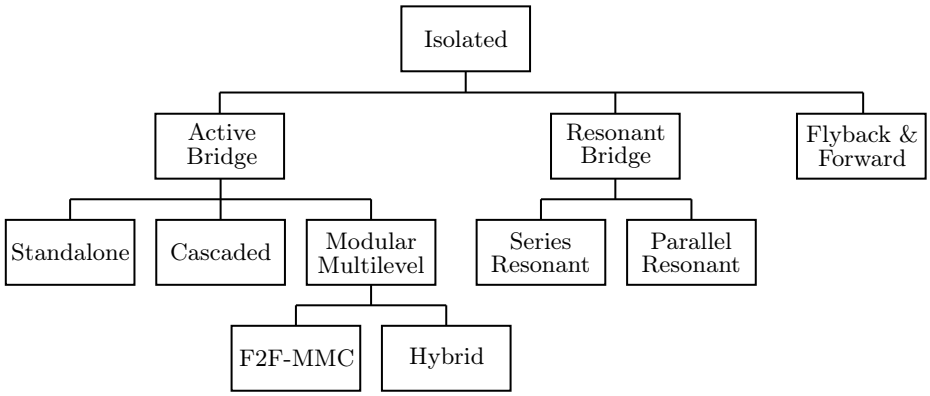

(a) Isolated topologies

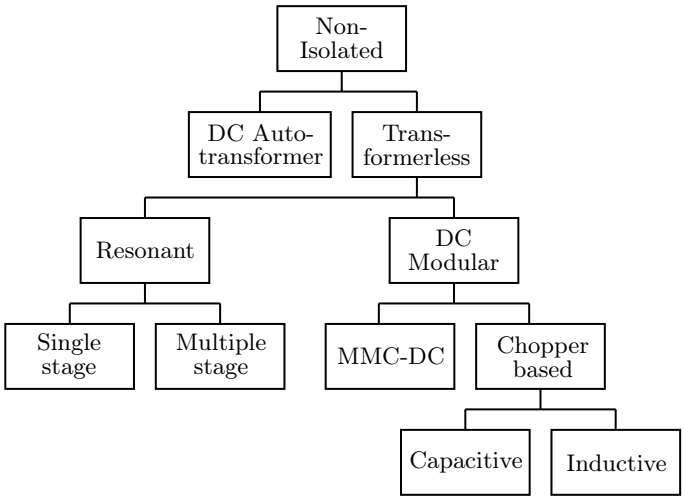

(b) Non-isolated topologies

Figure 4.1: DC/DC converter classification, based on [106]

4.2.1 Downselection

The fundamental requirements of DC/DC converters for wind energy applications include capabilities such as a high power rating, a high voltage step up ratio, high reliability, high efficiency, low cost, high power density, electrical safety, similar control to AC converters, and a compatible electrical interface with the generator [65].

Isolated DC/DC converters have a number of benefits over their non-isolated counterparts which make them more suited to offshore wind applications. The use of a transformer allows for galvanic isolation between the low voltage and high voltage side. Most of modern wind turbines use generators with a relatively low output voltage ranging from less than 1 kV to a few kV [98, 107]. Therefore, galvanic isolation is desirable for wind turbines as it allows for lower insulation requirements for the generator and improved safety [108, 109]. In addition, transformers are highly reliable equipment which can achieve a high voltage step up simply by increasing the turns ratio. However, the design and optimisation of a high power MFT is an ongoing challenge [98]. Higher frequency allows for a smaller and lighter transformer design but leads to increased semiconductor switching losses [110].

Isolated designs can largely be divided into three categories: active bridge, resonant bridge, and flyback or forward type converters. The flyback-type converter designs suffer from challenges with the high insulation and high current requirements in the inductor circuits, limiting their use in high power application [106]. Resonant converters use additional inductors and capacitors in the topology to achieve soft-switching over a wide range of voltage and power [111]. However, the efficiency benefits over non-resonant designs are not guaranteed [71, 100, 108]. For frequency-controlled resonant converters, the wide range of operating frequency complicates the design of passive components, filters, the transformer, and gate driver circuitry [112]. This additional complexity makes these topologies an unlikely candidate for near-term commercialisation.

The remaining active bridge topologies can be standalone, cascaded or modular multilevel. The standalone or bulk design consists of a single MFT with series and/or parallel connected switches. This has the benefit of relatively simple construction. However, the series connection of switches is challenging to implement in practice due to unequal voltage distribution issues [113] and can lead to lower converter reliability. The modular multilevel topologies were found by previous research [114] to have higher costs and lower efficiency compared to the cascaded designs for wind farm applications. Therefore, the topologies that were selected for this work are the cascaded active bridge topologies, which include the single active bridge [101, 115] and dual active bridge [114, 116].

Both converter topologies have a single-phase and a three-phase variant, resulting in the single-phase single active bridge (SAB1), the three-phase single active bridge (SAB3), the single-phase dual active bridge (DAB1), and the three-phase dual active bridge (DAB3). These topologies are investigated in further detail in the following sections.

4.2.2 SAB1

The SAB1 schematic is shown in Figure 4.2a. The SAB1 is characterised by an active inverting bridge at the input and a passive rectifying bridge at the output. An MFT provides galvanic isolation and steps up the voltage. The leakage inductance of the MFT can be used for the power transfer to remove the need for an external inductor.

The SAB1 can be operated in either continuous conduction mode (CCM) or discontinuous conduction mode (DCM), depending on the leakage inductance, duty cycle and voltage. In CCM, the converter can achieve soft-switching through the use of capacitors connected in parallel to the switches, but at lower output powers the converter loses this soft-switching capability as it operates in DCM, where the switch capacitors increase the turn-off losses of the converter at low power output [115, 117]. This is described in more detail in [118].

For large wind turbine applications, which do not operate at full power continuously, the SAB1 is therefore typically designed to operate exclusively in DCM, without the use of soft-switching capacitors. This simplifies the design and reduces the filter inductance requirements [115, 119], at the cost of higher current stresses [108]. The waveforms for the SAB1 operating in DCM are shown in Figure 4.2b. The maximum duty cycle which results in DCM is calculated using

The average output power in DCM is given by

$$P_2 = \frac{V_1}{fL}\left(V_1 - \frac{V_2}{a}\right)D^2 \tag{4.1}$$

where V_1 is the input DC link voltage, f is the switching frequency, L is the transformer leakage inductance, V_2 is the output DC link voltage, a is the ratio of secondary turns to primary turns, and D is the applied duty cycle.

The maximum power output is achieved for the largest duty cycle which still allows for discontinuous operation, given by

$$D_{max} = \frac{V_2}{2aV_1} \tag{4.2}$$

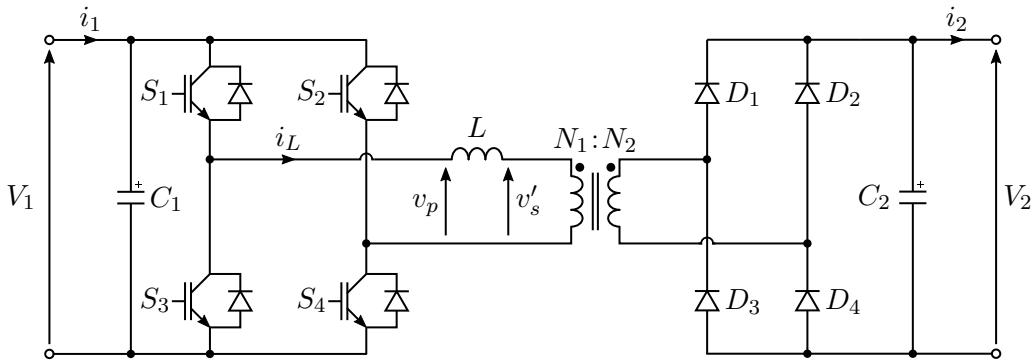

(a) Schematic

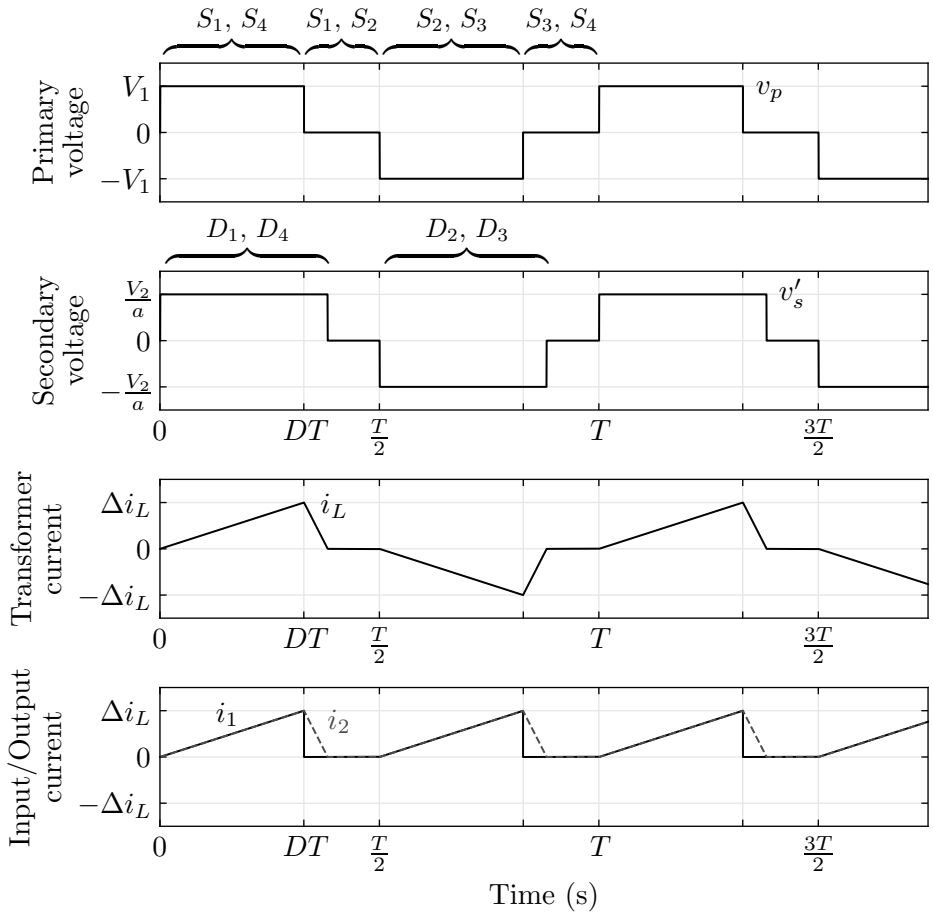

(b) Waveforms

Figure 4.2: The single-phase, single active bridge converter (SAB1), operating in discontinuous conduction mode

4.2.3 SAB3

The schematic for the SAB3 is shown in Figure 4.3a. It uses a three-phase active full bridge inverter at the primary side and a three-phase passive full bridge rectifier on the secondary. The bridges can be connected through three single-phase transformers or a single three-phase transformer. The primary and secondary windings are connected in a Y-Y arrangement [120].

The SAB3 operates by closing the switches in each phase (S_1, S_2, S_3) with a phase shift of 120 degrees. Similar to the SAB1, the duty cycle determines the duration of the ON state of each of these switches. The gate signals for the switches on the lower arms are complementary to those of the upper arm.

The SAB3 has a total of eight operating modes [120], depending on the applied duty cycle and the voltage conversion ratio. The voltage conversion ratio is defined as

$$m = \frac{V_2}{aV_1} \tag{4.3}$$

For wind turbine applications, this ratio tends to be high ($m > 0.5$), therefore the SAB3 will only see four of these operating modes, which include three different CCMs and one DCM. The operating mode depends on the applied duty factor.

The voltage and current waveforms of the SAB3 when operating at maximum power output are shown in Figure 4.3b. For a detailed description of the waveforms at other operating points, refer to [120].

The output power for all four high voltage conversion ratio operating modes [120] is

$$P_2 = \begin{cases} \frac{V_1^2}{fL}(1-m)D^2 & 0 < D \leq \frac{m}{3} \\ \frac{mV_1^2}{12fL}(4D - 3D^2 - m^2) & \frac{m}{3} < D \leq \frac{1}{3} \\ \frac{mV_1^2}{12fL}(4D - 3D^2 - m^2) & \frac{1}{3} < D \leq \frac{2-m}{3} \\ \frac{mV_1^2}{9fL}(1-m)(1+m) & \frac{2-m}{3} < D \leq \frac{1}{2} \end{cases} \tag{4.4}$$

where the maximum power occurs for a duty cycle of $\frac{2-m}{3}$.

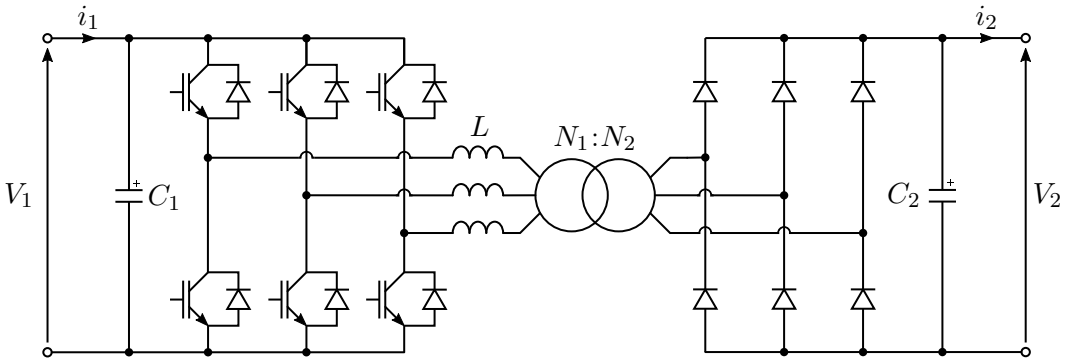

(a) Schematic

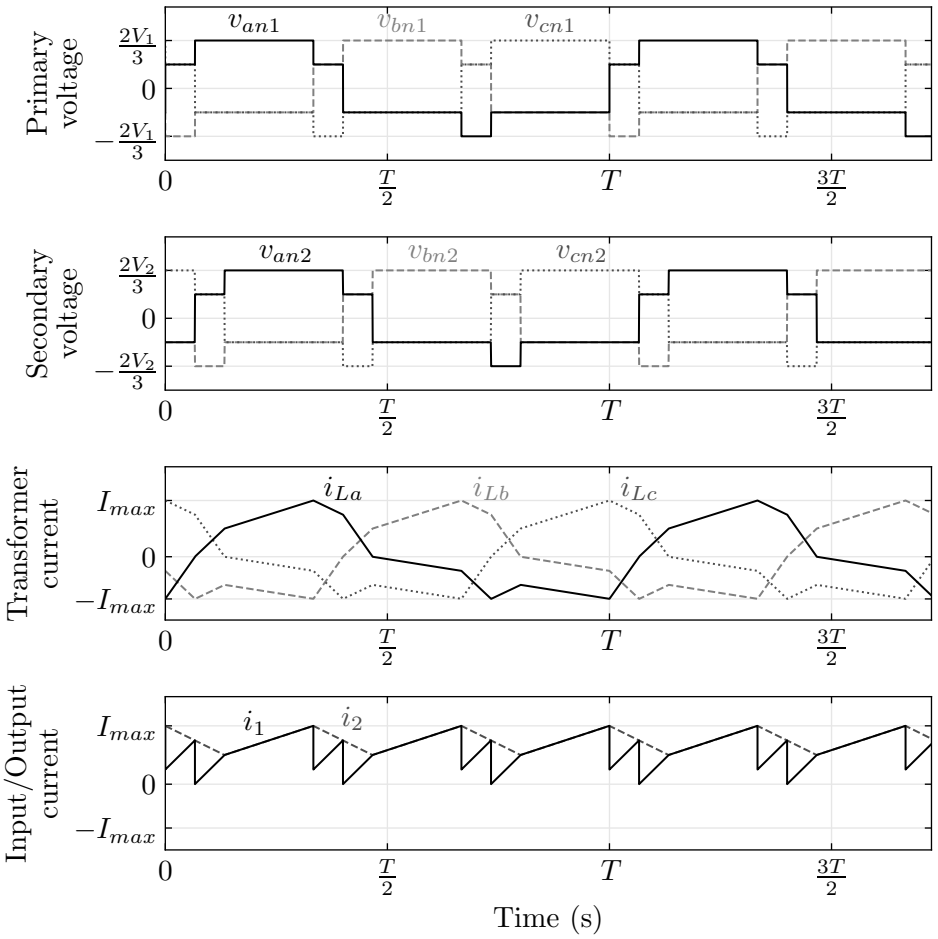

(b) Waveforms

Figure 4.3: The three-phase single active bridge converter (SAB3), operating in continuous conduction mode at nominal output power

4.2.4 DAB1

The schematic for the DAB1 is shown in Figure 4.4a. The DAB1 has a similar topology to the SAB1, with the main difference being an active bridge on the secondary. This allows for bidirectional power flow, which could be useful if the wind turbine needs self-start capabilities. As with the SAB1, the DAB1 transformer's leakage inductance can be used for the power transfer, resulting in a more compact overall design.

The DAB1 achieves soft-switching through the use of capacitors connected in parallel with each switch [117]. However, this ability of the DAB1 to achieve zero voltage switching is dependent on the operating conditions, with low power output and low voltage conversion ratios associated with a loss of soft-switching when using single-phase-shift control.

Several more complex control strategies have been proposed to extend the soft-switching operating range of the DAB1, including dual-phase-shift, extended-phase-shift, triple-phase-shift control, triangular current, and trapezoidal current control [121, 122]. However, in wind turbine applications, the wind turbine DC link voltage and collector system voltage are strictly controlled, which means a voltage conversion ratio of unity can be maintained. This allows for soft-switching at all operating points with the much simpler single-phase-shift control.

In single-phase-shift control, both pairs of switches on each bridge have a fixed duty cycle of one half of the switching period, creating a square wave voltage on both bridges. The bridge voltages are shifted by a phase angle, δ. This angle is the only control variable, which greatly simplifies the controller design. The phase angle determines both the magnitude of the power delivery and the direction of power exchange, with power flowing from the leading to lagging bridge. The drawback of this control strategy is that it leads to relatively large RMS currents in the transformer [122].

The voltage and current waveforms of the DAB1 are shown in Figure 4.4b. The average power output of the DAB1 is given by the equation

$$P_2 = \frac{V_1 V_2}{fLa}\delta(1 - 2\delta) \tag{4.5}$$

where δ is the phase shift angle. The maximum power output is achieved at a phase shift of 0.25, which provides an upper limit for the inductance value required to achieve a certain power output [122].

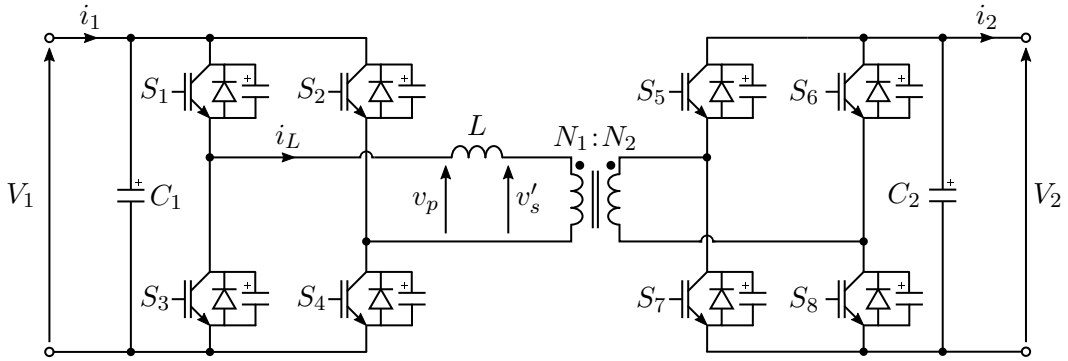

(a) Schematic

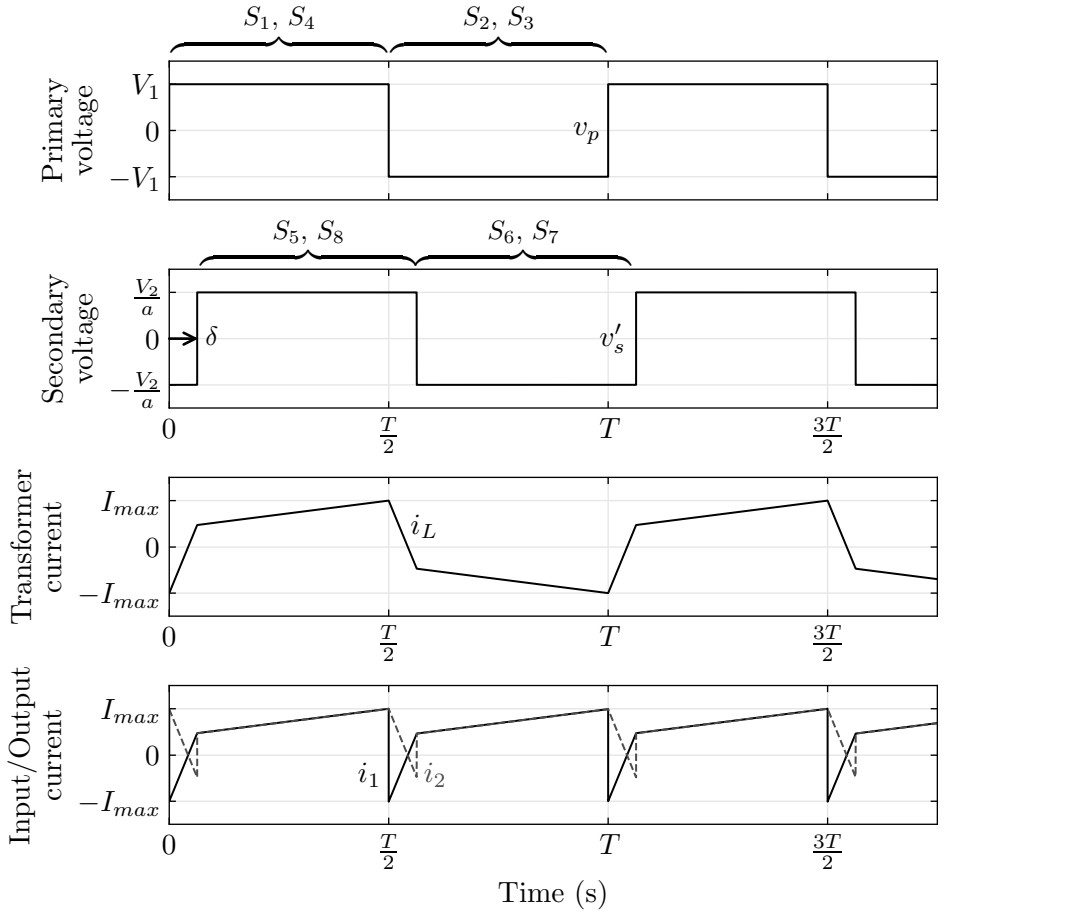

(b) Waveforms

Figure 4.4: The single-phase dual active bridge converter (DAB1), operating at nominal output with single-phase-shift control

4.2.5 DAB3

The schematic for the DAB3 is shown in Figure 4.5a. The DAB3, first introduced in [116] for aerospace applications, uses a three-phase active full bridge at the primary side and secondary side of the MFT. The magnetic link can be established using a three single-phase transformers or a single three-phase transformer [123]. If a three-phase transformer is used, this is traditionally connected in a Y-Y configuration [116].

The DAB3 operates by closing the switches for each phase of the inverter and rectifier side with a phase shift of 120 degrees, producing a typical six-step voltage waveform. As with the DAB1, multiple control strategies have been proposed for the DAB3, including single phase shift control, variable duty cycle control [124], instantaneous flux control [125], among others.

The single phase shift control is explained below, and the resulting waveforms are shown in Figure 4.5b. The primary side and secondary side are shifted by a controllable phase shift δ, which regulates the power output of the converter. The DAB3 has two operating modes, depending on the applied phase shift. The output power is given by

$$P_2 = \begin{cases} \dfrac{V_1 V_2}{fLa}\delta\left(\dfrac{2}{3} - \delta\right) & 0 \leq \delta \leq \dfrac{1}{6} \\ \dfrac{V_1 V_2}{fLa}\left(\delta - 2\delta^2 - \dfrac{1}{36}\right) & \dfrac{1}{6} < \delta \leq \dfrac{1}{3} \end{cases} \tag{4.6}$$

As with the DAB1, the maximum power output is achieved at $\delta = 0.25$, which can be used to obtain the maximum series inductance. The selected design inductance is typically a value below this upper limit and represents a trade-off between the peak current ripple and transformer size.

The DAB3 has the advantage of using three phase legs, which results in comparatively low current magnitudes due to the additional leg used to transfer the same converter power. In addition, the current profile is much more sinusoidal, which is associated with a reduction in the harmonic content [126]. From Figure 4.4b, it can be seen that the input and output DC current ripples, and therefore the associated voltage ripples, are significantly smaller for the DAB3 than the DAB1. This allows for smaller filter components [126].

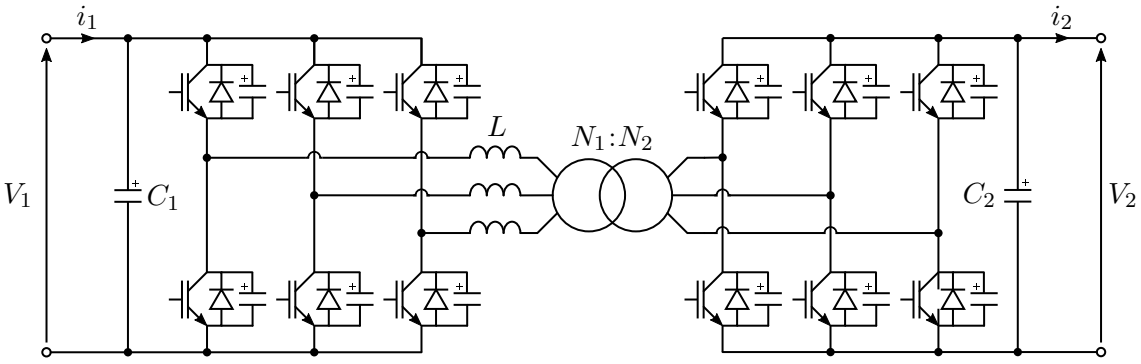

(a) Schematic

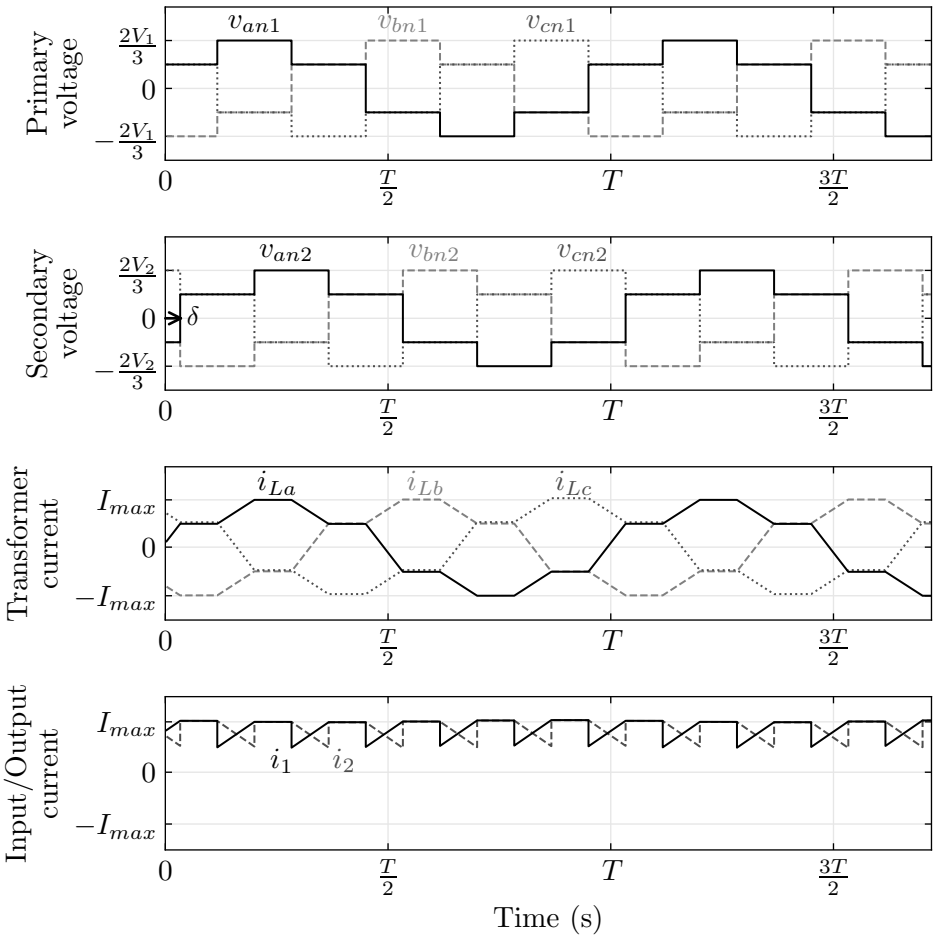

(b) Waveforms

Figure 4.5: The three-phase dual active bridge converter (DAB3), operating at nominal output with a unity voltage conversion factor

4.3. Methodology

The methodology used in the converter comparison is illustrated in Figure 4.6. The DC/DC converter design starts with the converter availability requirements and device data to calculate the number of redundant modules based on component stresses, failure rates and reliability requirements. For a given operating frequency, the MFT is then designed using a multi-objective optimisation, which minimises the transformer size and losses while meeting the isolation and inductance requirements. PLECS simulations are performed to determine the losses of the semiconductors, as well as to determine the capacitance and heat sink requirements. Once the optimal design is selected, the components are arranged into a minimum volume configuration, taking into account the insulation coordination requirements. The total volume and weight are then calculated for each of the converters. Finally, the frequency is increased and this process is repeated to determine an optimal operating frequency.

4.4. Modularity and Reliability

4.4.1 Connection options

The DC/DC converter can either be a standalone design, consisting of a single MFT with series and/or parallel connected switches, or a modular design, which consists of multiple series and/or parallel connected DC/DC converters, each with their own MFT. The standalone or bulk design has the benefit of relatively simple construction. However, modular designs have improved reliability [127] and avoid connecting switches in series, which is challenging to implement due to unequal voltage distribution issues [113].

Several options for cascaded connections are possible, including input-series output-series (ISOS), input-series output-parallel (ISOP), input-parallel output-parallel (IPOP), and input-parallel output-series (IPOS) [113]. More complicated arrangements are also possible, including combinations of these connections [128] and the connection of unequally rated converter modules [129], but these were considered beyond the scope of this study.

In general, a series connection results in higher voltage capability, whereas a parallel connection allows for a higher current capability. For the high-power, high voltage step-up requirements of a DC wind turbine, the IPOS connection is most suitable. This topology is illustrated in Figure 4.7.

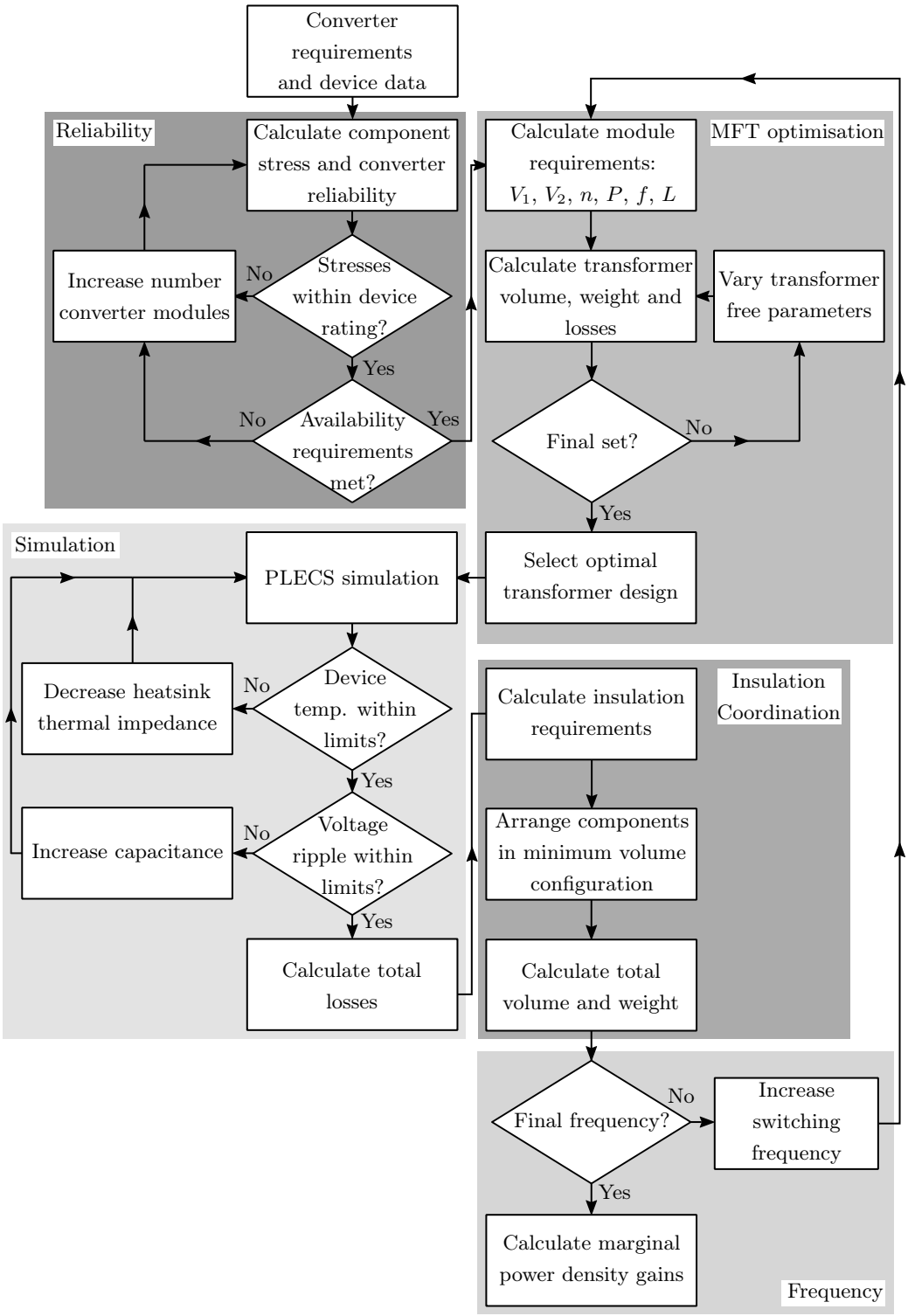

Figure 4.6: Converter comparison methodology flow diagram

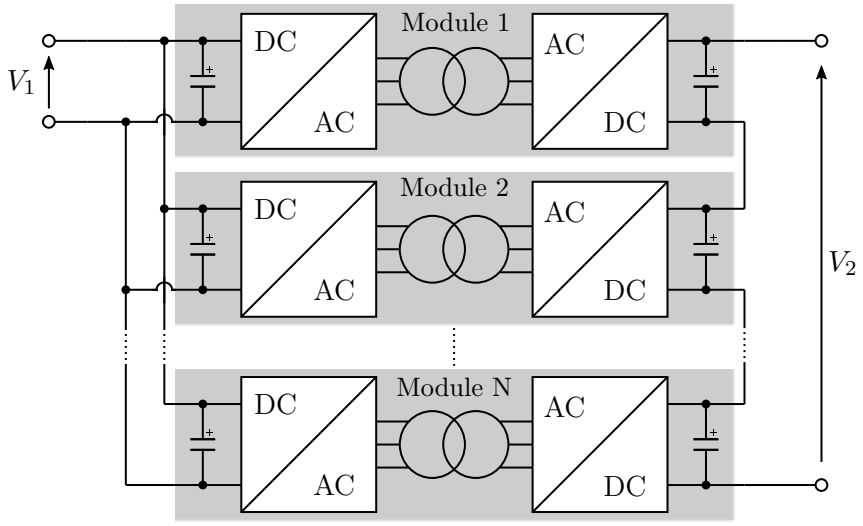

Figure 4.7: Schematic of an input-parallel, output-series DC/DC converter

4.4.2 Minimum number of modules

The selection of the number of converter modules will have a large impact on the overall converter design and performance metrics. Some papers [130] consider a basic approach where the MFT transformer turns ratio is considered to be 1:1. This has the benefit of reducing the transformer complexity but results in an exceedingly large number of modules required for large voltage step-ups. The inductance required in each module also increases as the total number of modules increases, resulting in a sub-optimal design.

A better approach is to select the number of modules based on semiconductor stresses and converter reliability [131, 132]. The minimum number of modules is determined based on the blocking voltage and current rating of the selected semiconductors, thereby avoiding the series-connection of individual switches, which may be difficult to implement in practice.

The minimum number of series-connected modules required to withstand the voltage can be calculated using

$$k_s = \left\lceil \frac{V_{sw}}{\gamma V_{max}} \right\rceil \tag{4.7}$$

where V_{sw} is the voltage experienced by the semiconductor, V_{max} is the maximum voltage rating of the semiconductor, and γ is the voltage de-rating factor. The de-rating factor ensures both that there is a safety margin for voltage transients, and that the semiconductor can achieve a reasonable failure-in-time (FIT) [133]. A de-rating

factor of 60% is assumed for all semiconductor components.

Similarly, the minimum number of parallel-connected modules required to withstand the current is calculated based on limits given in the datasheet. Semiconductors current limits are typically provided for average current, root-mean-square (rms) current and repetitive peak current.

$$k_p = \left\lceil \frac{I_{sw}}{I_{max}} \right\rceil \tag{4.8}$$

where I_{sw} is the average, rms, or peak current experienced by the semiconductor and I_{max} is the corresponding maximum current limit provided in the datasheet. Since the number of parallel- and series-connected modules must be equal, the minimum number of modules is given by

$$k = \max(k_s, k_p) \tag{4.9}$$

4.4.3 Reliability

Additional redundant modules can be added to increase the reliability of the converter to an acceptable level for offshore installation, where it is difficult to access and repair turbines located far from shore. The redundant modules can either be on standby until an active module fails, or operate continuously along with the other modules [134]. The second approach is taken here, as it is the industry standard and further reduces the voltage stresses on the semiconductors, thereby reducing their failure rate.

The converter reliability is calculated based on the method used in [132]. The failure rates of individual electrical components are given in Table 4.1. One converter module consists of the semiconductors of the input and output bridge, the MFT, and the DC capacitors, as shown in the reliability block diagram in Figure 4.8. One gate driver was assumed per leg of IGBT switches. The MFT failure rate is assumed to be negligible during the converter lifetime [132]. For the three-phase topologies, the converter is considered to be operational as long as at least two out of the three legs are healthy, although the maximum power output will be curtailed [120]. A failure of any other component results in the failure of the module.

The base failure rate of the module can be expressed using

$$\lambda_m = \sum N_c \lambda_a \tag{4.10}$$

where λ_m is the base failure rate of one module, N_c is the number of components with

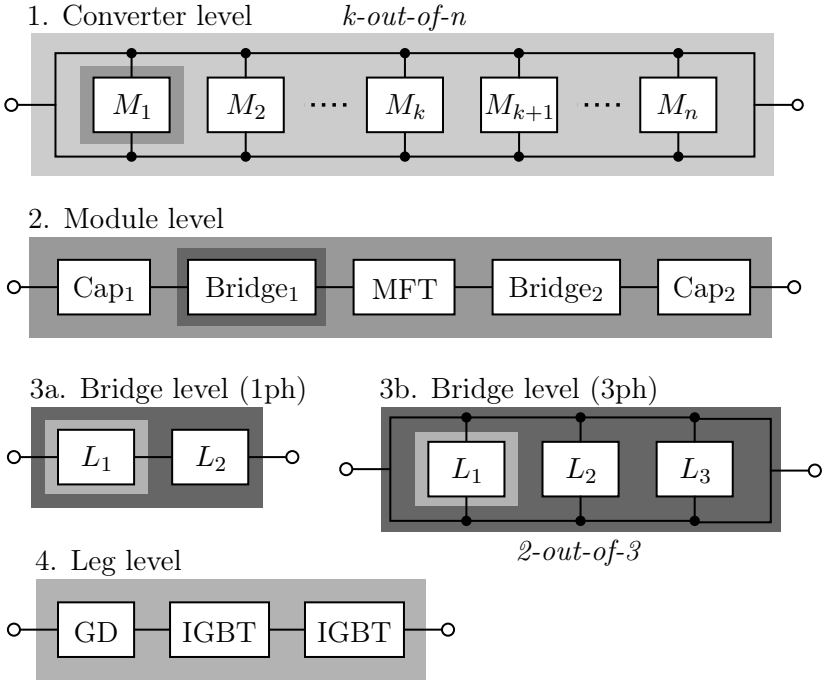

Figure 4.8: Hierarchical reliability block diagram

Parameter	Description	Unit	Value
λ_{IGBT}	IGBT failure rate	occ/year	0.001752
λ_{GD}	IGBT gate drive failure rate	occ/year	0.004380
λ_D	Diode failure rate	occ/year	0.000438
λ_{cap}	Capacitor failure rate	occ/year	0.000876
η_{IGBT}	Voltage stress factor for IGBTs		2.43
η_D	Voltage stress factor for diodes		2.43
η_{cap}	Voltage stress factor for capacitors		7.5

Table 4.1: Component failure rates and voltage stress factors, based on [132, 134]

voltage-adjusted failure rate λ_a. The impact of the voltage stress on the failure rate can be quantified using the equation

$$\lambda_a = \lambda_c \left(\frac{V_{app}}{V_{nom}} \right)^{\eta} \tag{4.11}$$

where λ_c is the nominal failure rate of the component, V_{app}, V_{nom} is the nominal voltage, assumed 60% of V_{max}, and η is the voltage stress factor, given in Table 4.1. The base availability of one module can then be calculated using

$$A_m = e^{-\lambda_m T_M} \tag{4.12}$$

where A_m is the module base availability and T_M is the preventative maintenance interval.

After obtaining the base availability of one module, the failure rate of the overall converter can then be calculated using the k-out-of-n model, which uses the equation

$$A_c = \sum_{i=k}^{k+R} \frac{(k+R)!}{i!(k+R-i)!} A_m^i (1 - A_m)^{(k+R-i)} \tag{4.13}$$

where k is the minimum number of healthy modules required for converter operation, R is the number of redundant modules and A_m is the availability of one module. Note that the reduction in voltage stresses for higher numbers of redundant modules is taken into account in this calculation. The total number of modules, n, is then simply $k + R$.

4.4.4 Results

The system under test considers a 15 MW DC/DC converter with a pole-to-pole output voltage of 80 kV (±40 kV). The input bridge semiconductors were assumed to have a voltage rating of 1.7 kV, which is a typical voltage level used in wind turbine converters [135]. The selected IGBT module for the input bridge of all converter topologies is the Infineon FF1800R171P5 [136]. This was selected as it has the highest current rating for an IGBT module for this application. For the output bridge, the highest voltage rating components were selected instead. For the SAB converters, the selected diode is the Infineon D471N [137]. For the output bridge of the DAB converter, the selected IGBT is the Infineon FD250R65KE3-K [138]. The converter and semiconductor parameters are given in Table 4.2.

Based on the semiconductor voltage and current ratings, the minimum number of modules required for the SAB1 and SAB3 was calculated to be 15. For the DAB1 and DAB3, this was calculated to be 21.

Parameter	Description	Unit	Value
P_1	Converter input power	MW	15
V_1	Converter input voltage	kV	1.2
V_2	Converter output voltage	kV	80
$V_{IGBT,1}$	Input IGBT voltage rating	kV	1.7
$I_{IGBT,1}$	Input IGBT current rating	kA	1.8
$V_{IGBT,2}$	Output IGBT voltage rating	kV	6.5
$I_{IGBT,2}$	Output IGBT current rating	kA	0.25
$V_{D,2}$	Output diode voltage rating	kV	9.0
$I_{D,2}$	Output diode current rating	kA	0.55
γ	Voltage de-rating factor	pu	0.6

Table 4.2: Converter and semiconductor parameters

Selecting the number of redundant modules presents a trade-off between converter reliability and cost. The target availability and maintenance interval heavily affect the calculations. For this research, a target availability of 99% was selected, with a preventative maintenance interval of one year. Offshore wind turbines typically undergo annual maintenance [139] with continuous condition monitoring allowing for early indication of failure.

The results of the reliability calculations are shown in Figure 4.9 and summarised in Table 4.3. To achieve a 99% probability of failure-free operation in each maintenance interval, the SAB1 converter requires two redundant modules, the DAB1 converter requires three redundant modules, whereas the SAB3 and DAB3 converters both require one redundant module.

Converter	Minimum modules	Redundant modules required	Total modules	Availability (%)
SAB1	15	2	17	99.64
SAB3	15	1	16	99.96
DAB1	21	3	24	99.41
DAB3	21	1	22	99.90

Table 4.3: Summary of reliability results for the tested converters

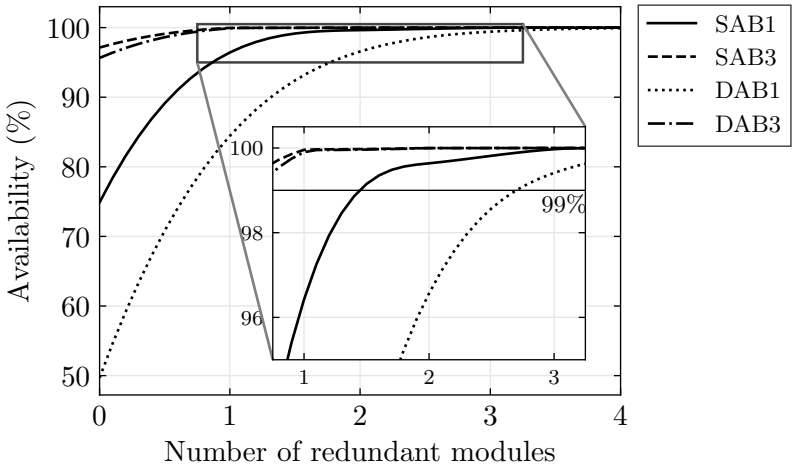

Figure 4.9: Converter availability by number of redundant modules

4.5. Size and Weight

The main components of the DC/DC converters are the MFT, the semiconductors and their associated heat sinks, and the DC link capacitors. Each of these needs to be assessed to determine the overall weight and volume of the converter.

4.5.1 Transformer

The MFT design is highly dependent on the selected frequency, which is a trade off between weight and efficiency. Based on [140], a frequency of 1 kHz is considered. An off-the-shelf transformer cannot be used due to the non-standard frequency, high power and specific leakage inductance requirements. Instead, the MFT must be designed for this application.

The transformer design procedure is based on that set out in [141] and [142]. The single-phase transformers are considered to be shell type with the low and high voltage windings concentrically wound around the central limb. The geometry is illustrated in Figure 4.10. The three-phase transformers are assumed to be core type with the low and high voltage windings wound concentrically around each of the three limbs.

The design procedure starts with the specification of fixed design parameters, such as nominal power, input and output voltages and frequency. In addition, the core and insulation materials are selected, shown in Table 4.4. The transformer windings are assumed to be copper foil in the primary and litz wires in the secondary. In the figure,

the subscripts 1 and 2 denote the primary and secondary windings, respectively.

Symbol	Property	Unit	Value
B_{sat}	Core magnetic saturation	T	1.17
ρ_c	Core density	kg/m^3	7330
k_c	Core fill factor		0.75
k_S	First Steinmetz constant	W/m^3	0.036
α_S	Second Steinmetz constant		1.64
β_S	Third Steinmetz constant		2.10
E_{max}	Max. insulation strength	kV/mm	29

Table 4.4: Material properties for the MFT [131, 141]

Once the fixed parameters are set, there are a series of free parameters which can be varied to obtain an optimal design. These include the number of parallel layers in the primary and secondary windings (m_1 and m_2), the number of turns per layer in the primary (N_{l1}), the number of core stacks (n_c), the ratio of the limb width to thickness (r_{AB}), and the current density of the primary and secondary windings (J_1 and J_2).

Firstly, the required core cross section is calculated using

$$A_{core} = \frac{\lambda_1}{2N_1 B_{max} k_c} \tag{4.14}$$

where N_1 is the number of turns in the primary, B_{max} is the maximum flux density, assumed to be 80% of the core material's saturation flux density, k_c is the core fill factor. The maximum flux linkage, λ_1, is calculated by integrating the positive half cycle of the induced voltage

$$\lambda_1 = \int_0^{T_{pos}} v_p(t)\, dt = \frac{k_\lambda V_1}{f} \tag{4.15}$$

where v_p is the instantaneous voltage in the primary winding, T_{pos} is the positive half cycle time, and k_λ is equal to D_{max} for the SAB1, $\frac{1}{2}$ for the DAB1, and $\frac{2}{9}$ for the SAB3 and DAB3, provided the duty cycle of the SAB3 is more than $\frac{1}{3}$.

The width A of each limb and yoke is calculated using

$$A = \sqrt{\frac{A_{core} r_{AB}}{2n_c}} \tag{4.16}$$

where r_{AB} is the ratio of the limb width to thickness, and n_c is the number of core stacks. Note that the width of the middle limb is $2A$ for the single-phase transformer. For the three-phase transformer, all three limbs are of equal width, which is calculated

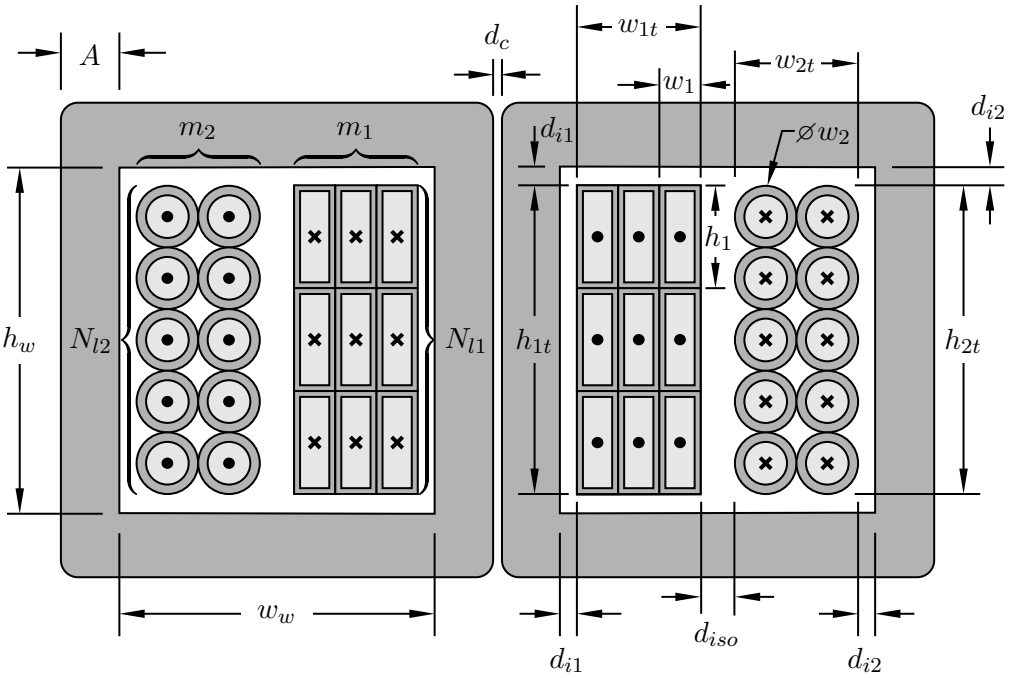

(a) Front view

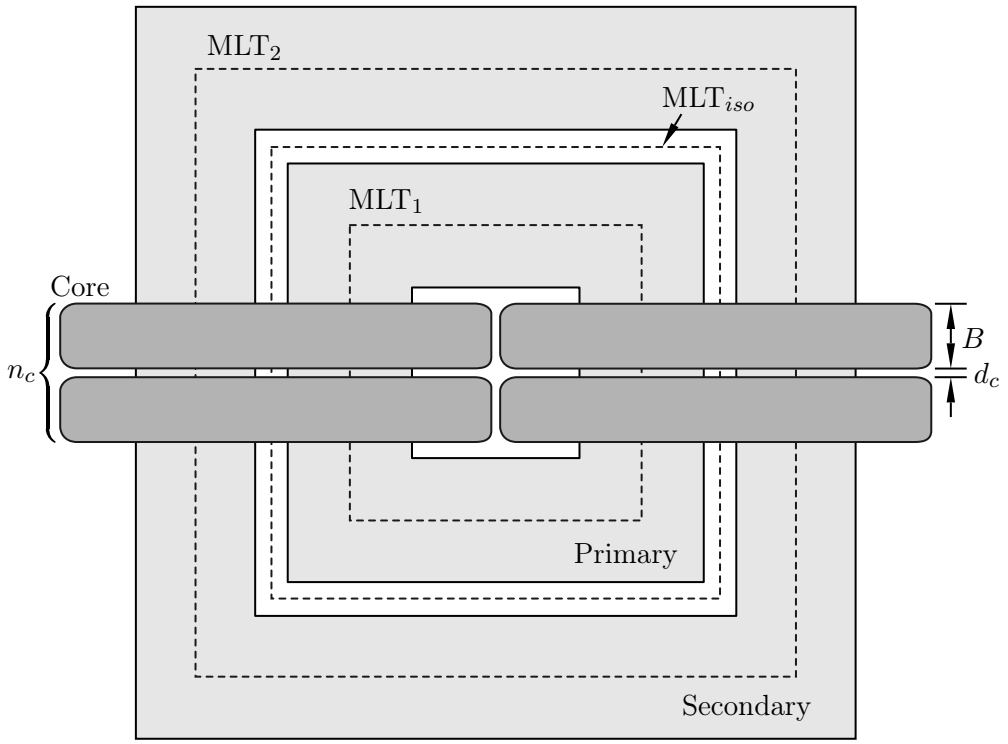

(b) Top view

Figure 4.10: Design parameters for the single-phase MFT

instead using

$$A = \sqrt{\frac{A_{core} r_{AB}}{n_c}} \tag{4.17}$$

The limb thickness is given by

$$B = \frac{A}{r_{AB}} \tag{4.18}$$

The insulation distances between the windings and the core are calculated using

$$d_i = \frac{V_{w,max}}{k_{saf} E_{max}} \tag{4.19}$$

where $V_{w,max}$ is the maximum voltage of the winding, assumed to be 1.05 pu of the nominal value, k_{saf} is the safety factor, assumed to be 0.3 [141], and E_{max} is the maximum electric field strength of the insulation material.

The required area of copper in the primary and secondary winding is based on the selected current density,

$$A_{Cu} = \frac{I_w}{J_w k_f} \tag{4.20}$$

where I_w is the rms current in the winding, J_w is the current density of the winding, and k_f is the copper fill factor, which is assumed to be unity for foil and 0.75 for Litz wire [142].

The dimensions of the turns in each winding are calculated based on the copper area. For the Litz wire in the secondary, this can be readily calculated. For the foil, the width is set to the skin depth at the switching frequency [142], allowing the height to be calculated based on the copper area.

$$w_1 = \sqrt{\frac{2\rho_{Cu}}{2\pi f \mu_{Cu}}} \quad ; \quad h_1 = \frac{A_{Cu1}}{w_1} \quad ; \quad w_2 = 2\sqrt{\frac{A_{Cu2}}{\pi}} \tag{4.21}$$

where ρ_{Cu} is the resistivity of copper, μ_{Cu} is the permeability of copper and f is the switching frequency.

The total height and width of the winding is calculated by multiplying these by the number of layers N_l and number of parallel windings m, respectively.

The required transformer window height is calculated using

$$h_w = \max(h_{1t}, h_{2t}) + 2d_i \tag{4.22}$$

To calculate the transformer window width, the isolation distance d_{iso} between the LV and HV windings must first be calculated. The transformer leakage inductance is used to design the isolation distance. The leakage inductance for a transformer with unequal winding height can be approximated based on an equation from the software ATP Draw [143]

$$L = \mu_0 N_1^2 \left(\frac{MLT_1 w_{1t}}{3h_{1t}} + \frac{MLT_2 w_{2t}}{3h_{2t}} + \frac{2MLT_{iso} d_{iso}}{h_{1t} + h_{2t}} \right) \tag{4.23}$$

where μ_0 is the permeability of free space and MLT is the mean length of a turn. The mean length of the turns are calculated as follows [141]:

$$MLT_1 = 2\big(2A + 4d_{i1} + n_c B + n_c d_c + 2w_{1t}\big) \tag{4.24}$$

$$MLT_{iso} = MLT_1 + 2(4w_{1t} + 2d_{iso}) \tag{4.25}$$

$$MLT_2 = MLT_{iso} + 2\big(2w_{2t} + 2d_{iso}\big) \tag{4.26}$$

where d_c is the distance between the cores, assumed to be 1 mm in both the frontal and lateral directions. Rearranging these equations allows the isolation distance to be calculated.

Finally, the magnetic mean path length for a single transformer core is given as

$$l_m = 2(h_w + A) + 2(w_w + A) \tag{4.27}$$

resulting in a volume of the transformer core of

$$V_{core} = 2n_c l_m AB \tag{4.28}$$

For the three-phase transformer, the total magnetic mean path length per core is instead calculated using

$$l_m = 3(h_w + A) + 2(2w_w + 2A) \tag{4.29}$$

with a transformer core volume of

$$V_{core} = n_c l_m AB \tag{4.30}$$

The transformer core weight can then be calculated using

$$M_{core} = V_{core}\rho_c. \tag{4.31}$$

Similarly, the volume and weight of the insulation and copper windings can be calculated using their dimensions and density.

The transformer design results for each of the converters are shown in Figure 4.11. The variation of free parameters results in a large space of solutions, for which a Pareto front between efficiency and total mass was calculated. The final design selection was performed by minimising the objective function

$$f_{obj} = \left(\frac{P_{tr}}{P_{tr,min}}\right)^2 + \frac{M_{tot}}{M_{tot,min}} + \frac{V_{tot}}{V_{tot,min}} \tag{4.32}$$

where P_{tr} are the nominal transformer losses, described in more detail in Section 4.6, M_{tot} is the total mass of the transformer, and V_{tot} is the total volume of the transformer. The subscript min indicates the designs with the lowest value for each of these parameters. The MFT dimensions and selected design parameters are provided in Appendix B.

4.5.2 Semiconductors and cooling

Most of the volume and weight associated with semiconductors devices are due to the thermal management system. For high-power applications, such as wind turbine converters, the heat generated by semiconductor losses is typically removed by a water-based cooling system.

The design of a water-based cooling system is beyond the scope of this research. However, existing commercially available components can be used to make a high-level volume and weight estimate. For example, Semikron-Danfoss produce a complete water-cooled 3-phase inverter for wind turbine applications. This system has a mass of 106 kg and volume of 0.125 m^3. It uses a glycol-water mixture resulting in a minimum thermal resistance of 0.006 °C/W [144]. For the 1-phase converters, the input and output bridges consist of two legs instead of three. These were therefore assumed to have two thirds the volume and weight of the 3-phase converters.

Simulations were performed in PLECS to determine the required heatsink resistance to limit the semiconductor junction temperature to 150°C. The semiconductor junction temperature was calculated in PLECS by using the semiconductor transient thermal impedance, obtained from datasheets, combined with the simulated switching and con-

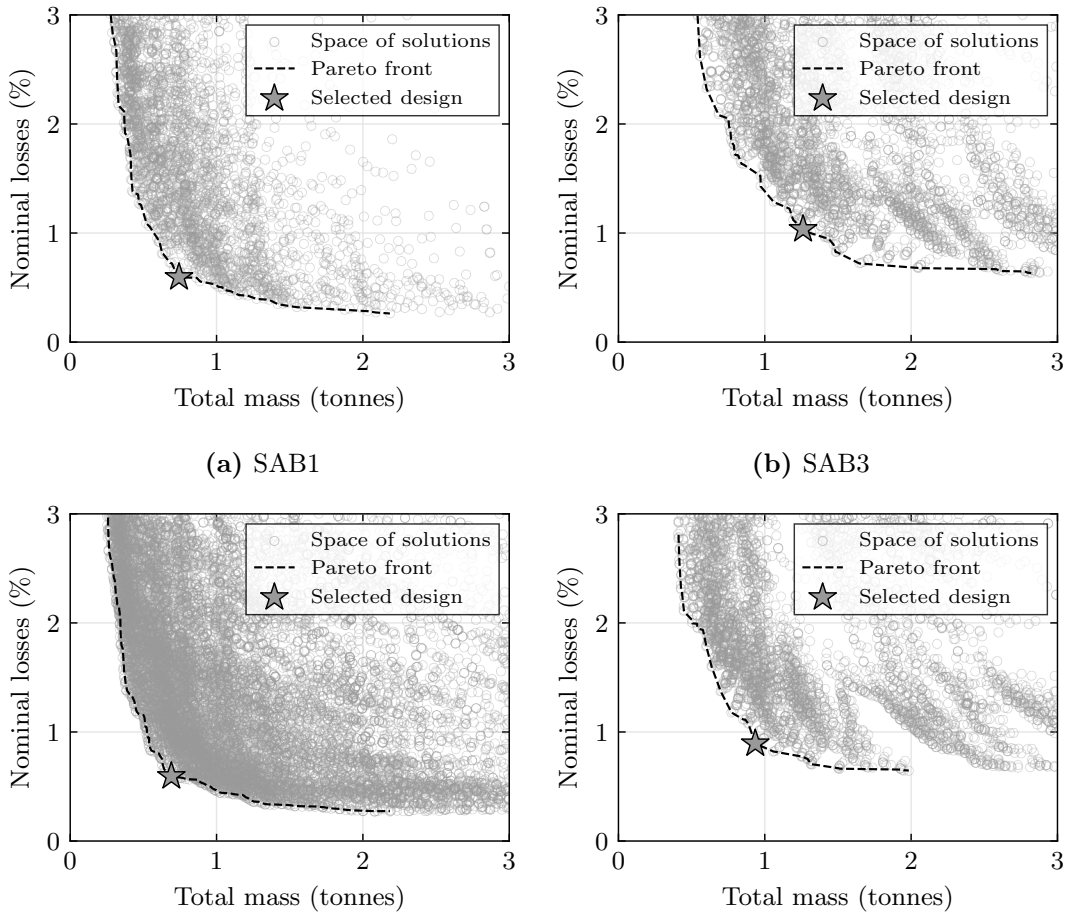

(a) SAB1 **(b)** SAB3

(c) DAB1 **(d)** DAB3

Figure 4.11: Base case pareto-optimal fronts for the transformer designs, showing the trade-off between nominal losses and total mass for each topology at an operating frequency of 1 kHz

duction losses. The losses are discussed in further detail in Section 4.6. The ambient temperature of the converter was assumed to be 50°C. For the 1 kHz base case, the required thermal resistance of the heatsink to the ambient are given in Table 4.5. The results show that these are all within the commercial water-cooling capabilities.

Converter	$R_{\theta hs}$ (K/W)	
	Input	Output
SAB1	0.02	10
SAB3	0.037	10
DAB1	0.056	0.052
DAB3	0.09	0.095

Table 4.5: Heat sink maximum thermal resistance per module for each converter type at the base case frequency of 1 kHz

4.5.3 Capacitors

The DC link capacitors are used to reduce the steady-state input and output voltage ripple, as well as to achieve the desired dynamic response. The capacitance influences the controller dynamics and transient converter response to disturbances [119]. The capacitor size was selected to obtain a maximum steady-state voltage ripple of ±1% on the input and output. This enables safe generator operation and DC/AC conversion at the grid. The capacitance for each converter module was set to the minimum value which could achieve this voltage ripple while maintaining stable converter operation. The resulting values are given in Table 4.6.

Converter	Capacitance (µF)	
	Input	Output
SAB1	7300	310
SAB3	1800	300
DAB1	1300	160
DAB3	340	50

Table 4.6: Converter module minimum input and output capacitance

The volume and weight estimation of the capacitors is based on the approach used in [93]. The capacitor volume is assumed to be proportional to the stored energy and therefore scales linearly with the capacitance, using the equation

$$V_{cap} = k_{c1}C + k_{c0} \tag{4.33}$$

where C is the capacitance in F, and the parameters k_{c1} and k_{c0} are calculated using linear regression of reference capacitor sizes and voltages. The EPCOS MKP 25680 series capacitors were used as a reference [145]. The resulting parameters were found to be

$$k_{c1} = 5.22\,U_{cap} - 4.06 \tag{4.34}$$

$$k_{c0} = 2.181 \times 10^{-4}\,U_{cap} - 6.812 \times 10^{-5} \tag{4.35}$$

where U_{cap} is the capacitor rated voltage in kV. The weight can then be calculated using

$$M_{cap} = \rho_{cap} V_{cap} \tag{4.36}$$

where V_{cap} is the capacitor volume and ρ_{cap} is the average density of the capacitor, calculated to be 1063 kg/m^3 from the reference datasheet.

4.5.4 Insulation coordination

The overall volume of the DC/DC converters will be significantly larger than the sum of the individual components due to insulation coordination requirements. There are currently no standards that specifically address high power medium voltage DC/DC converters. However, studies considering DC/DC converter insulation propose using the IEC 61800-5-1 standard [146, 147].

This standard provides clearance distances for electrical drive systems to be able to withstand impulse voltages, temporary overvoltages and the working voltage of the circuit. Equipment is categorized into one of four overvoltage categories (OVCs), depending on how it is connected to the supply mains. For high power DC/DC converters, previous studies have proposed using the OVCII or OVCIII categories [146, 147]. Since this study considers converters housed inside wind turbines, which are typically equipped with overvoltage protection, the less conservative OVCII category was used here.

The main converter components, including the MFT, semiconductors with cooling, and the capacitors, need to be arranged into a minimal volume taking into account these clearance requirements. This results in a variant of the classical 3D bin packing problem, for which there is no straightforward solution [148].

A stacking algorithm was created to arrange the components of each module into a minimum volume configuration. The algorithm uses a brute-force approach to find the

lowest volume by combining the components in any order, in any combination of the x-, y-, and z-directions, as well as by flipping each component on all three axes. This results in an exponentially increasing computational burden as more components are added together at once. The algorithm therefore combines a maximum of four components, namely the input bridge and cooling, the output bridge and cooling, the MFT, and the output capacitor. This is illustrated in Figure 4.12a. The clearance requirements were determined using the operating voltage and IEC standard. For example, for the SAB1, the output voltage of each module is 4.7 kV, resulting in a module clearance requirement d_{V_m} of 25 mm.

Once the dimensions of an individual module were calculated, a simplified algorithm was used to stack two modules at a time while leaving clearance between each module. Finally, the overall dimensions of the enclosure were calculated by adding a clearance d_{V_2} of 173.3 mm to the complete stack to account for the total stack voltage of ±40 kV. This is illustrated in Figure 4.12b.

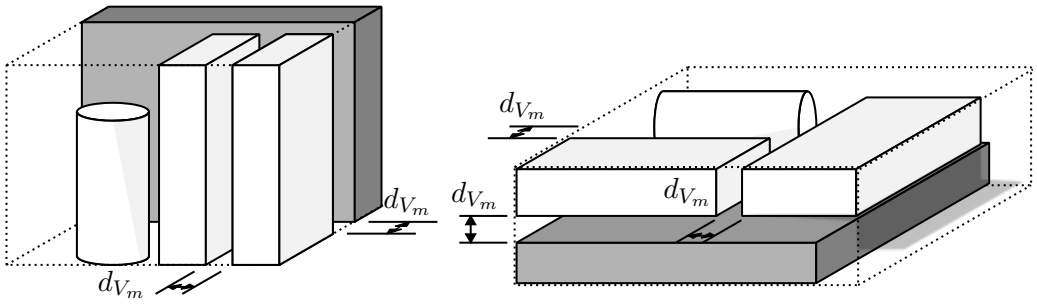

(a) Module-level

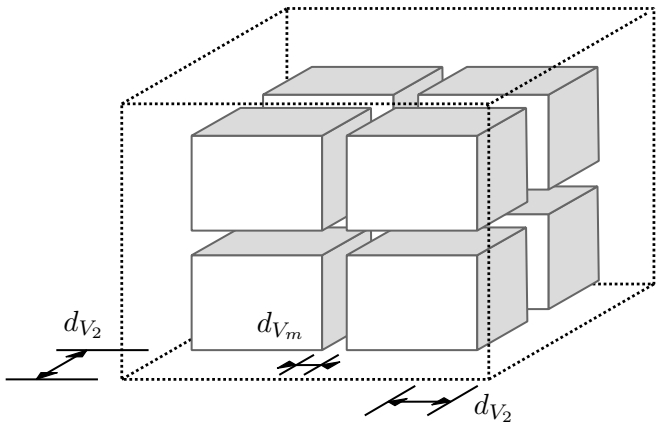

(b) Converter-level

Figure 4.12: Illustration of the stacking algorithm

4.5.5 Base case results

The results of the volume and weight comparison for an operating frequency of 1 kHz are shown in Figure 4.13. The results show that at this frequency, the transformers and IEC 61800-5-1 insulation clearance contributed approximately equally to the total converter volume, and together account for approximately 85% of the total for each converter topology. The bridge components, including the cooling and capacitors, account for the remaining 15%.

In terms of weight, the MFT is the single largest contributor, with both the iron core and the solid epoxy insulation making up most of the overall weight. The IEC 61800-5-1 insulation clearance uses air and therefore does not weigh anything. The bridge components make up between 15% and 24% of the overall weight.

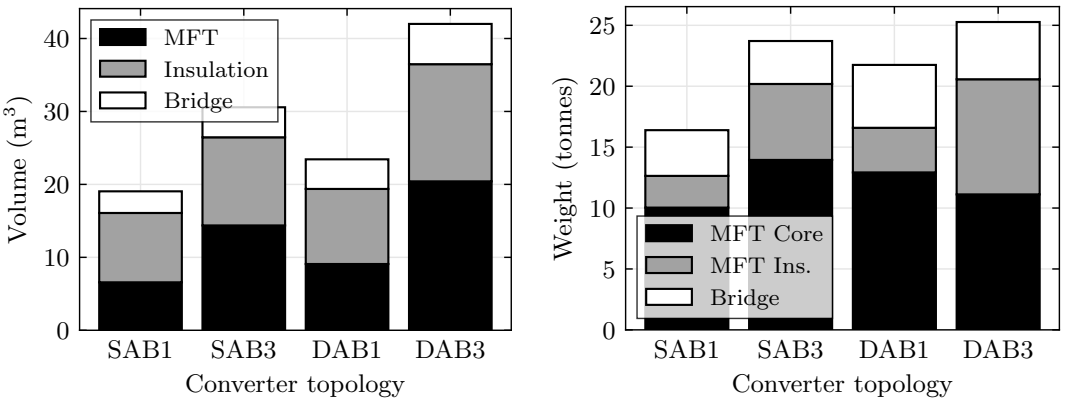

(a) Volume **(b)** Weight

Figure 4.13: Base case converter volume and mass results at an operating frequency of 1 kHz

The SAB1 has the lowest volume and weight of the four tested converters, at 19 m^3 and 16.4 tonnes, respectively. This is mainly due to the relatively low number of converter modules. The SAB3 has a volume approximately 61% higher and a weight 45% higher than its 1-phase counterpart, at 30.6 m^3 and 23.7 tonnes, respectively. This is primarily due to the larger 3-phase transformer used in each module.

The selected transformer for the DAB1 is relatively small and light, but the high number of converter modules results in a total volume and weight of 23.4 m^3 and 21.7 tonnes, respectively, which is larger than the unidirectional SAB1. The DAB3, which has a volume of 42.0 m^3 and a weight of 25.3 tonnes, represents an 80% increase in volume and 16% increase in weight, compared to its 1-phase counterpart.

The typical size and weight of a large offshore wind turbine nacelle, such as that of the GE Haliade-X, is 1700 m^3 and 600 tonnes [149]. This means that all of the tested converters are expected to comfortably fit inside the nacelle.

4.6. Efficiency

The efficiency of each of the four converter topologies was assessed using a combination of simulations and analytical equations. The main loss components considered include the transformer core and winding losses, and the semiconductor switching and conduction losses.

4.6.1 Transformer losses

The transformer copper winding losses are calculated using the methodology based on [150]. The DC winding resistance for each winding is calculated using

$$R_{dc} = \frac{\rho_{Cu} N \mathrm{MLT}}{A_{Cu}} \tag{4.37}$$

where ρ_{Cu} is the resistivity of copper, and A_{Cu} is the cross-sectional area of the copper.

To account for the skin effect, the ratio of AC to DC resistance at a given harmonic frequency f_h is calculated using the equations

$$K_{ac} = \frac{1}{2} y M_y + (2m-1)^2 D_y \tag{4.38}$$

where y is the normalised conductor thickness, given by

$$y = \frac{w_c}{\delta_s} \tag{4.39}$$

where w_c is the conductor width and $delta_s$ is the conductor skin depth, given by

$$\delta_s = \sqrt{\frac{\rho_{Cu}}{\pi \mu_0 \mu_r f_h}} \tag{4.40}$$

where μ_r is the relative permeability of copper.

$$M_y = \frac{\sinh(y) + \sin(y)}{\cosh(y) - \cos(y)} \tag{4.41}$$

$$D_y = \frac{\sinh(y) - \sin(y)}{\cosh(y) + \cos(y)} \tag{4.42}$$

The copper winding losses can then be calculated by summing the losses for each harmonic component

$$P_{Cu} = \sum_h I_h^2 K_{ac,h} R_{dc} \tag{4.43}$$

where I_h is the magnitude of the current with harmonic order h, and $K_{ac,h}$ is the ratio of AC to DC resistance at the frequency of harmonic order h.

To calculate the iron core losses per unit volume, the Improved Generalised Steinmetz Equation (IGSE) is used. This is defined as [151]

$$P_{core} = \frac{1}{T} \int_0^T k_i \left| \frac{dB(t)}{dt} \right|^{\alpha_S} (\Delta B)^{\beta_S - \alpha_S} dt \tag{4.44}$$

where $B(t)$ is the instantaneous magnetic flux density, ΔB is the peak-to-peak magnetic flux density excursion, and k_i is calculated using

$$k_i = \frac{k_S}{(2\pi)^{\alpha_S - 1} \int_0^{2\pi} |\cos\theta|^{\alpha_S} \, 2^{\beta_S - \alpha_S} d\theta} \tag{4.45}$$

where k_S, α_S, and β_S are the Steinmetz parameters of the iron core material.

4.6.2 Semiconductor losses

The semiconductor losses consist of the conduction losses and switching losses and were calculated using PLECS. The conduction losses are calculated using

$$P_{cond} = \frac{1}{T} \int_0^T v_{on} i_{on} dt \tag{4.46}$$

where P_{cond} are the conduction losses, v_{on} is the on-state forward voltage drop of the device, and i_{on} is the current through the device. The on-state voltage drop is determined through linear interpolation of a look-up table, which takes into account the non-linear device resistance and temperature-dependence [152], and is based on the publicly available datasheet [136].

The semiconductor switching losses are calculated using

$$P_{sw} = \frac{1}{T} \sum (E_{on} + E_{off} + E_{rr}) \tag{4.47}$$

where E_{on} are the turn-on losses, E_{off} are the turn-off losses and E_{rr} are the reverse recovery losses, which are calculated in PLECS using a 3D lookup table, given by

$$E = f(v_{block}, i_{on}, T_K) \tag{4.48}$$

where E is the relevant energy loss during switching, V_{block} is the semiconductor blocking voltage, i_{on} is the on-state current and T_K is the temperature in kelvin, all determined either pre- or post-switching [152].

4.6.3 Base case results

The results of the efficiency calculations at a base case operating frequency of 1 kHz are shown in Figure 4.14. The SAB1 has the lowest losses, ranging from around 1.1% at nominal power to 1.3% at 0.1 pu power output. The main source of losses for this topology are the inverter IGBTs, which experience hard turn-off. The rectifier, on the other hand, has very low losses due to the limited diode conduction losses.

The SAB3 has some of the highest losses at low power output, reaching 2.3% at 0.1 pu. At higher operating points, the converter losses are closer to 1.7%. At lower power outputs, the SAB3 operates in discontinuous current mode, resulting in high turn-off losses for all six inverter IGBTs. In addition, the presence of three phases leads to both higher core and winding losses.

The DAB1 has losses ranging from around 1.5% to 1.9%. The increase compared to the SAB1 is mainly due to the rectifier switching losses. The magnetising voltage for the DAB1 MFT does not change with the operating point, resulting in relatively high transformer core losses at low power outputs.

The DAB3 has similar, albeit slightly higher losses compared to its single phase counterpart, ranging from 1.5% to 2.0%. The additional phases result in higher transformer core and winding losses, which are more significant at lower power outputs. The rectifier losses for the DAB3 are lower than those for the DAB1. This is because the rectifier diodes conduct during more of the switching period, leading in lower currents at IGBT turn-off.

Overall, all four converter topologies have acceptable efficiencies for use in offshore wind turbines. Typical fully rated back-to-back converters used in existing AC-based wind turbines have nominal losses of around 2% [153].

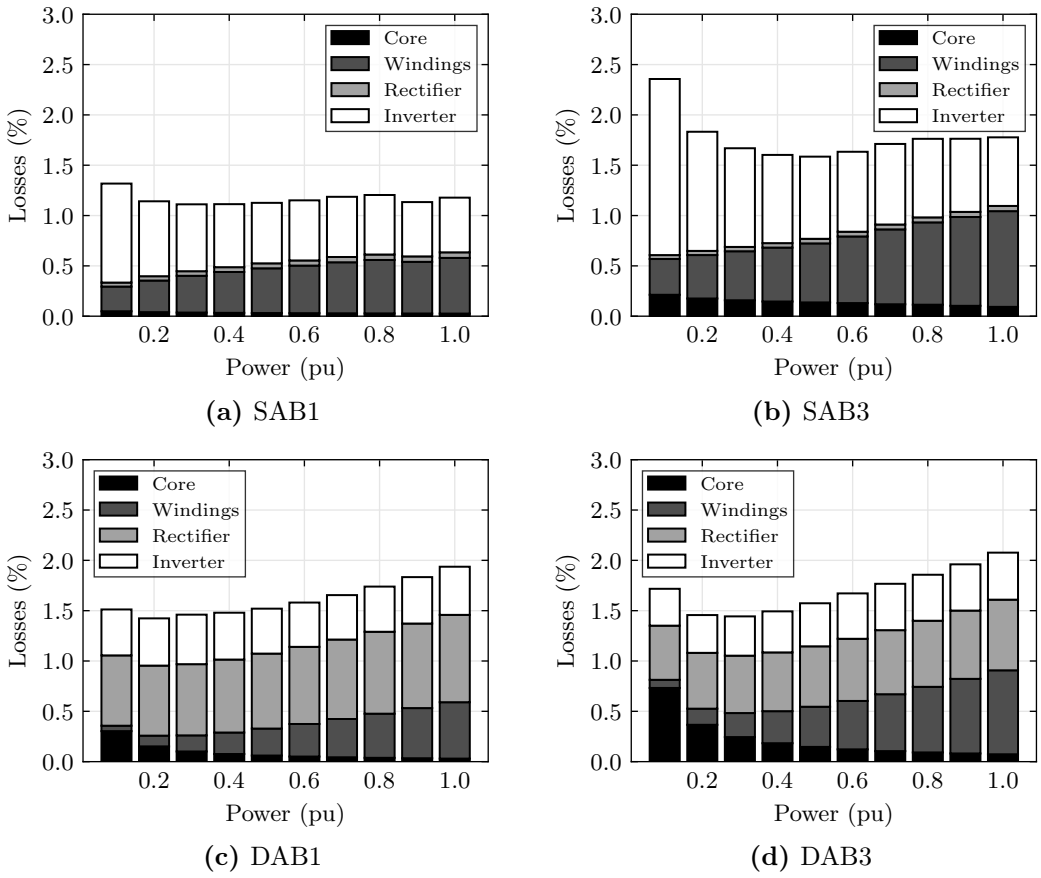

(a) SAB1 **(b)** SAB3

(c) DAB1 **(d)** DAB3

Figure 4.14: Base case converter loss results at an operating frequency of 1 kHz

4.7. Frequency Optimisation

The size and efficiency of the converters will be highly dependent on their operating frequency [154]. Therefore, the volume, weight, and losses analysis was repeated for frequencies ranging from 500 Hz to 5 kHz.

4.7.1 Representative losses

Since the converter does not operate at nominal power continuously, a representative measure of the losses needs to be calculated. To do this, first the converter losses are evaluated for operating points ranging from 0.1 pu to 1.0 pu using the methodology described in the previous subsections. This data can then be transformed into a representative measure based on the total losses the converter is expected to experience under typical wind conditions.

The power output of the wind turbine at each wind speed is calculated using a generic power curve and Weibull wind speed distribution, which were introduced in Chapter 3, and are shown in Figure 3.10a and Figure 3.10b. The power curve allows the required wind speed for each operating point to be extracted, and the Weibull distribution provides the number of annual hours the wind turbine will operate at each operating point.

The total annual losses are derived using the combination of loss data and the annual hours for each operating point. Finally, the representative loss figure is given by the ratio of the annual losses to the annual power production. The relative contribution of each operating point is illustrated in Figure 4.15.

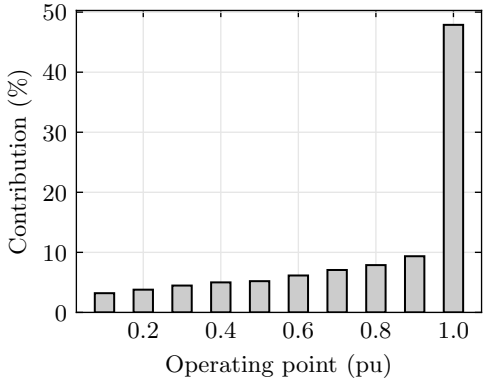

Figure 4.15: Relative contribution of each operating point used to calculate the representative losses

4.7.2 Transformer results

The results of the transformer optimisation are shown in Figure 4.16. The results show that for all topologies, a higher frequency is associated with a reduction in the MFT volume and weight.

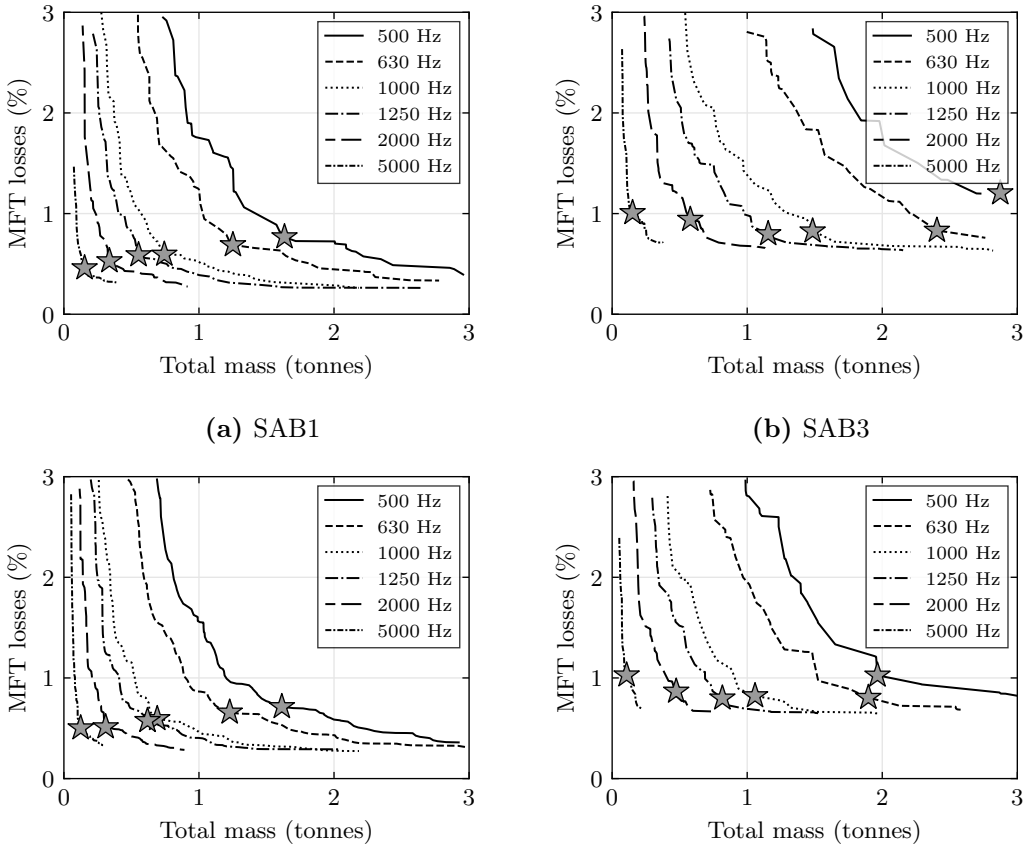

(a) SAB1 **(b)** SAB3

(c) DAB1 **(d)** DAB3

Figure 4.16: Transformer frequency optimisation results, showing the Pareto-optimal front and selected design for various frequencies

The highest frequency of 5 kHz is associated with MFT weights of around 150 kg to 250 kg per module, providing close to a twenty-fold reduction in weight compared to the 500 Hz case. Interestingly, the MFT losses remain relatively constant with frequency and even increase for the lowest tested frequencies. This is due to the reduction in core volume and the mean length of each turn which offset the more frequent core magnetisation and harmonic losses. However, it is important to note that smaller transformer sizes will have more challenges with heat management, which are not taken into

consideration here.

The three-phase MFTs, shown in Figure 4.16b and Figure 4.16d, exhibit both higher losses and mass for the same frequencies compared to their single-phase counterparts, primarily due to the additional core losses and mass from the additional phases. Note that not all the selected designs necessarily fall on the Loss-Mass Pareto-front. This is because the optimisation function also takes into account the transformer volume, which is not shown in the figure.

4.7.3 Converter results

The results of the frequency sensitivity study are shown in Figure 4.17. As expected, an increase in frequency is associated with an increase in losses and a reduction in the volume and weight of the converters. However, the rate of change for each of these factors is different, and they vary by converter topology. In general, the volume reduces more slowly than the mass, especially at higher frequencies. This is due to the insulation coordination requirements staying the same while the transformer becomes smaller. As a result, the clearance space contributes an increasingly large share to the overall volume. It can also be seen that the volume does not reduce perfectly uniformly as the frequency increases. This is because the MFT design procedure does not take into account stacking efficiency, which means that some MFT dimensions can result in higher overall converter volumes than expected.

The selection of the optimal frequency will be application-dependent. For this research, the optimal frequency was selected by taking into account the marginal volumetric and gravimetric power density gains, constrained by the thermal limitations. The volumetric and gravimetric power density gains can be calculated using

$$G_{V_f} = \frac{1 - \frac{V_f}{V_0}}{\frac{P_f}{P_0} - 1} \quad ; \quad G_{M_f} = \frac{1 - \frac{M_f}{M_0}}{\frac{P_f}{P_0} - 1} \tag{4.49}$$

where G_{V_f} and G_{M_f} are the marginal volumetric and gravimetric power density gains at frequency f, V_f, M_f and P_f are the volume, mass and losses at this frequency, and V_0, M_0 and P_0 are the volume, mass and losses of the converter at the lowest frequency. To determine the optimal operating frequency, a minimum value for the marginal power density gains can be selected, depending on the relative importance of each of the factors. For this research, the minimum required power density gains were set to a value of 2.

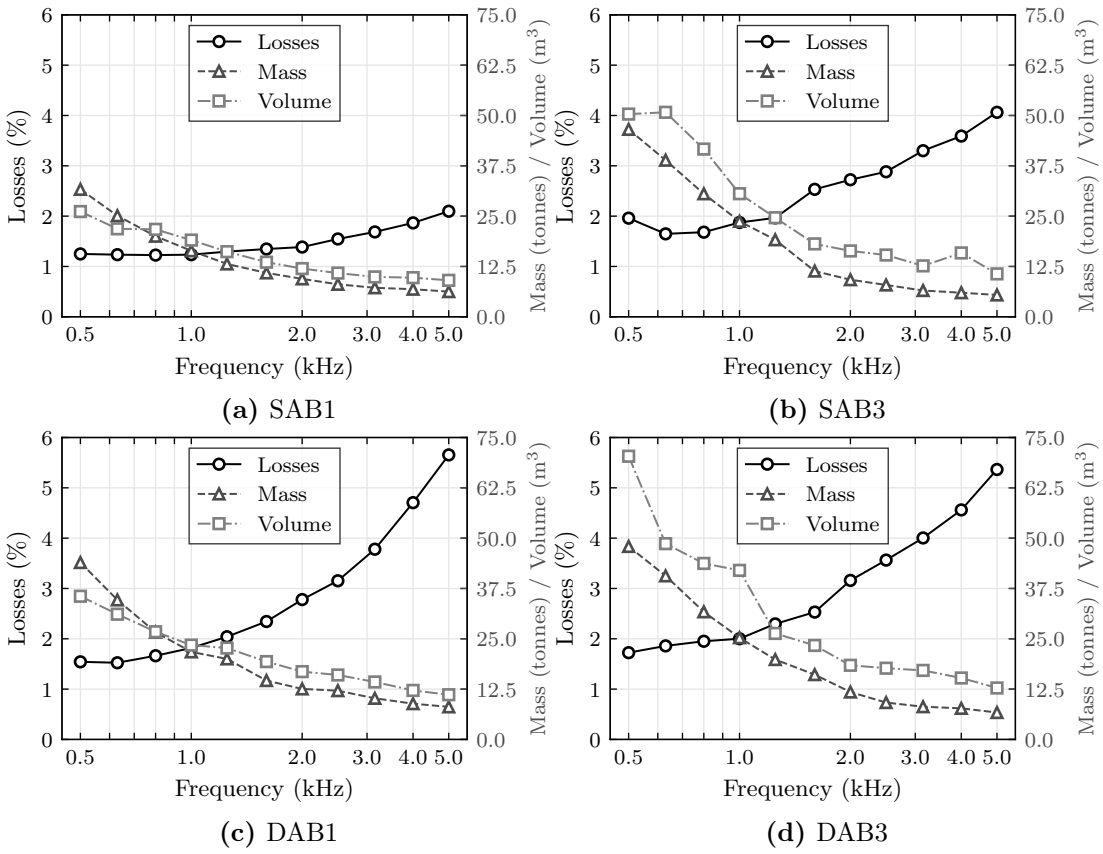

(a) SAB1 **(b)** SAB3

(c) DAB1 **(d)** DAB3

Figure 4.17: Converter frequency optimisation results, showing losses, volume and mass for operating frequencies ranging from 500 Hz to 5 kHz

Figure 4.17a shows that the losses for the SAB1 increase relatively slowly due to the low number of switching devices, from 1.3% at 500 Hz to 2.1% at 5 kHz. Both marginal power density gains are greater than 2 for frequencies up to 2.5 kHz. The high current stress in each device also means that this is the highest switching frequency the commercial water-cooled heatsink can accommodate. For higher frequencies the temperature of the IGBTs would exceed the safe operating range. At a frequency of 2.5 kHz, the losses are still only 1.5%, with a volume and weight reduction of 58% and 75%, respectively, compared to 500 Hz.

It can be seen from Figure 4.17b that the losses for the SAB3 increase more rapidly, from 2% to 4% over the tested operating frequency range. The current stresses for the SAB3 are lower, resulting in the cooling being able to manage switching frequencies up to 5 kHz. However, the marginal power density gains are above 2 only for frequencies up to 1.6 kHz. At this frequency, the losses are 2.5%, and the volume and mass are 64% and 76% lower than at 500 Hz, respectively.

The results for the DAB1 and DAB3 are shown in Figure 4.17c and Figure 4.17d, respectively. The losses for both topologies are similar, and increase much more rapidly with frequency than for the unidirectional converters. This is due to the additional switches in the output bridge. The losses for the DAB1 and DAB3 range from approximately 1.5% at 500 Hz to 5.5% at 5 kHz. The DAB1 reaches its thermal limit at a switching frequency of 2.5 kHz, whereas the lower losses per device for the DAB3 mean the converter can operate at switching frequencies up to 4 kHz. However, the marginal power density gains for both converters drops off very quickly, reaching less than 2 at frequencies above 1 kHz. At this frequency, the DAB1 has losses of 1.8%, with a reduction in the volume and weight of of 34% and 50% compared to 500 Hz, respectively. For the DAB3, the values are 2% losses, 40% volume reduction, and 47% weight reduction.

4.8. Conclusions

This chapter has presented the optimisation and comparison of four cascaded DC/DC converter topologies for a DC-connected offshore wind turbine, including the SAB1, SAB3, DAB1, and DAB3. For each converter, the reliability, size, weight, and losses were calculated at frequencies ranging from 500 Hz to 5 kHz. The MFT was designed by employing a multi-objective optimisation procedure, aimed at minimising the transformer size, weight, and losses. The overall converter volume was calculated using a stacking algorithm to minimise the volume while accounting for the IEC 61800-5-1

clearance requirements. The optimal frequency was selected by calculating the marginal gains in power density.

The SAB1 is a 1-phase unidirectional converter which uses diodes in the rectifier. It requires 17 IPOS connected modules to achieve an availability of 99%. The SAB1 can operate at a relatively high frequency of 2.5 kHz, making it the smallest, lightest, and most efficient of the tested converters. At this frequency, it has a volume of 10.9 m^3, a weight of 8.0 tonnes, and representative losses of 1.5%.

The SAB3 is the 3-phase equivalent of the SAB1. It requires a total of 16 IPOS connected modules to achieve 99% availability, which is the lowest of all tested converters. However, its optimal operating frequency is 1.6 kHz, and it has a higher volume, higher weight and higher losses than its 1-phase counterpart, at 18.1 m^3, 11.4 tonnes, and 2.5%, respectively. If only unidirectional power is needed, the SAB1 is therefore preferred over the SAB3.

The bidirectional DAB1 and DAB3 converters use IGBTs in both the inverter and rectifier. The lower voltage ratings and higher failure rate of these switches compared to diodes results in a larger number of IPOS connected modules required. The DAB1 and DAB3 require a total of 24 and 22 IPOS connected modules, respectively. The DAB1 and DAB3 both have an optimal operating frequency of 1 kHz due to the rapid increase in losses for higher frequencies. At 1 kHz, the DAB1 has losses of 1.8%, a volume of 23.4 m^3, and a weight of 21.7 tonnes. The DAB3 has slightly higher losses of 2%, but is significantly larger at 42.0 m^3 and 25.2 tonnes. If bidirectional power is needed, and there are no space concerns, the DAB3 is the preferred topology due to its higher reliability and lower device stresses.

Part II:

Chemical Energy

Chapter 5

Review of Offshore Wind Electrolysis

5.1. Introduction

Offshore wind energy has the potential to export chemical energy by using water electrolysers to produce hydrogen which can then be transported to shore. This chapter reviews the current commercial electrolyser technologies and their potential to be used in offshore wind energy systems. It investigates the steady-state and dynamic performance of modern electrolysers, reviews proposed modelling methodologies, and discusses the relative merits and current state of development of three offshore wind-electrolyer configurations.

Despite electrical water electrolysis having been used for commercial production more than 100 years [155], the technology continues to advance to this day [156]. A large range of electrolyser technologies are being developed. However, three main types of electrolyser technologies stand out for their potential use in renewable energy systems. These include alkaline, proton-exchange membrane (PEM), and solid oxide electrolysers [157]. These are investigated in the following sections.

5.2. Alkaline electrolysers

Alkaline electrolysers are the most well-established electrolyser technology. They use an aqueous alkaline media, such as potassium hydroxide or sodium hydroxide, as electrolyte [157], and a microporous membrane to separate the anode and cathode side. In alkaline electrolysers, water usually enters on the cathode side where it splits into hydrogen and

hydroxide (OH^-) ions [158], described by the hydrogen evolution equation

$$2H_2O + 2e^- \rightarrow H_2 + 2OH^- \tag{5.1}$$

The hydroxide ions move through the microporous membrane and combine into water and oxygen on the anode side [158], given by the oxygen evolution equation

$$2OH^- \rightarrow H_2O + \frac{1}{2}O_2 + 2e^- \tag{5.2}$$

The hydrogen gas remains at the cathode where it can be separated from the water for further processing. The overall chemical reaction is

$$H_2O \rightarrow H_2 + \frac{1}{2}O_2 \tag{5.3}$$

The alkaline electrolyser cell construction is shown in Figure 5.1. In the traditional design, solid nickel-based electrodes are submerged in the liquid electrolyte at a distance of at least 1 mm from the microporous membrane [159]. The gas bubbles form on both sides of the electrodes, leading to undesirable increases in the cell voltage.

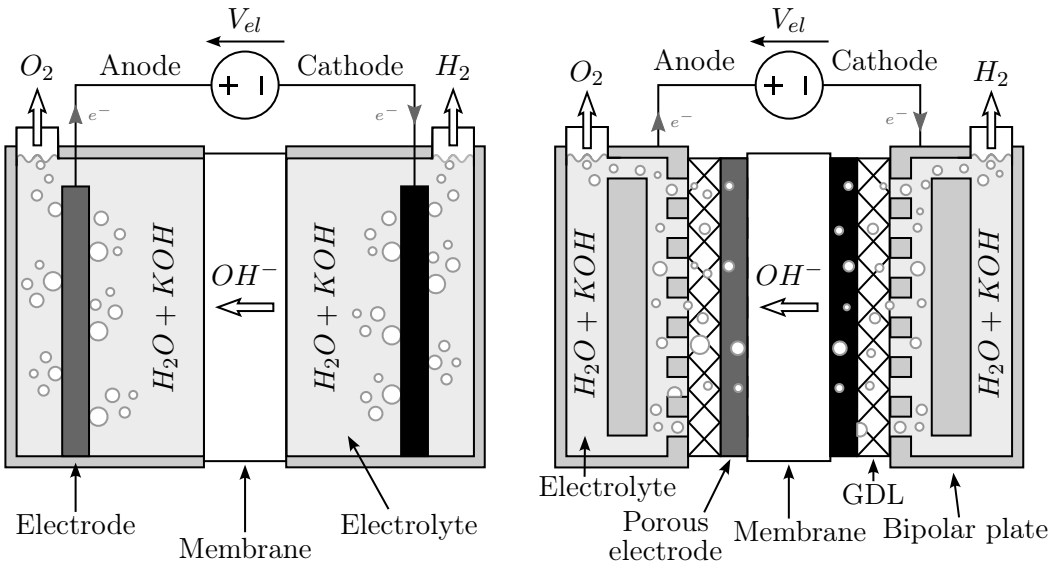

(a) Traditional **(b)** Zero gap

Figure 5.1: Alkaline electrolyser cell construction and operating principle

More modern designs employ a zero gap cell design to address this issue. Here, two porous electrodes are compressed on either side of the membrane, resulting in a smaller gap between the electrodes, thereby significantly reducing the ohmic resistance. It also

results in gas bubbles only being released from one side of the electrodes, reducing their contribution to the cell voltage [159]. A gas diffusion layer (GDL) is added, which provides the electrical connection to the bipolar plates, a path for the liquid electrolyte, and enables the removal of the hydrogen and oxygen gases [159].

The advantages of alkaline electrolysers are their mature technology and relatively low cost, due to the use of inexpensive nickel-based electrodes. By the end of 2022, alkaline electrolysers accounted for 60% of all commercially installed capacity [15]. However, they are predicted to lose market share to PEM electrolysers [15], and their development is hindered by their caustic liquid electrolyte, low operating pressure, and low current density, resulting in a larger footprint [156].

In addition, commercial alkaline electrolysers are characterised by long start-up times and a relatively slow dynamic response to changes in electric power, making them more challenging to integrate with variable renewable energy sources [160].

5.3. Proton-exchange membrane electrolysers

PEM electrolysers use an ultrathin acidic membrane film through which only protons can move to separate the cathode and anode electrodes [160]. The operating principle of the PEM electrolyser cell can be described as follows [161]. Water enters at the anode side and is oxidised into oxygen and protons, releasing electrons in the process. This oxygen evolution reaction is denoted by the equation

$$H_2O \rightarrow 2H^+ + \frac{1}{2}O_2 + 2e^- \tag{5.4}$$

The free electrons move through the electrical circuit, while the protons pass through the membrane to the cathode, where they combine to form hydrogen gas. This hydrogen evolution reaction is given by the equation

$$2H^+ + 2e^- \rightarrow H_2 \tag{5.5}$$

resulting in the same overall reaction as the alkaline electrolyser, given in Equation (5.3).

The standard design of PEM electrolyser cells is shown in Figure 5.2. The membrane electrode assembly (MEA) is located at the centre of the cell. This consists of the proton-conducting membrane, coated with very thin layers of electrocatalysts to accelerate the

chemical reaction. These catalysts are typically made of rare metals, such as iridium on the anode side and platinum on the cathode side [161].

A porous GDL is used to electrically connect the MEA to the bipolar distribution plates and facilitate the exchange of gases from the oxygen and hydrogen evolution reactions. The bipolar distribution plates are used to carry the water to the cell and the gases away from the cell, while also separating the cell from others in the stack [162].

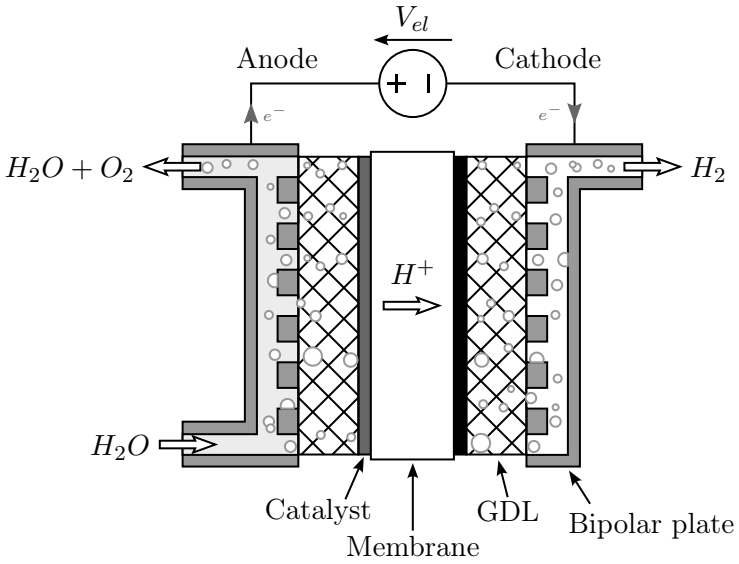

Figure 5.2: PEM electrolyser cell construction and operating principle

PEM electrolysers have a number advantages over other commercial electrolyser technologies. These include its high current density, efficiency, and gas purity, as well as good partial load operation and a rapid dynamic response time [156]. These last two features make it particularly suited to variable renewable energy connection [160]. They accounted for approximately 30% of installed commercial capacity by the end of 2022, and their market share is expected to increase in the coming years [15].

However, PEM electrolysers suffer from a relatively high capital cost, which is primarily due to their material cost. The oxidative and highly corrosive cell conditions limit the available materials that can be used to precious metals as catalysts, titanium-based materials in the bipolar plates, and expensive Nafion as the membrane [160].

5.4. Solid oxide electrolysers

Solid oxide electrolysers operate at high temperatures, typically between 700°C and 900°C, which lowers the energy required for chemical reactions. This allows the use of a solid ionically conducting electrolyte at its centre, which allows the transport of oxide ions from the anode to the cathode [163].

The solid oxide electrolyser operates by injecting water in the form of steam at the cathode, where it reduces to hydrogen and oxygen ions by taking on additional electrons, given by the chemical equation

$$H_2O + 2e^- \rightarrow H_2 + O^{2-} \tag{5.6}$$

The hydrogen gas leaves the cell while the oxygen ions travel through the ionically conducting electrolyte to the anode, where they combine into oxygen gas and release electrons.

$$O^{2-} \rightarrow \frac{1}{2}O_2 + 2e^- \tag{5.7}$$

This results in the identical overall reaction as the other electrolyser technologies, given in Equation (5.3).

The design of the solid oxide electrolyser cell is illustrated in Figure 5.3. The electrolyte forms the central layer of the cell. This must be highly conductive for O^{2-} ions, electrically insulating to avoid conduction between the anode and cathode, and dense enough to prevent gas exchange between the two sides of the cell. The typical material used for this is yttria-stabilized zirconia (YSZ) [164].

The hydrogen electrode is located on the cathode side of the electrolyte. This is where steam is reduced into hydrogen. Since this reaction occurs close to the electrolyte/electrode interface, the electrode must be a porous electronic-ionic conductor, and is typiclly made of a ceramic-metal material composed of YSZ and nickel [164].

The oxygen electrode is located on the anode side of the electrolyte and oxygen oxidises close to the interface with the electrolyte. This too must have good electronic-ionic conductivity, electrocatalytic activity, and be compatible with the electrolyte. The oxygen electrode is typically composed of perovskites [164].

Solid oxide electrolysers have the potential to higher efficiencies and lower capital costs over a wider range of current densities and cell voltages, compared to alkaline and PEM electrolysers [165]. Their high operating temperature lowers the energy requirements

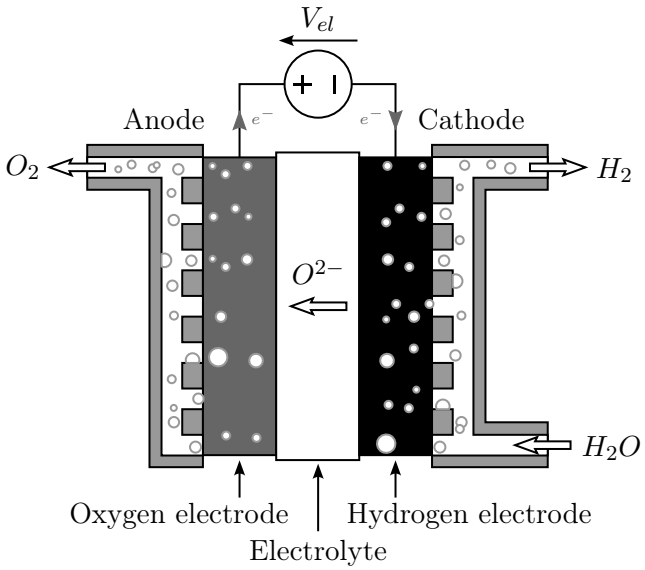

Figure 5.3: Solid oxide electrolyser cell construction and operating principle

and the use of abundant materials, such as yttria, zirconia, and nickel, result in lower costs and fewer scaling limitations [166].

However, historically, solid oxide electrolysers have had challenges with robustness and dynamic operation, such as during thermal cycling, emergency shutdown, and following variable power profiles. Recent research has aimed to address these challenges [166]. Despite these advances, solid oxide electrolysers are not yet at the large scale commercialisation stage, accounting for less than 1% of installed capacity today [15]. Their high temperature requirements also mean they are more suited to onshore connection near waste heat producing installations.

5.5. Electrolyser performance

5.5.1 Steady-state performance

The steady-state electrolyser cell performance is characterised by the J-V curve, which represents the relationship between the current density and the cell voltage. It can be modelled using parametric equations, such as those proposed by [167], given by

$$V_{cell} = V_{oc} + V_{act} + V_{\Omega} + V_{con} \tag{5.8}$$

where V_{oc} is the open circuit voltage, also known as the reversible voltage, which is the minimum voltage required to initiate the electrolysis process. It can be calculated using the Nernst equation, which takes into account the pressure and temperature of the cell [167], given by

$$V_{oc} = \frac{\Delta G}{2F} + \frac{R_g T_{cell}}{2F} \log\left(\frac{p_{H_2}\sqrt{p_{O_2}}}{p_{H_2O}}\right) \tag{5.9}$$

where ΔG is the change in Gibb's free energy, F is the Faraday constant, R_g is the ideal gas constant, T_{cell} is the cell temperature, and p_{H_2}, p_{O_2}, and p_{H_2O} are the partial pressures of hydrogen, oxygen, and water, respectively.

The remaining voltage terms represent process irreversibilities that reduce the cell efficiency [168]. The first of these is the activation overvoltage, V_{act}, which occurs due to the movement of protons and electrons between the cathode and anode [167]. It can be calculated using

$$V_{act} = \frac{R_g T_{cell}}{2F\alpha} \text{arcsinh}\left(\frac{J_{cell}}{2J_0}\right) \tag{5.10}$$

where α is the charge transfer coefficient, which can be considered the fraction electrostatic potential energy limiting the electrokinetic process [167], J_{cell} is the cell current density, and J_0 is the exchange current density, which is the current located at the surface of electrodes [167].

The ohmic overvoltage occurs due to the internal resistance of the cell, such as the resistance of the electrodes, membrane, electrolyte, bipolar plates, as well as contact resistances [167]. It is given by

$$V_\Omega = r J_{cell} \tag{5.11}$$

where r is the total resistance of the electrolyser in $\Omega \cdot \text{cm}^2$.

Finally, the concentration overvoltage, V_{con}, occurs at high current densities when the concentration of hydrogen and oxygen differs between the electrodes. It is given by

$$V_{con} = \frac{R_g T_{cell}}{2F} \ln\left(\frac{J_L}{J_L - J_{cell}}\right) \tag{5.12}$$

where J_L is the limiting current density, which acts as an upper ceiling for the allowable current density in the cell [167]. An example J-V curve with each overvoltage contribution is shown in Figure 5.4.

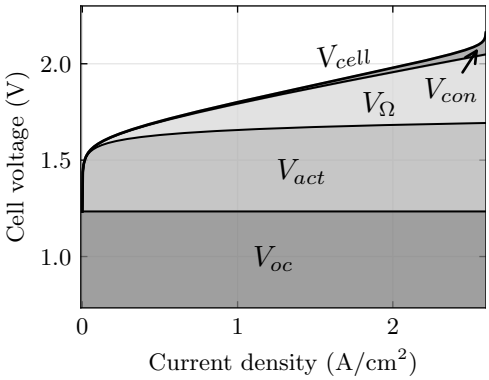

Figure 5.4: Electrolyser cell polarisation curve, showing overvoltage contributions

The hydrogen production of each cell is based on its specific energy consumption and the J-V curve. The specific energy consumption is a measure of the energy requirements to produce 1 kg of hydrogen. It can be calculated using

$$E_{H_2} = \frac{v_{cell} \cdot i_{cell}}{\dot{m}_{H_2}} \tag{5.13}$$

where v_{cell} is the cell voltage and i_{cell} is the cell current, calculated using

$$i_{cell} = J_{cell} \cdot A_{cell} \tag{5.14}$$

where J_{cell} is the current density as determined by the J-V characteristic, and A_{cell} is the cell area.

The hydrogen mass flow rate, $\dot{m}_{H_2}$, is calculated using

$$\dot{m}_{H_2} = \frac{i_{cell}}{2F}(1 - \phi_{H_2}) \tag{5.15}$$

where ϕ_{H_2} is the volume fraction of hydrogen in oxygen, which occurs due to hydrogen permeation through the membrane. To avoid spontaneous combustion, this volume fraction should remain below 2%. The permeation is dependent on the temperature, water content, pressure and current density. In [169], the hydrogen permeation was measured experimentally and linear fits were calculated for varying temperatures and pressures. In this study, the linear fit with the closest matching operating conditions was used. This is given by

$$N_{H_2}^{perm} = 0.223 i_{cell} + 0.414 \tag{5.16}$$

where $N_{H_2}^{perm}$ is the hydrogen permeation rate in mmol/(m^{2}s).The H_2 fraction can then

be calculated using

$$\phi_{H_2} = \frac{N_{H_2}^{perm}}{N_{H_2}^{perm} + N_{O_2}^{evo}} \tag{5.17}$$

where $N_{O_2}^{evo}$ is the flux related to the evolved oxygen, calculated with

$$N_{O_2}^{evo} = \frac{i_{cell}}{4F} \tag{5.18}$$

The specific energy consumption increases as the current density increases, meaning the electrolyser cell is more efficient at lower current densities. This represents a trade-off between efficiency and footprint. Commercial PEM electrolysers typically have a maximum current density of 2 A/mm^2 and operate with an average specific energy consumption of around 50 kWh/kg to 52 kWh/kg, which corresponds to an efficiency of around 75% to 78% [170–172].

5.5.2 Cell dynamic performance

The electrolyser cell reactions do not happen instantaneously due to phenomena such as the double layer effect and diffusion process. The response is highly non-linear, and typically consists of a rapid initial voltage change, followed by a slower drift to the steady-state operating point [173].

The dynamic response can be approximated using an equivalent circuit with one or more capacitors [173]. The simplest dynamic circuit uses a single capacitor, C_{dl}, in parallel with the activation resistance to model the double layer capacitance, such as the one used in [174]. This is illustrated in Figure 5.5a. The concentration overvoltage is typically not included in these equivalent circuits as it mostly plays a role at current densities beyond the nominal operating point.

More sophisticated circuits use multiple capacitors. One example is the Randles equivalent circuit [175], proposed in 1947, which has one capacitor for the double layer effect in parallel with a capacitor and resistor for the speed of the reaction [173]. However, it is not straightforward to match the steady-state cell performance described in Section 5.5.1 using these circuit components.

An alternative is to use a static-dynamic circuit, proposed in [168], which contains two sets of capacitors and controlled current sinks to represent the double layer in the anode and cathode separately. This is shown in Figure 5.5b. This circuit has the benefit of

being able to match the steady state performance more closely by using the current sinks. However, the capacitance value for both electrodes needs to be determined.

A third option is to model the electrolyser cell reaction using a controlled voltage source [173]. In this case, the voltage set point is determined by a look-up table using the J-V characteristic, followed by first order filter to represent the dynamics. This allows for an accurate representation of the cell characteristics and straightforward, albeit simplified, implementation of the electrolyser time constant.

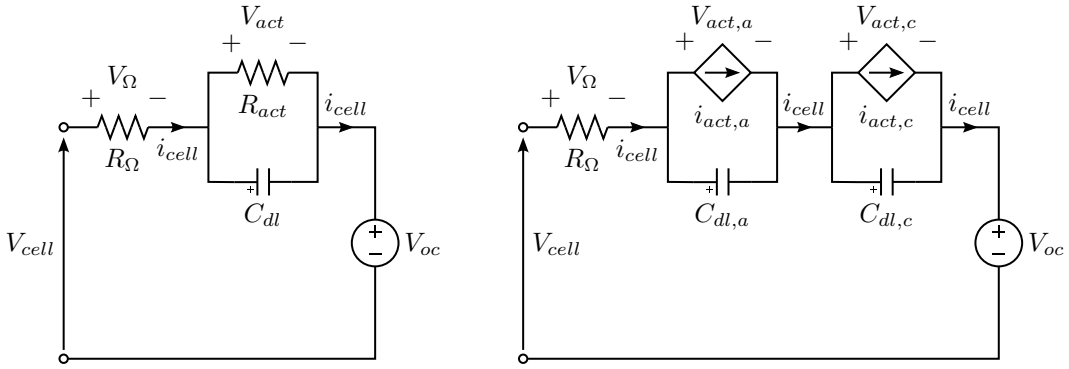

(a) Single capacitor circuit **(b)** Double capacitor circuit

Figure 5.5: Dynamic electrolyser equivalent circuits, adapted from [168, 174]

There are limited studies which use dynamic electrolyser cell models and even fewer which specifically investigate the double layer capacitance or the equivalent circuit time constants. In [176], a 400 W PEM electrolyser stack consisting of three series connected cells was tested by applying a set of current steps. The authors modelled the electrolyser using the double capacitor circuit of Figure 5.5b and found the time constant of the RC networks to be 1.3 s and 11.85 s, with a calculated double layer capacitance of 37.26 F. This was corroborated by the authors of [177], who tested the same electrolyser model and similarly found a capacitance of 37 F.

In [178], the authors use the single capacitor circuit to model an alkaline electrolyser. They use a time constant of 10 ms to 40 ms, based on in-house measurements of a 5.15 kW alkaline electrolyser stack consisting of 22 cells. However, the measurement data was not provided. Similarly, in [179], an alkaline electrolyser was modelled using the single capacitor circuit with a double layer capacitance of 15 mF or time constant of 0.3 ms. The authors claim to have verified this with measurements from an 80 kW electrolyser stack, but did not provide any supporting data.

The authors of [180] provide a much more rigorous assessment of the double layer capacitance of an alkaline electrolyser with 11 cells. They found an equivalent anode

capacitance of 163.8 F and an equivalent cathode capacitance of 9.0 F. They make the observation that comparing absolute capacitance values between electrolysers is meaningless due to differences in stack configuration and operating currents. This highlights the importance of considering the whole electrolyser, rather than just the individual cells.

5.5.3 Overall dynamic performance

The performance of commercial electrolysers is different from that of a single electrolyser cell, as their balance of plant consists of a much larger number of components. This is illustrated in Figure 5.6. At the heart of the electrolyser are the electrolysis stacks, which connect multiple cells in series with a typical voltage of several hundred volts. For the cell equivalent circuits introduced in Figure 5.5, the voltages are multiplied by the number of series-connected cells, whereas the double layer capacitances are divided by this number [173]. As a result, the combined cell dynamics can be very rapid.

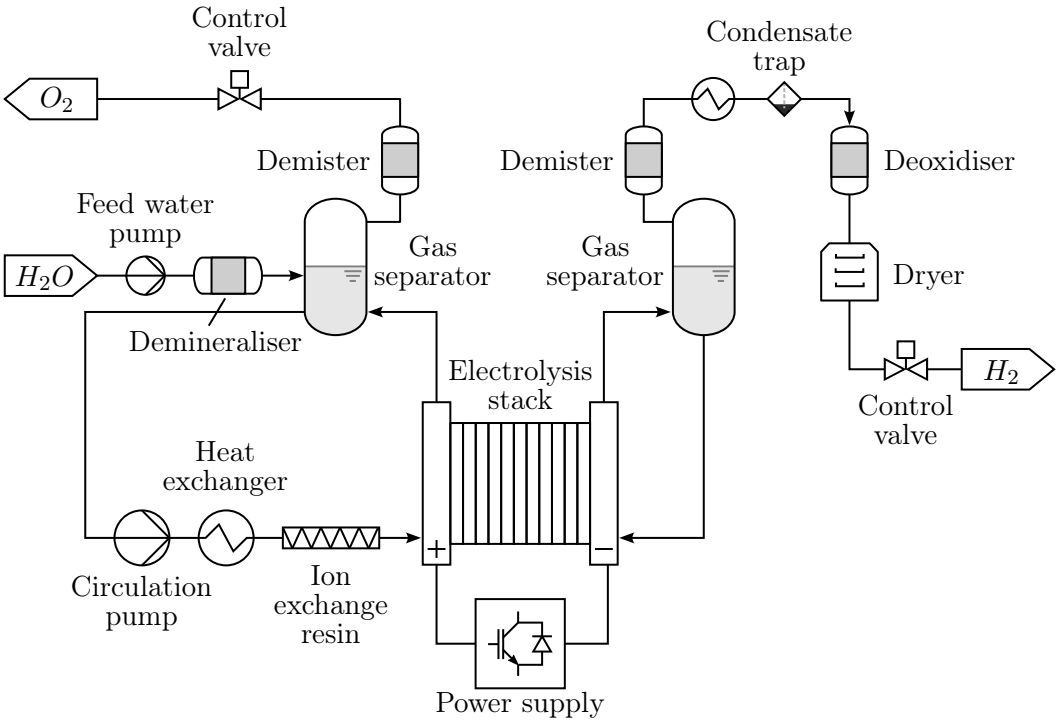

Figure 5.6: Commercial PEM electrolyser balance of plant, based on [181]

Despite this rapid reaction of the electrolyser cells to changes in current [177], the overall balance of plant will have a more limited ramp-up and ramp-down rate to ensure safe operation [182]. The slowest processes, such as controlling the pressure, temperature,

and gas venting, as well as the electrolyser internal control system, therefore determine the ramp rate limitations, rather than the electrical capability of the stack to manage the power changes [173].

In the literature, estimates for allowable power ramp rates vary wildly, with studies suggesting ramp rates ranging from 0.01 pu/s [183] to 2.5 pu/s [174]. The size and design of the electrolyser will have a large impact on this ramp rate. For this thesis, current commercially available PEM electrolysers specifically targeted towards wind turbine applications are used as a basis.

Examples of ramp rates include a 1.67%/s ramp-up and 6.67% ramp-down for the Plug EX-4250 [170], a 9.4%/s ramp rate for the Green Hydrogen Systems HyProvide X-1200 [171], and a 10 %/s ramp rate for the Siemens Silyzer [172]. The Silyzer is used as the base case in this thesis.

5.5.4 Minimum loading

The gases in electrolysers diffuse at a constant rate across the membrane. At high operating levels, this is not an issue since the volume of diffused gases is relatively small compared to the hydrogen production. However, at low operating levels, the gas diffusion start significantly affect the gas purity. Since the product gases form an explosive mixture once the hydrogen in oxygen concentration reaches 4% by volume, commercial electrolysers typically have a 2% gas concentration safety limit [184]. Electrolysers therefore have minimum operating limits, which cannot be violated as they present a safety risk [20].

The level at which the minimum loading is set varies by electrolyser technology and source of information. In general, alkaline electrolysers have relatively high minimum loading levels, with the literature suggesting minimum loading levels of 20% to 40% of its nominal capacity [173, 185]. PEM electrolyser technology is typically described as being more flexible, with the literature suggesting minimum loading levels as low as 5% [173]. However, current commercial electrolysers have stricter operating limits. The PEM-based HyProvide X-1200 has a minimum loading level of 25% [171], and PEM-based Siemens Silyzer has a minimum loading level of 40% [172]. The latter was used as the base case in this thesis.

An additional consideration is the use of multiple parallel connected stacks, which is common in commercial electrolysers that use a modular structure to achieve a high power rating. A higher number of stacks reduces the impact of the minimum loading,

since the individual stacks can be switched off when the generated power falls below the minimum load level. However, a higher number of stacks results in stricter ramp rate limitations, since any stacks not in operation must start up before being able to accept changes in loading.

5.6. Integration with offshore wind

There are three main configurations of offshore wind hydrogen production, including a centralised electrolyser located onshore powered by an offshore wind farm, a centralised electrolyser located offshore, and decentralised electrolysers co-located with individual wind turbines [21]. These are illustrated in Figure 5.7.

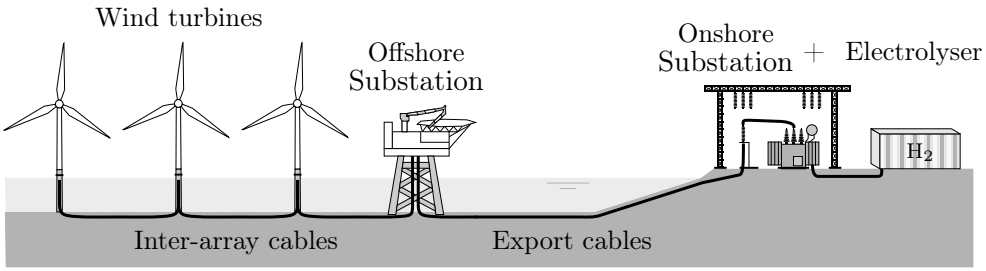

(a) Centralised onshore electrolyser

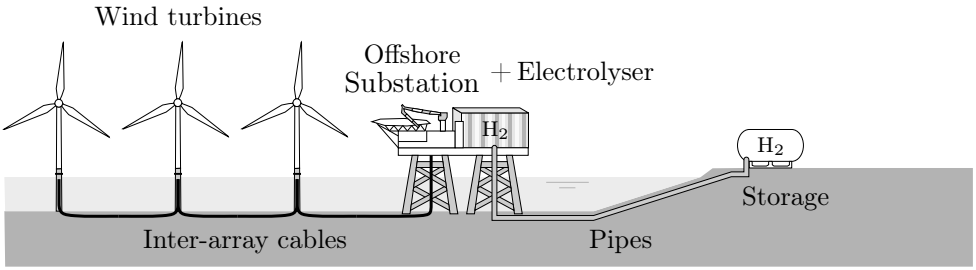

(b) Centralised offshore electrolyser

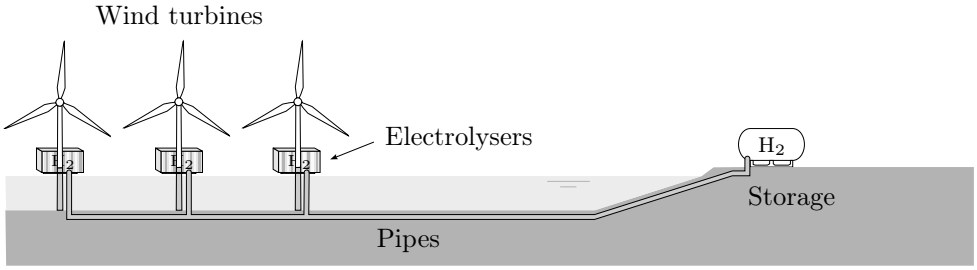

(c) Decentralised, co-located electrolyser

Figure 5.7: Offshore wind-powered electrolysis configurations

The centralised onshore electrolyser configuration is most similar to existing wind farms and therefore represent the lowest technological risk. The electrolyser is grid connected and is not too dissimilar from a regular load. In addition to its ease of integration, the main advantage of this configuration is flexibility in operation: depending on the moment-to-moment prices of electricity and hydrogen, the owner can decide to export electricity or produce hydrogen [186].

The central electrolyser will have power ratings in the hundreds of MW or even GW range. An example pilot project that uses this configuration is the Gigastack project, which proposed to connect a 100 MW PEM electrolyser to the onshore substation of Ørsted's Hornsea 2 wind farm [187], under the UK Low Carbon Hydrogen Supply Competition. This project has since been postponed, however.

The centralised offshore electrolyser configuration places the electrolyser on the offshore platform, where the hydrogen is produced and delivered to shore via a pipeline, which can be 10 to 20 times cheaper to build than transmission cables [13] and have a lifetime of 40 to 80 years [188]. Removing the need for the transmission cables, a high voltage conversion stage, and an onshore substation all result in infrastructure cost savings. The wind turbines can also still be operated as normal. However, the centralised nature of the electrolyser means it may take up significant space on the offshore platform. Also, since there is no redundancy, any failure in the electrolyser results in a complete loss of hydrogen production [21]. An example of an industrial project that incorporates this design is RWE and Neptune's H_2opZee project, which aims to build a centralised 300 MW to 500 MW demonstrator before 2030 [189].

The final configuration, co-locating an electrolyser with each individual wind turbine, uses the least electrical infrastructure, which can result in significantly reduced costs [28]. Without any electrical connection required beyond each wind turbine, they would instead only need pipelines to transport the hydrogen. This direct connection of wind turbine and electrolyser has the benefit of not requiring local grid reinforcements and the associated planning and construction costs [28]. The decentralised nature of the production offers a high degree of redundancy, with outages only affecting individual wind turbines.

There are multiple early-stage industrial projects exploring this option, including Dolphyn Hydrogen's demonstrator [190], Siemens Gamesa's Decentralised Offshore Hydrogen Platform (DOHP) project [191], and RWE's AquaPrimus project [189]. One of the challenges associated with this configuration is the operation and control of the wind turbines, which would need to be altered to accommodate the electrolyser dynamics.

This is explored in Chapter 6.

5.7. Conclusions

This chapter has reviewed the current commercial electrolyser technologies, including the construction and mode of operation of alkaline, PEM, and solid-oxide electrolysers. For variable renewable energy applications, the PEM electrolyser was found to be most suitable, due to its superior dynamic performance.

The review found that the steady-state performance of electrolysers is described by the J-V curve, with the electrolyser cell voltage rising for higher current densities. Commercial PEM electrolysers typically have a maximum current density of 2 A/mm^2 and an average specific energy consumption of around 50 kWh/kg.

In terms of dynamic performance, this chapter found that the electrolyser cell dynamics are generally rapid but difficult to characterise due to the unavailability of double-layer capacitance data. However, more important are the dynamics of the balance of plant, which are the limiting factor for the overall electrolyser response rate. A typical ramp rate limitation for commercial electrolysers was found to be 10%/s.

Industrial research into the integration of electrolysers with offshore wind is still in the early stages. Co-locating electrolysers with individual wind turbines has the potential to provide the largest cost savings, but requires more investigation to determine how the electrolyser and wind turbine can be controlled without a grid connection.

Chapter 6

Off-grid Wind Turbine & Electrolyser Control

6.1. Introduction

The electrolyser review in Chapter 5 showed that there are three main configurations of offshore wind hydrogen production, including a centralised electrolyser located onshore powered by an offshore wind farm, a centralised electrolyser located offshore, and decentralised electrolysers co-located with individual wind turbines [21]. This chapter investigates this third configuration. First, a complete control system for the wind turbine-electrolyser is designed. Then, three strategies to manage the dynamic power balance between the wind turbine and electrolyser are presented and assessed.

6.1.1 Previous research

Despite a significant increase over the last decade in the number of publications concerning hydrogen electrolysers [192], much of the work on wind-hydrogen systems has focused on the economic aspects [193–195]. Very little research considers off-grid wind turbines directly connected to electrolysers, and there are currently no studies on how such a system could be operated and controlled.

Standalone wind-powered electrolysis is not a new idea [196], but the wind industry has only recently started commercial research and development. Commercial wind power hydrogen production projects are still in the early development stages, and either consist of small-scale onshore test facilities, such as the Brande Hydrogen project [191], or larger scale grid-connected projects, such as the Holland Hydrogen I project [197]. There has been no research yet on the operation and control of an off-grid, commercial-scale offshore wind turbine with co-located electrolyser.

Academic research into the concept is also limited to small-scale systems that focus on hydrogen output over long time-scales without significant consideration of the system dynamics. In [198], a 10 kW vertical axis wind turbine directly connected to a PEM electrolyser was simulated. The electrolyser performance characteristics were determined based on a set of experiments on a 56 W electrolyser cell. The electrolyser was connected to the wind turbine through a full bridge diode rectifier followed by a buck converter. The hydrogen production was then calculated based on measured wind speed data from an observation facility. Despite using realistic wind speed and electrolyser data, this study did not use commercial-scale wind turbines or electrolysers. It also only included steady-state operation and did not investigate or account for the wind turbine or electrolyser dynamics.

Research by [199] investigated the integration of an alkaline electrolyser with a 6.8 kWp photovoltaic solar array and a 6 kW wind turbine in a stand-alone system. The study assessed the system efficiency and energy balance over the course of one year. One of the main findings is that the limitations of commercial electrolysers, such as the lower operating limit and the number of stops permitted by manufacturers, is a main challenge in this type of systems. The authors proposed running the electrolyser below the minimum operating limit for short durations or using battery storage to minimise the number of stops and increase the system efficiency. However, this study did not investigate the power conversion process in detail, instead simply taking into account conversion losses. The energy balancing performed in this study only included the minimum operating limit and did not account for electrolyser ramp rates.

A study by [200] looked into maximum power point tracking (MPPT) control strategies for a micro wind turbine rated at 250 W connected to an electrolyser stack. The authors considered how to increase the system efficiency by employing more complex MPPT strategies than the conventional hill climb and verified this experimentally. However, the study was limited to the MPPT algorithm for a DC/DC converter and did not include the control of any other wind turbine elements. It also did not consider commercial-scale power ratings or any of the commercial electrolyser limitations.

6.1.2 Contributions

This study is the first to investigate the operation and control of a commercial-scale standalone wind turbine with an integrated electrolyser, including the dynamic balancing of power between the wind turbine and electrolyser in such an off-grid system.

Currently, no research exists on how a standalone wind turbine can be controlled to

successfully integrate the electrolyser without any grid connection. This study develops a comprehensive control strategy, which includes grid-forming control of the line-side converter, as well as grid-following control of the generator converter and electrolyser converter.

In addition, this is the first research to demonstrate that off-grid wind turbines electrolyser systems cannot operate by simply using their existing control structures, due to the different dynamic responses of the wind turbine and electrolyser. Existing studies only consider steady-state operation of electrolysers, whereas this research takes into account the electrolyser ramp-rate limitations.

This study is the first to quantify the potential power and energy mismatch between the wind turbine and electrolyser due to their differing dynamic response, based on realistic wind speed variation.

In addition, this study proposes and assesses the viability of three novel mechanisms to balance the power between the input wind and the electrolyser, including energy storage, rotor inertia, and enhanced pitch control. This study also demonstrates how the wind turbine control can be enhanced to incorporate these balancing strategies.

Finally, this study is the first to quantify the trade-offs of each of the balancing mechanisms, including financial costs of the energy storage system, and the efficiency costs of the rotor inertia and enhanced pitch control strategies.

This chapter is organised as follows: in Section 6.2, the challenges of operating a ramp-rate limited electrolyser without grid connection are discussed, in Section 6.3 the modelling methodology and converter control structures are introduced. In Section 6.4, Section 6.5, and Section 6.6 the implementation of three power balancing strategies are described, including energy storage, rotor inertia and pitch control. Section 6.7 sets out the conclusions.

6.2. Challenges of Off-grid Operation

Practically all commercial electrolysers are connected to the grid, where they can operate continuously at rated power or adjust their loading to provide grid support services [201, 202]. However, when electrolysers are supplied by a single wind turbine without a grid connection, their loading will vary continuously depending on the available power in the wind. As a result, the electrolyser limitations such as its minimum loading and maximum power ramp rate become much more significant.

6.2.1 Electrolyser limitations

The electrolyser review in Chapter 5 has shown that commercial electrolysers have limited ramp-up and ramp-down rates to ensure safe operation [182]. For the base case, this research uses the limitations of the Siemens Silyzer, a commercially available PEM electrolyser specifically targeted towards wind turbine applications. These have a ramp rate limitation of 0.1 pu/s [172].

In addition, many commercial electrolysers use a modular structure where multiple stacks are connected in parallel to achieve high power ratings. A higher number of stacks reduces the impact of the minimum loading, since the individual stacks can be switched off when the generated power falls below the minimum load level. However, a higher number of stacks results in stricter ramp rate limitations, since any stacks not in operation must start up before being able to accept changes in loading.

For this study, a 15 MW PEM electrolyser was considered, consisting of three independent stacks of 5 MW each. Since the stacks are more efficient at lower operating points, they are set to equally share the power from the wind turbine. New stacks are added as soon as the power increases to allow all to operate at the minimum load [203]. This is illustrated in Figure 6.1.

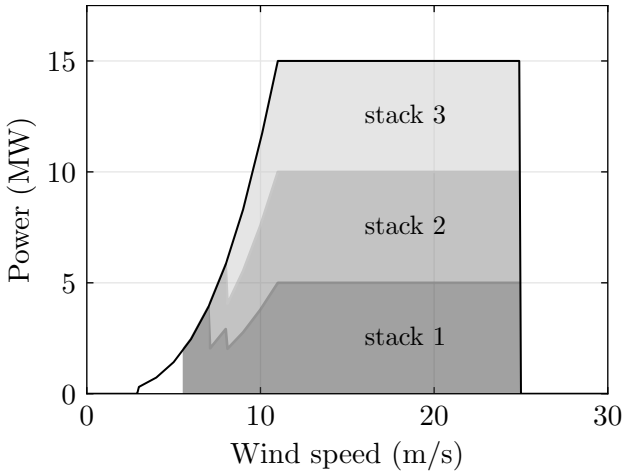

Figure 6.1: Power consumption per electrolyser stack for varying wind speeds

6.2.2 Power mismatch

When the wind speed changes rapidly, the power output from the wind turbine may exceed the ramp rate limitation of the electrolyser, resulting in a power mismatch. An

example of the impact of a rapid decrease in wind speed illustrated in Figure 6.2a. The electrolyser ramp-down limitation will cause the power demanded to be higher than the power available in the wind. The mismatch between power results in a slow down of the wind turbine. From the wind turbine aerodynamic curve, it can be seen that a decrease in rotational speed results in a further decrease in power, as shown in Figure 6.3a. The result is an unstable feedback loop where the slow down of the wind turbine causes the mismatch between electrolyser and wind turbine to increase, further slowing the turbine down until it completely stops and the electrolyser has to be disconnected.

Depending on the electrolyser specifications, frequent shutdown may result in significant hydrogen production losses due to the long restart time, and frequent shutdown may also affect the degradation and lifetime of the system [182]. To prevent this from happening, a mechanism must be introduced to balance the wind turbine and electrolyser power. This allows the wind turbine to maintain its speed long enough for the electrolyser demand to catch up. Once it does, the wind turbine can recover and continue operating at the new wind speed. This is shown in Figure 6.2b and Figure 6.3b.

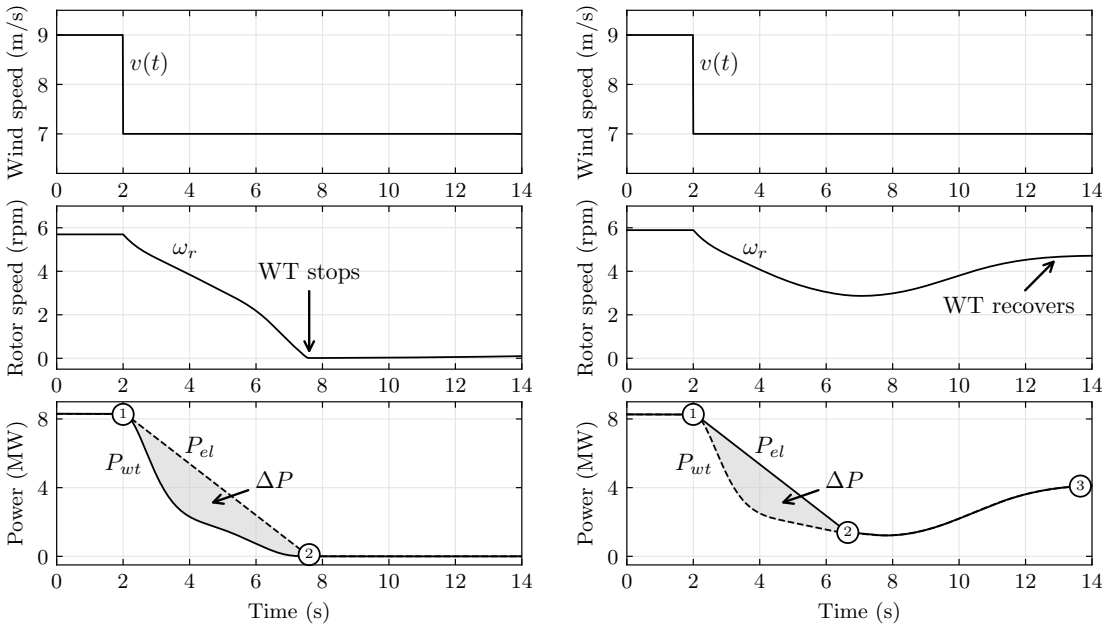

(a) Without power balancing **(b)** With power balancing

Figure 6.2: Example power mismatch between wind turbine and electrolyser following a rapid reduction in wind speed

If the wind speed increases, the wind power will be higher than the electrolyser demand, resulting in a potentially dangerous speed-up of the turbine or an unacceptable rise in the system voltage. Traditional wind turbines regularly experience a similar scenario at

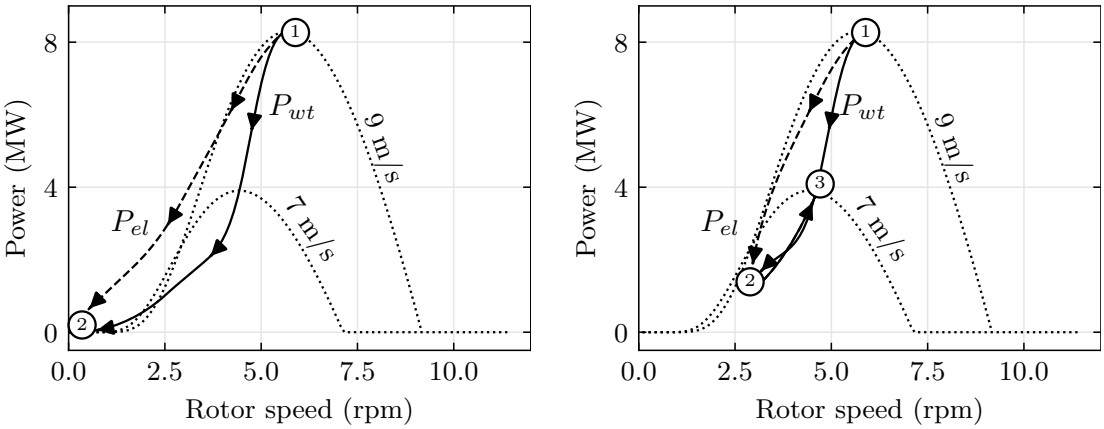

(a) Without power balancing **(b)** With power balancing

Figure 6.3: Wind turbine operating point following a wind speed reduction, showing the change in available aerodynamic power

high wind speeds where the wind power exceeds the rated power of the wind turbine. For this, pitch control can be used to feather the blades to reduce the power captured by the wind turbine. The same pitching mechanism can in theory be used to reduce the wind turbine power output when it exceeds the electrolyser ramp-up limitation.

However, the electrolyser ramp rate can interfere with the stable operation of this pitch control. Since the electrolyser ramp rate limits how fast the wind turbine power can change, this can cause the pitch controller to overcompensate. Any overshoot of the pitch can decrease the available power in the wind faster than the electrolyser ramp rate, which has the potential to result in the same unstable feedback loop encountered for a rapid wind speed decrease.

It is therefore necessary to design a wind control system that allows for off-grid operation, including the incorporation of mechanisms that can temporarily provide additional power to balance the wind turbine output and electrolyser demand.

6.3. Modelling and Control

The system under study is an off-grid commercial wind turbine directly connected to an electrolyser. The model was built using MATLAB/Simulink. The wind turbine is a generic type 4 configuration, with a nominal power rating of 15 MW. The wind turbine uses a low voltage PMSG and fully-rated back-to-back power converter. The power converters use a two-level VSC topology. A transformer is used to step up the converter

output to 66 kV before the power is transmitted by three-phase cables down the tower. At the base of the tower, a second transformer reduces the voltage and a VSC rectifies the voltage before delivering the power to the electrolyser.

An overview of the complete model with the high level control structures is shown in Figure 6.4. The following sections describe each of the components and their control in detail. The values for all components and controllers in the model can be found in Appendix C.

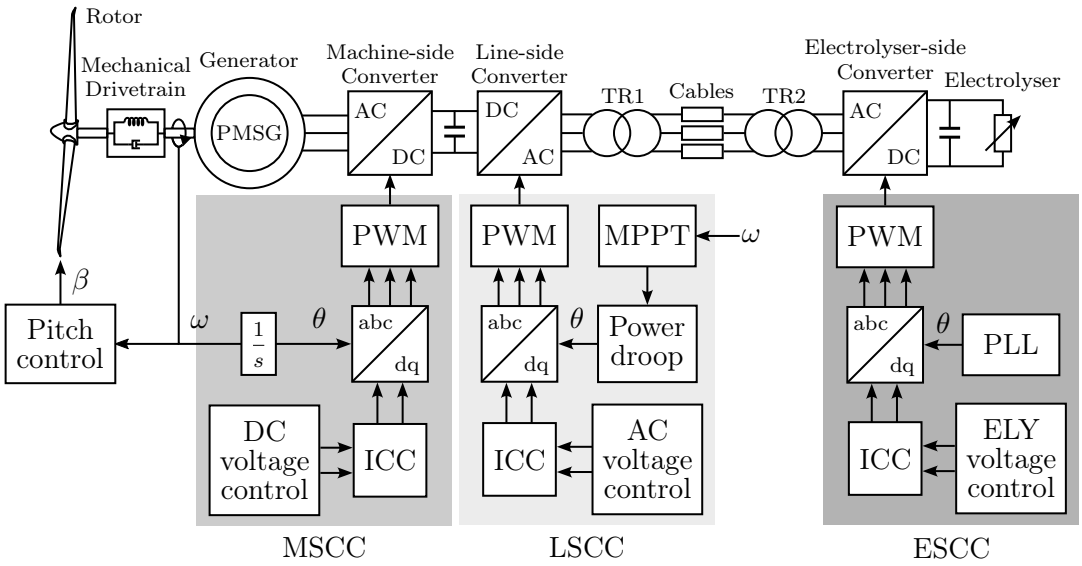

Figure 6.4: Overview of the complete model with high level control structure for the machine-side converter control (MSCC), line-side converter control (LSCC) and electrolyser-side converter control (ESCC)

6.3.1 Rotor

The wind turbine rotor model takes the wind speed, pitch angle and rotational speed as inputs, calculates the tip speed, power coefficient C_p, power extracted from the wind and outputs the resulting torque. The modelling approach taken is based on [204, 205]. The aerodynamic power input of the wind turbine can be calculated using the equation

$$P_{wt} = \frac{1}{2} C_p(\lambda, \beta) \rho A_r v^3 \tag{6.1}$$

where ρ is the air density, A_r is the swept area, v is the wind speed, and $C_p(\lambda, \beta)$ is the nonlinear power coefficient, which is dependent on the tip speed ratio, λ, and the blade

pitch angle, β. It can be calculated using a lookup table or parametric equations [205].

$$C_p(\lambda, \beta) = c_1\Big(c_2\frac{1}{\beta} - c_3\beta - c_4\beta^{c_5} - c_6\Big)e^{-c7\frac{1}{\Lambda}} \tag{6.2}$$

where c_1 to c_9 are characteristic constants of the wind turbine. The $\frac{1}{\Lambda}$ term is calculated as follows

$$\frac{1}{\Lambda} = \frac{1}{\lambda + c_8\beta} - \frac{c_9}{1+\beta^3} \tag{6.3}$$

The tip speed ratio is defined by

$$\lambda = \frac{\omega_r R_r}{v} \tag{6.4}$$

where ω_r is the rotational speed of the wind turbine rotor in rad/s, R_r is the rotor radius in m, and v is the wind speed in m/s.

The resulting aerodynamic torque on the rotor can then be calculated using

$$\tau_r = \frac{P_{wt}}{\omega_r} \tag{6.5}$$

where τ_r is the input rotor torque in Nm. The wind turbine rotor parameters are given in Table 6.1.

Parameter	Symbol	Value	Units
Rated power	P_{WT}	15	MW
Rotor radius	R_r	120	m
Rated speed	ω_{nom}	6.935	rpm
Air density	ρ	1.225	kg/m^3

Table 6.1: Wind turbine model parameters

6.3.2 Standard pitch control

The standard pitch control system aims to keep the wind turbine rotational speed at or below the nominal speed. The wind turbine pitch controller and actuator were modelled using the approach taken in [206, 207]. The control block diagram is shown in Figure 6.5. The standard pitch control system uses a proportional-integral (PI) controller to generate a pitch angle set point based on the difference of the nominal and

the measured rotor speed. The PI controller has the following transfer function

$$G_\beta(s) = K_{p_\beta} + \frac{K_{i_\beta}}{s} \tag{6.6}$$

where K_{p_β} and K_{i_β} are the proportional and integral gains of the pitch controller, respectively. Due to the highly nonlinear aerodynamic torque characteristic as a function of the pitch angle, the PI controller gains are adjusted using gain scheduling based on a look-up table (LUT) [206]. The pitch actuator system itself is represented by a low pass filter with a time constant of 0.3 seconds, a rate of change limiter with a 10°/s limit, and a saturation block with limits between 0° and 90°.

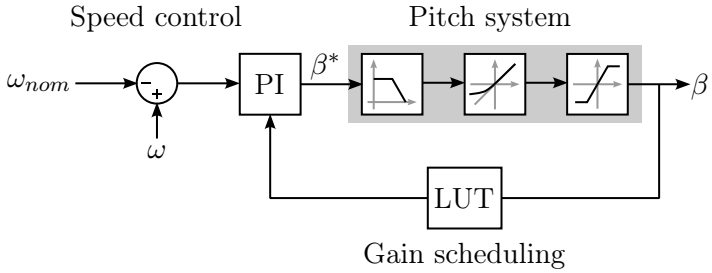

Figure 6.5: Control block diagram for the standard pitch controller and actuator

6.3.3 Mechanical drive-train

For geared wind turbines, the mechanical drive-train consists of the high- and low speed shafts and the gearbox. For direct-drive wind turbines, the system is simplified and consists of a single shaft.

The wind turbine rotor is connected to the generator via the mechanical drive-train. The conventional method of representing the response of this system is using a multiple mass model. A two-mass model was used as it can capture the dynamics that affect stability, whereas higher-order models are typically used to study mechanical details such as fatigue of the drive-train [208]. The two-mass model was implemented in the form of a state-space model following the procedure set out in [209], and is shown in Figure 6.6.

The equations for the two-mass model are derived from the free body diagram and can be written in state-space form as follows:

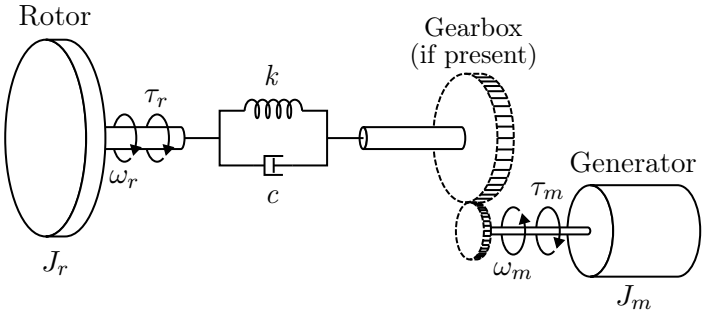

Figure 6.6: Illustration of two-mass mechanical drive-train model

$$\begin{bmatrix} \dot{\omega_r} \\ \dot{\omega_m} \\ \dot{\theta_t} \\ \dot{\theta_m} \end{bmatrix} = \begin{bmatrix} \frac{-c}{J_r} & \frac{c}{J_r} & \frac{-K}{J_r} & \frac{K}{J_r} \\ \frac{c}{J_m} & \frac{-c}{J_m} & \frac{K}{J_m} & \frac{-K}{J_m} \\ 1 & 0 & 0 & 0 \\ 0 & 1 & 0 & 0 \end{bmatrix} \begin{bmatrix} \omega_r \\ \omega_m \\ \theta_r \\ \theta_m \end{bmatrix} + \begin{bmatrix} \frac{1}{J_r} & 0 \\ 0 & \frac{-1}{J_m} \\ 0 & 0 \\ 0 & 0 \end{bmatrix} \begin{bmatrix} \tau_r \\ \tau_m \end{bmatrix} \tag{6.7}$$

where $\omega_{r,m}$ are the rotational speeds, $\theta_{r,m}$ are the rotational angles, $J_{r,m}$ are the rotational inertias, $\tau_{r,m}$ are the torques, K is the spring constant and C is the damping coefficient. Subscripts r and m refer to the wind turbine rotor and machine, respectively. Dot notation is used to denote derivatives.

These equations were implemented in Simulink using a state-space model. For a 15 MW wind turbine, the parameter values are estimated based on per unit values provided in [210], given in Table 6.2.

Parameter	Symbol	Value (pu)
Rotor inertia	J_r	3.36
Machine inertia	J_m	0.82
Spring constant	k	3.86
Damping constant	c	1.5

Table 6.2: Two-mass model mechanical drive-train parameters [210]

6.3.4 Permanent Magnet Synchronous Generator

The PMSG is modelled following the approach used by [209]. The voltage in each phase of the stator can be expressed in the dq rotating reference frame using the following

equations:

$$\begin{bmatrix} v_d \\ v_q \end{bmatrix} = \begin{bmatrix} R_s & -\omega_e L_q \\ \omega_e L_d & R_s \end{bmatrix} \begin{bmatrix} i_d \\ i_q \end{bmatrix} + \begin{bmatrix} L_d & 0 \\ 0 & L_q \end{bmatrix} \frac{d}{dt} \begin{bmatrix} i_d \\ i_q \end{bmatrix} + \lambda_m \omega_e \begin{bmatrix} 0 \\ 1 \end{bmatrix} \tag{6.8}$$

where $v_{d,q}$ are the voltages induced in the stator, $i_{d,q}$ are the stator currents, R_s is the stator resistance, λ_m is the flux linkage, and $L_{d,q}$ are the stator inductances. The subscripts d and q denote the direct and quadrature axes of the rotating reference frame, respectively. These are calculated from the instantaneous values using the Park transformation, given by

$$\begin{bmatrix} u_d \\ u_q \\ u_0 \end{bmatrix} = \frac{2}{3} \begin{bmatrix} \sin(\theta_e) & \sin(\theta_e - \frac{2\pi}{3}) & \sin(\theta_e + \frac{2\pi}{3}) \\ \cos(\theta_e) & \cos(\theta_e - \frac{2\pi}{3}) & \cos(\theta_e + \frac{2\pi}{3}) \\ \frac{1}{2} & \frac{1}{2} & \frac{1}{2} \end{bmatrix} \begin{bmatrix} u_a \\ u_b \\ u_c \end{bmatrix} \tag{6.9}$$

The electrical rotational speed ω_e is found using the following expression

$$\omega_e = p\omega_m \tag{6.10}$$

where p is the number of pole pairs in the generator and ω_m is the rotational speed of the PMSG. The electrical angle θ_e is obtained by integrating the rotational speed with respect to time.

The equations can be implemented in MATLAB/Simulink by rearranging (6.8) to express it in terms of the stator current derivatives. This becomes:

$$\frac{d}{dt} \begin{bmatrix} i_d \\ i_q \end{bmatrix} = \begin{bmatrix} \frac{-R_s}{L_d} & \frac{-\omega_e L_q}{L_d} \\ \frac{\omega_e L_d}{L_q} & \frac{-R_s}{L_q} \end{bmatrix} \begin{bmatrix} i_d \\ i_q \end{bmatrix} - \lambda_m \omega_e \begin{bmatrix} 0 \\ \frac{1}{L_q} \end{bmatrix} + \begin{bmatrix} \frac{1}{L_d} & 0 \\ 0 & \frac{1}{L_q} \end{bmatrix} \begin{bmatrix} v_d \\ v_q \end{bmatrix} \tag{6.11}$$

The torque developed by the PMSG can be calculated using

$$\tau_m = \frac{3}{2} p\big(\lambda_m i_q + (L_d - L_q) i_q i_d\big) \tag{6.12}$$

where p is the number of pole pairs, $i_{d,q}$ are the stator currents, λ_m is the flux linkage, and $L_{d,q}$ are the stator inductances. The subscripts d and q denote the direct and quadrature axes of the rotating reference frame, respectively. For salient pole machines, L_q and L_d are equal, simplifying the equation so that the generator torque is only dependent on the q-axis current. The selected generator parameters are given in Table 6.3.

Parameter	Symbol	Unit	Value
Stator resistance	R_s	mΩ	1.9
Stator inductance	$L_{d,q}$	µH	173.4
Flux linkage	λ_m	Wb	9.02
Pole pairs	p		86

Table 6.3: Permanent magnet synchronous generator parameters

6.3.5 Machine-side converter and control

The purpose of the machine-side converter is to generate the stator voltages of the PMSG to obtain the desired stator currents. Several control structures are possible to set the current references for type-4 wind turbines, depending on the task division of the converters [211]. For the off-grid wind turbine, the DC link voltage is controlled by the machine-side converter.

The outer voltage control loop compares the DC link voltage with the nominal DC link voltage. This difference is fed to a PI controller which outputs the current references to the inner current control, with the transfer function

$$G_{V_{DC}}(s) = K_{p_V} + \frac{K_{i_V}}{s} \tag{6.13}$$

where K_{p_V} is the proportional gain and K_{i_V} is the integral gain of the DC link voltage control. The output is the q-axis reference current which is then fed to the inner current control.

The current control objective is to obtain the maximum torque per ampere (MTPA), where the d-axis current reference is set to zero to maximise the q-axis current. The d- and q-axis voltage references are calculated in the current control loop. From the PMSG equation (6.8), we can see that the d- and q-axis voltages are coupled and the dynamic behaviour of the current depends on the rotor speed [209]. To control the d- and q-axis currents separately and to simplify the controller design, decoupling feedback is introduced.

$$\begin{bmatrix} v_d^* \\ v_q^* \end{bmatrix} = \begin{bmatrix} \hat{v}_d - \omega_e L_q i_q \\ \hat{v}_q + \omega_e L_d i_d + \lambda_m \omega_e \end{bmatrix} \tag{6.14}$$

where $\hat{v}_{d,q}$ are linear controller output voltages. The linear controllers use PI control,

with the transfer function

$$G_{ICC}(s) = K_{p_{ICC}} + \frac{K_{i_{ICC}}}{s} \tag{6.15}$$

The inner current control proportional and integral gains can be tuned using internal model control [209], resulting in

$$\begin{bmatrix} K_{p,ICC} \\ K_{i,ICC} \end{bmatrix} = \begin{bmatrix} \kappa & 0 \\ 0 & \kappa \end{bmatrix} \begin{bmatrix} L_q \\ R_s \end{bmatrix} \tag{6.16}$$

where κ is a design parameter that can be selected to obtain the desired bandwidth.

The converter itself is modelled using the average converter model to reduce the computational requirements of the simulation. This consists of a controlled voltage source connected to the AC side and a controlled current source connected to the DC side [212]. The voltage set points from the current control loop can then be used to directly control the voltage sources.

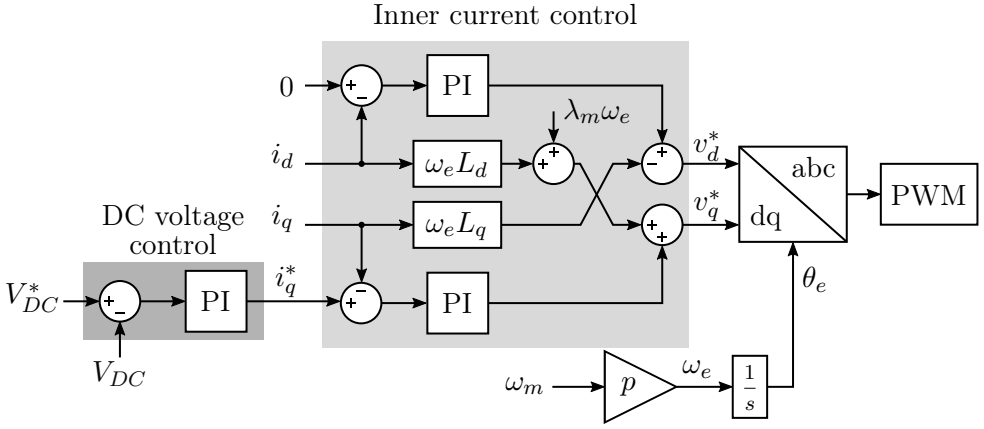

Figure 6.7: Control block diagrams for the machine-side converter

6.3.6 Line-side converter and control

In grid-connected wind turbines, the line-side converter uses grid-following control with a phase-locked loop (PLL) to synchronise with the grid. However, in the case of the off-grid wind turbine, there is no grid to synchronise to. Instead, the line-side converter uses grid-forming control to generate its own voltage and frequency.

The grid-forming control system for the line-side converter is illustrated in Figure 6.8a. The control strategy used is PI-based virtual synchronous machine (VSM) control, which

emulates the traditional swing equation of synchronous machines.

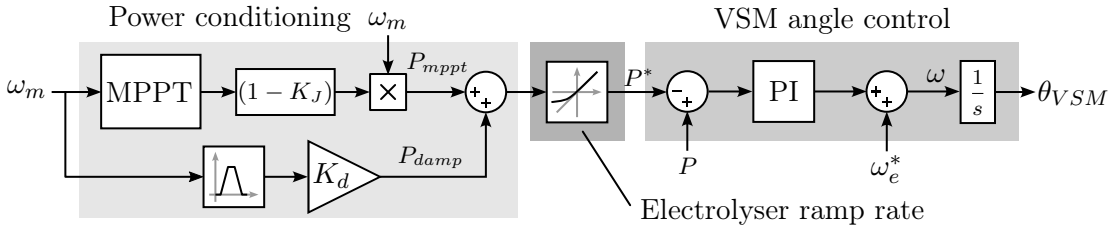

(a) Power conditioning and VSM control

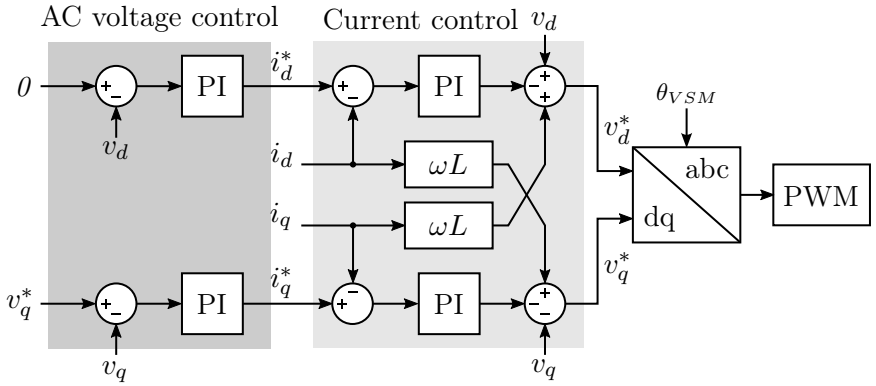

(b) Voltage and current control

Figure 6.8: Control block diagrams for the line-side converter

The VSM control can be implemented by using a PI controller which compares the active power reference and measured power [213].

The active power reference is set by the power conditioning control, which consists of the MPPT power calculation, drivetrain active damping and electrolyser ramp rate limitation. The MPPT power is calculated using

$$P_m^* = K_{Cp}\omega_m^3 \tag{6.17}$$

where K_{Cp} is a parameter based on the wind turbine characteristics to obtain the maximum power [205] given by the following equation

$$K_{Cp} = \frac{1}{2}\rho A_r R_r^3 \frac{c_1(c_2c_7c_9 + c_6c_7 + c_2)^3 \exp(-\frac{c_6c_7+c_2}{c_2})}{c_2^2 c_7^4} \tag{6.18}$$

In regular wind turbine operation, the MPPT provides inherent drivetrain damping due to its dependence on rotor speed [214]. However, in the proposed system, the power set point cannot always change fast enough due to the limited electrolyser ramp rate. As

a result, the system requires active damping to prevent unwanted speed oscillations.

The active damping is based on [214] and consists of a band-pass filter (BPF) followed by a gain. The BPF has the second-order transfer function

$$G_{BPF} = \frac{2\zeta\omega_{dt}s}{s^2 + 2\zeta\omega_{dt}s + \omega_{dt}^2} \tag{6.19}$$

where ζ is the damping factor and ω_{dt} is the drivetrain natural frequency, which is dependent on the drivetrain stiffness and inertia

$$\omega_{dt} = \sqrt{k\left(\frac{1}{J_r} + \frac{1}{J_m}\right)} \tag{6.20}$$

The resulting damping power is added to the MPPT set point.

In addition to generating the electrical angle, the line-side converter is also tasked with controlling the AC voltage of the tower cables and transformers. This is achieved through the use of PI controllers which compare the reference and measured voltages in the dq rotating frame, as shown in Figure 6.8b. The controller transfer functions are given by

$$G_{V_{AC}} = K_{p_{VAC}} + \frac{K_{i_{VAC}}}{s} \tag{6.21}$$

where $K_{p_{VAC}}$ and $K_{i_{VAC}}$ and the proportional and integral gains of the AC voltage controller, respectively. The outputs of the PI controllers are fed into an inner current control, which allows the converter to limit excessive currents under fault conditions.

The inner current control has a similar structure to that used in the machine side converter. The d-axis and q-axis currents are controlled using PI controllers which are decoupled by adding decoupling feedback, as shown in Figure 6.8b.

6.3.7 Electrolyser-side converter and control

The purpose of the electrolyser-side converter is to rectify and control the electrolyser voltage, transferring the remaining power after losses in the transformers and tower cables.

The electrical angle used for the dq transformations is obtained by employing a phase-locked loop (PLL) to synchronise with the line-side converter frequency. The block diagram for the PLL is shown in Figure 6.9a. It uses a PI controller to adjust the angular

frequency until the q-axis voltage is zero, which occurs when the rotating reference frame is aligned with the frequency.

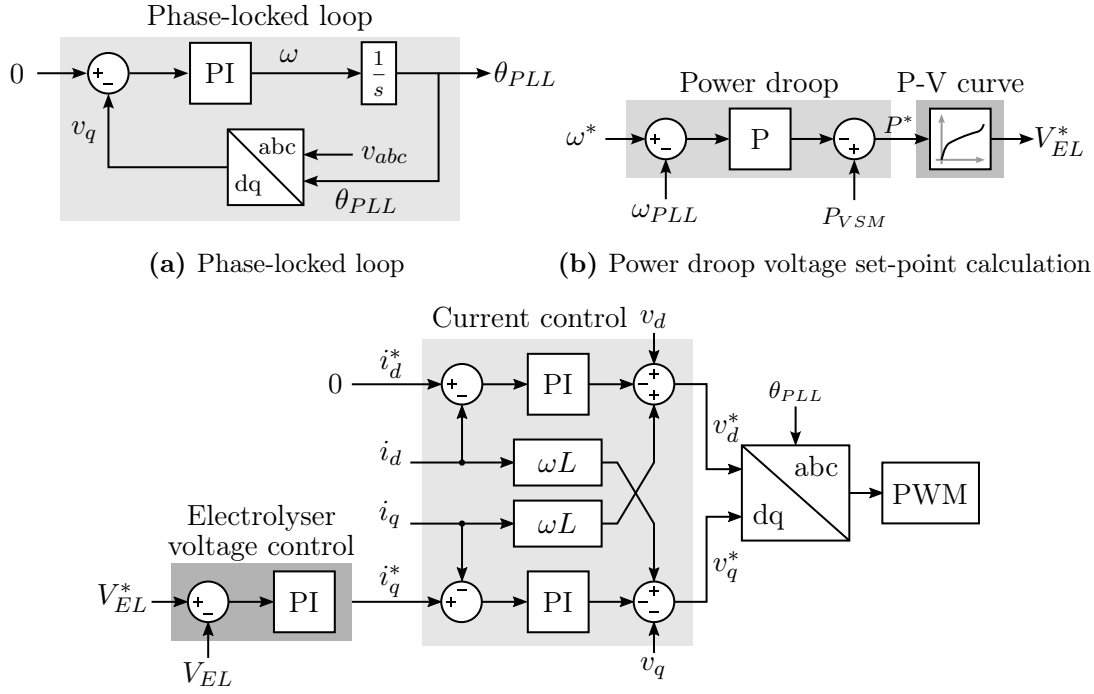

(a) Phase-locked loop

(b) Power droop voltage set-point calculation

(c) Electrolyser voltage and current control

Figure 6.9: Control block diagrams for the electrolyser-side converter

The electrolyser voltage needs to be controlled to match the power remaining in the line after losses in the transformers and cables. This is done through a power droop control, as shown in Figure 6.9b. The PLL angular velocity is compared with the nominal angular velocity with a P-controller. The output is subtracted from the line-side converter power to provide the remaining power set point. The electrolyser voltage is selected based on the electrolyser P-V curve, which is dependent on the electrolyser characteristics, which is discussed in more detail in Section 6.3.8. The electrolyser voltage can then be controlled using the same cascaded controller structure as for the line-side converter, shown in Figure 6.9c.

6.3.8 Electrolyser

The electrolyser is modelled using a controlled current sink. The current value is calculated based on the applied voltage using the electrolyser cell performance, fed through a low pass filter to represent the electrolyser cell dynamics.

The electrolyser J-V curve was modelled using the equations set out in Section 5.5. The parameters for the equations were selected to approximate the performance of a typical commercial electrolyser for this application. These are given in Table 6.4.

As the electrolyser ages, its performance deteriorates due to degradation. The electrolyser is considered to be at its end-of-life (EoL) when the required voltage is 10% higher compared to its beginning-of-life (BoL). The resulting J-V curves are shown in Figure 6.10a.

Parameter	Unit	Value
ΔG	kJ/mol	223.1
α		0.38
J_0	μA/cm^2	13.7
J_L	A/cm^2	2.6
r_{BoL}	Ω/cm^2	0.137
r_{EoL}	Ω/cm^2	0.236

(a) Fitting parameters

Parameter	Unit	Value
F	s·A/mol	96485
R_g	J/(K·mol)	8.3145
p_{H_2}	atm	35
p_{O_2}	atm	0.9
p_{H_2O}	atm	0.15
T_{cell}	K	333.15

(b) Constant parameters

Table 6.4: Parameters used to calculate the J-V characteristic

The specific energy consumption curve was calculated using the equations set out in Section 5.5, assuming a typical cell area of 2500 cm^2, and is shown in Figure 6.10b. It can be seen that at higher current densities, the efficiency of the electrolyser reduces, resulting in more energy required to produce hydrogen. The selection of the operating current density therefore represents a trade-off between power density and efficiency. For this study, a nominal current density of 2 A/cm^2 was selected.

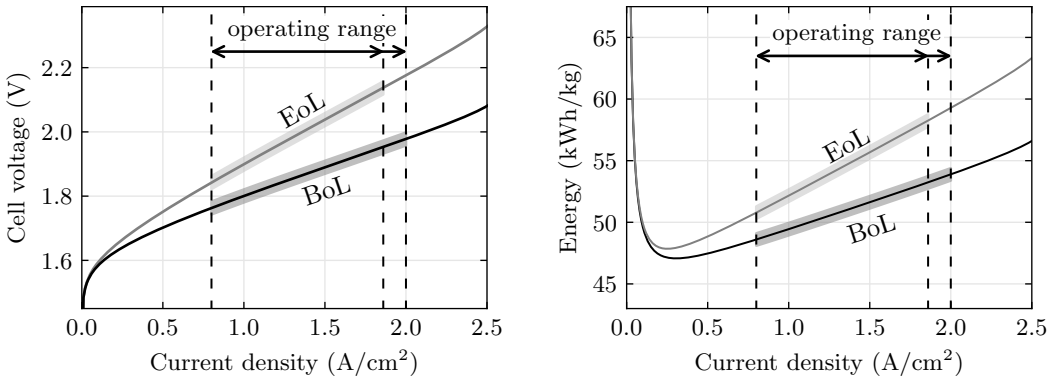

(a) J-V characteristic

(b) Specific energy consumption

Figure 6.10: Electrolyser cell properties

6.4. Power Balancing using Energy Storage

6.4.1 Mechanism

The most straightforward way of making up the difference in power between the wind turbine and the electrolyser is by introducing energy storage. This would likely be in the form of a supercapacitor, which has previously been proposed for use in wind turbines for grid power smoothing and fault ride through [215]. Supercapacitor energy storage would be highly suitable for the electrolyser power balancing due to its rapid dynamic response and high power delivery for a duration from seconds to minutes.

The supercapacitor is connected to the DC link of the back-to-back converter through a dedicated DC/DC converter. The storage-side converter now takes on the control objective of managing the DC link voltage. This allows the machine-side converter control to set the wind turbine power based solely on the optimal torque set by the unconstrained MPPT. Any difference in power between the generator and electrolyser is now compensated by the supercapacitor.

Using energy storage to balance the power has the advantage of enabling the wind turbine to operate at its maximum power point continuously. However, the main drawback of this balancing method is the high capital cost of the supercapacitor and the interfacing converter.

6.4.2 Energy storage sizing

To calculate the size and cost of the energy storage, the difference between the power generated by the wind turbine and the ramp-rate limited electrolyser power demand must be calculated. This power difference will be highly dependent on the wind conditions in which the turbine operates. Therefore, to estimate the requirements, first realistic wind speeds need to be modelled.

To simulate a realistic wind speed profile, the approach set out in [216] was adopted, which combines short-term wind turbulence with medium- and long-term wind variations based on the van der Hoven spectrum [217]. The wind speed is calculated using

$$v(t) = v_{ml}(t) + v_r(t) \tag{6.22}$$

where v_{ml} is the medium- and long-term wind variation component and v_r is the turbulence component. The first component is calculated based on the van der Hoven

spectrum [217], using

$$v_{ml} = \sum_{i=0}^{30} A_i \cos(\omega_i t + \phi_i) \tag{6.23}$$

The amplitude terms are calculated by

$$A_i = \frac{2}{\pi}\sqrt{\frac{1}{2}[S(\omega_{i+1}) + S(\omega_i)] \cdot [\omega_{i+1} - \omega_i]} \tag{6.24}$$

where $S(\omega_i)$ is the van der Hoven spectrum power, sampled at the following frequencies

$$f_i = i \cdot 10^j \tag{6.25}$$

where f_i are the sampled frequencies in cycles per hour, i ranges from 1 to 9, and j ranges from -3 to 2. This is illustrated in Figure 6.11.

The turbulence term in the wind speed calculation is obtained by passing a white noise signal through a Kalman filter. The white noise signal has a sampling period T_s, set to be 1 second, unitary variance, and a band-limited power spectral density of equal to T_s [216]. The Kalman filter can be represented by a simplified filter transfer function [216], given by

$$H_F(s) = K_F \frac{a_1 T_F s + 1}{a_2 T_F^2 s^2 + (a_2 + 1) T_F s + 1} \tag{6.26}$$

where a_1 is 0.4 and a_2 is 0.25. The terms T_F and K_F are calculated based on the site conditions, using the equations

$$T_F = \frac{L_F}{v_{ml}(t)} \tag{6.27}$$

where L_F is the length scale, assumed to be a typical value of 100 m for offshore wind sites [216]. The term K_F is calculated using

$$K_F = \sqrt{\frac{2\pi}{\mathcal{B}(\frac{1}{2}, \frac{1}{3})} \frac{T_F}{T_s}} \tag{6.28}$$

where B is the beta function. The output of the Kalman filter is multiplied with the turbulence intensity, which is given by

$$\sigma_v = k_{\sigma,v} \cdot v_{ml}(t) \tag{6.29}$$

where $k_{\sigma,v}$ is the slope of the regression curve that statistically describes the relation between the mean wind speed and the turbulence intensity. For this study, it was considered a typical value of 0.1 for offshore wind sites [216].

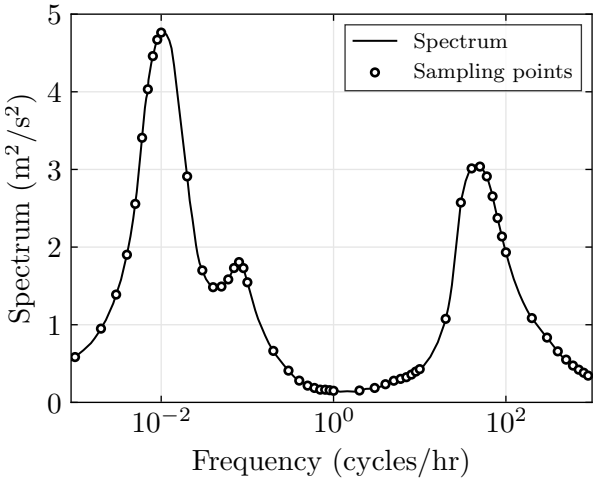

Figure 6.11: Sampled van der Hoven frequency spectrum

6.4.3 Power and energy requirements

The stochastic nature of the wind speed and delay between wind speed and wind turbine power output mean that the likely power and energy mismatch between the wind turbine and the electrolyser cannot be calculated analytically.

A Monte Carlo approach was therefore taken. One hundred hour-long realistic wind speed profiles were simulated with varying initial conditions with an average speed ranging from 6 m/s to 11 m/s, corresponding to the electrolyser cut-in and nominal wind speeds, respectively. The power output of the wind turbine was calculated using (6.1).

Due to the wind turbine inertia, the wind turbine power output will not immediately follow the wind speed. These wind turbine dynamics were simplified to reduce the computational cost of the hour-long simulations by using low pass filters to determine the wind turbine rotational speed and pitch blade angle. The filter constants were adjusted to provide a good match with the more complex dynamic model described in Section 6.3.

It is assumed that any increase in wind turbine power exceeding the electrolyser ramp-up rate can be shed by pitching the blades. The mechanism for this is explained in Section 6.6. However, any rapid decreases in wind turbine power will require additional

power to match the electrolyser ramp-down rate. The electrolyser ramp-rate limitation is assumed to be 0.1 pu/s and is dependent on the number of stacks in operation, taken from Figure 6.1. The maximum power difference can then be calculated using

$$P_{ess} = \max\left(P_{el}(t) - P_{wt}(t)\right) \tag{6.30}$$

where P_{ess} is the required balancing power of the energy storage system, P_{el} is the ramp-down limited electrolyser power and P_{wt} is the available power in the wind.

The required balancing energy can be calculated by integrating this power difference. However, additional energy may be required if multiple rapid wind speed decreases happen in succession without the energy storage being able to replenish. Therefore, a 25% safety margin was added to the total energy requirement. The resulting equation is

$$E_{ess} = 1.25 \cdot \max\left(\int_{t_0}^{t_1} \left(P_{el}(t) - P_{wt}(t)\right) dt\right) \tag{6.31}$$

where E_{ess} is the required energy of the energy storage system, t_0 is the start of each power mismatch event, and t_1 is the end of the power mismatch event.

Figure 6.12 shows example time-domain results for a challenging two-minute window in one of the hour-long realistic wind speed simulations. This case shows that a 5 MW, 7 kWh energy storage system allows the wind turbine to continue operating through the worst-case power mismatch event.

6.4.4 Results

The results of these calculations for each wind speed are shown in Figure 6.13. The mean power required to balance the wind turbine and electrolyser tends to increase with wind speed, reaching a peak at the nominal wind speed of 11 m/s. However, the energy requirements are more varied by wind speed. At lower wind speeds, the wind turbine power output is reduced, which means that fewer of the electrolyser stacks are in operation. The result is a stricter ramp rate limitation, which can occasionally lead to longer mismatch periods, despite the lower wind turbine power fluctuations at low wind speeds. However, the median energy requirements tend to be consistently higher at the nominal wind speed of 11 m/s. This wind speed was therefore used to size the energy storage.

The results for various electrolyser ramp rates are given in Figure 6.14. This shows

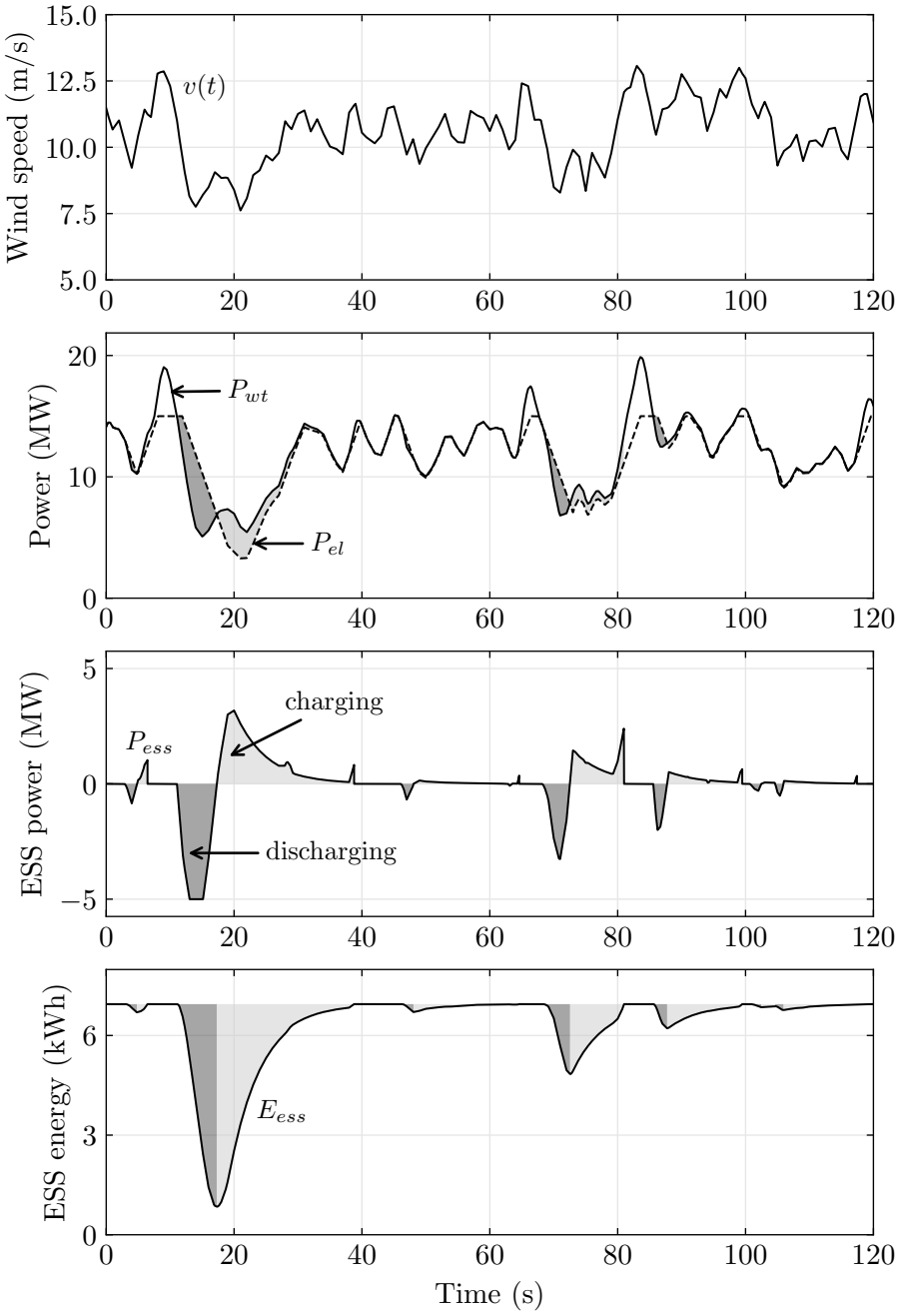

Figure 6.12: Energy storage system time domain results for a two-minute window of realistic wind speeds when using a 5 MW, 7 kWh energy storage system. Energy storage system charging and discharging periods are highlighted.

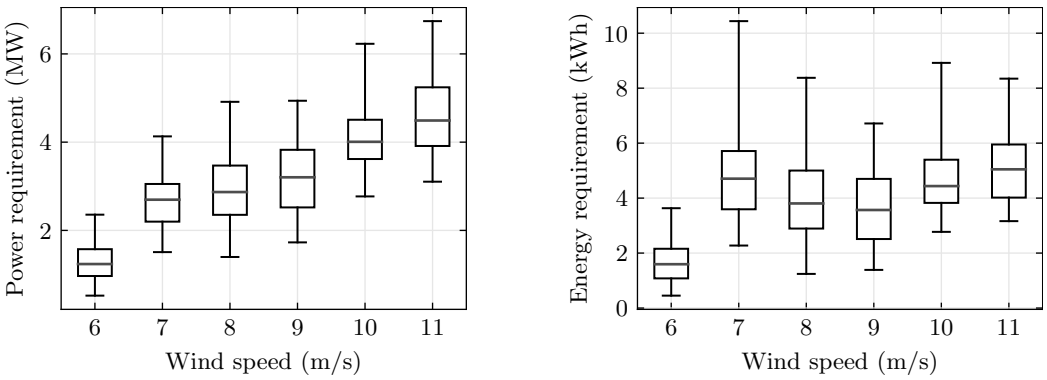

(a) Power requirements **(b)** Energy requirements

Figure 6.13: Maximum hourly balancing requirements by wind speed

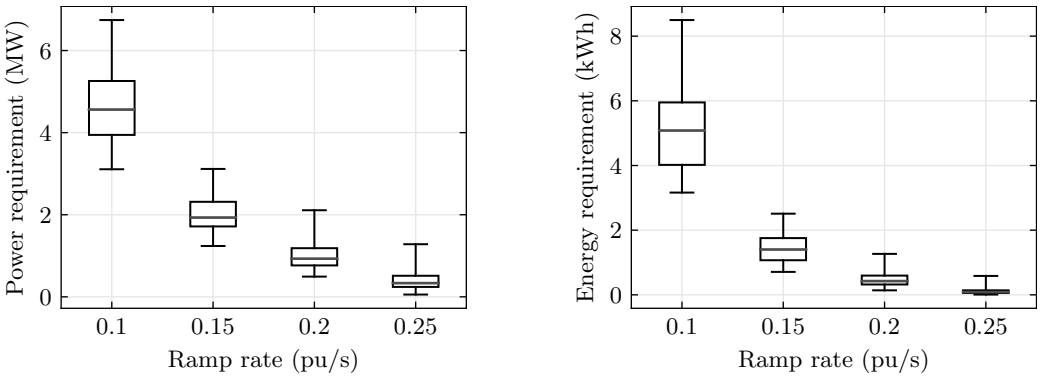

(a) Power requirements **(b)** Energy requirements

Figure 6.14: Maximum hourly balancing requirements by ramp rates

that for the electrolyser to continuously operate during 99% of the hours below rated wind speed, the balancing power and energy requirements are 6.7 MW and 8.5 kWh, respectively. The most suited energy storage technology to fulfil these requirements would be a supercapacitor, which has previously been proposed for use in wind turbines for grid power smoothing and fault ride through [215], due to its rapid dynamic response and high power delivery for a duration from seconds to minutes. The projected cost of supercapacitors in 2025 is $835/kW [218]. This corresponds to an additional capital cost of $5.6M. The associated DC/DC converter would add another $1.2M [99], which would significantly increase the cost of hydrogen production.

The electrolyser ramp rate is the main factor determining these power and energy requirements. In the base case, an electrolyser ramp rate of 0.1 pu/s is used. Further realistic wind speed simulations were performed for the nominal wind speed to determine how the requirements change with higher allowable ramp rates. The results of this investigation are shown in Figure 6.14. The results show that doubling the allowable ramp rate to 0.2 pu/s reduces the 99% survival power requirements by 70% to 2.1 MW and the corresponding energy requirements by 85% to 1.3 kWh. A supercapacitor of this size with its associated converter is projected to cost approximately $2.1M.

If the electrolyser has a ramp rate of 0.3 pu/s or above, power balancing is no longer required since the electrolyser can follow the wind turbine power output without any significant mismatch.

6.5. Power Balancing using Rotor Inertia

6.5.1 Mechanism

It is possible to use the wind turbine rotor to store energy in the form of inertia. This can then be used when the generator power drops faster than the electrolyser ramp-down rate. When the wind turbine is operating at the peak of the power coefficient curve, any changes in the wind turbine speed will result in a reduction in power.

However, if the operating speed is increased, it is possible to gain additional power that can be used to match the electrolyser ramp rate. This process is illustrated in Figure 6.15. The wind turbine operates at point A, which is faster than its optimal operating point. When the wind speed drops and the generator power reduces faster than the electrolyser ramp-down rate, the wind turbine will slow down, moving left along the Cp curve. This results in an increase in available power, until point B is

reached. In addition, the higher operating speed means there is additional time before the wind turbine stops, increasing the likelihood of the electrolyser power demand to reach the new output power.

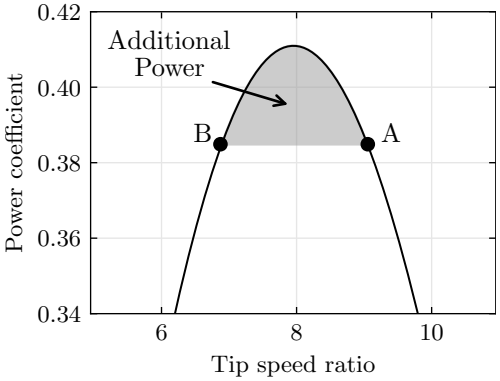

Figure 6.15: Additional power available from rotor inertia

The advantage of using the rotor inertia is that, unlike the energy storage solution, no additional expensive components are required. However, the wind turbine will need to operate at a higher rotational speed than it was designed for, which may lead to reliability issues. The wind turbine will also produce less energy during regular operation due to its suboptimal operating speed.

6.5.2 Implementation

For the wind turbine to operate at this higher rotational speed, the MPPT algorithm needs to be updated. This can be done by adding an inertia factor to the torque calculation, resulting in

$$\tau^*_{m,J} = (1 - K_J) K_{Cp} \omega_m^2 \tag{6.32}$$

where $\tau^*_{m,J}$ is the updated generator torque reference and K_J is the inertia factor that reserves part of the torque for rotor energy storage. Figure 6.16a shows how the new MPPT and torque influences rotor speed, and Figure 6.16b shows the resulting wind turbine power. It can be seen from the figure that the new MPPT torque reference results in a higher rotor speed but a small decrease in wind turbine power output.

Calculating the required inertia factor K_J is not straightforward. In the literature on power smoothing, the energy stored in the rotor can be calculated [219], using the equation

$$\Delta E = \frac{1}{2} J_t (\omega_{max}^2 - \omega_{min}^2) \tag{6.33}$$

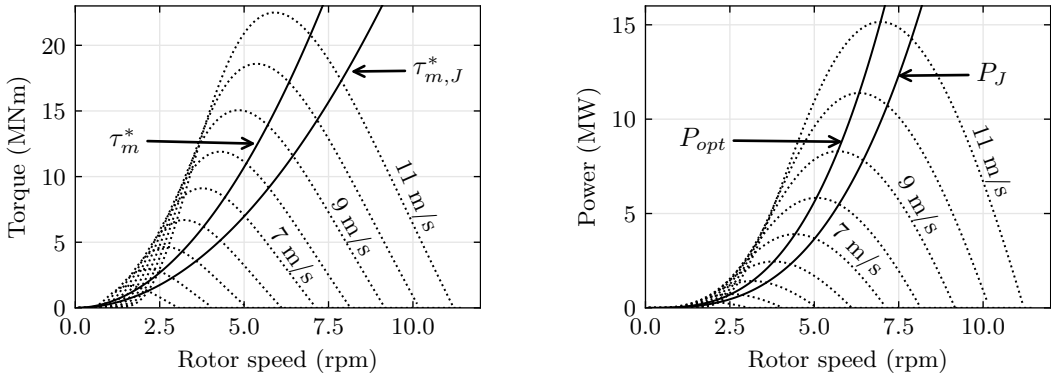

(a) Generator torque **(b)** Aerodynamic power

Figure 6.16: Comparison of standard and updated MPPT operating points per wind speed

where J_t is the combined inertia of the rotor and generator, ω_{max} and ω_{min} are the maximum and minimum rotational speeds, corresponding to point A and point B in Figure 6.15, respectively.

However, (6.33) assumes the desired output power of the wind turbine is constant for a given average wind speed. In the off-grid wind turbine with electrolyser system, the desired output power is rate-limited, linearly moving towards the wind turbine power instead. Therefore, (6.33) can only give an indication of the energy storage available, and cannot be used to directly calculate the required inertia factor K_J.

6.5.3 Results

To estimate the required inertia factor, the new MPPT algorithm was tested on all 100 realistic wind speed scenarios from Section 6.4.3. The inertia factor was adjusted iteratively, using (6.33) as a starting point, until the wind turbine managed to stay operational through the event. The time domain results for the most challenging wind speed reduction are shown in Figure 6.17. This shows that at inertia factors of less than 0.5, the wind turbine stalls and comes to a standstill, whereas at inertia factors of 0.5 and above, the wind turbine can survive the wind speed reduction.

The results for the remaining inertia balancing tests are shown in Figure 6.18. For the base case 0.1 pu/s ramp rate, to enable the wind turbine to operate continuously through 99% of the wind speed variation, the required inertia factor is 0.45. In steady-state operation, this suboptimal torque setting results in a 10.6% loss in energy production for wind speeds below nominal. The wind turbine rotational speed also increases by

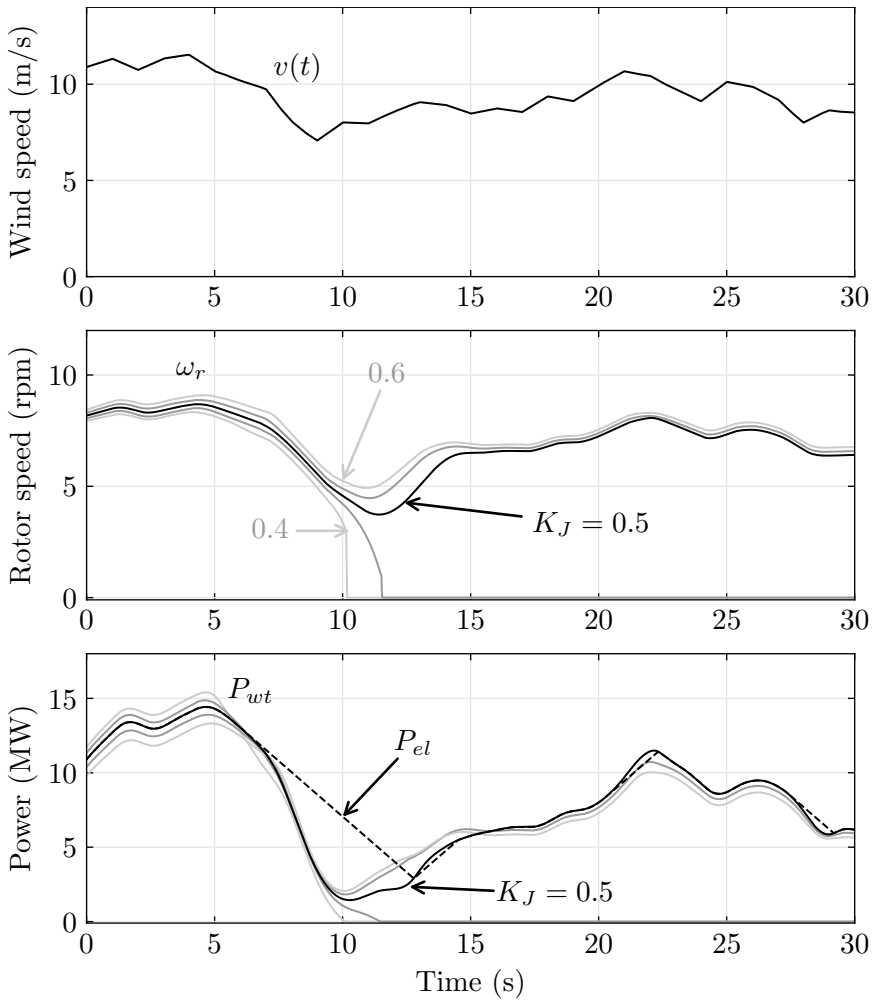

Figure 6.17: Time domain results for the inertia balancing mechanism showing the impact of the inertia factor during the most challenging wind speed reduction

17.8%. This is a significant increase, which could potentially result in a reduced wind turbine lifetime due to the additional stress on the rotor. It may also require a redesign of several control systems to prevent unwanted excitations.

If the electrolyser ramp rate can be increased, the required inertia factor can be reduced while still allowing the wind turbine to continue operating. For example, doubling the allowable electrolyser ramp rate to 0.2 pu/s was found to require an inertia factor of 0.05 for a 99% survival rate. This corresponds to a much more acceptable 0.3% energy loss and 2.7% rotational speed increase.

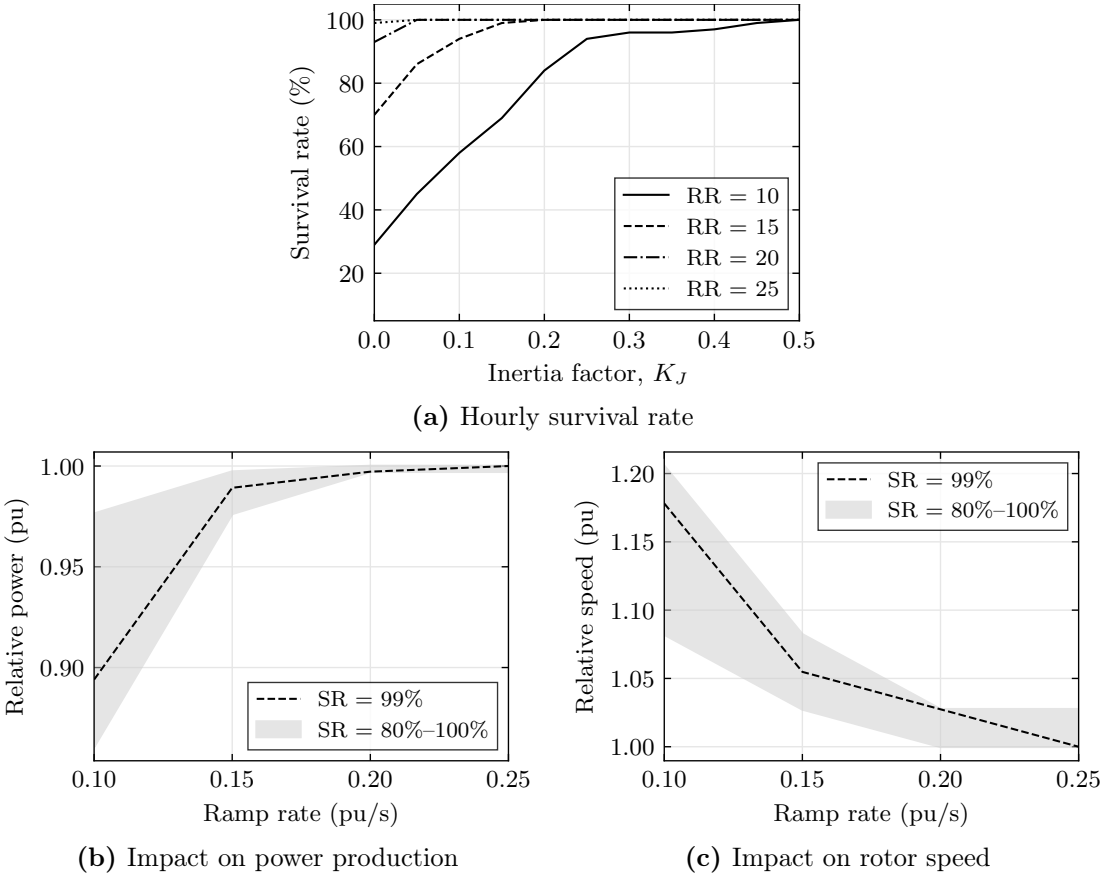

(a) Hourly survival rate

(b) Impact on power production

(c) Impact on rotor speed

Figure 6.18: Inertia balancing results for varying electrolyser ramp rates (RR) and hourly survival rates (SR)

6.6. Power Balancing using Pitch Control

6.6.1 Mechanism

Pitching the wind turbine blades is already used in wind turbines to limit the speed and power during high wind speeds. It is therefore well suited to balancing the wind turbine and electrolyser power for rapid wind speed increases. The pitch controller can control the power by adjusting the blade pitch angle, which impacts the power coefficient, $C_p(\lambda, \beta)$, as can be seen in (6.2). Increasing the pitch angle reduces the coefficient of performance and therefore the power extracted from the wind. However, this is highly dependent on the tip speed ratio, as shown in Figure 6.19a and Figure 6.19b.

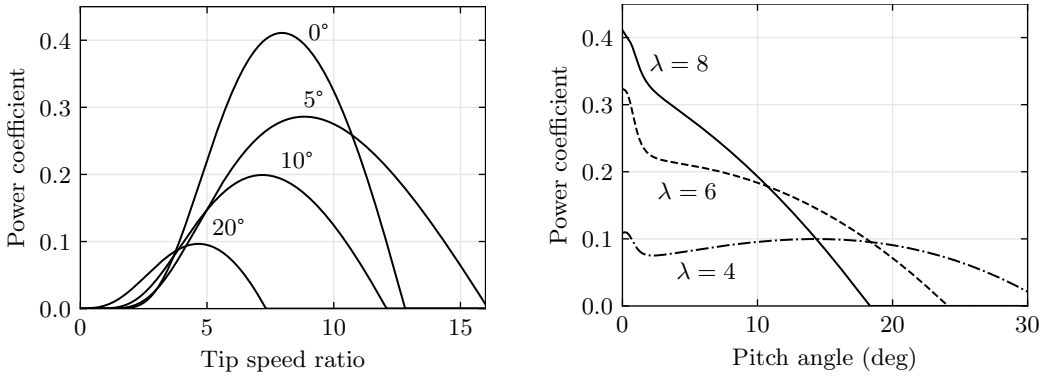

(a) Constant pitch angle **(b)** Constant tip speed ratio

Figure 6.19: Coefficient of performance variation with pitch angle and tip speed ratio

The main drawback with using pitch control for power balancing is that it cannot easily accommodate the electrolyser ramp-down limitation. When the wind turbine operates below rated speed, the pitch angle is set to zero for maximum power extraction. In this case, a reduction in wind speed cannot be mitigated as any pitching will only further reduce the power.

A potential solution to this is to operate the wind turbine with a non-zero pitch below rated power. This allows the wind turbine to increase its power production temporarily during a wind speed reduction by decreasing the pitch angle. Operating at this non-zero pitch will alter the power coefficient curve, which means that the MPPT algorithm will need to be updated to determine the new operating speed. There are two options for updating the MPPT. The first is to set the MPPT to maintain the existing tip speed ratio, resulting in the same rotational speed of the wind turbine. The second option is to update the MPPT to find the new optimal rotational speed for the non-zero pitch

curve.

The process for the first option is illustrated in Figure 6.20a using an example non-zero pitch of 1°. During regular operation, the wind turbine will operate with a 1° pitch at its original tip speed ratio, indicated by point A, which is below its optimal point. When the wind speed and associated power drops faster than the electrolyser ramp-down rate, the wind turbine will pitch the blades to zero, increasing the power production to the peak of the 0° curve, at point B. The power demand from the electrolyser exceeds the provided power from the wind, resulting in a slow-down of the wind turbine. As the wind turbine slows down, the tip speed ratio decreases, and the operating point moves down the 0° curve. At point C, the power provided by the wind turbine is equal to the original power production at 1°, which denotes the limit of the additional power available. This option results in slightly lower power extraction from the wind compared to using a higher tip speed ratio. However, it has the advantage of not requiring the wind turbine to operate above its design speed.

The alternative is to use the new optimal tip speed ratio for non-zero pitch operation. This process is illustrated in Figure 6.20b for an example non-zero pitch of 1°. During regular operation, the wind turbine will operate at the peak of the Cp curve for 1°, denoted by point A. When the wind speed drops, the blades are pitched to 0°, moving the operating point to the 0° curve, reaching point B. As the wind turbine slows down due to the electrolyser power demands, the operating point moves down the 0° curve, with point C indicating the limits of the additional power. This option results in the highest efficiency operation. However, similar to using the rotor inertia balancing, in this case the wind turbine will need to operate at a higher rotational speed than it was designed for, which may lead to reliability issues.

6.6.2 Implementation

The pitch controller can be enhanced to allow for power balancing below rated wind speed. This is done by adding a proportional-derivative (PD) controller to provide the pitch angle based on the difference between the aerodynamic power and the ramp-limited power demand, as shown in Figure 6.21. The transfer function for the PD controller is given by

$$G_{\Delta\beta}(s) = K_{p_{\Delta\beta}} + K_{d_{\Delta\beta}} \frac{N_{d_{\Delta\beta}}}{1 + N_{d_{\Delta\beta}} s} \tag{6.34}$$

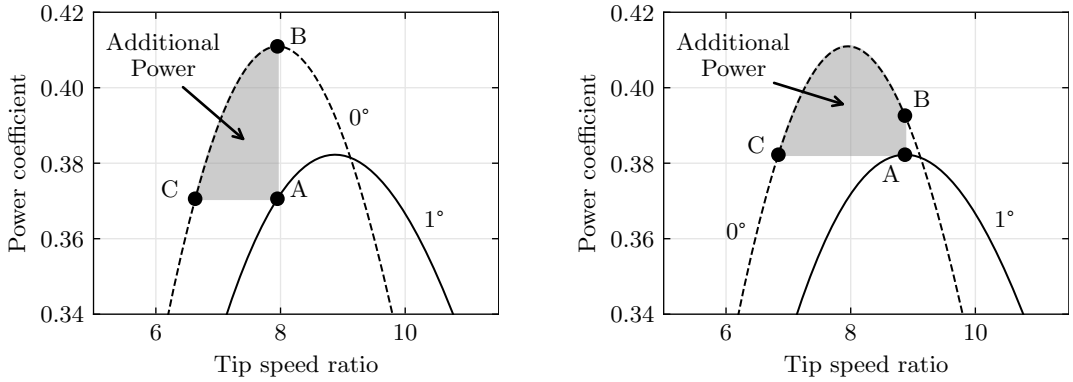

(a) Existing tip speed ratio **(b)** New optimal tip speed ratio

Figure 6.20: Additional power available from non-zero pitch operation for two MPPT strategies

where $K_{p_{\Delta\beta}}$ is the proportional gain, $K_{d_{\Delta\beta}}$ is the integral gain, and $N_{d_{\Delta\beta}}$ is the filter coefficient. The PD controller output is followed by a saturation block to only output positive pitch angles. The non-zero pitch angle strategy can be adopted by adding a non-zero pitch angle, β_{NZ} to the pitch set point and by expanding the power balancing saturation limit to allow negative angles up to the non-zero pitch value. In addition, the output from the speed control PI controller is saturated to stay above the non-zero pitch value when speed control is enabled.

To prevent excessive switching between the speed control and power balancing control around the nominal operating point, the selector uses hysteresis whereby speed control is activated at nominal rotor speed but only deactivated at 90% rotor speed.

6.6.3 Results

Calculating the amount of energy that can be used for balancing using the non-zero pitch operation is not straightforward. The duration the additional power is available is dependent on the rate of change in the wind turbine rotational speed, i.e. how long it takes for the operating point to move from point B to point C. This will depend on the difference between the required generator torque and the available aerodynamic torque.

In reality, the tip speed ratio does not remain constant during a wind decrease and will instead increase momentarily. The generator power does not change immediately with a change in wind speed due to the rotor inertia and the blades can also not pitch instantaneously, as the pitch angle rate of change is limited by the pitching actuators. This means the transition between power coefficient curves is not as smooth as Figure 6.20

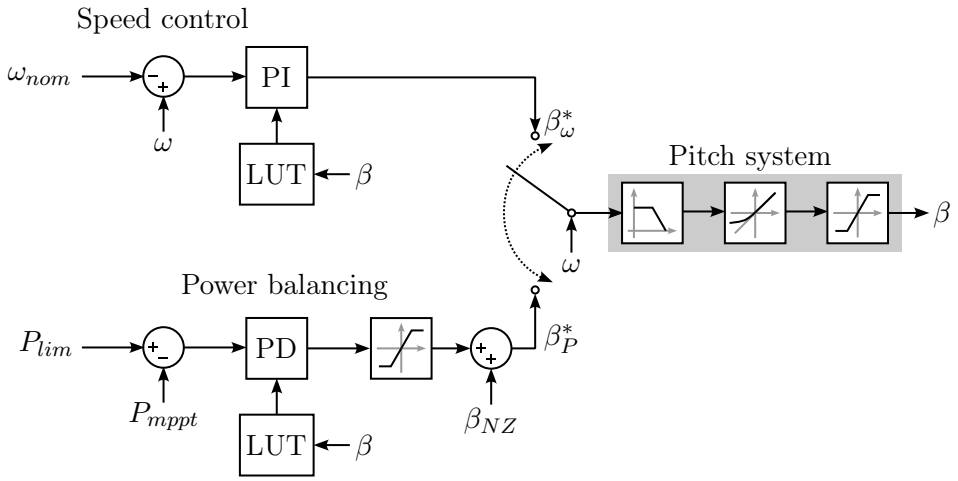

Figure 6.21: Control block diagram for the enhanced pitch controller with power balancing capability

suggests.

Therefore, to estimate the required non-zero pitch to prevent electrolyser shutdown, the pitch power balancing algorithm was tested on all 100 realistic wind speed scenarios from Section 6.4.3. The pitch angle was adjusted iteratively until the wind turbine could ride through the wind reduction event. In each case, the MPPT torque gain was adjusted to obtain either the original tip speed ratio (option 1) or to obtain the new optimal tip speed ratio at the non-zero pitch angle (option 2). The time domain results for one of the most challenging wind speed reductions for each option are shown in Figure 6.22. This shows that option 1 requires a minimum 3° non-zero pitch and option 2 requires a minimum 1.5° non-zero pitch to keep the wind turbine operational through the wind speed event.

The results are shown in Figure 6.23 and Figure 6.24. For the base case electrolyser ramp rate of 0.1 pu/s, to enable a 99% survival rate, a non-zero pitch of 3° is required when operating at the original tip speed. This results in a wind turbine power output reduction of 24.7%. By operating the wind turbine at its new optimal speed, a median pitch angle of 1.5° is required, resulting in a power reduction of 10.3% instead. However, this is also associated with a rotational speed increase of 19.3%.

If the electrolyser ramp rate can be increased, the required non-zero pitch decreases significantly. For example, at a ramp rate of 0.2 pu/s and using option 1, a non-zero pitch angle of 1° is required for a 99% survival rate. This results in a power reduction of 9.8%. When using option 2, the required non-zero pitch angle is 0.5°, corresponding

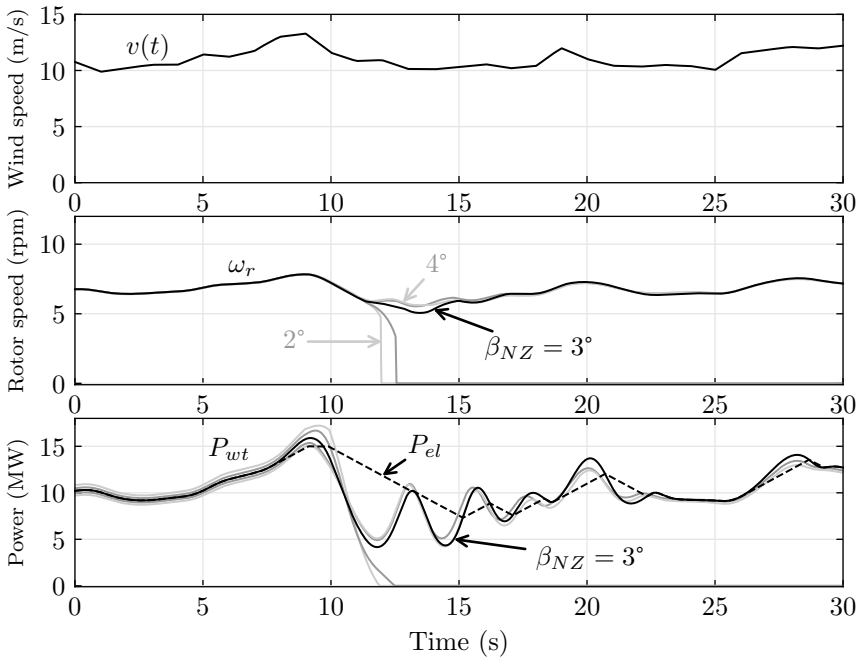

(a) Original tip speed ratio

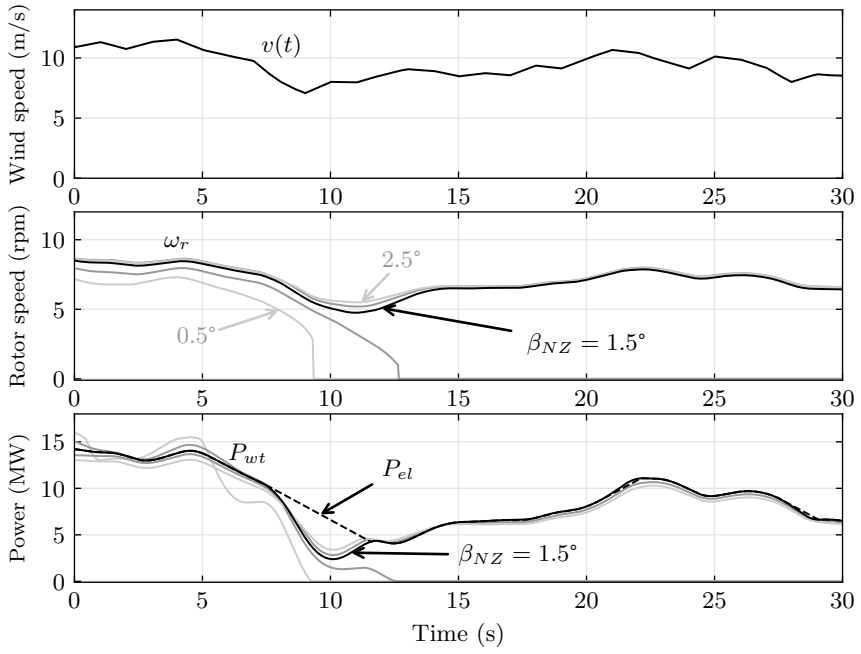

(b) New optimal tip speed ratio

Figure 6.22: Time domain results for the non-zero pitch balancing mechanisms, showing the impact of non-zero pitch setting during one of their respective most challenging wind speed reductions

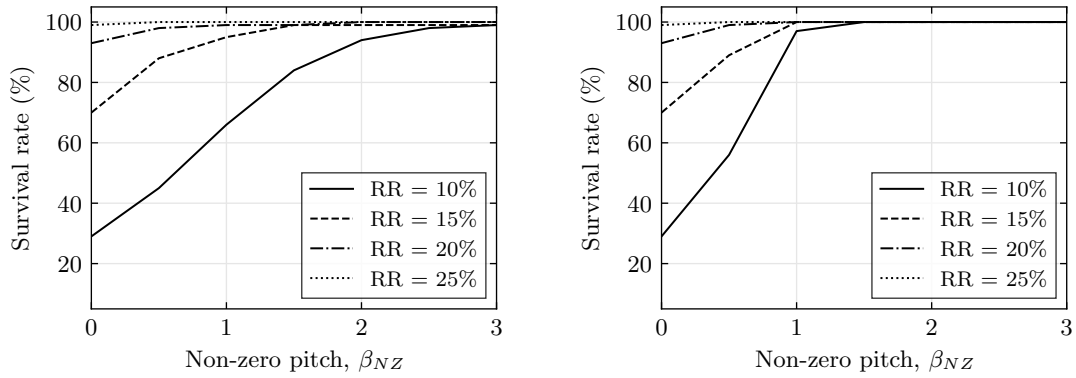

(a) Original tip speed ratio **(b)** New optimal tip speed ratio

Figure 6.23: Hourly survival rate by non-zero pitch setting

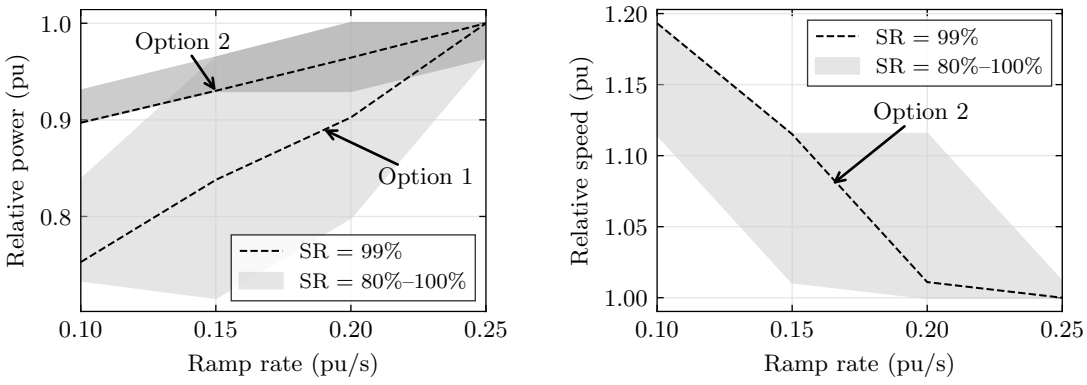

(a) Relative power output **(b)** Relative rotor speed

Figure 6.24: Pitch balancing results for varying electrolyser ramp rates, when keeping the original tip speed ratio (option 1) or finding the new optimal tip speed ratio (option 2)

to a power reduction of 3.6%, with a rotational speed increase of 1.1%.

6.7. Conclusions

This chapter investigated the control system for a standalone offshore wind turbine with co-located electrolyser and how the power between the wind turbine and electrolyser could be balanced taking into account the electrolyser ramp rate limitations.

The control system consisted of four main controllers, including the pitch controller, the machine-side converter controller, the line-side converter controller, and electrolyser-side converter controller. Under normal operation, the machine-side control objective was to maintain the DC link voltage. The power flow was regulated by the line-side converter control, which employed a grid-forming control structure to generate the electrical angle. The electrolyser-side converter control objective was to set the electrolyser voltage to control its power demand.

Three power balancing strategies were investigated, including energy storage, rotor inertia and non-zero pitch. The results showed that for the wind turbine to stay operational through 99% of the hourly wind speed variation while being limited to a 0.1 pu/s power ramp rate, a $6.8M supercapacitor is needed with a rating of 6.7 MW and 8.5 kWh. Alternatively, using rotor inertia to balance the power would reduce energy production by 11% and increase rotor speed by 18%. Using non-zero pitch control would result in a 25% energy reduction without speed increase or a 10% energy reduction with a 19% speed increase. Therefore, at existing commercial electrolyser ramp rates, none of the balancing strategies are very cost-effective. The most realistic solution would be using energy storage, although this would come at a significant additional capital cost.

Improvements in the power ramp rate of the next generation of electrolysers would make the production of hydrogen in this system more cost-effective. At higher ramp rates, the control-based power balancing methods become more attractive. For example, at a 0.2 pu/s ramp rate, using rotor inertia balancing results in a power reduction and speed increase of less than 1% and 3%, respectively. For the non-zero pitch balancing strategy with speed increase, these values are 4% and 1%, respectively. These options are therefore both realistic and cost-effective solutions.

If electrolyser power ramp rates can be increased to 0.3 pu/s, no power balancing or control modifications would be required at all. This should therefore be the design target for future electrolysers used in off-grid offshore wind systems.

Chapter 7

Cost-effective hydrogen production

7.1. Introduction

This chapter investigates the most cost-effective wind turbine configurations for offshore hydrogen production. The previous chapter has shown how electrolysers can be connected with standalone wind turbines using several possible power balancing methods. This chapter builds on these results, as well as the findings from previous chapters, to determine how the cost of hydrogen production is impacted by the wind turbine electrical drivetrain and power balancing strategy, with the aim of reducing the levelised cost of hydrogen (LCOH).

7.1.1 Previous research

The direct connection of wind turbines and electrolysers is a relatively understudied topic. To the author's knowledge, there are currently no publications which investigate power balancing in this system, beyond those resulting from Chapter 6. However, there are a handful of publications which propose novel electrical drivetrains to directly connect wind turbines and electrolysers. The scope of these studies tends to be limited, with either a single drivetrain being investigated, or without any quantification of the relative merits of their proposed drivetrain compared to existing solutions.

The authors of [220] connected a 5 kW PMSG-based wind turbine with multiple 400 W electrolyser stacks using a three-phase diode rectifier, followed by one DC/DC converter per stack stack. They mention that their system provides improved conversion efficiency, but do not provide quantitative evidence for this. One interesting finding was that in this configuration, the DC output voltage from the rectifier would vary from 75 V to 500 V, depending on the wind speed. Such a large voltage range will have implications for the DC/DC converter performance, and highlight one of the potential compatibility

challenges in directly coupling a wind turbine and electrolyser.

A patent by Vestas [221] shows six possible concepts for the off-grid connection of a wind turbine and electrolyser. The simplest proposed design consists of a single AC/DC converter that connects the generator to the electrolyser, which is located either inside the wind turbine nacelle or in the tower. Other proposed designs include the use of a transformer before the AC/DC stage, as well as an AC/DC converter followed by a DC/DC converter, both of which allowing the use of higher voltages. Other proposed configurations enhance these options with the addition of a hydraulic torque converter or dynamic voltage restoration unit. The authors also put forward modular designs, using half bridge, full bridge, or modular multilevel converter cells to connect to individual electrolyser stacks. While the patent provides a large range of possible designs and a basic description of their use cases, it does not include any details or assessment of their performance or relative merits.

The study by [203] provides a good approach to assess the performance of a novel electrical drivetrain for hydrogen production. Similar to [220], the authors propose using a rectification stage, followed by a modular dual active bridge DC/DC converter, with each module connected to a single electrolyser stack. However, their study is much more rigorous: they consider a full-scale wind turbine of 15 MW, and their investigation includes the calculation of the LCOH for various electrolyser ratings, taking into account capital costs, wind turbine annual power production, DC/DC converter efficiency, and electrolyser polarisation curves. The main drawbacks of this study include that it only investigates a single drivetrain and does not use discounting in the LCOH calculation.

7.1.2 Contributions

This chapter carries out the first detailed investigation of the cost-effectiveness of various wind turbine drivetrains and power balancing strategies for water electrolysis. It quantitatively compares the hydrogen production of multiple DC electrical drivetrains and compares the resulting LCOH of these drivetrains with the standard AC connection with a back-to-back converter.

The assessment is comprehensive as it provides a complete LCOH calculation, taking into account the capital costs, losses, and hydrogen production over the lifetime of the system. Unique in the study is the inclusion of the capital costs and/or efficiency reduction that result from the power balancing systems proposed in Chapter 6.

In addition, the study includes a detailed loss estimate for the DC/DC converter, based

on the previous work done on DC/DC converter optimisation. It also takes into account often overlooked factors, such as the electrolyser performance degradation, stack replacement costs, and hydrogen pipeline costs.

Another main contribution of the investigation is an assessment of the control strategy and technological challenges with each of the drivetrains. A basic control overview is given for each of the drivetrains, and the technological readiness level of the components is taken into account in the recommendations.

7.2. Drivetrain designs

Four electrical drivetrain designs were investigated as part of this study. The first design is the conventional AC drivetrain, which serves as a basis for comparison with the novel drivetrains. In the conventional AC drivetrain, illustrated in Figure 7.1a, the wind turbine nacelle contains the PMSG, a back-to-back converter and a step-up transformer. Three single phase cables transport the power down the tower to the platform, where a second transformer and rectifier connect to the electrolyser.

The simplest electrolyser connection is the direct connection of the electrolyser, shown in Figure 7.1b. In this drivetrain, the nacelle only houses the PMSG and a single AC/DC converter. This is directly followed by two tower cables that connect to the electrolyser on the platform. This configuration has the potential to reduce the losses associated with the conversion steps but has challenges associated with low voltage operation.

A variation of the direct DC connection is the nacelle-only connection, where all electrical components are housed in the nacelle, as shown in Figure 7.1c. This has the potential to avoid some of the low voltage challenges of the direct connection, but requires the electrolyser to be able to fit inside the nacelle. It also requires a flexible hydrogen pipe to transport the hydrogen down the rotating tower.

The third considered wind turbine drivetrain, illustrated in Figure 7.1d, uses a single DC/DC converter at the tower base or platform before connecting to the electrolyser. This allows the generator and electrolyser voltages to be decoupled, but will increase the semiconductor switching losses compared to the direct electrolyser connection.

The final DC electrical drivetrain uses two DC/DC converters, as shown in Figure 7.1e. This allows for the use of a high voltage of the cables in the tower, as well as independent voltage control of the generator and electrolyser. However, this configuration also requires the most power electronics, resulting in higher losses.

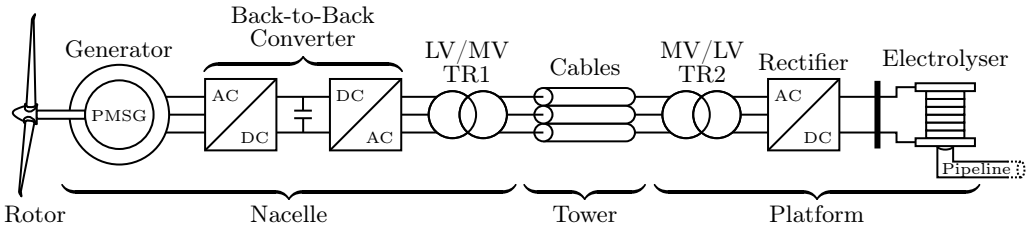

(a) Conventional AC connection

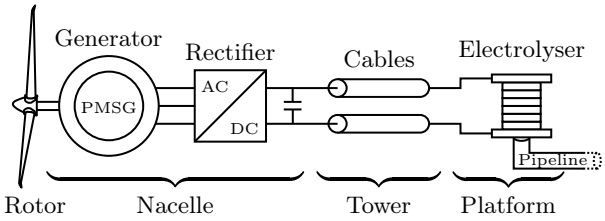

(b) Direct DC connection

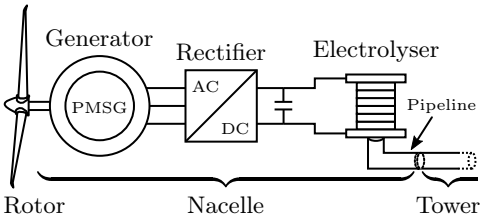

(c) Nacelle-only direct DC connection

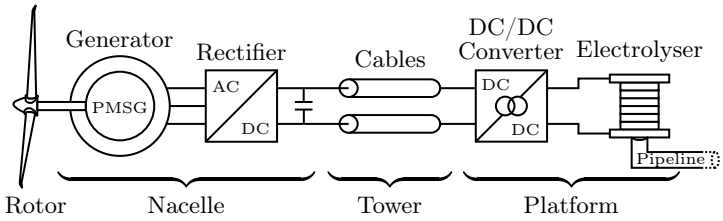

(d) DC connection with one DC/DC converter

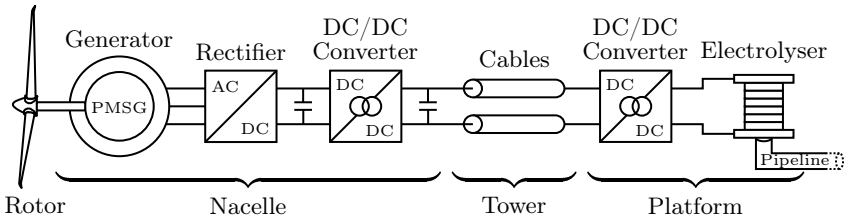

(e) DC connection with two DC/DC converters

Figure 7.1: Wind turbine drivetrain designs for electrolyser connection

7.3. Methodology

The methodology is partly based on the work of previous chapters, and has the aim of determining the LCOH for each of the configurations. The LCOH can be calculated using

$$\text{LCOH} = \frac{\sum_{t=0}^{T_t} \frac{C_t+O_t+V_t}{(1+D_r)^t}}{\sum_{t=0}^{T_t} \frac{H_{2,t}}{(1+D_r)^t}} \tag{7.1}$$

where t is the year of operation, C_t is the capital cost, O_t is the fixed operating cost, V_t is the variable operating cost (including fuel cost), $H_{2,t}$ is the hydrogen production, D_r is the discount rate, and T_t is the final year of operation [64].

The average number of operational years for an offshore wind farm is 27 years [64]. The discount rate used in the LCOH calculation is typically based on the weighted average cost of capital, which is currently about 6% for offshore wind farms [64]. However, to take into account the additional risk of the relatively novel standalone wind turbine electrolyser system, a discount rate of 8% was assumed instead.

The LCOH estimate therefore requires calculating the capital costs and maintenance costs of the components, the gross annual energy production, the costs and losses from power balancing, the electrical losses of the converters and cables, and the hydrogen production from the electrolyser. The following sections describe these aspects of the LCOH calculation in more detail.

7.3.1 Cost calculation

The main components considered in the cost calculation include the wind turbine, electrolyser, converters, energy storage, and hydrogen pipeline. Since standalone wind turbine and electrolyser systems are not yet commercially available, the cost calculation is based on the predicted cost of these components in 2030, following the procedure used in [203]. The annual operation and maintenance cost is assumed to be 4% of the initial capital cost, based on [64, 203].

Wind turbine

A number of projections for wind turbine CAPEX in 2030 have been made in the literature, with [222] providing a good overview. The cost for offshore wind turbines in 2030,

including project planning, turbine, foundation, and installation, but excluding the grid connection costs is 2 M€$_{2020}$/MW [222], which is equivalent to 2.42 M€$_{2024}$/MW when adjusted for inflation [80].

Electrolyser

The cost of electrolysers is changing rapidly, and recent years have been marked by a significant increase. This evolution of electrolyser costs can be seen in recent estimates put forward by several sources [15, 223, 224]. A 2020 report by IRENA [223] estimates PEM electrolyser costs to be 700 $\$_{2020}$/kW to 1400 $\$_{2020}$/kW. A 2022 report by the Oxford Insitute for Energy Studies estimates the current PEM electrolyser price at 1400 $\$_{2022}$/kW to 2100 $\$_{2022}$/kW [224], whereas a 2023 report by the IEA suggests a PEM electrolyser price of 2000 $\$_{2023}$/kW [15].

Over the longer term, the cost of electrolysers is predicted to fall as components scale up, stack technology improves, and production expands [225]. The 2030 cost estimate of the bottom-up study [225] can be approximated using the equation [203]

$$C_{el} = 0.893 \cdot P_{EL}^{0.874} \tag{7.2}$$

where C_{el} is the electrolyser capital cost in M€$_{2021}$, and P_{EL} is the electrolyser rated power in MW. This is multiplied by an inflation factor of 1.177 [80] to obtain the M€$_{2024}$ value.

Electrolysers have a shorter expected operating life than wind turbines. The electrolyser stack requires replacement roughly every 10 years. The approach in [203] was taken here, which assumes that the stack replacement cost is half of the total electrolyser cost.

Converters

The converter cost was estimated based on the approach used in Chapter 3. From [64], the back-to-back converter cost is 6.6% of the total cost, resulting in

$$C_{conv} = 0.16 \cdot P_{conv} \tag{7.3}$$

where C_{conv} is the converter cost in M€$_{2024}$/MW, and P_{conv} is the converter rated power in MW. This is similar to the 2003 converter cost estimate from [59], which, adjusted for inflation and exchange rate, gives a converter cost estimate of 0.169 M€$_{2024}$/MW.

A single converter bridge is assumed to cost half of the back-to-back converter. The cost of DC/DC converters is assumed to be similar cost to that of back-to-back converters by 2030, which is also the base case assumption in Chapter 3.

Energy storage

The results from Chapter 6 showed that supercapacitor energy storage is one of the methods that can be used to balance the power between the wind turbine and electrolyser. The estimated the cost of the supercapacitor was $6.8M based on a report predicting the cost in 2025 using 2018 prices. Adjusted for inflation and exchange rate, this results in an energy storage cost of 7 M€$_{2024}$.

The other power balancing methodologies do not have any capital costs associated with them, but will influence the system losses instead, which are discussed in the next sections. If electrolyser technology develops to be able to reach 0.3 pu/s ramp rates by 2030, the energy storage costs and losses associated with power balancing can be avoided.

Pipeline

The cost of the hydrogen pipeline depends on the size and length of pipe required. A 2021 study by [226] estimated the cost to be 28,170 €/cm/km. Adjusted for inflation, this is equivalent to 33,179 €$_{2024}$/cm/km.

The standalone wind turbine is assumed to have a 2 km individual pipeline that connects to a larger, farm-wide pipeline with a length of 100 km. The diameter of these two pipes can be calculated based on the expected hydrogen flow rate. A study by [227] provides the relationship between various hydrogen flow rates and pipe diameter size. An upper limit of the hydrogen flow rate of can be estimated using the wind turbine rated power and higher heating value (HHV) of hydrogen, which corresponds to a 100% efficient conversion of electricity to hydrogen.

The upper limit of hydrogen production per wind turbine per second can be calculated using

$$\dot{m}_{H_2} = \frac{P_{WT}}{HHV} \tag{7.4}$$

This results in a theoretical maximum hydrogen mass flow rate of 0.106 kg/s per wind turbine. Assuming an inlet pressure of 5 MPa, the resulting diameter for the individual pipeline was calculated to be 7.5 cm, based on [227]. Assuming a 1000 MW wind farm

with 67 wind turbines, the diameter of the farm-wide pipeline was calculated to be 39 cm [227].

Levelised capital costs

The capital costs described in the previous sections are used in the LCOH calculation, but their contributions to the overall LCOH cannot be compared directly. To do this, the costs need to be discounted and levelised over the wind turbine lifetime.

One issue with this calculation is that the hydrogen production is not equal for the different drivetrains and power balancing methods. This affects the denominator in the LCOH calculation, and can skew the comparison of each of the cost inputs.

To avoid this issue, the capital costs were levelised using the generator power production before losses, as well as the HHV of hydrogen, which is the energy contained within the hydrogen. Together, these represent the theoretical maximum hydrogen production a 100% efficient system can produce. For example, the contribution of the wind turbine capital cost to the LCOH, $LCOH_{C_{WT}}$, can be calculated using

$$LCOH_{C_{WT}} = \frac{\sum_{t=0}^{L_T} \frac{C_{WT,t}}{(1+Dr)^t}}{\sum_{t=0}^{L_T} \frac{P_{gen,t}}{HHV(1+Dr)^t}} \tag{7.5}$$

where $P_{gen,t}$ is the wind turbine generator power output before losses, and $C_{WT,t}$ is the wind turbine capital cost in year t.

Levelised cost of losses

Similar to the levelised cost of the components, the cost of losses is not an explicit part of the LCOH calculation. It is instead accounted for in the total hydrogen production. However, the cost of losses provides a useful measure to compare the impact of efficiency on the LCOH value for the various drivetrains.

The traditional method to calculate the cost of losses is to assign a monetary value to the cost of energy. However, since there is currently no well established market price for hydrogen, an alternative calculation method is to compare the LCOH with losses to the LCOH for a 100% efficient system. This is given by

$$C_{loss} = \text{LCOH} - \text{LCOH}_{\text{ideal}} \tag{7.6}$$

where $\mathrm{LCOH}_{\mathrm{ideal}}$ is the ideal levelised cost of hydrogen for a 100% efficient system.

Since the levelised cost of losses and the levelised capital costs are used for comparison only and not directly a part of the LCOH calculation, their sum total will be marginally different from the actual LCOH, typically by a few percent. Both of these factors were therefore scaled so that their total matches the actual LCOH.

7.3.2 Annual energy production

The annual energy production of the generator is calculated based on the Weibull distribution of the wind speed and the wind turbine power curve. The annual hours for each wind speed can be calculated using Equation (3.17) from Chapter 3, reproduced below

$$T(v) = 8760 \cdot \frac{k}{c}\left(\frac{v}{c}\right)^{k-1} \cdot \exp\left[-\left(\frac{v}{c}\right)^{k}\right] \tag{7.7}$$

As in Chapter 3, the shape and scale parameters, k and c were assumed to be a typical value of 2.3 and 11, respectively. The Weibull distribution is illustrated in Figure 7.2a.

The generator energy output will be slightly higher than the wind turbine power curve, taken from Chapter 3. This is because the wind turbine power curve is measured at the turbine output, where it has already taken into account losses in the drivetrain. This is undesirable for a drivetrain comparison. Therefore, the losses of the conventional drivetrain were added to the wind turbine power curve to create the generator power curve, shown in Figure 7.2b.

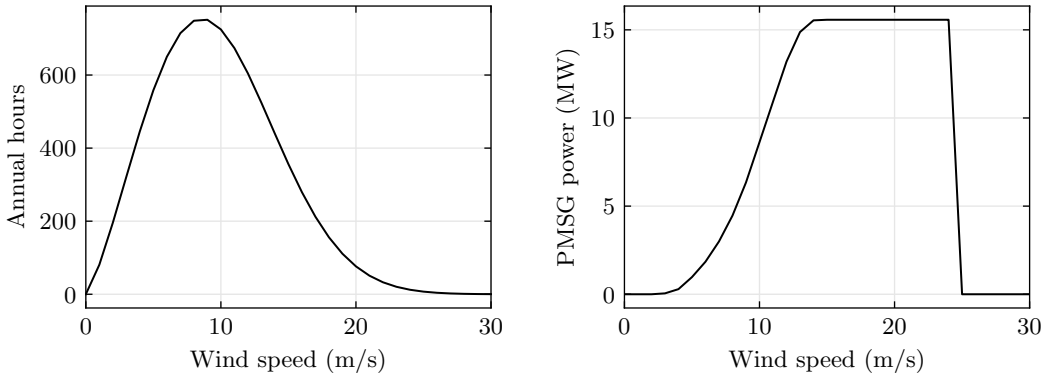

(a) Wind speed distribution **(b)** Generator power

Figure 7.2: Annual generator energy production inputs

If power balancing is required between the wind turbine and electrolyser due to their

differing dynamics, the annual energy production is reduced when the wind turbine operates at a suboptimal operating point. In Chapter 6, it was calculated that using rotor inertia for power balancing reduces the energy production by 11%, whereas using a non-zero pitch reduces the energy production by 25% without speed increase or a 10% energy reduction with speed increase.

7.3.3 Efficiency calculation

Back-to-back converter

The back-to-back converter efficiency is based on measurements of a Siemens Gamesa D7 wind turbine. The efficiency curves were approximated using no-load losses and full-load losses. The converter losses can then be calculated for any operating point using

$$P_{loss,conv} = P_{NLL} \cdot P_{conv} + P_{FLL} \cdot P_1 \tag{7.8}$$

where P_{NLL} and P_{FLL} are the no-load and full-load losses in p.u., P_{conv} is the converter rated power, and P_1 is the converter input power.

The approximated no-load losses were 0.75% and the full-load losses were 2.25%. The resulting losses at each operating point are shown in Figure 7.3. The losses for a single rectification stage, such as the one used in the direct electrolyser connection, were assumed to be half of the back-to-back converter losses.

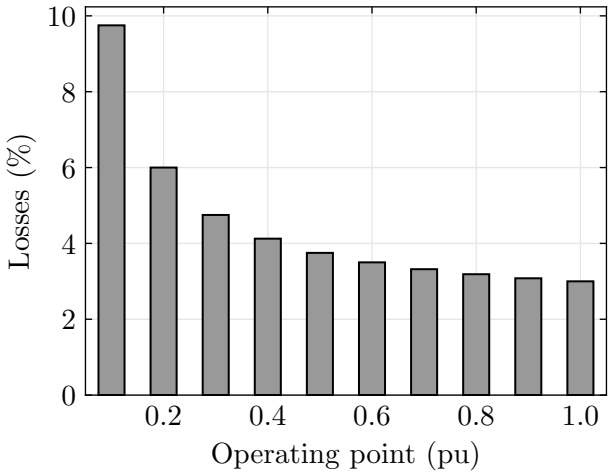

Figure 7.3: Back-to-back converter approximated losses by operating point

Tower cables

The tower cables data is calculated based on the Electric Cable Handbook [228], and IEC standard 60364-5-52 [229]. For DC cables, the DC resistance at 20°C is calculated using the standard equation

$$R_{dc,20} = \frac{\rho_c L_{cab}}{A_c} \tag{7.9}$$

where ρ_c is the electrical resistivity of the conductor material, L_{cab} is the cable length, and A_c is the conductor cross-sectional area. This value is adjusted to the 90°C operating temperature using the equation

$$R_{dc,90} = R_{dc,20}\big(1 + \alpha_c(90 - 20)\big) \tag{7.10}$$

where α_c is the temperature coefficient of resistance of the conductor material. The values for ρ_c and α_c were taken from the handbook, given in Table 7.1.

Material	ρ_c ($\mu\Omega$cm)	α_c ($\Omega/°C$)
Copper	1.724	0.0039
Aluminium	2.803	0.004

Table 7.1: Cable conductor material properties [228]

The calculation for the AC cable resistance is not as straightforward due to nonlinear effects such as the skin effect and proximity effect [228]. The AC resistance values are therefore taken directly from tables with electrical characteristics for low voltage XLPE distribution cables provided in [228].

The cable ampacity was determined using the tables provided in the IEC standard [229]. All cables are assumed to be single core, with two cables per circuit for the DC configuration, and three cables per circuit for the AC system. The cable installation is assumed to be in air, with adjacent cables touching. This corresponds to installation method F in the standard. Ampacity values were extracted from Table B.52.12 and B.52.13 for the copper and aluminium cables, respectively.

If multiple cable circuits were required, their individual ampacity was derated using the factors in Table 7.2, assuming an arrangement where multiple circuits would be bunched in air or on a surface. The new cable ampacity is calculated iteratively, since the derating may require more circuits, leading to further derating. The total cable resistance is also divided by the number of cable circuits.

Circuits	Derating factor	Circuits	Derating factor
1	1.00	7	0.54
2	0.80	8	0.52
3	0.70	9	0.50
4	0.65	12	0.45
5	0.60	16	0.41
6	0.57	20	0.38

Table 7.2: Derating factors by number of circuits, taken from Table B52,17 of [229]

For the DC configurations, the DC current through each cable circuit is calculated as

$$I_{cab} = \frac{P_c}{V_{cab} N_{cab}} \tag{7.11}$$

where P_c is the power delivered through the cable, N_{cab} is the number of parallel cable circuits, and V_{cab} is the pole-to-pole DC voltage of the cables.

Since there are two cables per circuit, the losses can be calculated using

$$P_{loss,cab} = 2 I_{cab}^2 R_{cab} N_{cab} \tag{7.12}$$

For the AC configuration, the tower cables are considered to be part of a 3-phase AC circuit. Hence, the cable current is calculated using

$$I_{cab} = \frac{P_c}{\sqrt{3} V_{cab} N_{cab}} \tag{7.13}$$

Since there are three cables per circuit, the losses are calculated using

$$P_{loss,cab} = 3 I_{cab}^2 R_{cab} N_{cab} \tag{7.14}$$

Transformers

The losses of the 50 Hz transformers used in the conventional connection were calculated using the methodology from Chapter 3. It is estimated using an efficiency curve based on no-load and full-load losses, similar to the back-to-back converter calculations. The no-load losses are assumed to be 0.055% and the full-load losses are 0.3% [87], resulting in the loss distribution shown in Figure 7.4.

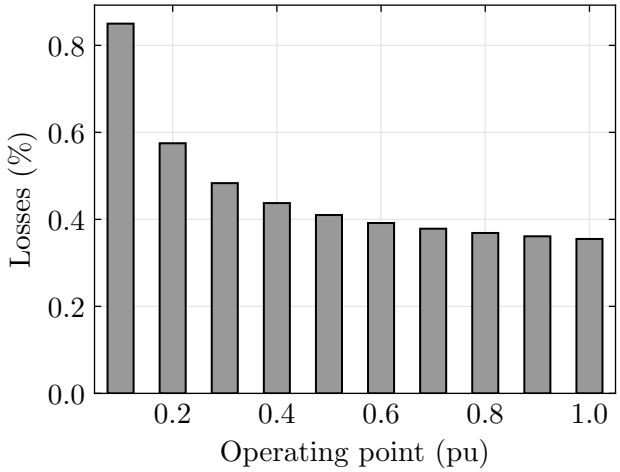

Figure 7.4: AC transformer approximated losses by operating point

DC/DC converters

The DC/DC converter efficiency was based on the results from Chapter 4. For a 15 MW, 1.2 kV/80 kV SAB1 DC/DC converter, the optimal operating frequency was calculated to be 2.5 kHz. At this frequency, the converter loss distribution is shown in Figure 7.5.

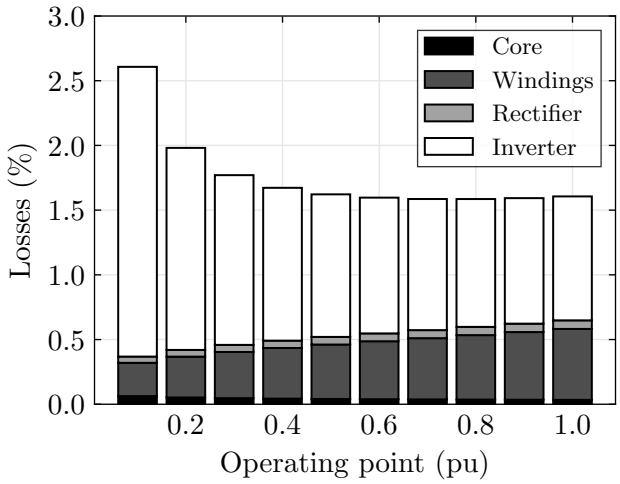

Figure 7.5: DC/DC converter losses at 2.5 kHz by operating point

7.3.4 Hydrogen production

The annual hydrogen production can be calculated using the power remaining after losses, the electrolyser stack loading, and the specific energy consumption curve of the electrolyser cells. The electrolyser design is taken directly from Chapter 6.

The electrolyser is assumed to consist of three stacks, each with a 5 MW rating and a minimum loading of 40%. To achieve the highest efficiency, the stacks are considered to share the input power evenly, as shown in Figure 6.1. The specific energy consumption of the stack was calculated using the procedure set out in Section 5.5.1, resulting in the efficiency curves shown in Figure 6.10b.

The electrolyser stack efficiency is assumed to decrease as it ages. The end-of-life voltage is assumed to be 10% higher compared to the beginning-of-life. Since only the cell current is used for hydrogen production, this means the annual hydrogen production decreases over the electrolyser stack's lifetime. For a stack lifetime of 10 years, this corresponds to an increase in the stack voltage of 1% per year.

7.4. Results

7.4.1 Conventional AC drivetrain

The conventional AC drivetrain has the least technological risk as it can use existing wind turbine components, with the developed control system from Chapter 6. The LCOH was calculated for several possible power balancing scenarios. These include using a supercapacitor energy storage system (ESS), increasing the rotor speed and using the additional rotor inertia, operating with a non-zero pitch while maintaining the original rotor speed (NZpitch1), or operating with a non-zero pitch with increased rotor speed (NZpitch2). The LCOH was also calculated for the future scenario where electrolyser dynamics are fast enough to avoid any need for power balancing.

The results for the conventional AC drivetrain are shown in Figure 7.6. It can be seen that the future scenario has the lowest LCOH, at 3.24 €/kg. The most cost-effective power balancing scenarios are the rotor inertia and NZpitch2 scenarios, which both increase the cost of hydrogen to approximately 3.58 €/kg. The additional costs are a result of the reduction in produced hydrogen due to the suboptimal power set points. Both of these scenarios require the wind turbine to rotate significantly faster, however, which may have implications for the wind turbine reliability.

The energy storage system is the most cost-effective option if rotor speed-up is avoided, with an LCOH of 3.75 €/kg. The hydrogen production for this scenario is practically identical to the future scenario since the balancing process has negligible losses. Although the supercapacitor and associated converter are not perfectly efficient, they do not need to operate continuously and when they do, the required power is often low. The NZpitch1 scenario is the least cost-effective. The 25% power loss incurred due to the non-zero pitch and suboptimal speed results in the highest LCOH of 4.16 €/kg.

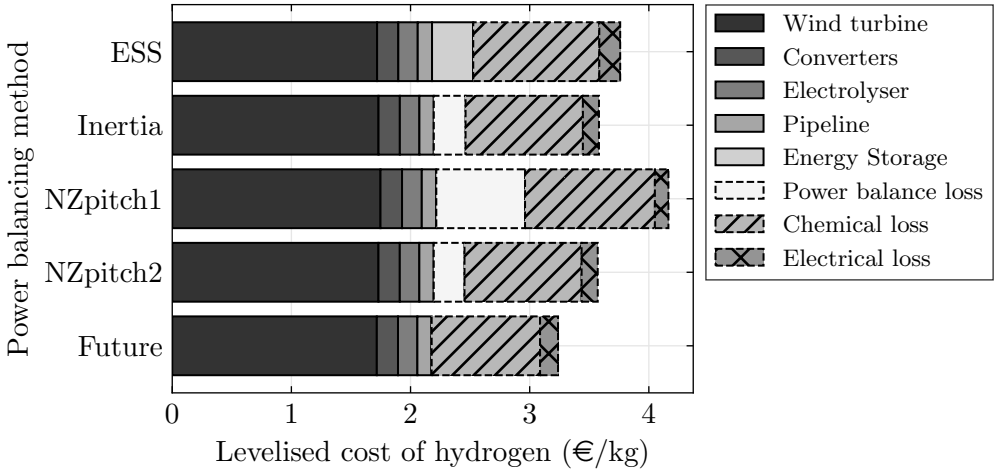

Figure 7.6: Levelised cost of hydrogen by power balancing scenario for the conventional AC drivetrain

7.4.2 Direct DC drivetrain

The direct DC drivetrain has the fewest required components and can use the existing wind turbine generator and rectifier. However, with only a single converter, the controllability of the system is more limited. The converter is used to control the power flow and uses a classical cascaded control. The outer control loop uses the measured rotor speed to set the q-axis current reference, based on the MPPT and ramp-rate limitations. The inner control loop is identical to the classical inner current control. The control structure is shown in Figure 7.7. Despite the limited controllability, all power balancing strategies can still be used for this configuration, since they either alter the MPPT, pitch control, or introduce an additional converter in the case of ESS.

Since the only converter is being used to control the power flow, the DC link and electrolyser voltage are uncontrolled. This means that the DC voltage will be variable, rather than held constant, and its magnitude will depend entirely on the electrolyser

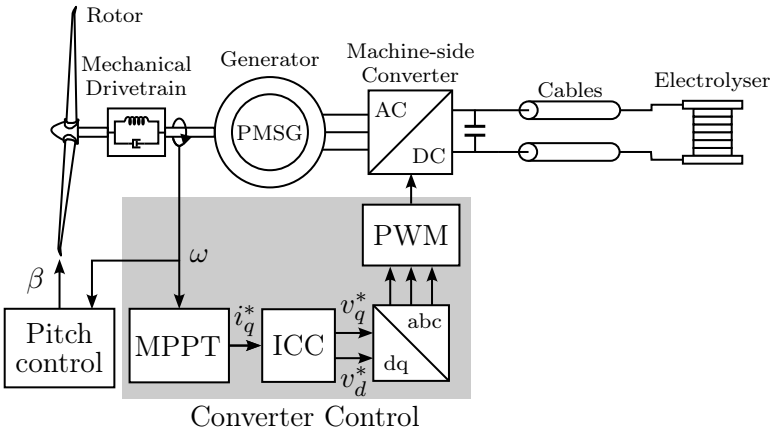

Figure 7.7: Constrol structure for a direct DC drivetrain

polarisation characteristics. Since the AC/DC converter draws on the DC link voltage to generate the PMSG stator voltages, the operation of the PMSG could be compromised if the voltage drops too low.

If the electrolyser nominal voltage is similar to the DC link design voltage of 1200 V, the variable DC link voltage is unlikely to pose any issues. Figure 7.8a shows the DC link voltage when it is entirely dependent on the electrolyser polarisation curve, described in Figure 6.10. It can be seen that the DC link voltage at the minimum operating point is less than 10% below the nominal voltage.

The corresponding modulation index is shown in Figure 7.8b. A modulation index of 1.0 represents the upper limit of the converter's capability (when neglecting overmodulation). The modulation index required for the variable DC link voltage is close to the one required in the case of a constant DC link voltage, and well within the converter's capability. The main drawback of the uncontrolled DC link voltage is the relatively high nominal voltage requirement for the electrolyser, which are typically rated well below 1 kV. This will severely limit the number of off-the-shelf electrolysers that are able to operate in this configuration.

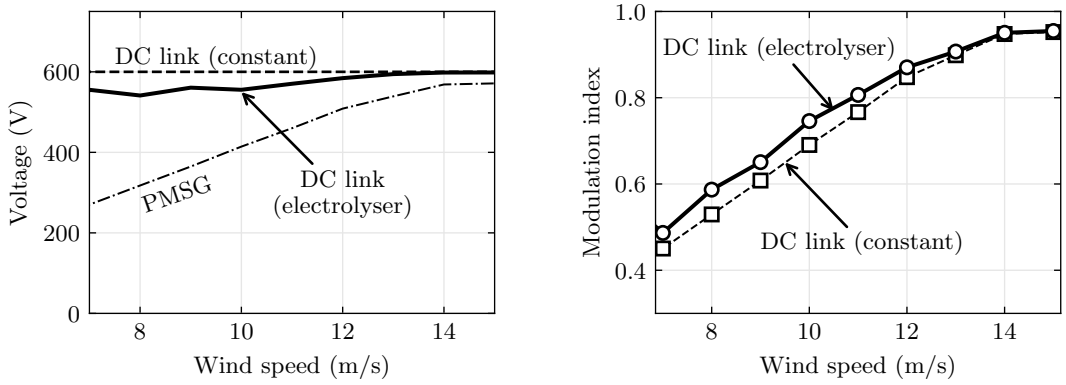

(a) Voltages (pole-to-neutral)

(b) Modulation indices

Figure 7.8: Comparison of DC link voltages and converter modulation indices for a controlled and uncontrolled DC link voltage

The low voltage of the DC link also causes issues for the tower cables. Since the cables have to transport multi-megawatt levels of power, the currents at such a low voltage will exceed the cable ampacity. The largest tower cables normally have a cross-section of 400 mm^2. To be able to handle 15 MW at a voltage of 1.2 kV, a total of 36 cable circuits are required. This is an unrealistic number for the tower to accommodate, especially given the fact that the cable bundle is put under torsion as the nacelle rotates to face the wind.

A solution to this problem is to move the electrolyser inside the wind turbine nacelle, instead of having it located at the wind turbine platform. This configuration would likely require a custom-designed, highly compact electrolyser to be able to achieve this.

In addition, the construction of the hydrogen pipeline will become much more challenging. The pipeline will need a rotating, leak-proof connection to connect the rotating nacelle and static tower sections of the pipeline. At the same time, it will need to be able to withstand the same torsional forces that the electrical cables would normally be subjected to.

If these technological barriers can be overcome, this configuration can result in a reduction in the LCOH, as shown in Figure 7.9. The converter costs and electrical losses are significantly lower compared to the AC configuration. For the future scenario without power balancing requirements, the calculated LCOH was 2.86 €/kg. The LCOH for the ESS, inertia, NZpitch1, and NZpitch2 scenarios was found to be 3.36 €/kg, 3.18 €/kg, 3.69 €/kg, and 3.17 €/kg, respectively. This corresponds to a 10.5% to 11.5% reduction in the cost of hydrogen compared to the AC configuration.

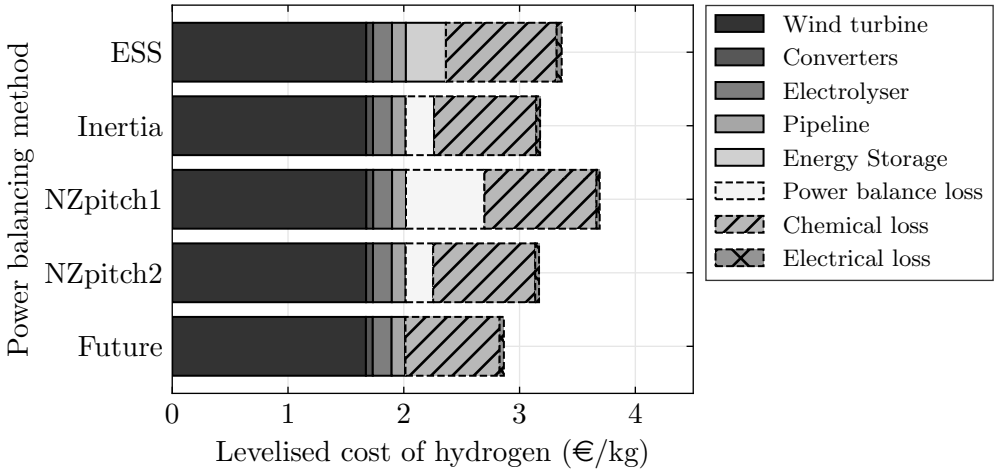

Figure 7.9: Levelised cost of hydrogen by power balancing method for the Direct DC drivetrain

7.4.3 DC drivetrain with one DC/DC converter

The DC drivetrain with one DC/DC converter allows for simultaneous control of the wind turbine power and the DC link voltage, while having a lower number of converters than the AC drivetrain. This also means that the generator and electrolyser voltages no longer need to match. The control structure for this drivetrain is illustrated in Figure 7.10. Note that either converter can be set to achieve each control objective.

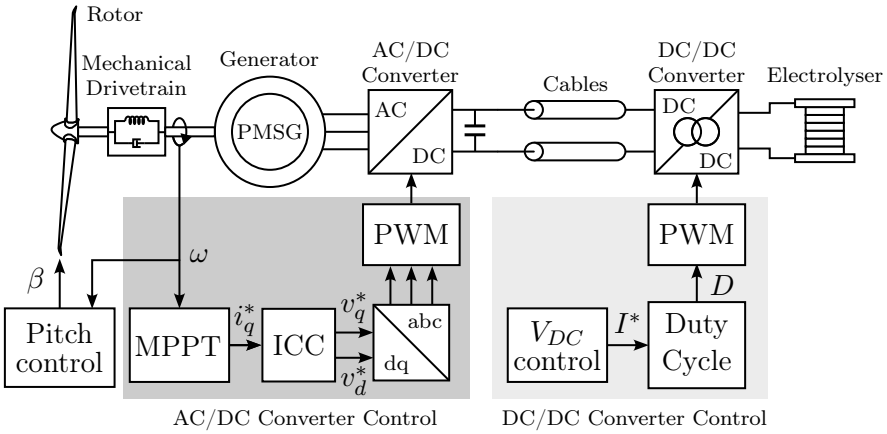

Figure 7.10: Control structure for a DC drivetrain with one DC/DC converter

There are two potential locations for the DC/DC converter: inside the nacelle, or at the wind turbine platform. If the converter is located in the nacelle, the voltage of the tower

cables will be equal to the electrolyser voltage. If it is located at the tower platform, the cable voltage will be determined by the generator voltage instead. To reduce the number of cable circuits required, it is advantageous to have a cable voltage that is as high as possible.

Practically all commercially available electrolysers have operating voltages below 1 kV, whereas some commercial wind turbines are able to operate at a higher voltage. For example, the GE Haliade-X 14 MW generator is rated at 3.3 kV [230], and the IEA's 15 MW offshore reference wind turbine uses a 4.77 kV PMSG [107]. The DC/DC converter was therefore assumed to be located at the tower platform. Even so, a cable voltage of 3.3 kV still results in an impractical 10 cable circuits being required to handle the power. To reduce the number of cable circuits to two, a generator voltage of 11 kV is required.

If the generator can be redesigned to operate at a voltage of 11 kV, this configuration achieves a small reduction in the LCOH compared to the conventional AC drivetrain. Figure 7.11 shows the calculated LCOH for each of the scenarios. The LCOH for the future scenario was calculated to be 3.08 €/kg. The LCOH for the ESS, inertia, NZpitch1, and NZpitch2 scenarios was found to be 3.59 €/kg, 3.42 €/kg, 3.97 €/kg, and 3.41 €/kg, respectively. This corresponds to a reduction in the cost of hydrogen of approximately 4.5% to 4.8% compared to the AC configuration.

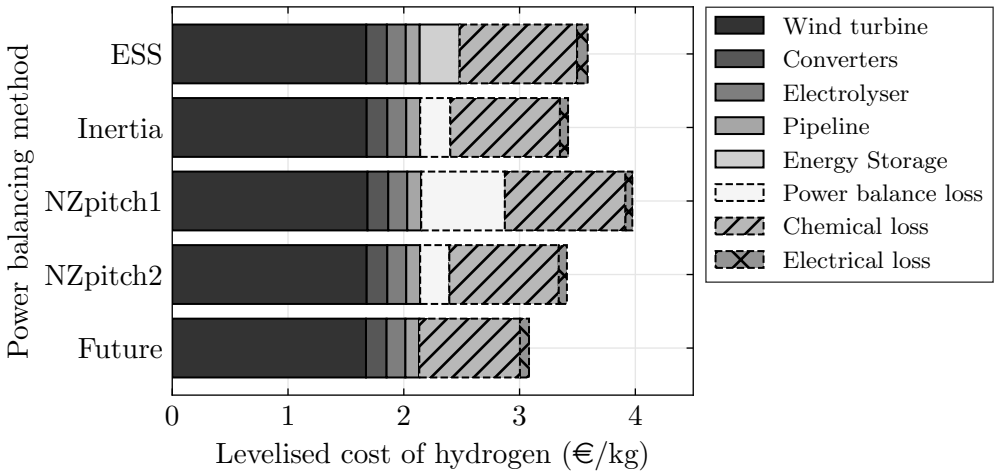

Figure 7.11: Levelised cost of hydrogen by power balancing method for the DC drivetrain with one DC/DC converter

7.4.4 DC drivetrain with two DC/DC converters

The DC drivetrain with two DC/DC converters is most similar to the conventional AC drivetrain. The DC/DC converters take on the role of the transformers to change the voltage level, with the first DC/DC converter stepping up the voltage to 80 kV for the tower cables, and the second DC/DC converter stepping down the voltage to around 800 V for the electrolyser.

The high-level control structure for the DC drivetrain with two DC/DC converters is similar to that of the conventional AC drivetrain, as shown in Figure 7.12. The converters have the same control objectives, namely the machine-side converter controls the DC link voltage, the line-side converter controls the power flow, and the electrolyser-side converter controls the electrolyser voltage. However, since it is a fully DC system, the control structure can be simplified since grid-forming control and power synchronisation loops are no longer required.

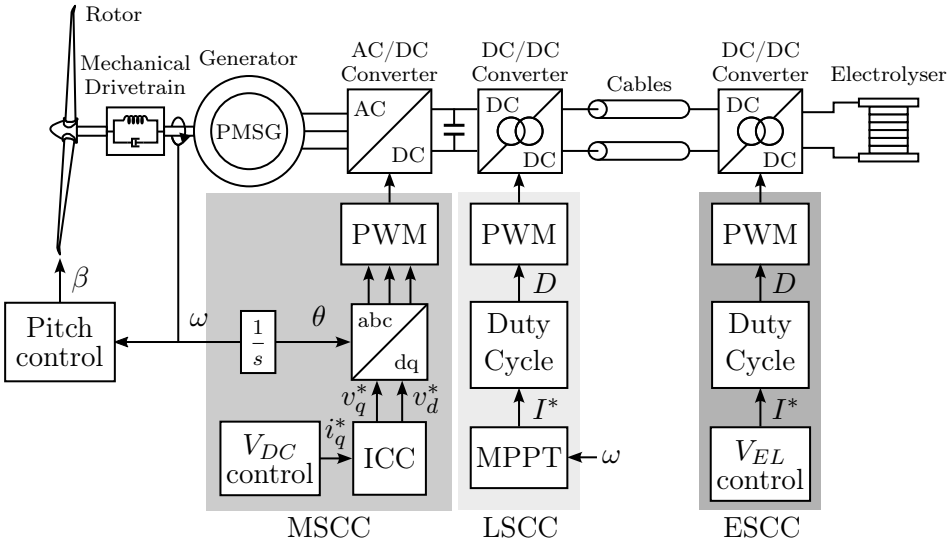

Figure 7.12: Control structure for a DC drivetrain with two DC/DC converters

Despite the marginal increase in efficiency, the cost of the two DC/DC converters results in a higher calculated LCOH for this configuration, as shown in Figure 7.13. The LCOH for the ESS, inertia, NZpitch1, NZpitch2, and future scenarios was found to be 3.81 €/kg, 3.66 €/kg, 4.26 €/kg, 3.65 €/kg, and 3.30 €/kg, respectively. This corresponds to an increase in the cost of hydrogen of 1.4% to 2.2% compared to the AC configuration.

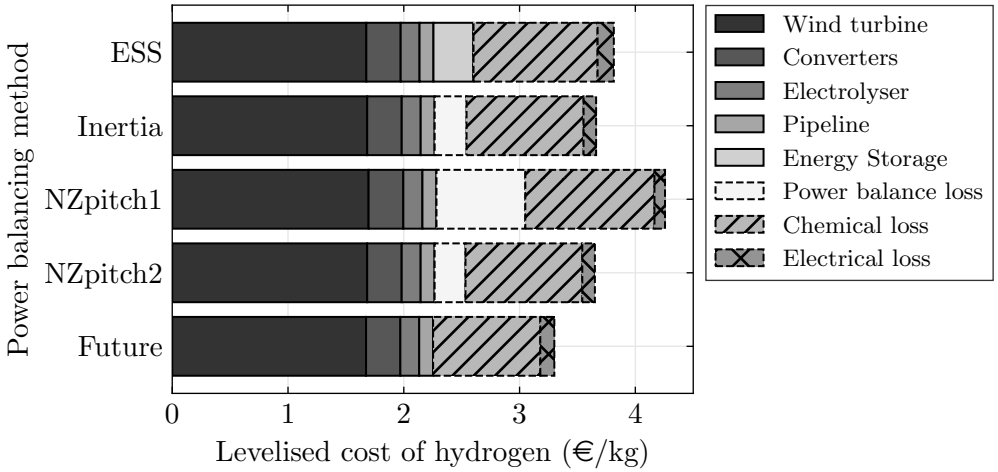

Figure 7.13: Levelised cost of hydrogen by power balancing method for the DC drivetrain with two DC/DC converters

7.5. Conclusions

This chapter investigated the LCOH of the power balancing strategies proposed in Chapter 6, and the potential for three alternative DC-based wind turbine drivetrains to improve the system cost-effectiveness. The alternative drivetrains considered were a direct DC connection with only a single AC/DC converter, a DC connection with one additional DC/DC converter, and a DC connection with two additional DC/DC converters. The control strategy and practical challenges for each of the drivetrains was also assessed.

The results of the LCOH calculation for the conventional AC drivetrain showed that the most cost-effective power balancing strategies were inertia and non-zero pitch control with speed-up, giving an LCOH of 3.58 €/kg. However, the practical feasibility of these strategies is dependent on the wind turbine's ability to operate at 20% higher speed than normal. The ESS power balancing method was found to be the most cost-effective option if the rotor speed increase is avoided, with an LCOH of 3.75 €/kg. The non-zero pitch control without speed-up performed the worst with an LCOH of 4.16 €/kg. Without power balancing, an LCOH of 3.24 €/kg can be achieved for the conventional AC drivetrain.

The direct DC drivetrain requires the electrolyser to operate at the design voltage of the DC link, which is typically 1.2 kV, to prevent overmodulation in the AC/DC converter. In addition, the electrolyser must be able to fit in the nacelle to avoid requiring an

unrealistic number of tower cable circuits. As a result, it is unlikely that an off-the-shelf commercial electrolyser can be used. If these challenges can be overcome, this configuration has the potential to reduce the LCOH by 10.5% to 11.5%.

The DC connection with one additional DC/DC converter allows the electrolyser and generator voltage to be decoupled, which means that the generator voltage now determines the tower cable voltage. A generator voltage of 11 kV is required to limit the number of tower cable circuits to a realistic number. If the generator can be redesigned to operate at this voltage, this configuration results in an LCOH reduction of 4.5% to 4.8%.

The drivetrain with two DC/DC converters does not have the same practical challenges, as the cable voltage can be 80 kV. However, the calculated LCOH for this configuration is higher than the conventional AC drivetrain.

Given the practical challenges of the first two DC drivetrains and the lack of improvement of the third DC drivetrain, the conventional AC drivetrain with ESS is the best candidate for offshore wind electrolysis for the foreseeable future.

Chapter 8

Conclusions

Cost continues to be one of the main barriers to the rapid expansion of offshore wind and green hydrogen production. The use of DC collection systems in offshore wind farms has the potential make the production of electricity more cost-effective, primarily by reducing the costs of the offshore platform. However, a multitude of such all-DC wind farm designs has been proposed, none of which have reached commercialisation.

The DC/DC converter is a key enabling technology for all-DC wind farms and its cost, losses, and reliability are all important drivers for the overall wind farm cost-effectiveness. Similar to the DC wind farm as a whole, a large number of DC/DC converter topologies have been proposed in the literature, and no consensus has been reached yet about which one is the most promising for this application.

Green hydrogen production can be made more cost-effective by directly connecting offshore wind turbines with electrolysers located at the wind turbine. This would reduce the capital costs by removing the need for an offshore substation, export cables, or collector cables. However, there is no research on how such an off-grid system can be controlled, especially given the difference in the dynamic response of the wind turbine and electrolyser. Furthermore, there is a lack of research on how the wind turbine drivetrain can be optimised for hydrogen production.

This thesis has investigated the most cost-effective all-DC wind farm designs, the optimisation and comparison of several DC/DC converter designs, as well as how the power can be balanced in off-grid wind turbine-electrolyser systems, and how the wind turbine drivetrain influences the cost of hydrogen. The following section sets out the findings of these investigations.

8.1. Summary of findings

Part I

A systematic review was performed of the literature that formally assesses the cost, losses or reliability of DC wind farm configurations. Series and series-parallel DC designs without offshore platform performed well in terms of costs, but were found to have challenges in operation and reliability that limit the short-term opportunity for commercialisation. The standard DC parallel topology was found to have the lowest technological risk, but the mean cost reported in the literature is similar to that of AC topologies. The dispersed all-MVDC parallel topology has the potential to reduce costs, but little data is available on its losses and reliability.

Based on the results of the systematic literature review, a comprehensive LCOE analysis of two AC and two all-DC wind farm designs was performed, including sensitivity studies on wind farm size, distance from shore, collector voltage, and component costs. The considered wind farm configurations included the all-AC topology, the AC/HVDC topology, the standard MVDC/HVDC topology, and the dispersed all-MVDC topology.

The results showed that the standard MVDC/HVDC wind farm can be more cost-effective than equivalent AC/HVDC wind farms for large wind farms located far from shore, provided the DC/DC converter cost is less than 90% of the cost of an equivalent MMC, and the DC platform provides a 25% cost reduction. Alternatively, if cost reductions of 30% can be achieved for the DC platform, then the DC/DC converter can be the same cost as an equivalent MMC.

For all-MVDC wind farms without HVDC conversion stage to have the lowest LCOE, the collector voltage must be increased, preferably to ±100 kV or above. The all-MVDC configuration can also become cost-effective if a reduction of more than 50% in the cable installation cost can be achieved, for example, through the simultaneous burial of multiple cables.

A key enabling technology for DC collection systems in offshore wind farms is a suitable wind turbine DC/DC converter. An optimisation and comparison study of four DC/DC converter topologies was carried out, including 1-phase, 3-phase, unidirectional, and bidirectional converters. The converters were compared in terms of their reliability, volume, weight and losses at switching frequencies ranging from 500 Hz to 5 kHz. The MFT for each converter was designed using multi-objective optimisation, and the overall converter volume calculation takes into account the insulation requirements and physical

configuration of the components.

The results showed that if only unidirectional operation is required, the 1-phase single active bridge is the preferred option due to its high reliability, small size and low losses with an optimal operating frequency of up to 2.5 kHz. For bidirectional systems, the 1-phase and 3-phase dual active bridge topologies have a similar efficiency and optimal operating frequency of 1 kHz. Despite its higher volume, the 3-phase version is the preferred option due to its higher reliability and lower device stresses, provided there is enough available space.

Part II

A literature review on electrolysis was performed, with a focus on electrolysers for green hydrogen production. The results showed that PEM electrolysis was most likely to be suited to connection with variable renewable energy, due to its relatively high current density, efficiency, and gas purity, as well as good partial load operation and a rapid dynamic response time.

The steady-state and dynamic performance of the electrolyser cell were reviewed. It was found that the balance of the plant was the main limiting factor for the overall electrolyser response, with current commercial electrolyser power ramp-rates reaching up to 10%/s. Several methods to connect electrolysers with offshore wind turbines were presented. The configuration with the most potential to reduce the cost of hydrogen was co-locating electrolysers and offshore wind without a grid connection.

However, without a grid connection, a new control paradigm is required for the electrolyser to follow the variable power supplied by the wind turbine. The power ramp rate limitations of commercial electrolysers result in a mismatch between the wind turbine and electrolyser power, leading to frequent shutdown and potentially unstable operation.

A new control system was developed for this off-grid operation with three mechanisms to dynamically balance the power, including energy storage, rotor inertia, and enhanced pitch control. The results showed that a $6.8M supercapacitor is required with a power rating and capacity of approximately 6.7 MW and 8.5 kWh to enable the system to operate through 99% of the annual wind variation. If the electrolyser ramp rates can be doubled, the same operating hours can be achieved using only control-based power balancing methods at the cost of a marginal reduction in energy production. If commercial electrolyser ramp rates can be tripled, the system is able to operate without the need for any power balancing.

The LCOH was calculated for each of the power balancing methods, as well as for the future scenario in which power balancing is no longer required. The results showed that the most cost-effective power balancing strategies are inertia and enhanced pitch control with speed-up, giving an LCOH of 3.58 €/kg. However, both of these require the wind turbine to operate at a higher speed than normal, which may not be feasible. Out of the remaining strategies that do not affect rotor speed, the ESS was found to be more cost-effective, at 3.75 €/kg, compared to enhanced pitch control without speed-up, at 4.16 €/kg. Without power balancing, an LCOH of 3.24 €/kg can be achieved.

The conventional AC connection of the wind turbine with the co-located electrolyser has a lot of conversion stages, which may lead to a reduced system efficiency and lower the LCOH, compared to a more direct DC connection. A calculation and comparison of the LCOH for four different drivetrain designs was carried out, including the conventional AC connection and three DC-based designs.

A direct DC connection of the electrolyser using a single rectification stage resulted in an LCOH reduction of up to 11.5%. However, this configuration has several practical challenges, including the need for an electrolyser operating voltage of 1.2 kV, and a highly compact electrolyser design or unrealistic number of cables. Adding one DC/DC converter to this drivetrain allows the electrolyser voltage to be decoupled, and still results in an LCOH reduction of up to 4.8%. However, this is dependent on a redesign of the wind turbine generator to operate at voltages of 11 kV or higher. The drivetrain with two DC/DC converters does not have the same practical challenges, but also did not provide any LCOH reduction. Therefore, the conventional AC drivetrain is the best candidate for offshore wind electrolysis for the foreseeable future.

8.2. Future work

The research and results presented in this thesis have given rise to several potential areas for future investigation, listed below.

- The cost-benefit comparison of AC and DC offshore wind farm configurations showed that the platform cost reduction is an important sensitivity factor in making DC-based offshore wind the most cost-effective option. The impact of replacing the 50 Hz transformer with a smaller DC/DC converter on the cost of the offshore platform is still an open question. The design of the offshore platform consists of many elements beyond the transformers, such as switchgear, earthing systems, auxiliary systems and the structure, which may be impacted by changing to an

all-DC configuration.

- The next step in commercialising the standalone wind turbine with co-located electrolyser design would be to perform increasingly realistic tests of the system. This could involve using real-time simulation to verify the proposed power balancing control system, using measurements of wind speed and power output of existing offshore wind turbines, and building a prototype system with commercially available electrolysers.

- Given the importance of electrolyser dynamics on the power balancing requirements and its resulting impact on LCOH, there is a need for further research on how to improve the electrolyser ramp-up and ramp-down speeds, especially considering the wider balance of plant. Similarly, there is a lack of research investigating the impact of frequent electrolyser stopping and starting on reliability, since practically all commercial electrolysers are grid-connected. This could have implications for the LCOH of off-grid systems and is therefore worth investigating.

- In this thesis, only a single off-grid wind turbine and co-located electrolyser have been considered. One area of interest is the electrical connection of multiple off-grid wind turbines, each with their own co-located electrolyser. The difference in wind turbine operating powers due to geographic wind speed variation may be used to alleviate some of the power balancing requirements between the wind turbine and electrolyser, at the cost of additional cables.

- This research primarily focused on the main electrical components within the wind turbine. However, changing the wind turbine electrical drivetrain to be DC-based would also have implications on the connection of the auxiliary systems, which include a variety of motors controlling blade and turbine positioning, oil pumps, cooling, ventilation, controllers, communication systems and navigation lights. There is currently a lack of research investigating the location, connection, and challenges associated with a DC connection of these auxiliary systems.

References

[1] DNV, "Energy transition outlook 2023 - a global and regional forecast to 2050," DNV, Tech. Rep., 2023, [Online]. Available: dnv.com/energy-transition-outlook.

[2] NASA, "Global temperature," 2024, [Online]. Available: climate.nasa.gov/vital-signs/global-temperature. Accessed: 2024-06-26.

[3] H. Lee, K. Calvin, D. Dasgupta, G. Krinner, A. Mukherji, P. Thorne, C. Trisos, J. Romero, P. Aldunce, K. Barret *et al.*, "Climate change 2023: Synthesis report, summary for policymakers," Intergovernmental Panel on Climate Change (IPCC), Tech. Rep., 2023, [Online]. Available: ipcc.ch/report/ar6/syr/downloads/report/IPCC_AR6_SYR_SPM.pdf.

[4] International Energy Agency, "World energy outlook 2023," International Energy Agency, Tech. Rep., 2023, [Online]. Available: iea.org/reports/world-energy-outlook-2023.

[5] B. Lasse and W. A. Benjamin, "Eu energy security and the war in ukraine: From sprint to marathon," EPRS: European Parliamentary Research Service, Tech. Rep. PE 739.362, 2023, [Online]. Available: europarl.europa.eu/RegData/etudes/BRIE/2023/739362/EPRS_BRI(2023)739362_EN.pdf.

[6] M. Mier, "European electricity prices in times of multiple crises," Leibniz Institute for Economic Research at the University of Munich, Tech. Rep. ifo Working Paper No. 394, 2023, [Online]. Available: ifo.de/DocDL/wp-2023-394-mier-electricity-prices-crises.pdf.

[7] WFO, "Global offshore wind report," World Forum Offshore Wind, Tech. Rep., 2023, [Online]. Available: wfo-global.org/wp-content/uploads/2024/04/WFO-Report-2024Q1.pdf.

[8] 4C Offshore, "Global offshore wind farm database and intelligence," 2024, [Online]. Available: 4coffshore.com/windfarms. Accessed: 2024-07-02.

[9] Vestas, "V236-15MW," 2024, [Online]. Available: vestas.com/en/products/offshore/V236-15MW. Accessed: 2024-02-08.

[10] Dogger Bank Wind Farm, "Dogger bank reveals world-first in hvdc offshore platforms, slashing topside weight by 70%," 2021, [Online]. Available: doggerbank.com/press-releases/dogger-bank-reveals-world-first-in-hvdc-offshore-platforms-slashing-topside-weight-by-70/. Accessed: 2024-10-24.

[11] TenneT, "The 2 GW program," [Online]. Available: tennet.eu/about-tennet/innovations/2gw-program. Accessed: 2022-11-03.

[12] R. Williams, F. Zhao *et al.*, "Global offshore wind report 2023," Global Wind Energy Council, Tech. Rep., 2023, [Online]. Available: gwec.net/wp-content/uploads/2023/08/GWEC-Global-Offshore-Wind-Report-2023.pdf.

[13] S. van Renssen, "The hydrogen solution?" *Nature Climate Change*, vol. 10, no. 9, pp. 799–801, 2020, DOI: 10.1038/s41558-020-0891-0.

[14] A. Mayyas, M. Wei, and G. Levis, "Hydrogen as a long-term, large-scale energy storage solution when coupled with renewable energy sources or grids with dynamic electricity pricing schemes," *International Journal of Hydrogen Energy*, vol. 45, no. 33, pp. 16 311–16 325, 2020, DOI: 10.1016/j.ijhydene.2020.04.163.

[15] T. Gül, U. Remme, J. M. Bermudez-Menendez *et al.*, "Global hydrogen review 2023," International Energy Agency, Tech. Rep., 2023, [Online]. Available: iea.org/reports/global-hydrogen-review-2023.

[16] C. Gulli, B. Heid, J. Noffsinger, M. Waardenburg, and M. Wilthaner, "Global energy perspective 2023: Hydrogen outlook," 2024, [Online]. Available: mckinsey.com/industries/oil-and-gas/our-insights/global-energy-perspective-2023-hydrogen-outlook. Accessed: 2024-06-26.

[17] IRENA, "Geopolitics of the energy transformation: The hydrogen factor," International Renewable Energy Agency, Tech. Rep., 2022, [Online]. Available: www.irena.org/publications.

[18] B. Parkinson, P. Balcombe, J. Speirs, A. Hawkes, and K. Hellgardt, "Levelized cost of CO_2 mitigation from hydrogen production routes," *Energy & environmental science*, vol. 12, no. 1, pp. 19–40, 2019, DOI: 10.1039/c8ee02079e.

[19] M. Nasser, T. F. Megahed, S. Ookawara, and H. Hassan, "A review of water electrolysis–based systems for hydrogen production using hybrid/solar/wind energy systems," *Environmental Science and Pollution Research*, vol. 29, no. 58, pp. 86 994–87 018, 2022, DOI: 10.1007/s11356-022-23323-y.

[20] C. Varela, M. Mostafa, and E. Zondervan, "Modeling alkaline water electrolysis for power-to-x applications: A scheduling approach," *International journal of hydrogen energy*, vol. 46, no. 14, pp. 9303–9313, 2021, DOI: 10.1016/j.ijhydene.2020.12.111.

[21] O. S. Ibrahim, A. Singlitico, R. Proskovics, S. McDonagh, C. Desmond, and J. D. Murphy, "Dedicated large-scale floating offshore wind to hydrogen: Assessing design variables in proposed typologies," *Renewable and Sustainable Energy Reviews*, vol. 160, p. 112310, 2022, DOI: 10.1016/j.rser.2022.112310.

[22] S. Dresp, T. N. Thanh, M. Klingenhof, S. Brückner, P. Hauke, and P. Strasser, "Efficient direct seawater electrolysers using selective alkaline NiFe-LDH as OER catalyst in asymmetric electrolyte feeds," *Energy & Environmental Science*, vol. 13, no. 6, pp. 1725–1729, 2020, DOI: 10.1039/d0ee01125h.

[23] G. Abeynayake, G. Li, J. Liang, and N. A. Cutululis, "A review on MVdc collection systems for high-power offshore wind farms," in *2019 14th Conference on Industrial and Information Systems (ICIIS)*. IEEE, 2019, pp. 407–412, DOI: 10.1109/iciis47346.2019.9063352.

[24] V. Hamadi, U. Brosnan, I. Loftus, and G. Montgomery, "Offshore substation design: High-level overview of the industry best practices," *IEEE Power and Energy Magazine*, vol. 17, no. 4, pp. 67–74, 2019, DOI: 10.1109/mpe.2019.2909008.

[25] S. Hay, C. Cleary, G. McFadzean, J. McGray, and N. Kelly, "MVDC technology study – market opportunities and economic impact," TNEI, Tech. Rep., 2015, [Online]. Available at: evaluationsonline.org.uk.

[26] J. Pan, S. Bala, M. Callavik, and P. Sandeberg, "Platformless DC collection and transmission for offshore wind," in *11th IET International Conference on AC and DC Power Transmission*, 2015, pp. 1–6, DOI: 10.1049/cp.2015.0075.

[27] J. Carr, J. Li, D. Das, and J. Pan, "Wind turbine drivetrain for direct MVDC connection," in *2014 IEEE Symposium on Power Electronics and Machines for Wind and Water Applications*. IEEE, 2014, pp. 1–6, DOI: 10.1109/pemwa.2014.6912231.

[28] M. Müller, K. Litty, and H. Gehritz, "H2Mare update 02/2022," Technology Platform Office, Newsletter, 2022, [Online]. Available: wasserstoff-leitprojekte.de.

[29] B. Kitchenham and S. Charters, "Guidelines for performing systematic literature reviews in software engineering," University of Durham, Tech. Rep. EBSE-2007-01, 2007, [Online]. Available: researchgate.net/publication/302924724.

[30] A. Oakley, D. Gough, S. Oliver, and J. Thomas, "The politics of evidence and methodology: lessons from the eppi-centre," *Evidence & Policy: A Journal of Research, Debate and Practice*, vol. 1, no. 1, pp. 5–32, 2005, DOI: 10.1332/1744264052703168.

[31] O. Adeuyi and J. Liang, "Integration of power from offshore wind turbines into onshore grids," in *Offshore Wind Farms*. Elsevier, 2016, pp. 441–457, DOI: 10.1016/b978-0-08-100779-2.00014-3.

[32] S. Lumbreras and A. Ramos, "Offshore wind farm electrical design: a review," *Wind Energy*, vol. 16, no. 3, pp. 459–473, 2013, DOI: 10.1002/we.1498.

[33] O. Anaya-Lara, "Offshore wind farm arrays," in *Offshore Wind Farms*. Elsevier, 2016, pp. 389–417, DOI: 10.1016/b978-0-08-100779-2.00012-x.

[34] H. J. Bahirat, B. A. Mork, and H. K. Høidalen, "Comparison of wind farm topologies for offshore applications," in *2012 IEEE power and energy society general meeting*. IEEE, 2012, pp. 1–8, DOI: 10.1109/pesgm.2012.6344689.

[35] P. Gardner, L. Craig, G. Smith *et al.*, "Electrical systems for offshore wind farms," in *Proceedings of the 20th British Wind Energy Association Conference, Cardiff, UK*, 1998, pp. 2–4.

[36] P. Bresesti, W. L. Kling, R. L. Hendriks, and R. Vailati, "HVDC connection of offshore wind farms to the transmission system," *IEEE Transactions on energy conversion*, vol. 22, no. 1, pp. 37–43, 2007, DOI: 10.1109/tec.2006.889624.

[37] TenneT, "BorWin1 Factsheet," TenneT TSO GmbH, Tech. Rep., 2022, [Online]. Available at: tennet.eu/projects/borwin1.

[38] TenneT, "DolWin1 Factsheet," TenneT TSO GmbH, Tech. Rep., 2022, [Online]. Available at: tennet.eu/projects/dolwin1.

[39] RWE, "Sofia Offshore Wind Farm, Dogger Bank," 2024, [Online]. Available at: sofiawindfarm.com.

[40] T. Ackermann, *Wind power in power systems*. John Wiley & Sons, 2012, ISBN: 978-0-470-97416-2.

[41] S. Lundberg, "Evaluation of wind farm layouts," *Epe journal*, vol. 16, no. 1, pp. 14–21, 2006, DOI: 10.1080/09398368.2006.11463608.

[42] C. Meyer, M. Hoing, A. Peterson, and R. W. De Doncker, "Control and design of DC grids for offshore wind farms," *IEEE Transactions on Industry applications*, vol. 43, no. 6, pp. 1475–1482, 2007, DOI: 10.1109/tia.2007.908182.

[43] M. A. Parker and O. Anaya-Lara, "Cost and losses associated with offshore wind farm collection networks which centralise the turbine power electronic converters," *IET Renewable Power Generation*, vol. 7, no. 4, pp. 390–400, 2013, DOI: 10.1049/iet-rpg.2012.0262.

[44] P. Lakshmanan, J. Liang, and N. Jenkins, "Assessment of collection systems for HVDC connected offshore wind farms," *Electric Power Systems Research*, vol. 129, pp. 75–82, 2015, DOI: 10.1016/j.epsr.2015.07.015.

[45] M. De Prada Gil, J. L. Domínguez-García, F. Díaz-González, M. Aragüés-Peñalba, and O. Gomis-Bellmunt, "Feasibility analysis of offshore wind power plants with DC collection grid," *Renewable Energy*, vol. 78, pp. 467–477, 2015, DOI: 10.1016/j.renene.2015.01.042.

[46] S. C. Raval, R. Botta, and H. N. Raval, "Comparison of energy production cost for MVAC and MVDC offshore wind farm distribution system," in *2017 Asian Conference on Energy, Power and Transportation Electrification (ACEPT)*. IEEE, 2017, pp. 1–6, DOI: 10.1109/acept.2017.8168543.

[47] S. Kucuksari, N. Erdogan, and U. Cali, "Impact of electrical topology, capacity factor and line length on economic performance of offshore wind investments," *Energies*, vol. 12, no. 16, p. 3191, 2019, DOI: 10.3390/en12163191.

[48] P. Hu, R. Yin, Z. He, and C. Wang, "A modular multiple DC transformer based DC transmission system for pmsg based offshore wind farm integration," *IEEE Access*, vol. 8, pp. 15 736–15 746, 2019, DOI: 10.1109/access.2019.2962620.

[49] Q. Huang, X. Wang, J. Fan, X. Zhang, and Y. Wang, "Reliability and economy assessment of offshore wind farms," *The Journal of Engineering*, vol. 2019, no. 16, pp. 1554–1559, 2019, DOI: 10.1049/joe.2018.8472.

[50] R. Sun, G. Abeynayake, J. Liang, and K. Wang, "Reliability and economic evaluation of offshore wind power DC collection systems," *Energies*, vol. 14, no. 10, p. 2922, 2021, DOI: 10.3390/en14102922.

[51] W. Tang, M. Shi, Z. Li, and N. Yu, "Loss comparison study of MMC-HVDC and all-DC offshore wind farm," in *2019 IEEE Innovative Smart Grid Technologies-Asia (ISGT Asia)*. IEEE, 2019, pp. 171–175, DOI: 10.1109/isgt-asia.2019.8880884.

[52] F. Rong, G. Wu, X. Li, S. Huang, and B. Zhou, "All-DC offshore wind farm with series-connected wind turbines to overcome unequal wind speeds," *IEEE Transactions on Power Electronics*, vol. 34, no. 2, pp. 1370–1381, 2018, DOI: 10.1109/tpel.2018.2834965.

[53] A. Prasai and D. Divan, "DC collection for wind farms," in *2008 IEEE Energy 2030 Conference*. IEEE, 2008, pp. 1–7, DOI: 10.1109/energy.2008.4781054.

[54] N. Holtsmark, H. J. Bahirat, M. Molinas, B. A. Mork, and H. K. Hoidalen, "An all-DC offshore wind farm with series-connected turbines: An alternative to the classical parallel AC model?" *IEEE Transactions on industrial Electronics*, vol. 60, no. 6, pp. 2420–2428, 2012, DOI: 10.1109/tie.2012.2232255.

[55] H. J. Bahirat, G. H. Kjølle, B. A. Mork, and H. K. Høidalen, "Reliability assessment of DC wind farms," in *2012 IEEE Power and Energy Society General Meeting*. IEEE, 2012, pp. 1–7, DOI: 10.1109/pesgm.2012.6344691.

[56] M. Pape and M. Kazerani, "On the efficiency of series-connected offshore DC wind farm configurations," in *2019 IEEE Energy Conversion Congress and Exposition (ECCE)*. IEEE, 2019, pp. 921–926, DOI: 10.1109/ecce.2019.8911891.

[57] M. H. Johnson, D. C. Aliprantis, and H. Chen, "Offshore wind farm with dc collection system," in *2013 IEEE Power and Energy Conference at Illinois (PECI)*. IEEE, 2013, pp. 53–59, DOI: 10.1109/peci.2013.6506034.

[58] S. Chuangpishit, A. Tabesh, Z. Moradi-Shahrbabak, and M. Saeedifard, "Topology design for collector systems of offshore wind farms with pure DC power systems," *IEEE Transactions on Industrial Electronics*, vol. 61, no. 1, pp. 320–328, 2013, DOI: 10.1109/tie.2013.2245619.

[59] S. Lundberg, "Performance comparison of wind park configurations," Chalmers University of Technology, Tech. Rep., 2003, Available: chalmers.se.

[60] M. Dicorato, G. Forte, M. Pisani, and M. Trovato, "Guidelines for assessment of investment cost for offshore wind generation," *Renewable energy*, vol. 36, no. 8, pp. 2043–2051, 2011, DOI: 10.1016/j.renene.2011.01.003.

[61] National Grid plc, "Electricity Ten Year Statement 2015: Appendix E - Technology," National Grid, Tech. Rep., 2015, Available: nationalgrideso.com.

[62] A. Flament, P. Joseph, G. Gerdes, L. Rehfeldt, A. Behrens, A. Dimitrova, F. Genoese, I. Gajic, M. Jafar, N. Tidemand, Y. Yang, J. Jansen, F. Nieuwenhout, K. Veum, I. Konstantelos, D. Pudjianto, and G. Strbac, "NorthSeaGrid - Annexes to the Final Report," 3E, DWG, DNG GL, ECN, CEPS, Imperial College, Tech. Rep., 2014, Available: northseagrid.info.

[63] ENTSO-E, "Offshore Transmission Technology," European Network of Transmission System Operators for Electricity, Tech. Rep., 2011, Available: entsoe.eu.

[64] BVG Associates, "Guide to an offshore wind farm," The Crown Estate, Tech. Rep., 2019, Available: bvgassociates.com.

[65] C. Dincan, "High power medium voltage DC/DC converter technology for DC wind turbines," Ph.D. dissertation, Aalborg University, 2018, DOI: 10.5278/vbn.phd.eng.00072.

[66] Working Group B1.10, "TB379: Update of service experience of HV underground and submarine cable systems," CIGRE, Tech. Rep., 2009, Available: e-cigre.org.

[67] Working Group B4.60, "Designing HVDC grids for optimal reliability and availability performance," CIGRE, Tech. Rep., 2017, Available: e-cigre.org.

[68] H. Zhang, F. Gruson, D. M. F. Rodriguez, and C. Saudemont, "Overvoltage limitation method of an offshore wind farm with DC series-parallel collection grid," *IEEE Transactions on Sustainable Energy*, vol. 10, no. 1, pp. 204–213, 2018, DOI: 10.1109/tste.2018.2829929.

[69] GE Grid Solutions, "DolWin3 HVDC Voltage Source Converters for Efficient Connection of Renewable Energy," [Online]. Available: gegridsolutions.com/products/applications/hvdc/hvdc-vsc-dolwin3-case-study-en-2018-11-grid-pea-0578.pdf.

[70] N. Skopljak, "TenneT's OSS-Less Connection for Ørsted and EnBW German Projects," [Online]. Available: offshorewind.biz/2019/09/06/tennets-oss-less-connection-for-orsted-and-enbw-german-projects. Accessed: 2024-06-21.

[71] Y. Zhou, D. Macpherson, W. Blewitt, and D. Jovcic, "Comparison of DC-DC converter topologies for offshore wind-farm application," in *6th IET International Conference on Power Electronics, Machines and Drives (PEMD 2012)*. IET, 2012, pp. 1–6, DOI: 10.1049/cp.2012.0196.

[72] ABB, "Xlpe submarine cable systems: Attachment to xlpe land cable systems - user's guide," ABB, Tech. Rep., 2010, Available: abb.com.

[73] ABB, "HVDC light® cables submarine and land power cables," ABB, Tech. Rep., 2006, Available: abb.com.

[74] DNV GL Energy, "66 kV systems for offshore wind farms," TenneT, Tech. Rep., 2015, Available: tennet.eu.

[75] T. Krieg and J. Finn, *CIGRE Green Book - Substations*. CIGRE, 2021, Available: e-cigre.com.

[76] National Grid ESO, "The Grid Code - Issue 6," National Grid Electricity System Operator Limited, Tech. Rep., 2021.

[77] J. Dakic, M. Cheah-Mane, O. Gomis-Bellmunt, and E. P. Araujo, "Hvac transmission system for offshore wind power plants including mid-cable reactive power compensation: Optimal design and comparison to VSC-HVDC transmission," *IEEE Transactions on Power Delivery*, 2020, DOI: 10.1109/tpwrd.2020.3027356.

[78] S. Lauria, M. Schembari, F. Palone, and M. Maccioni, "Very long distance connection of gigawatt-size offshore wind farms: extra high-voltage AC versus high-voltage DC cost comparison," *IET Renewable Power Generation*, vol. 10, no. 5, pp. 713–720, 2016, DOI: 10.1049/iet-rpg.2015.0348.

[79] OFX, "Historical exchange rates," [Online]. Available: ofx.com/en-gb/forex-news/historical-exchange-rates. Accessed: 2021-03-15.

[80] InflationTool, "Inflation calculator - euro," [Online]. Available: inflationtool.com/euro. Accessed: 2021-03-15.

[81] A. G. Gonzalez-Rodriguez, "Review of offshore wind farm cost components," *Energy for Sustainable Development*, vol. 37, pp. 10–19, 2017, DOI: 10.1016/j.esd.2016.12.001.

[82] G. Stamatiou, "Techno-Economical Analysis of DC Collection Grid for Offshore Wind Parks," Master's thesis, University of Nottingham, 2010, DOI: 10.13140/rg.2.1.1902.6649.

[83] ABB, "XLPE Submarine Cable Systems: Attachment to XLPE Land Cable Systems - User's Guide," ABB, Tech. Rep., 2010, Available: new.abb.com.

[84] G. Guidi and O. Fosso, "Investment cost of HVAC cable reactive power compensation off-shore," in *2012 IEEE International Energy Conference and Exhibition (ENERGYCON)*. IEEE, 2012, pp. 299–304, DOI: 10.1109/energycon.2012.6347771.

[85] ABB Wind Power Solutions, "PCS6000 wind turbine converters," ABB, Dataheet, 2019. [Online]. Available: new.abb.com/power-converters-inverters/wind-turbines/utility-scale/pcs6000

[86] R. Li and L. Xu, "A unidirectional hybrid HVDC transmission system based on diode rectifier and full-bridge MMC," *IEEE Journal of Emerging and Selected Topics in Power Electronics*, 2020, DOI: 10.1109/jestpe.2020.3015342.

[87] R. Walling and T. Ruddy, "Economic optimization of offshore windfarm substations and collection systems," in *Fifth international workshop on large scale integration of wind power and transmission networks for offshore windfarms, Glasgow*, 2005, available: www.ofgem.gov.uk.

[88] O. Dahmani, S. Bourguet, M. Machmoum, P. Guerin, P. Rhein, and L. Josse, "Optimization and reliability evaluation of an offshore wind farm architecture," *IEEE Transactions on Sustainable Energy*, vol. 8, no. 2, pp. 542–550, 2016, DOI: 10.1109/tste.2016.2609283.

[89] B. Frankén, "Reliability study: Analysis of electrical systems within offshore wind parks," Elforsk, Tech. Rep., 2007, Available: neplan.ch.

[90] C. MacIver, "A reliability evaluation of offshore HVDC transmission network options," Ph.D. dissertation, University of Strathclyde, 2015, DOI: 10.48730/svmq-fv57.

[91] K. Fischer and J. Wenske, "Towards reliable power converters for wind turbines: Field-data based identification of weak points and cost drivers," *Scientific Proceedings of EWEA*, 2015, DOI: 10.24406/publica-fhg-391310.

[92] N. B. Negra, O. Holmstrom, B. Bak-Jensen, and P. Sorensen, "Aspects of relevance in offshore wind farm reliability assessment," *IEEE Transactions on energy conversion*, vol. 22, no. 1, pp. 159–166, 2007, DOI: 10.1109/tec.2006.889610.

[93] R. Barrera-Cardenas and M. Molinas, "Comparative study of wind turbine power converters based on medium-frequency ac-link for offshore DC-grids," *IEEE Journal of Emerging and Selected Topics in Power Electronics*, vol. 3, no. 2, pp. 525–541, 2014, DOI: 10.1109/jestpe.2014.2360578.

[94] T. Jimichi, M. Kaymak, and R. W. De Doncker, "Comparison of single-phase and three-phase dual-active bridge DC-DC converters with various semiconductor devices for offshore wind turbines," in *2017 IEEE 3rd International Future Energy Electronics Conference and ECCE Asia (IFEEC 2017-ECCE Asia)*. IEEE, 2017, pp. 591–596, DOI: 10.1109/ifeec.2017.7992105.

[95] W. Chen, G. Wang, and X. Zhu, "A family of bidirectional DC/DC converters suitable for asymmetrical power flow requirement," in *2013 IEEE Energy Conversion Congress and Exposition*. IEEE, 2013, pp. 4878–4881, DOI: 10.1109/ecce.2013.6647357.

[96] T. Lagier and P. Ladoux, "A comparison of insulated DC-DC converters for HVDC off-shore wind farms," in *2015 International Conference on Clean Electrical Power (ICCEP)*. IEEE, 2015, pp. 33–39, DOI: 10.1109/iccep.2015.7177597.

[97] Carbon Trust, "Unlocking the next generation of offshore wind: step change to 132kV array systems," Offshore Wind Accelerator, Tech. Rep., 2022.

[98] W. Chen, A. Huang, S. Lukic, J. Svensson, J. Li, and Z. Wang, "A comparison of medium voltage high power DC/DC converters with high step-up conversion ratio for offshore wind energy systems," in *2011 IEEE Energy Conversion Congress and Exposition*. IEEE, 2011, pp. 584–589, DOI: 10.1109/ecce.2011.6063822.

[99] V. Timmers, A. Egea-Àlvarez, A. Gkountaras, R. Li, and L. Xu, "All-DC offshore wind farms: When are they more cost-effective than AC designs?" *IET Renewable Power Generation*, vol. 17, no. 10, pp. 2458–2470, 2023, DOI: 10.1049/rpg2.12550.

[100] L. Max and S. Lundberg, "System efficiency of a DC/DC converter-based wind farm," *Wind Energy: An International Journal for Progress and Applications in Wind Power Conversion Technology*, vol. 11, no. 1, pp. 109–120, 2008, DOI: 10.1002/we.259.

[101] K. Park and Z. Chen, "Analysis and design of a parallel-connected single active bridge DC-DC converter for high-power wind farm applications," in *2013 15th European Conference on Power Electronics and Applications (EPE)*. IEEE, 2013, pp. 1–10, DOI: 10.1109/epe.2013.6631854.

[102] S. P. Engel, N. Soltau, H. Stagge, and R. W. De Doncker, "Dynamic and balanced control of three-phase high-power dual-active bridge DC–DC converters in dc-grid applications," *IEEE Transactions on Power Electronics*, vol. 28, no. 4, pp. 1880–1889, 2012, DOI: 10.1109/tpel.2012.2209461.

[103] W. Chen, A. Q. Huang, C. Li, G. Wang, and W. Gu, "Analysis and comparison of medium voltage high power DC/DC converters for offshore wind energy systems," *IEEE Transactions on Power Electronics*, vol. 28, no. 4, pp. 2014–2023, 2012, DOI: 10.1109/tpel.2012.2215054.

[104] D. Jovcic, "Step-up DC–DC converter for megawatt size applications," *IET Power Electronics*, vol. 2, no. 6, pp. 675–685, 2009, DOI: 10.1049/iet-pel.2008.0101.

[105] A. Parastar and J.-K. Seok, "High-gain resonant switched-capacitor cell-based DC/DC converter for offshore wind energy systems," *IEEE Transactions on Power Electronics*, vol. 30, no. 2, pp. 644–656, 2014, DOI: 10.1109/tpel.2014.2314110.

[106] J. D. Paez, D. Frey, J. Maneiro, S. Bacha, and P. Dworakowski, "Overview of DC–DC converters dedicated to HVdc grids," *IEEE Transactions on Power Delivery*, vol. 34, no. 1, pp. 119–128, 2018, DOI: 10.1109/tpwrd.2018.2846408.

[107] E. Gaertner, J. Rinker, L. Sethuraman, F. Zahle, B. Anderson, G. E. Barter, N. J. Abbas, F. Meng, P. Bortolotti, W. Skrzypinski *et al.*, "IEA wind TCP task 37: definition of the IEA 15-megawatt offshore reference wind turbine," National Renewable Energy Lab (NREL), Golden, CO (United States), Tech. Rep., 2020, DOI: 10.2172/1603478.

[108] C. Dincan, P. Kjaer, Y.-h. Chen, S.-M. Nielsen, and C. L. Bak, "Selection of DC/DC converter for offshore wind farms with MVDC power collection," in *2017 19th European Conference on Power Electronics and Applications (EPE'17 ECCE Europe)*. IEEE, 2017, pp. P–1, DOI: 10.23919/epe17ecceeurope.2017.8099408.

[109] A. Follo, O. Saborío-Romano, E. Tedeschi, and N. A. Cutululis, "Challenges in all-DC offshore wind power plants," *Energies*, vol. 14, no. 19, p. 6057, 2021, DOI: 10.3390/en14196057.

[110] C. Cecati, H. A. Khalid, M. Tinari, G. Adinolfi, and G. Graditi, "DC nanogrid for renewable sources with modular DC/DC llc converter building block," *IET Power Electronics*, vol. 10, no. 5, pp. 536–544, 2016, DOI: 10.1049/iet-pel.2016.0200.

[111] D. Xu, Y. Guan, Y. Wang, and W. Wang, "A review of high frequency resonant DC-DC power converters: Topologies and planar magnetic technologies," *Science China Technological Sciences*, pp. 1–13, 2020, DOI: 10.1007/s11431-020-1665-3.

[112] Y. Wei, Q. Luo, and H. A. Mantooth, "Llc and cllc resonant converters based DC transformers (dcxs): Characteristics, issues, and solutions," *CPSS Transactions*

on Power Electronics and Applications, vol. 6, no. 4, pp. 332–348, 2021, DOI: 10.24295/cpsstpea.2021.00031.

[113] Y. Lian, "Dc/dc converter for offshore DC collection network," Ph.D. dissertation, University of Strathclyde, 2016, DOI: 10.48730/nm9g-h006.

[114] S. P. Engel, M. Stieneker, N. Soltau, S. Rabiee, H. Stagge, and R. W. De Doncker, "Comparison of the modular multilevel DC converter and the dual-active bridge converter for power conversion in HVDC and MVDC grids," *IEEE Transactions on Power Electronics*, vol. 30, no. 1, pp. 124–137, 2014, DOI: 10.1109/tpel.2014.2310656.

[115] L. Max and T. Thiringer, "Control method and snubber selection for a 5 MW wind turbine single active bridge DC/DC converter," in *2007 European Conference on Power Electronics and Applications*. IEEE, 2007, pp. 1–10, DOI: 10.1109/epe.2007.4417324.

[116] R. W. De Doncker, D. M. Divan, and M. H. Kheraluwala, "A three-phase soft-switched high-power-density DC/DC converter for high-power applications," *IEEE Trans. Ind. Appl.*, vol. 27, no. 1, pp. 63–73, 1991, DOI: 10.1109/28.67533.

[117] C. Fontana, M. Forato, K. Kumar, M. T. Outeiro, M. Bertoluzzo, and G. Buja, "Soft-switching capabilities of SAB vs. DAB converters," in *IECON 2015-41st Annual Conf. IEEE Ind. Electron. Soc.* IEEE, 2015, pp. 003 485–003 490, DOI: 10.1109/iecon.2015.7392640.

[118] C. Fontana, M. Forato, M. Bertoluzzo, and G. Buja, "Design characteristics of SAB and DAB converters," in *2015 Int. Aegean Conf. Elec. Mach. & Power Electron. (ACEMP)*. IEEE, 2015, pp. 661–668, DOI: 10.1109/optim.2015.7427025.

[119] K. Park and Z. Chen, "Control and dynamic analysis of a parallel-connected single active bridge DC–DC converter for dc-grid wind farm application," *IET Power Electronics*, vol. 8, no. 5, pp. 665–671, 2015, DOI: 10.1049/iet-pel.2014.0420.

[120] Y. Sang, A. Junyent-Ferre, and T. C. Green, "Operational principles of three-phase single active bridge DC/DC converters under duty cycle control," *IEEE Transactions on Power Electronics*, vol. 35, no. 8, pp. 8737–8750, 2020, DOI: 10.1109/tpel.2020.2964901.

[121] N. Hou and Y. W. Li, "Overview and comparison of modulation and control strategies for a nonresonant single-phase dual-active-bridge DC–DC converter,"

IEEE Transactions on Power Electronics, vol. 35, no. 3, pp. 3148–3172, 2019, DOI: 10.1109/tpel.2019.2927930.

[122] F. Krismer, "Modeling and optimization of bidirectional dual active bridge DC–DC converter topologies," Ph.D. dissertation, ETH Zurich, 2010, DOI: 10.3929/ethz-a-006395373.

[123] N. Soltau, H. Stagge, R. W. De Doncker, and O. Apeldoorn, "Development and demonstration of a medium-voltage high-power DC-DC converter for DC distribution systems," in *2014 IEEE 5th International Symposium on Power Electronics for Distributed Generation Systems (PEDG)*. IEEE, 2014, pp. 1–8, DOI: 10.1109/pedg.2014.6878696.

[124] J. Huang, Z. Li, L. Shi, Y. Wang, and J. Zhu, "Optimized modulation and dynamic control of a three-phase dual active bridge converter with variable duty cycles," *IEEE Transactions on Power Electronics*, vol. 34, no. 3, pp. 2856–2873, 2018, DOI: 10.1109/tpel.2018.2842021.

[125] J. Hu, S. Cui, S. Wang, and R. W. De Doncker, "Instantaneous flux and current control for a three-phase dual-active bridge DC–DC converter," *IEEE Transactions on Power Electronics*, vol. 35, no. 2, pp. 2184–2195, 2019, DOI: 10.1109/tpel.2019.2922299.

[126] D. Segaran, D. G. Holmes, and B. P. Mcgrath, "Comparative analysis of single-and three-phase dual active bridge bidirectional dc-dc converters," *Australian Journal of Electrical and Electronics Engineering*, vol. 6, no. 3, pp. 329–337, 2009, DOI: 10.1080/1448837x.2009.11464251.

[127] V. Timmers, A. Egea-Àlvarez, and A. Gkountaras, "Review and comparison of single and dual active bridge converters for MVDC-connected wind turbines," in *21st Wind & Solar Integration Workshop*, 2022, DOI: 10.1049/icp.2022.2819.

[128] Y. Lian, G. P. Adam, D. Holliday, and S. J. Finney, "Medium-voltage DC/DC converter for offshore wind collection grid," *IET Renewable Power Generation*, vol. 10, no. 5, pp. 651–660, 2016, DOI: 10.1049/iet-rpg.2015.0376.

[129] K. Park and Z. Chen, "A double uneven power converter-based DC–DC converter for high-power DC grid systems," *IEEE Transactions on Industrial Electronics*, vol. 62, no. 12, pp. 7599–7608, 2015, DOI: 10.1109/tie.2015.2458301.

[130] M. Kaymak, R. W. De Doncker, and T. Jimichi, "Design and verification of a medium-frequency transformer in a three-phase dual-active bridge DC-DC

converter for medium-voltage grid connection of offshore wind farms," in *2020 IEEE Appl. Power Electron. Conf. (APEC)*. IEEE, 2020, pp. 2694–2701, DOI: 10.1109/apec39645.2020.9124482.

[131] M. Mogorovic and D. Dujic, "Sensitivity analysis of medium-frequency transformer designs for solid-state transformers," *IEEE Trans. Power Electron.*, vol. 34, no. 9, pp. 8356–8367, 2018, DOI: 10.1109/tpel.2018.2883390.

[132] G. Abeynayake, G. Li, T. Joseph, J. Liang, and W. Ming, "Reliability and cost-oriented analysis, comparison and selection of multi-level MVDC converters," *IEEE Transactions on Power Delivery*, vol. 36, no. 6, pp. 3945–3955, 2021, DOI: 10.1109/tpwrd.2021.3051531.

[133] M. Stieneker and R. W. De Doncker, "Dual-active bridge DC-DC converter systems for medium-voltage DC distribution grids," in *2015 IEEE 13th Brazilian Power Electronics Conference and 1st Southern Power Electronics Conference (COBEP/SPEC)*. IEEE, 2015, pp. 1–6, DOI: 10.1109/cobep.2015.7420246.

[134] J. Guo, X. Wang, J. Liang, H. Pang, and J. Gonçalves, "Reliability modeling and evaluation of MMCs under different redundancy schemes," *IEEE Transactions on Power Delivery*, vol. 33, no. 5, pp. 2087–2096, 2017, DOI: 10.1109/tpwrd.2017.2715664.

[135] Infineon, "Full power converter wind turbine," 2024, [Online]. Available: infineon.com/cms/en/applications/renewables/wind/full-converters. Accessed: 2024-02-09.

[136] Infineon Technologies AG, "Datasheet FF1800R17IP5," 2020, [Online]. Available: infineon.com/cms/en/product/power/igbt/igbt-modules/ff1800r17ip5.

[137] Infineon Technologies AG, "Datasheet D471N," 2014, [Online]. Available: infineon.com/cms/en/product/power/diodes-thyristors/thyristor-diode-discs/diode-discs/rectifier-diodes/d471n90t.

[138] Infineon Technologies AG, "Datasheet FD250R65KE3-K," 2021, [Online]. Available: infineon.com/cms/en/product/power/igbt/igbt-modules/fd250r65ke3-k.

[139] Royal HaskoningDHV, "Outline offshore operations and maintenance plan," Norfolk Vanguard Offshore Wind Farm, Tech. Rep. 8.11 (version 2), 2018, [Online]. Available: national-infrastructure-consenting.planninginspectorate.gov.uk.

[140] L. Max, "Design and control of a DC collection grid for a wind farm," Ph.D. dissertation, Chalmers University of Technology, 2009, iSBN: 978-91-7385-333-0.

[141] M. A. Bahmani, T. Thiringer, and M. Kharezy, "Design methodology and optimization of a medium-frequency transformer for high-power DC–DC applications," *IEEE Trans. Ind. Appl.*, vol. 52, no. 5, pp. 4225–4233, 2016, DOI: 10.1109/tia.2016.2582825.

[142] L. Max, "Energy evaluation for DC/DC converters in dc-based wind farms," Lic. Thesis, Chalmers University of Technology, 2007, available: research.chalmers.se.

[143] M. Lambert, F. Sirois, M. Martinez-Duro, and J. Mahseredjian, "Analytical calculation of leakage inductance for low-frequency transformer modeling," *IEEE Transactions on Power Delivery*, vol. 28, no. 1, pp. 507–515, 2012, DOI: 10.1109/tpwrd.2012.2225451.

[144] Semikron-Danfoss, "Semistack® renewable energy - size W2," Semikron-Danfoss, Datasheet, 2013, [Online]. Available: semikron-danfoss.com.

[145] EPCOS AG, "Film Capacitors - Power Electronic Capacitors," TDK Group, 2022, [Online]. Available: tdk-electronics.tdk.com.

[146] A. Christe, E. Coulinge, and D. Dujic, "Insulation coordination for a modular multilevel converter prototype," in *2016 18th European Conference on Power Electronics and Applications (EPE'16 ECCE Europe)*. IEEE, 2016, pp. 1–9, DOI: 10.1109/epe.2016.7695527.

[147] S. Ozdemir, N. Altin, A. Nasiri, and R. Cuzner, "Review of standards on insulation coordination for medium voltage power converters," *IEEE Open Journal of Power Electronics*, vol. 2, pp. 236–249, 2021, DOI: 10.1109/ojpel.2021.3065813.

[148] S. Martello, D. Pisinger, and D. Vigo, "The three-dimensional bin packing problem," *Operations research*, vol. 48, no. 2, pp. 256–267, 2000, DOI: 10.1287/opre.48.2.256.12386.

[149] Z. Jiang, "Installation of offshore wind turbines: A technical review," *Renewable and Sustainable Energy Reviews*, vol. 139, p. 110576, 2021, DOI: 10.1016/j.rser.2020.110576.

[150] R. Petkov, "Optimum design of a high-power, high-frequency transformer," *IEEE Transactions on power electronics*, vol. 11, no. 1, pp. 33–42, 1996, DOI: 10.1109/63.484414.

[151] K. Venkatachalam, C. R. Sullivan, T. Abdallah, and H. Tacca, "Accurate prediction of ferrite core loss with nonsinusoidal waveforms using only steinmetz parameters," in *Proc. IEEE Workshop Comput. Power Electron.* IEEE, 2002, pp. 36–41, DOI: 10.1109/cipe.2002.1196712.

[152] Plexim GmbH, "PLECS User Manual Version 4.6," Plexim GmbH, 2022, [Online]. Available: plexim.com/sites/default/files/plecsmanual.pdf.

[153] ABB, "Technical data PCS6000 medium voltage wind turbine converter," 2024, [Online]. Available: new.abb.com/power-converters-inverters/wind-turbines/utility-scale/pcs6000/technical-data. Accessed: 2024-03-05.

[154] V. Timmers, A. Egea-Àlvarez, and A. Gkountaras, "Frequency optimisation for DC/DC converters in DC-connected offshore wind turbines," in *2023 25th European Conference on Power Electronics and Applications (EPE'23 ECCE Europe)*. IEEE, 2023, pp. 1–8, DOI: 10.23919/epe23ecceeurope58414.2023.10264511.

[155] R. LeRoy, "Industrial water electrolysis: present and future," *International Journal of Hydrogen Energy*, vol. 8, no. 6, pp. 401–417, 1983, DOI: 10.1016/0360-3199(83)90162-3.

[156] S. M. Abu, M. Hannan, P. J. Ker, M. Mansor, S. K. Tiong, and T. I. Mahlia, "Recent progress in electrolyser control technologies for hydrogen energy production: A patent landscape analysis and technology updates," *Journal of Energy Storage*, vol. 72, p. 108773, 2023, DOI: 10.1016/j.est.2023.108773.

[157] A. Mohammadi and M. Mehrpooya, "A comprehensive review on coupling different types of electrolyzer to renewable energy sources," *Energy*, vol. 158, pp. 632–655, 2018, DOI: 10.1016/j.energy.2018.06.073.

[158] A. S. Ansar, A. S. Gago, F. Razmjooei, R. Reißner, Z. Xu, and K. A. Friedrich, "Alkaline electrolysis—status and prospects," *Electrochemical Power Sources: Fundamentals, Systems, and Applications*, pp. 165–198, 2022, DOI: 10.1016/b978-0-12-819424-9.00004-5.

[159] R. Phillips and C. W. Dunnill, "Zero gap alkaline electrolysis cell design for renewable energy storage as hydrogen gas," *RSC advances*, vol. 6, no. 102, pp. 100 643–100 651, 2016, DOI: 10.1039/c6ra22242k.

[160] K. Zhang, X. Liang, L. Wang, K. Sun, Y. Wang, Z. Xie, Q. Wu, X. Bai, M. S. Hamdy, H. Chen *et al.*, "Status and perspectives of key materials for PEM elec-

trolyzer," *Nano Res. Energy*, vol. 1, no. 3, p. e9120032, 2022, DOI: 10.26599/nre.2022.9120032.

[161] M. S. Thomassen, A. H. Reksten, A. O. Barnett, T. Khoza, and K. Ayers, "PEM water electrolysis," in *Electrochemical Power Sources: Fundamentals, Systems, and Applications*. Elsevier, 2022, pp. 199–228, DOI: 10.1016/b978-0-12-819424-9.00013-6.

[162] G. Chisholm, P. J. Kitson, N. D. Kirkaldy, L. G. Bloor, and L. Cronin, "3d printed flow plates for the electrolysis of water: an economic and adaptable approach to device manufacture," *Energy & Environmental Science*, vol. 7, no. 9, pp. 3026–3032, 2014, DOI: 10.1039/c4ee01426j.

[163] A. Brisse, J. Schefold, and A. Léon, "High-temperature steam electrolysis," in *Electrochemical Power Sources: Fundamentals, Systems, and Applications*. Elsevier, 2022, pp. 229–280, DOI: 10.1016/b978-0-12-819424-9.00009-4.

[164] A. Nechache and S. Hody, "Alternative and innovative solid oxide electrolysis cell materials: A short review," *Renewable and Sustainable Energy Reviews*, vol. 149, p. 111322, 2021, DOI: 10.1016/j.rser.2021.111322.

[165] B. Vad Mathiesen, I. Ridjan, D. Connolly, M. Pagh Nielsen, P. Vang Hendriksen, M. Bjerg Mogensen, S. Højgaard Jensen, and S. Dalgaard Ebbesen, "Technology data for high temperature solid oxide electrolyser cells, alkali and PEM electrolysers," Aalborg University, Tech. Rep. NEI-DK-5976, 2013, available: osti.gov.

[166] A. Hauch, R. Küngas, P. Blennow, A. B. Hansen, J. B. Hansen, B. V. Mathiesen, and M. B. Mogensen, "Recent advances in solid oxide cell technology for electrolysis," *Science*, vol. 370, no. 6513, p. eaba6118, 2020, DOI: 10.1126/science.aba6118.

[167] A. M. Abomazid, N. A. El-Taweel, and H. E. Farag, "Novel analytical approach for parameters identification of PEM electrolyzer," *IEEE Transactions on Industrial Informatics*, vol. 18, no. 9, pp. 5870–5881, 2021, DOI: 10.1109/tii.2021.3132941.

[168] A. Ursúa and P. Sanchis, "Static–dynamic modelling of the electrical behaviour of a commercial advanced alkaline water electrolyser," *International journal of hydrogen energy*, vol. 37, no. 24, pp. 18 598–18 614, 2012, DOI: 10.1016/j.ijhydene.2012.09.125.

[169] P. Trinke, B. Bensmann, and R. Hanke-Rauschenbach, "Current density effect on hydrogen permeation in PEM water electrolyzers," *International Journal of Hy-*

drogen Energy, vol. 42, no. 21, pp. 14 355–14 366, 2017, DOI: 10.1016/j.ijhydene.2017.03.231.

[170] Plug, "The Plug EX-4250D," Plug, Tech. Rep., 2024, available at: plugpower.com.

[171] Green Hydrogen Systems, "HyProvide® X-Series," [Online]. Available: greenhydrogensystems.com/electrolysers/hyprovide-x-series-6mw-modular-electrolyser. Accessed: 2024-06-20.

[172] Siemens Energy, "Hydrogen and Power-to-X solutions," 2023, [Online]. Available: p3.aprimocdn.net/siemensenergy/03b60af1-899b-4c1d-ab9c-b0f100bcca9d/Brochure-Electrolyzer_Hydrogen-and-Power-to-X-solutions_16_9-pdf_Original%20file.pdf.

[173] V. M. Lopez, H. Ziar, J. Haverkort, M. Zeman, and O. Isabella, "Dynamic operation of water electrolyzers: A review for applications in photovoltaic systems integration," *Renewable and Sustainable Energy Reviews*, vol. 182, p. 113407, 2023, DOI: 10.1016/j.rser.2023.113407.

[174] B. W. Tuinema, E. Adabi, P. K. Ayivor, V. García Suárez, L. Liu, A. Perilla, Z. Ahmad, J. L. Rueda Torres, M. A. van der Meijden, and P. Palensky, "Modelling of large-sized electrolysers for real-time simulation and study of the possibility of frequency support by electrolysers," *IET Generation, Transmission & Distribution*, vol. 14, no. 10, pp. 1985–1992, 2020, DOI: 10.1049/iet-gtd.2019.1364.

[175] J. E. B. Randles, "Kinetics of rapid electrode reactions," *Discussions of the faraday society*, vol. 1, pp. 11–19, 1947, DOI: 10.1039/df9470100011.

[176] D. Guilbert and G. Vitale, "Experimental validation of an equivalent dynamic electrical model for a proton exchange membrane electrolyzer," in *2018 IEEE international conference on environment and electrical engineering*. IEEE, 2018, pp. 1–6, DOI: 10.1109/eeeic.2018.8494523.

[177] Á. Hernández-Gómez, V. Ramirez, D. Guilbert, and B. Saldivar, "Development of an adaptive static-dynamic electrical model based on input electrical energy for PEM water electrolysis," *International Journal of Hydrogen Energy*, vol. 45, no. 38, pp. 18 817–18 830, 2020, DOI: 10.1016/j.ijhydene.2020.04.182.

[178] N. Chiesa, M. Korpås, O. Kongstein, and A. Ødegård, "Dynamic control of an electrolyser for voltage quality enhancement," in *International Conference on Power Systems Transients (IPST2011)*, 2011, available: ipstconf.org.

[179] F.-W. Speckmann, S. Bintz, and K. P. Birke, "Influence of rectifiers on the energy demand and gas quality of alkaline electrolysis systems in dynamic operation," *Applied Energy*, vol. 250, pp. 855–863, 2019, DOI: 10.1016/j.apenergy.2019.05.014.

[180] L. Sha, J. Lin, R. Qi, and Y. Song, "Low-frequency experimental method for measuring the electric double-layer capacitances of multi-cell electrolysis stacks based on equivalent circuit model," *Journal of Power Sources*, vol. 579, p. 233263, 2023, DOI: 10.1016/j.jpowsour.2023.233263.

[181] A. Reyes, "Balance of plant (BoP) of an electrolyser," 2022, [Online]. Available: synerhy.com/en/2022/02/balance-of-plant-bop-of-an-electrolyser. Accessed: 2024-06-21.

[182] J. Gu, B. Guo, S. Hu, S. Ding, T. Zhang, Z. Tian, F. Yang, and M. Ouyang, "Experimental studies on dynamic performance of 250-kW alkaline electrolytic system," *Journal of Power Sources*, vol. 592, p. 233920, 2024, DOI: 10.1016/j.jpowsour.2023.233920.

[183] Y. Zheng, C. Huang, J. Tan, S. You, Y. Zong, and C. Træholt, "Off-grid wind/hydrogen systems with multi-electrolyzers: Optimized operational strategies," *Energy Conversion and Management*, vol. 295, p. 117622, 2023, DOI: 10.1016/j.enconman.2023.117622.

[184] P. Cavaliere, *Alkaline Liquid Electrolyte Water Electrolysis*. Springer International Publishing, 2023, pp. 203–232, DOI: 10.1007/978-3-031-37780-8_5.

[185] A. Ursúa, I. San Martín, E. L. Barrios, and P. Sanchis, "Stand-alone operation of an alkaline water electrolyser fed by wind and photovoltaic systems," *International Journal of Hydrogen Energy*, vol. 38, no. 35, pp. 14 952–14 967, 2013, DOI: 10.1016/j.ijhydene.2013.09.085.

[186] G. Calado and R. Castro, "Hydrogen production from offshore wind parks: Current situation and future perspectives," *Applied Sciences*, vol. 11, no. 12, p. 5561, 2021, DOI: 10.3390/app11125561.

[187] UK Deparment for Business, Energy & Industrial Strategy, "Gigastack phase 2: Pioneering UK renewable hydrogen," UK Deparment for Business, Energy & Industrial Strategy, Tech. Rep., 2022, available: gov.uk/government/publications/hydrogen-supply-competition.

[188] International Energy Agency, "The future of hydrogen - seizing today's opportunities," International Energy Agency, Tech. Rep., 2019. [Online]. Available: https://www.oecd.org/fr/publications/the-future-of-hydrogen-1e0514c4-en.htm

[189] S. Utermöhlen, "Green hydrogen offshore wind projects by RWE," RWE, Tech. Rep., 2022, [Online]. Available: energyforum.in/fileadmin/user_upload/india/media_elements/Presentations/20220926_WindEnergy/202209_3.PDF. Accessed: 2024-06-21.

[190] D. Caine, W. Wahyuni, B. Pizii, M. Iliffe, Z. Whitlock, B. Ryan, and L. Bond, "Erm dolphyn hydrogen," Department for Business, Energy and Industrial Strategy, Tech. Rep. 0536873, 2021, available: .gov.uk/government/publications/hydrogen-supply-competition.

[191] Siemens Gamesa, "Green hydrogen unlocked: The Brande hydrogen project," SGRE, Tech. Rep., 2024, [Online]. Available: www.siemensgamesa.com/products-and-services/hybrid-and-storage/green-hydrogen/unlocked-brande-hydrogen-project.

[192] A. Arsad, M. Hannan, A. Q. Al-Shetwi, M. Hossain, R. Begum, P. J. Ker, F. Salehi, and K. Muttaqi, "Hydrogen electrolyser for sustainable energy production: A bibliometric analysis and future directions," *International Journal of Hydrogen Energy*, vol. 48, no. 13, pp. 4960–4983, 2023, DOI: 10.1016/j.ijhydene.2022.11.023.

[193] T. Ayodele and J. Munda, "Potential and economic viability of green hydrogen production by water electrolysis using wind energy resources in south africa," *International Journal of Hydrogen Energy*, vol. 44, no. 33, pp. 17 669–17 687, 2019, DOI: 10.1016/j.ijhydene.2019.05.077.

[194] H. Groenemans, G. Saur, C. Mittelsteadt, J. Lattimer, and H. Xu, "Techno-economic analysis of offshore wind PEM water electrolysis for H_2 production," *Current Opinion in Chemical Engineering*, vol. 37, p. 100828, 2022, DOI: 10.1016/j.coche.2022.100828.

[195] A. Giampieri, J. Ling-Chin, and A. P. Roskilly, "Techno-economic assessment of offshore wind-to-hydrogen scenarios: A UK case study," *International Journal of Hydrogen Energy*, 2023, DOI: 10.1016/j.ijhydene.2023.01.346.

[196] A. G. Dutton, A. J. Ruddell, L. Barra, M. Falchetta, H. Dienhart, W. Seeger, J. A. Bleijs, and A. W. Chung, "Hydrogen generation from stand-alone wind-powered electrolysis systems," in *British Wind Energy Association conference on*

wind energy conversion 1995, Warwick, United Kingdom, Dec 1995, pp. 117–122, ISBN: 0 85298 961 X.

[197] Shell, "Shell to start building europe's largest renewable hydrogen plant," 2024, [Online]. Available: shell.com/news-and-insights/newsroom/news-and-media-releases/2022/shell-to-start-building-europes-largest-renewable-hydrogen-plant.html.

[198] T. Wilberforce, A. Olabi, M. Imran, E. T. Sayed, and M. A. Abdelkareem, "System modelling and performance assessment of green hydrogen production by integrating proton exchange membrane electrolyser with wind turbine," *International Journal of Hydrogen Energy*, vol. 48, no. 32, pp. 12 089–12 111, 2023, DOI: 10.1016/j.ijhydene.2022.12.263.

[199] A. Ursúa, E. L. Barrios, J. Pascual, I. San Martín, and P. Sanchis, "Integration of commercial alkaline water electrolysers with renewable energies: Limitations and improvements," *International Journal of Hydrogen Energy*, vol. 41, no. 30, pp. 12 852–12 861, 2016, DOI: 10.1016/j.ijhydene.2016.06.071.

[200] C. Dixon, S. Reynolds, and D. Rodley, "Micro/small wind turbine power control for electrolysis applications," *Renewable Energy*, vol. 87, pp. 182–192, 2016, DOI: 10.1016/j.renene.2015.09.055.

[201] A. E. Samani, A. D'Amicis, J. D. De Kooning, D. Bozalakov, P. Silva, and L. Vandevelde, "Grid balancing with a large-scale electrolyser providing primary reserve," *IET Renewable Power Generation*, vol. 14, no. 16, pp. 3070–3078, 2020, DOI: 10.1049/iet-rpg.2020.0453.

[202] S. D. Tavakoli, M. G. Dozein, V. A. Lacerda, M. C. Mañe, E. Prieto-Araujo, P. Mancarella, and O. Gomis-Bellmunt, "Grid-forming services from hydrogen electrolyzers," *IEEE Transactions on Sustainable Energy*, 2023, DOI: 10.1109/tste.2023.3270295.

[203] T. Runser, S. Arend, and R. De Doncker, "Stand-alone offshorewind energy andwater electrolysis: A study on optimal electrolyzer sizing," in *2023 25th European Conference on Power Electronics and Applications*. IEEE Power Electronics Society, 2023, pp. 1–9, DOI: 10.23919/epe23ecceeurope58414.2023.10264298.

[204] A. Rolan, A. Luna, G. Vazquez, D. Aguilar, and G. Azevedo, "Modeling of a variable speed wind turbine with a permanent magnet synchronous generator," in

2009 IEEE international symposium on industrial electronics. IEEE, 2009, pp. 734–739, DOI: 10.1109/isie.2009.5218120.

[205] A. Junyent-Ferré and O. Gomis-Bellmunt, "Wind turbine generation systems modeling for integration in power systems," in *Handbook Of Renewable Energy Technology*. World Scientific, 2011, pp. 53–68, DOI: 10.1142/9789814289078_0003.

[206] J. Licari, "Control of a variable speed wind turbine," Ph.D. dissertation, Cardiff University, 2013. [Online]. Available: orca.cardiff.ac.uk/id/eprint/46516

[207] F. D. Bianchi, H. De Battista, and R. J. Mantz, *Wind turbine control systems: principles, modelling and gain scheduling design*. Springer, 2007, vol. 19, DOI: 10.1007/1-84628-493-7.

[208] O. Alizadeh and A. Yazdani, "A strategy for real power control in a direct-drive PMSG-based wind energy conversion system," *IEEE transactions on Power Delivery*, vol. 28, no. 3, pp. 1297–1305, 2013, DOI: 10.1109/tpwrd.2013.2258177.

[209] A. Junyent Ferré, "Control of power electronic converters for the operation of wind generation," Ph.D. dissertation, Universitat Politècnica de Catalunya, 2011, DOI: 10.5821/dissertation-2117-94751.

[210] K. Clark, N. W. Miller, and J. J. Sanchez-Gasca, "Modeling of GE wind turbine-generators for grid studies," *GE energy*, vol. 4, pp. 0885–8950, 2010, available: researchgate.net/profile/Kara-Clark-2.

[211] T.-T. Nguyen, T. Vu, S. Paudyal, F. Blaabjerg, and T. L. Vu, "Grid-forming inverter-based wind turbine generators: Comprehensive review, comparative analysis, and recommendations," *arXiv preprint arXiv:2203.02105*, 2022, DOI: 10.48550/arxiv.2203.02105.

[212] A. Egea-Alvarez, A. Junyent-Ferré, and O. Gomis-Bellmunt, "Active and reactive power control of grid connected distributed generation systems," in *Modeling and control of sustainable power systems*. Springer, 2012, pp. 47–81, DOI: 10.1007/978-3-642-22904-6_3.

[213] S. Harrison, "Advancements in converter-based frequency stability: recommendations for industrial applications," Ph.D. dissertation, University of Strathclyde, 2023, DOI: 10.48730/s53p-z861.

[214] H. Geng, D. Xu, B. Wu, and G. Yang, "Active damping for torsional vibrations in PMSG based WECS," in *2010 Twenty-Fifth Annual IEEE Applied Power*

Electronics Conference and Exposition (APEC). IEEE, 2010, pp. 2126–2131, DOI: 10.1109/apec.2010.5433530.

[215] C. Abbey and G. Joos, "Supercapacitor energy storage for wind energy applications," *IEEE transactions on Industry applications*, vol. 43, no. 3, pp. 769–776, 2007, DOI: 10.1109/tia.2007.895768.

[216] C. Nichita, D. Luca, B. Dakyo, and E. Ceanga, "Large band simulation of the wind speed for real time wind turbine simulators," *IEEE Transactions on energy conversion*, vol. 17, no. 4, pp. 523–529, 2002, DOI: 10.1109/tec.2002.805216.

[217] I. van der Hoven, "Power spectrum of horizontal wind speed in the frequency range from 0.0007 to 900 cycles per hour," *Journal of Atmospheric Sciences*, vol. 14, no. 2, pp. 160–164, 1957, DOI: 10.1175/1520-0469(1957)014<0160:psohws>2.0.co;2.

[218] K. Mongird, V. Fotedar, V. Viswanathan, V. Koritarov, P. Balducci, B. Hadjerioua, and J.Alam, "Energy storage technology and cost characterization report," Pacific Northwest National Laboratory, Tech. Rep., 2019. [Online]. Available: energystorage.pnnl.gov/pdf/PNNL-28866.pdf

[219] A. Abedini and A. Nasiri, "Output power smoothing for wind turbine permanent magnet synchronous generators using rotor inertia," *Electric Power Components and Systems*, vol. 37, no. 1, pp. 1–19, 2008, DOI: 10.1080/15325000802321998.

[220] D. Guilbert and G. Vitale, "Improved hydrogen-production-based power management control of a wind turbine conversion system coupled with multistack proton exchange membrane electrolyzers," *Energies*, vol. 13, no. 5, p. 1239, 2020, DOI: 10.3390/en13051239.

[221] C. G. Dincan, R. Wu, and P. C. Kjær, "Wind turbine with integrated hydrogen generation," U.S. Patent US 2023/0 167 804 A1, June 1, 2023, [Online]. Available: patentimages.storage.googleapis.com/5b/de/d5/bc332fa1c0cb3a/US20230167804A1.pdf.

[222] L. Sens, U. Neuling, and M. Kaltschmitt, "Capital expenditure and levelized cost of electricity of photovoltaic plants and wind turbines–development by 2050," *Renewable Energy*, vol. 185, pp. 525–537, 2022, DOI: 10.1016/j.renene.2021.12.042.

[223] E. Taibi, H. Blanco, R. Miranda, M. Carmo, D. Gielen, and R. Roesch, "Green hydrogen cost reduction: Scaling up electrolysers to meet the 1.5°c climate goal," IRENA, Tech. Rep., 2020, [Online]. Available: irena.org/publications.

[224] A. Patonia and R. Poudineh, "Cost-competitive green hydrogen: how to lower the cost of electrolysers?" Oxford Institute for Energy Studies, Tech. Rep. OIES Paper: EL 47, 2022, [Online]. Available: oxfordenergy.org/wpcms/wp-content/uploads/2022/01/Cost-competitive-green-hydrogen-how-to-lower-the-cost-of-electrolysers-EL47.pdf.

[225] M. Holst, S. Aschbrenner, T. Smolinka, C. Voglstätter, and G. Grimm, "Cost forecast for low temperature electrolysis-technology driven bottom-up prognosis for pem and alkaline water electrolysis systems," Fraunhofer Institute for Solar Energy Systems ISE, Tech. Rep., 2021, [Online]. Available: https://www.ise.fraunhofer.de/content/dam/ise/de/documents/publications/studies/cost-forecast-for-low-temperature-electrolysis.pdf.

[226] B. A. Franco, P. Baptista, R. C. Neto, and S. Ganilha, "Assessment of offloading pathways for wind-powered offshore hydrogen production: Energy and economic analysis," *Applied Energy*, vol. 286, p. 116553, 2021, DOI: 10.1016/j.apenergy.2021.116553.

[227] S. Kuczyński, M. Łaciak, A. Olijnyk, A. Szurlej, and T. Włodek, "Thermodynamic and technical issues of hydrogen and methane-hydrogen mixtures pipeline transmission," *Energies*, vol. 12, no. 3, p. 569, 2019, DOI: 10.3390/en12030569.

[228] G. F. Moore, *Electric Cables Handbook*. Oxford, UK: Blackwell Science, 1997, ISBN: 9780632040759.

[229] IEC 60364-5-54, "Low voltage electrical installations - part 5-52: Selection and erection of electrical equipment - wiring systems," International Electrotechnical Commission, IEC Int. Eng. Standard, 2009.

[230] wind-turbine-models.com, "GE General Electric GE Haliade-X 14 MW," 2024, [Online]. Available: en.wind-turbine-models.com/turbines/2320-ge-general-electric-ge-haliade-x-14-mw. Accessed: 2024-08-13.

[231] National Grid plc, "Electricity Ten Year Statement 2013: Appendix E - Technology," National Grid, Tech. Rep., 2013, Available: nationalgrideso.com.

Appendix A

Wind Farm Cost Equations

This appendix sets out additional cost equations for offshore wind farm components, which provided higher or lower costs than the median estimate used in the base case.

Wind turbines

The wind turbines cost equation provided by Dicorato *et al.* [60] is based on a 2007 report from the Department of Trade and Industry. This equation is also used in [45]. The cost of a fully-equipped wind turbine, adjusted to M€$_{2021}$, is given as

$$C_{ACWT} = \underbrace{1.1495}_{\text{inflation}} \cdot \Big(\underbrace{1.1}_{\text{inst.}} \cdot \underbrace{(2.95 \cdot \ln(P_{WT}) - 0.3752)}_{\text{wind turbine}} + \underbrace{1.5}_{\text{inst.}} \cdot \underbrace{(0.0082 \cdot D + 0.3893)}_{\text{foundation}} \Big) \tag{A.1}$$

where C_{ACWT} is the cost of the AC wind turbines in M€$_{2021}$, P_{WT} is the rated power of the wind turbine in MW, D is the sea depth in m. The installation costs are assumed to be 10% of the acquisition cost for the wind turbine and 50% for the foundation [60].

The BVG Associates cost estimate [64] gives a breakdown of the costs in £$_{2019}$ for a 1 GW wind farm with wind turbine ratings of 10 MW. The costs of the wind turbine, including foundation, transport and installation, can then be calculated using

$$C_{ACWT} = \underbrace{1.1517}_{\text{conversion}} \cdot \Big(\underbrace{1.0}_{\text{WT}} + \underbrace{0.28}_{\text{found.}} + \underbrace{0.15}_{\text{inst.}} \Big) \cdot P_{WT} \tag{A.2}$$

where C_{ACWT} is the cost of the AC wind turbines in M€$_{2021}$ and P_{WT} is the rated power of the wind turbine in MW.

AC collector cables

The Dicorato *et al.* estimate [60] used least-squares linear regression of manufacturer data in 2009 to calculate the cost of MVAC cables and cable installation. This equation is given by

$$C_{ACcab} = \underbrace{1.1495}_{\text{inflation}} \cdot \big(\underbrace{4.818 \cdot 10^{-4} \cdot CSA + 0.099}_{\text{cable}} + \underbrace{0.365}_{\text{inst.}} \big) \tag{A.3}$$

where C_{ACcab} is the cable cost in M€$_{2021}$/km, CSA is the cable cross sectional area in mm^2.

Gonzalez-Rodriguez [81] also provides cost data from two manufacturers of inter-array cables based on a 2007 report from NREL. Least-squares linear regression shows the cost data can be approximated by the equation

$$C_{ACcab} = \underbrace{1.051}_{\text{inflation}} \cdot \big(\underbrace{4.26 \cdot 10^{-4} \cdot CSA + 0.2324}_{\text{cable}} + \underbrace{0.1284}_{\text{inst.}} \big) \tag{A.4}$$

where C_{ACcab} is the cable cost in M€$_{2021}$/km, CSA is the cable cross sectional area in mm^2.

AC transmission cables

The NSG report [62] provides low, median, and high cost estimates for three-core HVAC submarine cables based on the rated power. However, the cost is only estimated for two power ratings: 350 MW and 600 MW. The median installation cost used in this report is 2 M€$_{2021}$/km, which is almost twice the value of the ETYS report, and more than four times the costs found for MVAC cable installation. The provided median costs can be approximated using the following linear equation

$$C_{HVACcab} = \underbrace{1.0519}_{\text{inflation}} \cdot \big(\underbrace{9.16 \cdot 10^{-4} \cdot P_{cab} + 0.6354}_{\text{cable}} + \underbrace{1.905}_{\text{inst.}} \big) \tag{A.5}$$

AC platform

The equation provided by Lundberg [59], and subsequently used by Dicorato *et al.*, is [60]

$$C_{ACpl} = \underbrace{0.1437}_{\text{conversion}} \cdot\big(0.7 \cdot P_{WF} + 20\big) \tag{A.6}$$

The ETYS provides cost ranges for AC platforms of wind farms with overall ratings between 200 MW and 600 MW. The median cost can be approximated using the equation

$$C_{ACpl} = \underbrace{1.452}_{\text{conversion}} \cdot\big(0.09 \cdot P_{WF} + 16\big) \tag{A.7}$$

AC/DC converters

The ETYS provides costs for onshore and offshore converters with a rated voltage of 320 kV or 500 kV, covering rated powers from 800 MW to 2.2 GW. This data was combined and linear regression was applied to approximate the cost of the AC/DC converter as a function of the rated power. This resulted in the equation

$$C_{AC/DCconv} = \underbrace{1.452}_{\text{conversion}} \cdot\big(80.4 \cdot P_{WF} + 39.334\big) \tag{A.8}$$

The NSG report provides cost ranges for converters with power ratings of 1 GW and 1.4 GW. The costs for the onshore and offshore converters were considered to be equal. The median costs can be approximated using the linear equation

$$C_{AC/DCconv} = \underbrace{1.0519}_{\text{inflation}} \cdot\big(74.5 \cdot P_{WF} + 41.892\big) \tag{A.9}$$

DC/DC converters

Lundberg [59] assumed the costs of DC/DC converters is equal to that of AC/DC converters at 1 SEK_{2003}/VA or 143.7 M€_{2021}/GW.

The estimate by Stamatiou [82] based the cost of DC/DC converters on discussions with ABB experts. They estimated costs for DC/DC converters set out in Table A.1. This estimation was also used in other cost-benefit analyses [45].

Converter Rating	Application	Cost (M€$_{2021}$/GW)
2 MW	Series DC layout	358.1
≥150 MW	Large DC layout	238.7
2 MW	Small or large DC layout	179.1

Table A.1: Stamatiou cost estimate of DC/DC converters [82]

Parker and Anaya-Lara [43] estimated the cost per conversion stage to be 60 £$_{2012}$/kVA, using a bottom-up approach. Passive rectifiers were assumed to be 20% of the full converter cost. The MFT was assumed to have the same cost as regular 50 Hz transformers. The high power DC/DC converter is assumed to consist of an inverter stage, MFT and passive rectifier, resulting in the cost function

$$C_{DC/DCconv} = \underbrace{1.3374}_{\text{conversion}} \cdot\big(1.2 \cdot \underbrace{60 \cdot P_{conv}}_{\text{one stage}}\big) + C_{TR} \tag{A.10}$$

where $C_{DC/DCconv}$ is the DC/DC converter cost in M€$_{2021}$, P_{conv} is the converter rated power in GW, and C_{TR} is the transformer cost, calculated using Equation (3.8).

DC platform

The 2011 ENTSO-E report's DC platform cost estimate is based on two case studies, including a 3500 tonnes platform supporting a 400 MW VSC converter, and a 8000 tonne platform supporting an 800 MW VSC converter. The costs can be approximated using the linear equation

$$C_{DCplat} = \underbrace{1.1143}_{\text{inflation}} \cdot\big(183.4 \cdot P_{conv} - 6.75\big) \tag{A.11}$$

The ETYS 2015 is based on larger platform sizes supporting converters with ratings of 1 GW to 2.5 GW. Weight ranges for each of these platform sizes are provided in the 2013 version of the ETYS [231]. The platform costs can be approximated using linear regression, resulting in the equation

$$C_{DCplat} = \underbrace{1.452}_{\text{conversion}} \cdot\big(311.8 \cdot P_{conv} + 106.16\big) \tag{A.12}$$

Appendix B

DC/DC Converter Design Parameters

This appendix sets out the selected design parameters of the MFT for each of the four tested DC/DC converter topologies, based on the multi-objective optimisation results.

Parameter	Unit	Value										
f	Hz	500	630	800	1000	1250	1600	2000	2500	3150	4000	5000
a		4.6	4.6	4.6	4.6	4.6	4.6	4.6	4.6	4.6	4.75	4.67
N_1		10	10	10	10	10	10	10	10	10	8	6
N_2		46	46	46	46	46	46	46	46	46	38	28
m_1		2	2	2	2	2	2	2	2	2	2	3
m_2		2	2	2	2	2	2	2	2	2	2	2
N_{l1}		5	5	5	5	5	5	5	5	5	4	2
N_{l2}		23	23	23	23	23	23	23	23	23	19	14
n_c		1	1	1	1	2	2	2	2	1	1	2
J_1	A/mm^2	3	3	3	3	4	4	4	5	5	5	5
J_2	A/mm^2	1	1	1	1	1	1	1	1	1	1	1
r_{AB}		1	1	1	1	1.5	1.5	1.5	1.5	1	1	1.5
A_{core}	m^2	0.073	0.058	0.046	0.036	0.029	0.023	0.018	0.015	0.012	0.011	0.012
A	m	0.191	0.170	0.151	0.135	0.105	0.092	0.083	0.074	0.076	0.074	0.067
B	m	0.191	0.170	0.151	0.135	0.070	0.062	0.055	0.049	0.076	0.074	0.045
A_{Cu1}	mm^2	258.0	258.0	258.0	258.0	193.5	193.5	193.5	154.8	154.8	154.8	154.8
A_{Cu2}	mm^2	263.2	263.2	263.2	263.2	263.2	263.2	263.2	263.2	263.2	263.2	263.2
w_1	mm	3.0	2.6	2.3	2.1	1.9	1.7	1.5	1.3	1.2	1.0	0.9
w_2	mm	18.3	18.3	18.3	18.3	18.3	18.3	18.3	18.3	18.3	18.3	18.3
w_w	m	0.215	0.199	0.184	0.171	0.156	0.144	0.134	0.119	0.105	0.109	0.118
h_w	m	0.652	0.652	0.652	0.652	0.652	0.652	0.661	0.652	0.663	0.598	0.398
d_{iso}	m	0.167	0.152	0.138	0.125	0.111	0.100	0.090	0.075	0.061	0.065	0.054
L	μH	80.0	63.1	49.2	39.0	33.2	25.7	20.3	16.0	11.6	9.2	7.4
MLT_1	m	1.180	1.052	0.935	0.838	0.725	0.642	0.576	0.517	0.477	0.465	0.475
MLT_2	m	2.705	2.452	2.217	2.019	1.793	1.615	1.469	1.289	1.137	1.158	1.159
MLT_{iso}	m	1.881	1.690	1.512	1.363	1.193	1.062	0.955	0.835	0.739	0.743	0.713
V_{core}	m^3	0.182	0.138	0.104	0.080	0.059	0.045	0.035	0.027	0.021	0.019	0.016
M_{core}	kg	1333.7	1009.6	759.5	583.7	434.8	327.6	256.4	196.4	156.0	138.2	114.0
V_{tot}	m^3	0.764	0.606	0.479	0.387	0.285	0.227	0.188	0.144	0.119	0.112	0.087
M_{tot}	kg	1633.3	1251.4	954.2	743.5	552.8	423.4	336.9	258.4	208.2	187.8	153.2

Table B.1: SAB1 MFT parameters

Parameter	Unit	Value										
f	Hz	500	630	800	1000	1250	1600	2000	2500	3150	4000	5000
a		5.25	5.3	5.3	5.25	5.25	5.25	5.25	5.25	5.4	5.25	5.25
N_1		8	10	10	8	8	8	8	8	10	8	8
N_2		42	53	53	42	42	42	42	42	54	42	42
m_1		2	2	2	2	2	2	2	2	2	2	2
m_2		1	1	1	1	1	2	2	2	2	2	2
N_{l1}		4	5	5	4	4	4	4	4	5	4	4
N_{l2}		42	53	53	42	42	21	21	21	27	21	21
n_c		1	1	1	1	1	1	1	1	1	1	1
J_1	A/mm^2	2	2	2	2	2	2	3	3	3	4	4
J_2	A/mm^2	3	1	1	2	2	1	1	1	1	1	1
r_{AB}		1.5	1.5	1.5	1.5	1.5	1.5	1.5	1.5	1.5	1.5	1.5
A_{core}	m^2	0.047	0.030	0.024	0.024	0.019	0.015	0.012	0.009	0.006	0.006	0.005
A	m	0.189	0.150	0.133	0.133	0.119	0.105	0.094	0.084	0.067	0.067	0.060
B	m	0.126	0.100	0.089	0.089	0.080	0.070	0.063	0.056	0.045	0.044	0.040
A_{Cu1}	mm^2	137.1	137.1	137.1	137.1	137.1	137.1	91.4	91.4	91.4	68.5	68.5
A_{Cu2}	mm^2	29.2	87.7	87.7	43.9	43.9	87.7	87.7	87.7	87.7	87.7	87.7
w_1	mm	3.0	2.6	2.3	2.1	1.9	1.7	1.5	1.3	1.2	1.0	0.9
w_2	mm	6.1	10.6	10.6	7.5	7.5	10.6	10.6	10.6	10.6	10.6	10.6
w_w	m	0.453	0.438	0.398	0.363	0.334	0.246	0.208	0.193	0.165	0.156	0.145
h_w	m	0.677	1.091	1.091	0.735	0.735	0.433	0.433	0.433	0.557	0.433	0.433
d_{iso}	m	0.204	0.188	0.169	0.158	0.144	0.094	0.075	0.068	0.054	0.050	0.045
L	μH	90.0	71.1	55.9	44.8	35.7	26.5	21.0	16.6	13.0	10.1	8.0
MLT_1	m	0.922	0.739	0.657	0.655	0.587	0.520	0.466	0.418	0.336	0.332	0.298
MLT_2	m	3.176	2.791	2.505	2.389	2.165	1.684	1.449	1.314	1.071	1.032	0.935
MLT_{iso}	m	2.305	1.947	1.738	1.690	1.523	1.216	1.055	0.949	0.762	0.740	0.664
V_{core}	m^3	0.271	0.196	0.147	0.118	0.090	0.049	0.036	0.028	0.018	0.015	0.012
M_{core}	kg	1988.5	1439.6	1077.0	866.6	657.5	362.0	266.8	202.4	132.4	112.5	86.1
V_{tot}	m^3	1.647	1.712	1.352	0.898	0.720	0.298	0.212	0.171	0.132	0.102	0.083
M_{tot}	kg	2682.1	2206.1	1687.3	1261.6	976.9	491.9	358.9	277.9	192.5	158.5	124.3

Table B.2: SAB3 MFT parameters

Parameter	Unit	Value										
f	Hz	500	630	800	1000	1250	1600	2000	2500	3150	4000	5000
a		2.8	2.8	2.8	2.8	3	2.8	2.8	3	2.8	2.89	2.89
N_1		10	10	10	10	8	10	10	8	10	9	9
N_2		28	28	28	28	24	28	28	24	28	26	26
m_1		2	2	2	2	2	2	2	2	2	3	3
m_2		2	2	2	2	2	2	2	2	2	2	2
N_{l1}		5	5	5	5	4	5	5	4	5	3	3
N_{l2}		14	14	14	14	12	14	14	12	14	13	13
n_c		1	1	1	1	3	1	1	1	1	1	1
J_1	A/mm^2	3	3	4	4	5	5	5	5	5	5	5
J_2	A/mm^2	1	1	1	1	1	1	1	1	1	1	1
r_{AB}		0.5	0.5	0.5	0.5	1	0.5	0.5	0.5	0.5	0.5	0.5
A_{core}	m^2	0.085	0.068	0.053	0.043	0.043	0.027	0.021	0.021	0.014	0.012	0.009
A	m	0.146	0.130	0.116	0.103	0.084	0.082	0.073	0.073	0.058	0.054	0.049
B	m	0.292	0.260	0.231	0.207	0.084	0.163	0.146	0.146	0.116	0.109	0.097
A_{Cu1}	mm^2	182.7	182.7	137.1	137.1	109.6	109.6	109.6	109.6	109.6	109.6	109.6
A_{Cu2}	mm^2	263.2	263.2	263.2	263.2	263.2	263.2	263.2	263.2	263.2	263.2	263.2
w_1	mm	3.0	2.6	2.3	2.1	1.9	1.7	1.5	1.3	1.2	1.0	0.9
w_2	mm	18.3	18.3	18.3	18.3	18.3	18.3	18.3	18.3	18.3	18.3	18.3
w_w	m	0.332	0.306	0.264	0.244	0.256	0.198	0.184	0.193	0.158	0.151	0.141
h_w	m	0.397	0.397	0.397	0.397	0.340	0.397	0.397	0.341	0.471	0.369	0.369
d_{iso}	m	0.285	0.260	0.218	0.199	0.211	0.154	0.140	0.149	0.115	0.087	0.076
L	μH	255.3	201.5	158.6	126.1	110.8	78.0	62.0	49.6	38.6	29.3	23.1
MLT_1	m	1.204	1.074	0.954	0.855	0.874	0.678	0.608	0.607	0.487	0.464	0.416
MLT_2	m	3.668	3.337	2.878	2.625	2.736	2.082	1.899	1.972	1.576	1.414	1.283
MLT_{iso}	m	2.375	2.143	1.852	1.675	1.739	1.313	1.186	1.221	0.963	0.835	0.745
V_{core}	m^3	0.175	0.131	0.095	0.072	0.065	0.041	0.031	0.029	0.020	0.015	0.012
M_{core}	kg	1279.5	958.5	698.5	531.3	479.1	297.0	227.8	212.9	148.4	109.5	84.5
V_{tot}	m^3	0.823	0.651	0.472	0.379	0.331	0.227	0.184	0.176	0.140	0.102	0.084
M_{tot}	kg	1613.5	1227.6	894.1	691.1	618.9	395.3	309.1	291.1	212.2	156.8	124.1

Table B.3: DAB1 MFT parameters

Parameter	Unit	Value										
f	Hz	500	630	800	1000	1250	1600	2000	2500	3150	4000	5000
a		3.07	3.1	3.1	3.07	3.1	3.1	3.25	3.2	3.2	3.25	3.2
N_1		15	10	10	15	10	10	8	10	10	8	10
N_2		46	31	31	46	31	31	26	32	32	26	32
m_1		3	2	2	3	2	2	2	2	2	2	2
m_2		1	1	1	1	1	1	2	2	2	2	2
N_{l1}		5	5	5	5	5	5	4	5	5	4	5
N_{l2}		46	31	31	46	31	31	13	16	16	13	16
n_c		1	1	1	1	1	1	1	1	1	1	1
J_1	A/mm^2	1	2	2	1	3	3	4	4	4	5	5
J_2	A/mm^2	1	2	2	1	2	2	1	1	1	1	1
r_{AB}		1.5	1.5	1.5	1.5	1.5	1.5	1.5	1.5	1.5	1.5	1.5
A_{core}	m^2	0.025	0.030	0.024	0.013	0.015	0.012	0.012	0.008	0.006	0.006	0.004
A	m	0.138	0.150	0.133	0.097	0.107	0.094	0.094	0.075	0.067	0.067	0.053
B	m	0.092	0.100	0.089	0.065	0.071	0.063	0.063	0.050	0.045	0.044	0.036
A_{Cu1}	mm^2	199.4	99.7	99.7	199.4	66.5	66.5	49.8	49.8	49.8	39.9	39.9
A_{Cu2}	mm^2	87.7	43.9	43.9	87.7	43.9	43.9	87.7	87.7	87.7	87.7	87.7
w_1	mm	3.0	2.6	2.3	2.1	1.9	1.7	1.5	1.3	1.2	1.0	0.9
w_2	mm	10.6	7.5	7.5	10.6	7.5	7.5	10.6	10.6	10.6	10.6	10.6
w_w	m	0.502	0.468	0.426	0.389	0.335	0.305	0.241	0.201	0.186	0.182	0.153
h_w	m	0.947	0.543	0.543	0.947	0.543	0.543	0.268	0.330	0.330	0.268	0.330
d_{iso}	m	0.204	0.209	0.189	0.150	0.144	0.130	0.092	0.072	0.065	0.063	0.049
L	μH	186.7	150.0	118.0	92.3	75.1	58.5	44.9	35.3	27.8	21.9	17.1
MLT_1	m	0.698	0.739	0.657	0.498	0.527	0.467	0.466	0.376	0.336	0.332	0.268
MLT_2	m	2.905	2.936	2.643	2.152	2.077	1.862	1.582	1.280	1.158	1.138	0.920
MLT_{iso}	m	1.952	2.032	1.819	1.413	1.432	1.276	1.122	0.898	0.805	0.792	0.632
V_{core}	m^3	0.157	0.150	0.111	0.068	0.061	0.045	0.032	0.019	0.014	0.013	0.008
M_{core}	kg	1153.0	1102.1	810.0	497.8	448.3	329.1	235.2	141.6	106.1	95.5	59.3
V_{tot}	m^3	1.761	1.202	0.936	0.928	0.536	0.418	0.198	0.136	0.109	0.093	0.067
M_{tot}	kg	1964.6	1632.9	1227.1	935.1	688.7	518.5	322.1	203.3	156.4	138.1	90.9

Table B.4: DAB3 MFT parameters

Appendix C

Model Parameters

Parameter	Symbol	Value	Unit
Rated power	P_{WT}	15	MW
Rotor radius	R_r	120	m
Rated speed	ω_{nom}	6.935	rpm
Air density	ρ	1.225	kg/m^3

(a) Wind turbine

Parameter	Symbol	Value
1st coefficient	c_1	0.5
2nd coefficient	c_2	116
3rd coefficient	c_3	0.4
4th coefficient	c_4	0
5th coefficient	c_5	0
6th coefficient	c_6	5
7th coefficient	c_7	21
8th coefficient	c_8	0.08
9th coefficient	c_9	0.035

(b) Characteristic coefficients

Parameter	Symbol	Value	Unit
Rotor inertia	J_r	3.36	pu
Machine inertia	J_m	0.82	pu
Spring constant	k	3.86	pu
Damping constant	c	1.5	pu
Natural freq.	ω_{dt}	0.385	rad/s

(c) Mechanical drivetrain

Parameter	Symbol	Value	Unit
Voltage	V_{DC}	1200	V
Capacitance	C	33	mF

(d) DC link

Parameter	Symbol	Value	Unit
Nominal frequency	f_{nom}	10	Hz
Line voltage	V_{gen}	690	V
Stator resistance	R_s	1.9	mΩ
Stator inductance	$L_{d,q}$	173.4	µH
Flux linkage	λ_m	9.02	Wb
Pole pairs	p	86	

(e) PMSG

Parameter	Symbol	Value	Unit
Rated power	P_{conv}	15	MW
Line voltage	V_{gen}	690	V
Resistance	R_{conv}	0.317	mΩ
Inductance	L_{conv}	10.1	µH

(f) AC/DC converter

Parameter	Symbol	Value	Unit
Rated power	P_{EL}	15	MW
Nominal voltage	V_{EL}	800	V
Num. stacks	N_{EL}	3	
Minimum power	P_{ELmin}	2	MW
Nom. density	i_{nom}	2.0	A/mm^2
Cell area	A_{cell}	2500	mm^2
Gibb's change	ΔG	223.1	kJ/mol
Transfer coeff.	α	0.38	
Exchange dens.	J_0	13.7	μA/cm^2
Limiting dens.	J_L	2.6	A/cm^2
BoL cell resist.	r_{BoL}	0.137	Ω/cm^2
EoL cell resist.	r_{EoL}	0.236	Ω/cm^2

(g) Electrolyser

Table C.1: Model parameters

Parameter	Symbol	Value
Speed P. gain	$K_{p\beta}$	5
Speed I. gain	$K_{i\beta}$	5
Power balance P. gain	$K_{p_{\Delta\beta}}$	5
Power balance D. gain	$K_{d_{\Delta\beta}}$	5
Power balance filter coeff.	$N_{d_{\Delta\beta}}$	10

(a) Pitch controller

Parameter	Symbol	Value
DC voltage P. gain	K_{p_V}	5
DC voltage I. gain	K_{i_V}	20
ICC P. gain	$K_{p_{ICC}}$	0.00867
ICC I. gain	$K_{i_{ICC}}$	0.09522

(b) Machine-side converter control

Parameter	Symbol	Value
VSM P. gain	$K_{p_{VSM}}$	1.274×10^{-6}
VSM I. gain	$K_{i_{VSM}}$	1.047×10^{-4}
AC voltage P. gain	$K_{p_{VAC}}$	200
AC voltage I. gain	$K_{i_{VAC}}$	500
ICC P. gain	$K_{p_{ICC}}$	1.01×10^{-3}
ICC I. gain	$K_{p_{ICC}}$	0.03174

(c) Line-side converter control

Parameter	Symbol	Value
PLL P. gain	$K_{p_{PLL}}$	0.3219
PLL I. gain	$K_{i_{PLL}}$	314.2
Droop P. gain	$K_{p_{droop}}$	5×10^{6}
EL voltage P. gain	$K_{p_{VEL}}$	3.665
EL voltage I. gain	$K_{p_{VEL}}$	407.12
ICC P. gain	$K_{p_{ICC}}$	1.01×10^{-3}
ICC I. gain	$K_{p_{ICC}}$	0.03174

(d) Electrolyser-side converter control

Table C.2: Model control parameters